

PROTONATABLE HYDROGEN-BONDED NETWORKS IN MICROBIAL RHODOPSINS STUDIED BY INFRARED SPECTROSCOPY



Im Fachbereich Physik der Freien Universität Berlin eingereichte
Dissertation zur Erlangung des Grades eines Doktors der
Naturwissenschaft (Dr. rer. nat.)

Author: *Mattia Saita*

October 18, 2019

First supervisor: Prof. Dr. Joachim Heberle

Second supervisor: Prof. Dr. Holger Dau

Date of defence: 20/10/2018

Abstract

Microbial rhodopsins are a class of widely studied membrane proteins that harbour a form of vitamin A as a cofactor and are therefore capable to detect visible light. These proteins have recently raised interest thanks to the application of some of them, typically the light-gated channels called channelrhodopsins, in the growing field of optogenetics. Optogenetics makes use of microbial rhodopsins to remotely activate specific neuronal cells with light, aiming to understand the function of complex neural networks in mammals and other organisms. In this thesis I propose an essay to test the function of yeast-expressed channelrhodopsins and I report on the photochemistry of the last intermediate in the photocycle of channelrhodopsin-2, with direct implications to the design of optimized optogenetic tools.

Another microbial rhodopsin is bacteriorhodopsin, a light activated proton pump. As for most proteins in the rhodopsin family, proton transfers are fundamental steps in the functional mechanism of bacteriorhodopsin. Important players in proton translocation are hydrogen-bonded networks of amino acids and water molecules, and the protonation of such networks can be detected as unusually broad transient signatures in the infrared spectral range, called continuum bands.

In this frame, the main contribution of this thesis work was to investigate the continuum band in bacteriorhodopsin with new approaches, based on infrared spectroscopy. We investigated the kinetics of the continuum band and compared it to the proton release and uptake from bacteriorhodopsin to and from the bulk solution. The results led us to identify two distinct hydrogen-bonded networks that give rise to two continuum bands at different times during the photoreaction. The first continuum band reflects the proton release from the protein to the bulk water and further measurements with polarization-resolved spectroscopy revealed an unexpected dichroism. The protonated network is in fact oriented along the membrane plane, a result that is supported by theoretical simulations. Investigations of the effect of protein solubilization in bacteriorhodopsin showed also that the membrane environment is important for the stabilization of such hydrogen-bonded networks.

In conclusion these novel approaches could be applied to study continuum bands in other proteins. Chloride pumping rhodopsins are good candidates as in this thesis work I show the presence of continuum bands in two proteins of this class. Furthermore, the deep understanding of protonation dynamics via hydrogen-bonded networks is highly relevant not only for the study of microbial rhodopsins but can be applied to more complex systems.

Zusammenfassung

Mikrobielle Rhodopsine bilden eine Klasse intensiv charakterisierter Membranproteine. Als Chromophor tragen sie ein Vitamin A-Derivat, den sogenannten Retinal Kofaktor. Lichtgetriebene Ionenkanäle wie Kanalrhodopsine spielen im Bereich der Optogenetik eine zentrale Rolle. In der Optogenetik werden mikrobielle Rhodopsine verwendet, um einzelne Neuronen durch Licht anzuregen. Ziel ist es, das komplexe Neuronennetzwerk von Säugetieren und anderen Organismen zu verstehen. In dieser Arbeit stelle ich ein Konzept vor, mit dem die Funktion von Kanalrhodopsinen untersucht werden kann. Am Beispiel von Channelrhodopsin-2 stelle ich dar, wie das finale Intermediat des Fotozyklus charakterisiert werden konnte. Das hat direkte Auswirkungen auf die Kanaleigenschaften und stellt einen wichtigen Schritt in der Optimierung für optogenetische Anwendungen dar.

Ein anderes mikrobielles Rhodopsin ist die lichtgetriebene Protonenpumpe Bakteriorhodopsin. Wie für viele andere Proteine dieser Proteinfamilie wird der Reaktionsmechanismus vor allem durch Protonentransferschritte bestimmt. Kandidaten für Protonierungsreaktionen sind Wasserstoffbrückennetzwerke aus polaren und protonierbaren Aminosäuren sowie konservierte Wassermoleküle. Die Protonierung dieser Netze führt zu ungewöhnlich breiten Absorptionsbanden im Infraroten, den sogenannten Kontinuumsbanden.

Kern dieser Arbeit ist die Untersuchung der Kontinuumsbanden in mikrobiellen Rhodopsinen per zeitaufgelöster Infrarot Spektroskopie. Dazu werden kinetische Infrarotdaten mit dem zeitlichen Verlauf von Protonenaufnahme und -abgabe aus dem und an das umgebenden Medium verglichen. Die Ergebnisse erlauben die Identifizierung von individuellen Wasserstoffbrückennetzwerken, deren Protonierungsdynamik mit zwei zeitlich getrennten Kontinuumsbanden korreliert. Das erste Kontinuumsband zeigt die Protonenabgabe vom Protein an das Medium. Dabei ließ polarisationsaufgelöste Infrarotspektroskopie einen unerwarteten Dichroismus erkennen, und tatsächlich konnte gezeigt werden, dass das Wasserstoffbrückennetzwerken entlang der Membranebene orientiert ist. Dies wurde durch theoretische Betrachtungen unterstützt. Untersuchungen mit solubilisiertem Bakteriorhodopsin zeigten, dass die Membranumgebung für die Stabilisierung der Wasserstoffbrückennetzwerke von entscheidender Bedeutung ist.

Zusammenfassend sollte erwähnt sein, dass diese neue Untersuchungsmethode auch für die Untersuchung von Kontinuumsbanden in anderen Proteinen geeignet sind. Ich konnte in dieser Arbeit bereits zeigen, dass Chlorid-pumpende Rhodopsine ein Kontinuumsband besitzen. Ein tiefgreifendes Verständnis der Protonierungsdynamiken ist von universeller Relevanz für Proteine und Enzyme, deren Funktion an Protonentransferreaktionen gekoppelt ist, nicht nur für mikrobielle Rhodopsine.

Publications related to the PhD

V. A. Lorenz-Fonfria, M. Saita, T. Lazarova, R. Schlesinger, & J. Heberle (2017). "pH-sensitive vibrational probe reveals a cytoplasmic protonated cluster in bacteriorhodopsin." *Proc. Natl. Acad. Sci.*, 201707993.

A. Harris, M. Saita, T. Resler, A. Hughes-Visentin, R. Maia, F. Pranga-Sellnau, A. N. Bondar, J. Heberle, & L. S. Brown (2018). "Molecular details of the unique mechanism of chloride transport by a cyanobacterial rhodopsin." *Phys. Chem. Chem. Phys.*, 20(5), 3184-3199

J. O. Daldrop*, M. Saita*, M. Heyden, V. A. Lorenz-Fonfria, J. Heberle, & R. R. Netz (2018). "Orientation of non-spherical protonated water clusters revealed by infrared absorption dichroism." *Nat. Commun.*, 9(1), 311.

*the authors contributed equally to the work

M. Saita, F. Pranga-Sellnau, T. Resler, R. Schlesinger, J. Heberle, & V. A. Lorenz-Fonfria (2018). "Photoexcitation of the P_4^{480} state induces a secondary photocycle that desensitizes channelrhodopsin-2." *J. Am. Chem. Soc.*, 140(31), 9899–9903

Contents

1	Introduction	1
1.1	Integral membrane proteins	1
1.1.1	Protein-bound water molecules in microbial rhodopsins	2
1.2	Bacteriorhodopsin and proton pumping	3
1.2.1	The photocycle of bacteriorhodopsin	3
1.2.2	Bacteriorhodopsin and the continuum band	5
1.2.3	Protonated and neutral water clusters in proteins can give rise to continuum bands	7
1.2.4	An unusual broad infrared absorption	8
1.2.5	Molecular probes for proton release and uptake in proteins	9
1.3	Retinal proteins and optogenetics	10
1.3.1	Channelrhodopsin-2 and its photocycle(s)	11
1.3.2	Chloride pumps	14
1.4	Aim of the thesis	15
2	Methods	16
2.1	Infrared spectroscopy	16
2.1.1	Fourier transform infrared spectroscopy	18
2.1.2	Time-resolved FTIR spectroscopy	20
2.1.3	Attenuated total reflection spectroscopy	21
2.1.4	Polarization-resolved FTIR spectroscopy	22
2.1.5	Quantum cascade lasers as infrared light source	28
2.2	Visible and fluorescence spectroscopy	29
2.2.1	Time-resolved visible spectroscopy	31
2.3	Data analysis	31
2.3.1	Global fit kinetic analysis	31
2.3.2	Singular value decomposition	32
2.4	Sample preparation	33
2.4.1	Preparation of hydrated films for FTIR	33
2.4.2	Preparation of samples for flash photolysis	33
2.4.3	Proteoliposomes formation	34
3	Results	35
3.1	The kinetics of the continuum band in BR	35

3.1.1	MES buffer as pH-sensitive vibrational probe: an accurate kinetic study of the proton release and uptake in BR	35
3.1.2	The proton uptake complex, a new protonated cluster in the photocycle of BR	46
3.1.3	Other potential vibrational probes	48
3.2	The dichroism of broad IR difference bands during the photocycle of BR	51
3.2.1	The dichroism of the continuum band in BR	51
3.2.2	The dichroism of a broad IR band above 2200 cm^{-1} . . .	64
3.3	The influence of the protein environment on the continuum band	68
3.4	Continuum bands measured in Cl-pumping rhodopsins	73
3.4.1	A continuum band in halorhodopsin	73
3.4.2	A broad transient band in MastR	74
3.5	The functionality of lipid-reconstituted ChR2	76
3.5.1	The influence of the reconstitution of ChR2 on the protein photocycle	76
3.5.2	Co-reconstitution of BR and ChR2 in proteoliposomes to probe the functionality of yeast-expressed ChR2 . . .	80
3.6	The photocycle of the P_4 intermediate of ChR2	82
3.6.1	The P_4^{480} intermediate is photoactive	83
3.6.2	The excitation of P_4^{480} leads to a low accumulated P_2 -like and a P_3 -like intermediates	84
3.6.3	The P_4^{480} photocycle	88
4	General discussion	90
4.1	A novel method for the investigation of solvent-proton transfers with IR spectroscopy	90
4.2	New insight on bacteriorhodopsin's photoreaction	90
4.3	Polarization-resolved FTIR is a powerful method for the shape determination of water clusters in proteins	92
4.4	The continuum band is not a prerequisite for proton pumping in bacteriorhodopsin	93
4.5	Continuum bands are not exclusive to proton pumping proteins	94
4.6	Yeast-expressed and reconstituted CrChR2 is functional as a channel	95
4.7	The photocycle of the P_4^{480} intermediate of ChR2 and its relevance for optogenetic applications	96
A	Appendix	119
A.0.1	Determination of ATR incident angle from water dichroism	119
A.0.2	IR and visible Kinetics of pH-sensitive probes during the photocycle of BR	120
A.0.3	Polarization-resolved ATR difference spectroscopy with samples at different hydrations	122
A.0.4	Polarization-resolved transmission difference spectroscopy with a serie of tilting angles	127

A.0.5	Photoselection experiment in the xy plane of BR	129
A.0.6	Effect of the protein environment on the continuum band: absorption spectra and pumping essays	131
A.0.7	ChR2 reconstituted in liposomes	132
A.0.8	BR proteoliposomes inwardly pump protons with light .	138
A.0.9	Proton transfers in MastR	139
A.0.10	The photocycle of the P_4 intermediate of ChR2	141

Chapter 1

Introduction

1.1 Integral membrane proteins

A biological membrane is a selectively permeable barrier that encloses living cells or organelles. Biomembranes are fundamental for compartmentization, bioenergetics and communication. The inner part of the membrane is hydrophobic while the surface is hydrophilic and interacts with the surrounding medium.

One of the main components of biological membranes are lipids, with hydrophobic tails and hydrophilic headgroups, they form the structure of the membrane. Another important component of biomembranes are transmembrane proteins, they span across the membrane and are responsible for communication, sensing and transport among other functions. Transmembrane proteins perform key tasks for all living organisms such as respiration and photosynthesis [1].

Typically biomembranes have the thickness of a few nanometers therefore cannot be studied in details with standard microscopy methods where the diffraction limit is one order of magnitude higher than the dimensions of proteins and lipids. Proteins consist of chains of amino acid residues, bonded together via peptide bonds and arranged in regular conformations called secondary structures. The canonical method to visualize proteins is to arrange them in a crystalline lattice and analyse the x-ray diffraction.

Transmembrane proteins are more difficult to crystalize than soluble proteins and often their functions involve conformational and protonation changes that are difficult to track with x-ray crystallography. Spectroscopy plays therefore a fundamental role in the study of this biological machineries.

Among the many transmembrane protein families, there is a group harbouring a retinal molecule as cofactor, which is an external molecule that is important for the protein function. Retinal is a form of vitamin A and is capable of absorbing visible light. The most important protein of this family is visual rhodopsin, that is responsible for vision and is found in the rod cells of higher organisms like humans [2].

In the same family of visual rhodopsin are microbial rhodopsins, proteins that are found in simpler organisms like Archaea and Bacteria, but also in

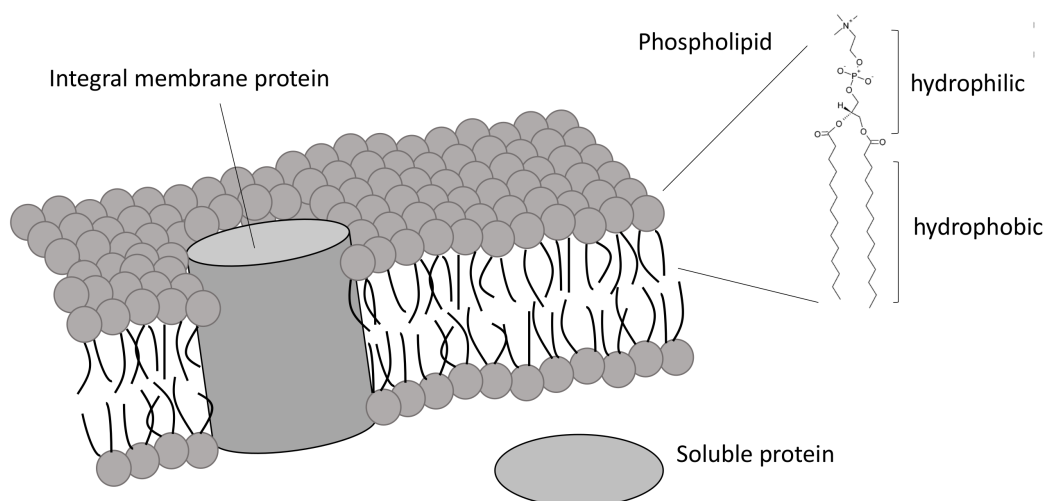


Figure 1.1: Schematic figure of a simplified biomembrane.

Eukaryota like green algae [2]. Their function spans from proton [3], cation [4] or anion [5] pumping, to channeling [6] and sensing [7]. All this microbial rhodopsins share a common structural motif with seven transmembrane helices (usually labelled from A to G) and the retinal molecule covalently attached to a lysine on helix G [2]. Another common feature is the isomerization of the retinal from *trans* to *cis* upon light absorption [2].

As water is essential for life, biomembranes are surrounded by water molecules and membrane proteins count on them for their function.

1.1.1 Protein-bound water molecules in microbial rhodopsins

Crystal structures of microbial rhodopsins revealed that also their membrane-embedded part is rich of water molecules that can be considered as cofactors [8]. The most studied protein of the family is bacteriorhodopsin (BR). It harbours in the ground state up to 17 water molecules that are stable enough to appear in a crystal structure, 9 of which are in the transmembrane part (PDB: 5b6v [9]). Intra-protein water molecules are often arranged in clusters, this is the case for BR where they form two clusters in the extracellular side of the protein in the ground state and a transiently-formed cluster in the cytoplasmic side during one of the intermediates [8], see subsection 1.2.2 for more details. In BR, a proton pump, water is necessary to stabilize protonated amino acids, to store protons and to efficiently shuttle them during the protein photocycle [8]. Changing the hydration level in a BR sample strongly affects its functional mechanism [10].

Water clusters similar to the ones found in BR can be observed also in other microbial rhodopsins with different functions, as the chloride pump halorhodopsin [11] or the phototaxis receptor sensory rhodopsin II [7]. Recently, spectroscopic signatures of functional water molecules have been found

for a cyanobacterial chloride pump [12]. Water molecules play also a crucial role in channelrhodopsins, where the hydration of helices correlates with cation conductance [13].

1.2 Bacteriorhodopsin and proton pumping

Bacteriorhodopsin is a model for retinal proteins and for membrane proteins in general as its structure was the first to be determined with electron crystallography in 1975 [14]. More than 40 years of research on this protein led to around 2000 publications that have "bacteriorhodopsin" in the title (source: pubmed.gov) and a deep understanding of its structure [15] and its molecular mechanism [16].

BR is a transmembrane protein found in Archea that generates an electrochemical proton gradient across the membrane by outwardly pumping protons upon visible light illumination. Transmembrane proton pumping is central in bioenergetics and is one of the most common chemical reaction in living organisms [17]. In *Halobacterium salinarum* the protein, ~ 26 kDa in size, is expressed in low oxygen conditions in a part of the membrane called purple membrane (PM) where it is the only protein constituent and forms a two-dimensional lattice. The proteins are arranged in tightly packed trimers with ~ 10 lipids per monomer [3].

1.2.1 The photocycle of bacteriorhodopsin

After light absorption BR undergoes a photocycle consisting in several intermediate states eventually going back to the resting state. During the photocycle the protein translocates one proton from the cytoplasmic to the extracellular side. The protein structure, recently obtained in a time-resolved experiment with an x-ray free electron laser [9], is shown in Fig. 1.2, together with a scheme of the photocycle.

After the absorption of a green photon (the protein maximum absorption in the visible is at 570 nm), the retinal isomerizes from an all-*trans* to a 13-*cys* conformation. This ultra-fast reaction triggers a series of thermal reactions that result in spectrally-distinguishable intermediate states called K, L, M, N and O. Each reaction step consists of a number of specific events, some of the steps are unidirectional (single arrows in Fig. 1.2), others bidirectional [3]; the whole photocycle is over within 100 ms at neutral pH [18].

As BR is a proton pump, key events in the photocycle are the proton transfer reactions, highlighted in Fig. 1.2 [16, 19]. The retinal molecule is covalently bound to the protein via a protonated Schiff base, formed with the amino acid K216 and hydrogen-bonded via a water molecule to the aspartates D85 and D212. The first proton transfer happens between the Schiff base and D85, in the L to M transition. D85 will remain protonated until the end of the photocycle. Consequent to the protonation of D85 is the appearance of a proton at the protein surface [20, 21].

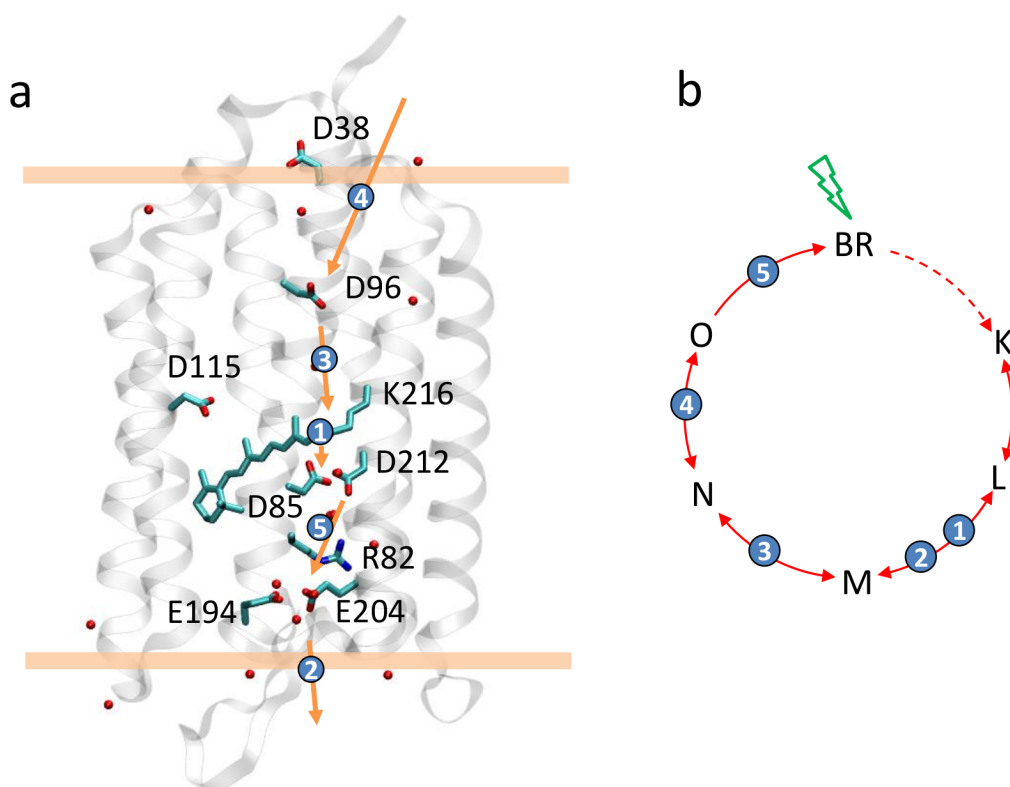


Figure 1.2: The protein structure in the ground state (a) shown with some key amino acids highlighted and labelled (PDB entry 5b6v). In cyan carbon atoms, oxygen atoms are red (red dots are the oxygens of water molecules) and blue is for nitrogen. Yellow horizontal bars represent the limits of the hydrophobic membrane. Proton transfer steps are shown with arrows, the order of the events is summarized in the photocycle (b).

The proton release to the extracellular side is caused by the deprotonation of an unknown group, called proton release complex (PRC). The identity of the PRC has been debated for a long time and is one of the main focuses of this thesis work.

A closer investigation of the M intermediate led to the splitting into two separate intermediates M_1 and M_2 , connected via an irreversible and spectrally invisible (detectable in the IR) transition that allows a switch mechanism in the proton pumping function that prevents protons to flow back [22, 23]. The intermediates after M decay in an equilibrated mixture to the ground state at standard conditions (room temperature and neutral pH) [24], although pure intermediates can be obtained in particular conditions [25].

The decay of the M intermediate (or M_2) to N is defined by the reprotonation of the Schiff base from D96 (step 3 in Fig. 1.2) [26] after their pK_a adjust to allow for this transition [27]. Like the M intermediate, N can be split into two intermediates N_1 and N_2 whose relative population is pH-dependent in a way that favours N_1 at high pH and vice versa [28, 29].

The next step of proton transfer is believed to be the reprotonation of

D96 from the bulk solution, from the N to the O intermediates. There is no agreement whether this reaction happens in the N_1 to N_2 transition [17] or in the N_2 to O transition [30]. The last step of the photocycle is the deprotonation of D85 in favour of the PRC, this reaction is affected by mutations of the glutamates E204 and E194 [31]; in this step D212 is transiently protonated [32, 33]. The aspartic acid D115 is protonated throughout the whole photocycle but is not involved in proton transfer reactions [34].

1.2.2 Bacteriorhodopsin and the continuum band

The term "continuum band" has been used recently to describe a transient negative difference-absorption band measured with time-resolved infrared spectroscopy during the photocycle of BR [35, 8].

In the proton translocation pathway of BR from the intracellular to the extracellular membrane side, the first step of the proton transfer is from the Schiff base to D85, as already mentioned in 1.2.1. The steps of proton release from D85 to the extracellular side of the purple membranes are under debate and the unusual continuum band is believed to come from the proton release complex of BR.

Investigating the identity of the PRC as a bridge between D85 and the bulk, a first candidate was E204 [36]; later it has been shown via mutation of E204 and time-resolved FTIR measurements that no bands could be assigned to a deprotonation of E204 during the L-to-M transition [35]. A H-bonded network of water molecules and amino acids including R82, E204 and E194 has been instead proposed as PRC. This scenario is after 20 years still widely accepted [19, 8] although an alternative hypothesis describes the deprotonation of R82 during the M state, with the proton reaching the surface via E204 or E194 [37]. Molecular dynamics simulations showed the possibility of a shared proton between the two glutammates [38, 39] and E194 has been indicated as the possible final release group [40], completing a large group of candidates for the role of proton release complex.

The accepted model is that of a protonated group consisting of a hydrogen-bonded network of several water molecules, charged amino acid side chains and backbone atoms. This protonated network has a broad IR absorption, reminiscent of that of a solution with high concentration of protons [41] (see 1.2.4), called continuum absorption. The pK_a of the PRC is 5.8 [21]. This protonated group is believed to deprotonate after the protonation of D85 and the subsequent down-flip of R82 [3](see the crystal structures in the resting state and after 250 ns from the laser flash in Fig. 1.3 [9]).

The deprotonation results into a transient broad negative band observed above 1770 cm^{-1} in a time-resolved FTIR experiment [35]. This band vanishes or its intensity is drastically affected when E204, E194 and R82 are mutated [42], localizing its molecular origin to this cluster of amino acids. A small spectral shift has been observed in a experiment using isotopically labelled water [43], indicating an important role of water molecules in the continuum band signal.

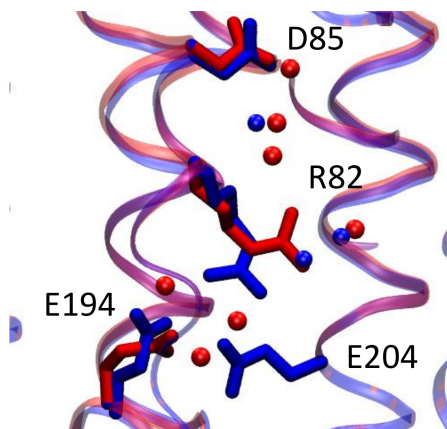


Figure 1.3: Comparison of the BR resting state (red, PDB:5b6v the same showed in Fig. 1.2) and the M state (blue, PDB:5h2o) of the extracellular side of BR [9]. The amino acids D85, R82, E194 and E204 have been highlighted together with the water molecules. The major differences are the downflip of R82, the turn of E194 and the rearrangement of several water molecules.

In BR also another stable cluster of water molecules is present in the protein ground state, forming a neutral hydrogen-bonded network that is often referred to as the "pentagonal cluster" due to its geometry [44, 45]. These waters, showed in Fig. 1.4 stabilize an electric quadrupole inside the protein, with the two positive charges of the protonated Schiff base and R82 balanced by the two aspartates D85 and D212.

The three water molecules W401, W402 and W406 of this cluster give rise to clear bands in a FTIR light-induced difference experiment, marker of the profound changes in the arrangement of this hydrogen-bonded network after the retinal isomerization [46, 45, 47, 43].

The infrared absorption of intraprotein water molecules can differ from the absorption of the bulk water due to the different environment and the different character of the hydrogen bonds, that can be weaker or stronger than in bulk [48, 49]. Water molecules in the pentagonal cluster can give rise to broad infrared bands between 2400 cm^{-1} and 3000 cm^{-1} [49]. It has been also proposed that a chain of water molecules forming during the photocycle of BR in the Schiff base reprotonation pathway could give rise to broad infrared bands in the same spectral range, due to their strong hydrogen bonding character [48].

According to theoretical models [50], infrared continuum bands generated by protonated hydrogen-bonded networks can potentially span over the whole Mid-IR range. The infrared broad bands calculated from neutral hydrogen bonded networks, instead, are only in exceptional cases off from the characteristic absorption of bulk water and in no case appear below 2400 cm^{-1} [49, 48]. It is therefore relevant to discuss continuum bands below 2400 cm^{-1} only in terms of H-bonded clusters that are protonated.

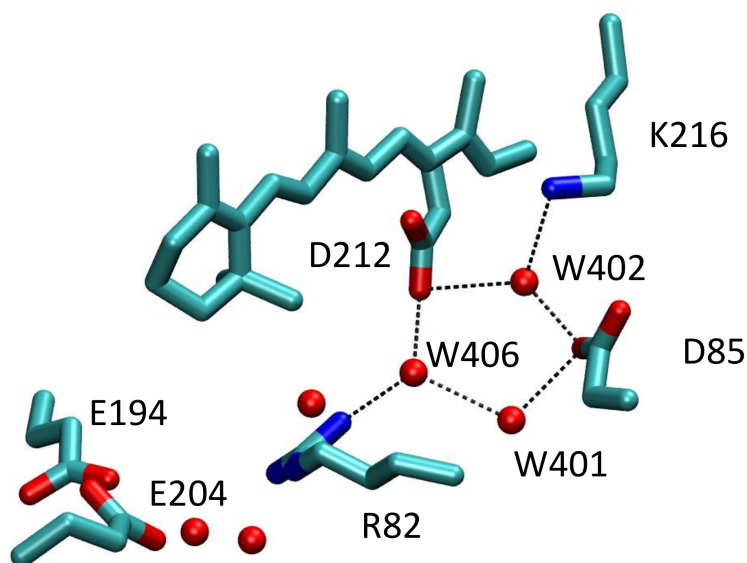


Figure 1.4: Detail of the structure of the resting state of BR (PDB:5b6v). The protein backbone is not shown and only water molecules (red dots) and some key residues are represented. Dotted lines show the hydrogen-bonding interactions in the pentagonal cluster.

1.2.3 Protonated and neutral water clusters in proteins can give rise to continuum bands

Infrared broad transient bands have been found first in the membrane protein bacteriorhodopsin [51, 35] and assigned to collective proton fluctuations in H-bonded chains. A detailed description of the continuum band in BR is provided in the previous section 1.2.2, here an overview is given on the appearance or potential appearance of broad transient IR bands in other proteins.

Archeorhodopsin-3 is a microbial rhodopsin and a proton-pump, sharing many similarities with BR, one of these is a similar behaviour in the IR difference absorption spectra in the region between 3000 cm^{-1} and 1800 cm^{-1} [52] indicating a similar mechanism and the same assignment to neutral and protonated H-bonded clusters.

Transient protonated water clusters have been detected also in other membrane proteins that don't belong to the family of the microbial rhodopsins, an example is photosystem II where a positive broad band with maximum at 2880 cm^{-1} appears during the oxidation of the manganese cluster [53]. This band has been assigned to a cluster of five water molecules that gets transiently protonated, the position of this band is reminiscent of what has been assigned in BR to a neutral cluster of water molecules [54].

The bacterial reaction center gives also rise to transient positive broad IR bands, in the interval 2200 cm^{-1} to 2000 cm^{-1} [55] and in the interval 3000 cm^{-1} to 2400 cm^{-1} [56], both assigned to protonated clusters containing water molecules. The existence of a protonated water cluster was also

proposed for cytochrome c oxydase, where molecular dynamics simulations reveal the possibility of a proton storage site in the D proton transfer channel [57], hypothesis that remains untested.

The presence of such IR continua is therefore not a property of BR and is also not present only in microbial rhodopsins. Among all these proteins the most studied is bacteriorhodopsin, which is convenient to investigate due to its light activation, its fast and cyclic photoreaction and its presence in densely packed native membranes [3]. It is then of central interest to further investigate broad absorbing IR bands in BR, gaining information that might help understanding the behaviour of many other proteins.

BR has also been used as model to demonstrate the importance of intraprotein water clusters for the protein function in general. Infact, more than one water molecule is thought to play a crucial role in the proton transfer mechanism [44, 43, 58].

1.2.4 An unusual broad infrared absorption

Infrared "continuous" absorption refers to unusually broad bands absorbing over the whole mid-infrared range. To my knowledge the first experimental observations of such continua were performed by Thomas Ackermann [59] in 1961 where he measured the IR spectrum of hydrochloric acid. At the same time (in 1962 and 1968) Georg Zundel also applied IR spectroscopy to the study of polystyrenesulfonic acid. The acid dissociates into $-SO_3^-$ and $H_5O_2^+$ (as he writes) when hydrated, giving rise to a broad absorption over the broad measured range between 4000 cm^{-1} and 650 cm^{-1} . The intensity of this continuum absorption band scaled in proportion with the degree of dissociation of the acid in water [41]. The experimental evidence is that excess protons in water give rise to broad bands in the mid-IR range. What is behind this peculiar property of protonated water molecules? Where does the broad absorption come from?

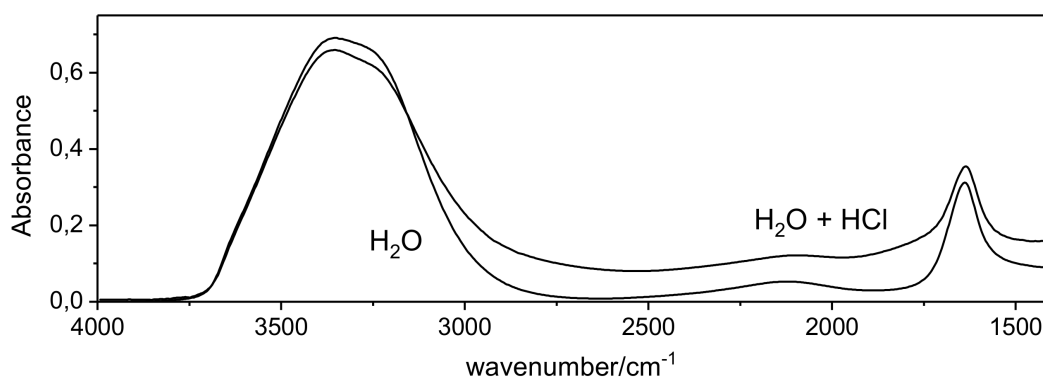


Figure 1.5: Infrared absorption spectrum of a 2M HCl solution compared with pure water absorption spectrum at pH=7.

Water has the unusual property to form and brake hydrogen bonds with the energy of the thermal fluctuations, as the strength of the hydrogen bond in a

water dimer is $\approx 5 \text{ kcal mol}^{-1}$ is just one order of magnitude higher of $RT = 0.6 \text{ kcal mol}^{-1}$ [60]. A solvated proton in this hydrogen-bonded network of water molecules can be imagined in the form of an Eigen ion $H_3O^+ \cdot (H_2O)_3$ [61] or in the form of a Zundel ion $H_5O_2^+$ [41]. When a proton is transferred among water molecules, these two complexes are both needed and are not mutually exclusive [62]. Protons easily move between water molecules as a result of a low barrier in the proton energy landscape between donor and accepting water molecules. It is now widely accepted that the proton tunneling between neighbouring water molecules is just a secondary process that is statistically negligible. The high proton-diffusion coefficient in water comes mainly from the low energy barrier between the two oxygens [62]. In a pure Zundel ion the broad IR absorption is mainly due to the "large amplitude floppy-motion of the symmetric hydrogen bond" and in a pure Eigen state, it comes from the symmetric and antisymmetric stretching modes of the ion [62]. In other words it is the polarization fluctuations of the proton between the two oxygens that gives rise to the continuum band, in a first extent. The system reacts to this charge fluctuations as both electrons and the other protons respond to it.

1.2.5 Molecular probes for proton release and uptake in proteins

Extensive and comprehensive reviews have been recently published on the characteristics and the role of molecular pH sensors [63, 64, 65]. Optical pH sensors represent an alternative way to measure the concentration of H_3O^+ ions in solution respect to pH electrodes and pH strips. Indicator dyes are typically weak organic acids or bases that change their optical properties upon protonation or deprotonation: their absorption or fluorescence changes with the pH in solution. The optical signal measures only indirectly the pH via the concentrations of acidic and basic forms of the probes.

Considering the dyes that operate in the visible range and at near-neutral pH, the most used dyes are fluorescein derivatives, benzoxanthene dyes, tri-arylmethane dyes and pyranine (8-Hydroxypyrene-1,3,6-trisulfonic acid, also called HPTS). Among the applications are the monitoring of the intracellular and extracellular pH (crucial in cell biology), the identification of membrane protein function in artificial liposomes and the kinetics of proton release and uptake in proton pumps. In this work I focused my interest on the proton transfer reaction of specific proteins, therefore only the last two applications will be discussed.

The study of protein function with pH-sensitive dyes can be performed in artificial proteoliposomes. Typically the membrane proteins are reconstituted and oriented in proteoliposomes, the dyes are placed either in the liposomes inner or outer unbuffered volume and the pH monitored after the stimulation of the proteins [66, 67, 68]. This kind of measurements require a net protein orientation that can be achieved forming the liposomes from real biological membranes where the proteins have only one orientation. Alternatively a net orientation in artificial proteoliposomes can be also achieved and is discussed

in 2.4.3.

Detail kinetic information about uptake and release of protons in proton-pumping proteins can be obtained in a time-resolved experiment, where the absorption changes of the dyes account for the time-constants of the proton translocation between proteins and bulk solution. This approach was successful to determine the sequence of proton pumping events in the photocycles of the two proteins in the focus of this thesis, BR [69, 70] and ChR2 [71].

Molecular probes can also be covalently attached to a specific site of the protein water-exposed surface. In the case of BR, where the sample consists of patches of native membranes, the comparison of the proton release and uptake kinetics between water-soluble and covalently-attached dyes revealed differences [20]. Water-soluble pH-sensors in weakly buffered solutions detect the proton release and uptake in BR purple membranes with a delay of > 0.5 ms depending on the buffer used, and its concentration [72]. Surface-attached probes have a faster reaction to the protons released from BR [20, 73, 74] but their response can be affected by polarity changes at the protein-water interface [75] or by the distance between the probe and the position of the proton release group in the protein [76, 74]. In low-buffered detergent-solubilized protein solutions the protons reside less time on the micelle surface if compared to the purple membrane, with a $\sim 100 \mu\text{s}$ delay [73] between the detection from surface bound probes and water soluble probes.

Pyranine, the pH-sensitive probe used in this work has been extensively used to probe the release and uptake of protons in BR [77, 20, 73, 76, 74], due to its pH-sensitive absorption peak at ~ 455 nm, a spectral region with small contribution from the difference absorption signals of the BR photocycle; this requirement is infact important for a precise calculation of the double-difference absorption of the signal of the probe. It has also been used in artificial proteoliposomes systems, to detect the net protein proton pumping during excitation [66, 78].

Pyranine has been also succesfully used to probe proton pumping from other membrane proteins both in single turnover conditions [79, 80] and under continuous illumination [81].

1.3 Retinal proteins and optogenetics

Optogenetics is the use of genetically-encoded light-sensitive proteins for the stimulation of neuronal activity and cells in general with light [82, 83].

Channelrhodopsin-2, a cation channel that is light activated via the retinal chromophore, is the most commonly used protein in optogenetic applications and recently has been used in biomedical treatments aimed to restore vision [84] or hearing [85].

Other retinal proteins or genetically engineered constructs have proven to be important tools for optogenetics. The chloride pump halorhodopsin (HR) for example can suppress single action potentials with the inward chloride pumping [86].

1.3.1 Channelrhodopsin-2 and its photocycle(s)

Channelrhodopsins (ChRs) are integral membrane proteins from the family of the microbial rhodopsins. Similar to BR, they are formed by 7 transmembrane helices and harvest light via the retinal chromophore covalently linked to a lysine residue forming a protonated Schiff base. As suggested by the name, ChRs function as light-activated ion channels. Some species have been found permeable to cations [6], others to anions [87].

Among ChRs the best studied is ChR2 from *Chlamydomonas reinhardtii* (CrChR2, from now on always referred as ChR2): it has a broad application in optogenetics [88] and it has been extensively studied spectroscopically and by electrophysiology [89].

The crystal structure of the ground (closed) state ChR2 has been recently resolved at 2.39 Å resolution [90]. This crystal structure and the purified protein used in this and other works consist of the truncated version of the first 316 amino acids [89]. This construct of the transmembrane part of the protein lacks the 422 amino acids of the cytoplasmic domain, and is the part of the protein responsible for the channel activity as it showed identical photocurrents to the full-length protein [6]. Little is known about the cytoplasmic domain.

The crystal structure confirms previous electron crystallography results [91] indicating seven transmembrane helix proteins arranged in dimers. The dimers are stabilized by two disulfite bridges at the extracellular site. The crystallized closed state presents four water-enriched cavities between helices B and G (or TM2 and TM7 according to another nomenclature).

Two amino acids D156 and C128, highly conserved in channelrhodopsins, are connected via a water molecule and for the DC gate, a molecular switch that is close to the retinal chromophore and plays an important role in regulating the lifetime of the channel opening [92]. The two protomers forming the dimer show some heterogeneity in the hydrogen-bonded network of the SB, E90, E123 and D253 region [90].

The protein photocycle has been characterized under single turnover conditions, that is after a short laser pulse, and under continuous illumination.

The photocycle after a short laser pulse

The ground state of the protein is characterized by a mixed isomer composition of the retinal chromophore of $\sim 70\%$ all-*trans* and $\sim 30\%$ 13-*cis* [93, 94]; the contribution to the photocycle from the excitation of 13-*cis* retinal is of minor functional relevance [95]. If kept in complete dark for more than 1 hour, the isomer composition shifts to a fully all-*trans* retinal in what is called a fully dark-adapted sample [94]; all results reported in this thesis and in the vast majority of the literature come from light-adapted samples.

The first intermediate after photoexcitation by a short flash is the red shifted P_1^{500} (hereafter the subscript indicates the intermediate and the superscript indicates the spectral absorption maximum in nm) that is formed within 40 ns. This intermediate is characterized by an isomerized retinal, from all-*trans* to 13-*cis*, and a substantially different backbone conformation respect

to the ground state[96, 89] that could be the result of a helix tilt or kink. Such conformational changes are expected in a protein that opens a conductive ion channel through the membrane.

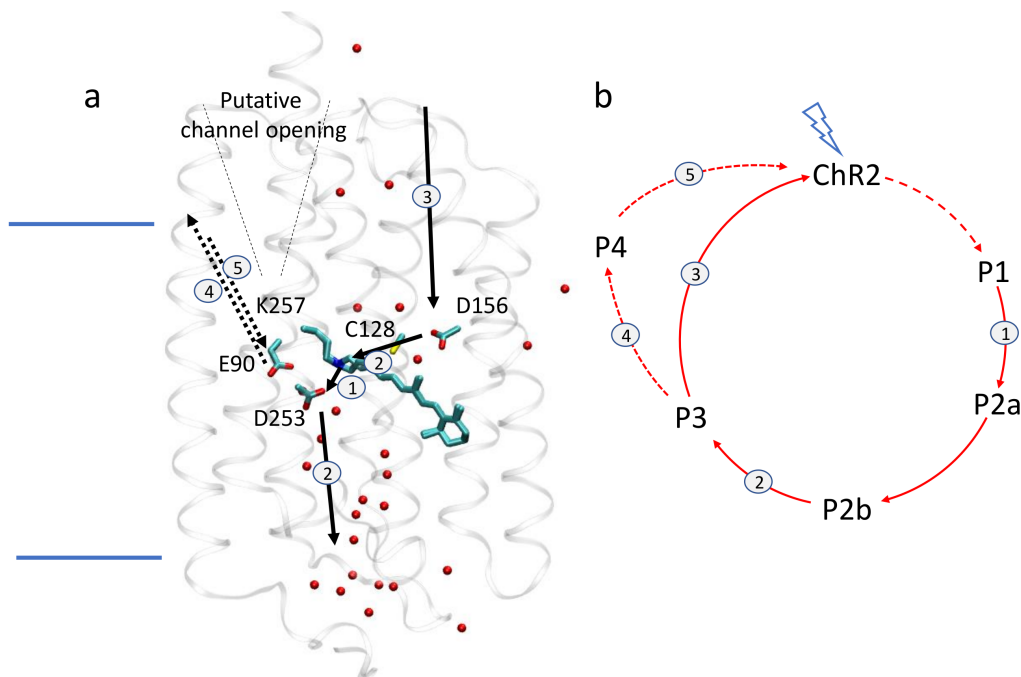


Figure 1.6: a) Structure of ChR2 (PDB:6eid). The relevant amino acids involved in the proton transfer steps and the retinal chromophore are highlighted, the crystallographic water molecules are represented as red dots. b) Simplified scheme of the photocycle of ChR2 after a short laser pulse. Events accompanying the transitions between intermediates have the same numbers as in a).

After $\sim 10 \mu\text{s}$ the transient absorption maximum blue-shifts to 390 nm during the formation of P_2^{390} . This change in the retinal absorption is due to the deprotonation of the Schiff base and subsequent rearrangement of the conjugated electron system. The proton is transferred to D253 that is called the Schiff base proton acceptor [97].

P_2^{390} decays in favour of P_3^{520} with the reprotonation of the Schiff base from D156 in ~ 2 ms. The red shifted absorption of this intermediate is reminiscent of the O intermediate of bacteriorhodopsin but here has higher accumulation and is present at neutral pH. During the transition between P_2^{390} and P_3^{520} a proton appears in the bulk, released from ChR2 [71]. The proton uptake happens with the decay of P_3^{520} [71] and when no potential is applied the proton release and uptake result in a net proton translocation across the membrane, typical of a proton pump [98].

From P_3^{520} most of the proteins ($\sim 75\%$) decay back to the ground state with a time constant of ~ 10 ms while the remaining fraction populates the long living P_4^{480} intermediate that decays to the ground state only after 3 decades, ending the photocycle. Only at this point the conformational changes observed

from the formation of the P_1^{500} are reversed [97, 89].

The P_4^{480} is characterized by the transient deprotonation of E90 followed by the transient appearance of a proton in the bulk [97], the decay of this intermediate to the ground state is pH-dependent [99]. It is still not clear if this proton is pumped or released and uptaken from the same membrane side. This intermediate is characterized by a different protein backbone conformation with respect to the ground state [99] that reflects the outward movement of the Helix B at the cytoplasmic side [100]. The residue E90 is of key importance for the channel selectivity [101] and might act as a filter, giving its position in the putative channel.

The cation channel opens during the lifetimes of the P_2^{390} and P_3^{520} , although given the longer lifetime of the second, it is P_3^{520} that mostly contributes to the photocurrents [102, 89]. It is more precisely during the transition between the two substates of P_2^{390} : P_{2a}^{390} and P_{2b}^{390} that a major water influx permeates the protein forming a transmembrane channel [89, 13]. The channel opening is accompanied by the movement of helices B and F [103]. The photocurrents decay monoexponentially, concomitant with the monoexponential decay of P_3^{520} .

The photocycle under continuous illumination

The typical illumination protocol used for the optogenetic applications of ChR2 consists of a train of light pulses, each with a duration longer than 10 ms (longer than the ChR2 photocycle, excluding P_4^{480}) [83]. Also, most of electrophysiology protein characterizations are performed illuminating the sample for ~ 100 ms to 1 s [6, 104].

In contrast to the experiments performed with short laser pulses, the photocurrents exhibit a biphasic decay after light off and new phenomena can be observed such as light-adaptation and inactivation. Light-adaptation means that the photocurrents are not equally intense during the time of illumination, but show instead a peak current after the first milliseconds that evolves into a stationary current of lower intensity that does not change during the rest of the illumination. Inactivation is the decrease of the intensity of the peak currents after repetitive illuminations: in a serie of illumination pulses the first one has a higher peak current than the others. The peak current and the stationary current have different cation selectivity [6, 104, 83].

Spectroscopically, under continuous illumination, the intermediate that is mostly accumulated is the long-lived P_4^{480} [99].

These findings led to the definition of a different model for the photocycle that could explain the new features emerged with the different illumination protocol [6, 105, 104, 106]. The photocycle is shown in Fig. 1.7.

This simple model consists of a dark state C1 that after photon excitation evolves into an open state O1, from here a different open state O2 can be reached followed by a second dark state C2 that can either be photoexcited or relax slowly to the first dark state.

According to this model the channel inactivation is due to the lower conductance of O2 with respect to O1 and the higher population of O2 during

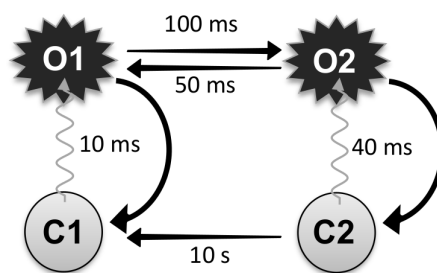


Figure 1.7: Photocycle model obtained from the electrophysiology results under multiple turnover or continuous illumination conditions. Indicative time constants accompany the transitions. C1 and C2 are the two closed states, O1 and O2 are the open states.

continuous illumination, generated from the excitation of C2 [105]. The light adaptation comes from the slow decay of C2 to C1 and the accumulation of C2 during illumination.

1.3.2 Chloride pumps

Among microbial rhodopsins there are proteins capable of pumping chloride ions across the membrane after light excitation.

At first the inward chloride transport has been found in *Halobacteria*, performed by halorhodopsins [107]. Among these, the most studied are *HsHR* and *NpHR*, respectively from *Halobacterium salinarium* and *Natronobacterium pharaonis*; The measurements in this thesis were performed with *HsHR* that will be referred only as HR from here on. A second group of chloride pumping rhodopsins has been found in *Flavobacteria* and called ClRs. A third family comes from cyanobacteria; one of these is MastR, a chloride pump from *Mastigocladopsis repens*.

A general mechanism in halorhodopsins involves two chloride binding sides and the translocation of the chloride ion from one to the other, in the close vicinity of the protonated Schiff base [108, 109]. As the photoisomerization of the retinal does not involve the deprotonation of the Schiff base [5], no proton transfer is expected and none has been detected. Recently a pumping mechanism has been proposed where the chloride translocation is coupled to the movement of a proton, but evidences of the involvement of a protonation/deprotonation of a group are lacking [110, 109, 111].

The protein photocycle involves the presence of at least four intermediates that can be best described by the scheme: $HR \rightarrow K \Leftrightarrow L_1 \Leftrightarrow L_2 \Leftrightarrow N \rightarrow HR$ where double arrows indicate equilibrium between the photoproducts and not an unidirectional transition [112].

Interestingly, *NpHR* can be converted into a proton pump with the presence of azide, a weak base that helps shuttling protons from and to the surface [113]. HR from *Halobacterium salinarium* can also transport protons under a particular illumination pattern that involves two photon absorption [114]; in both cases no internal groups involved in the proton transfer mechanism have

been identified.

The crystal structures of all the reaction intermediates, with the different positions of the chloride ions, have been resolved recently [109] for NpHR. The crystal structure of the intermediates following L_1 of halorhodopsin from *Halobacterium salinarium* is still not available [115].

1.4 Aim of the thesis

The growing field of optogenetics brought new interest in the microbial rhodopsin's research. Despite the numerous applications of channelrhodopsins and related proteins, the basic research on the fundamental mechanisms at the base of the retinal proteins' functions lags behind.

An example is the use of ChR2 for the depolarization of the neuronal membrane: the desensitization and deactivation of the proteins represent a drawback for the optogenetic applications. It has been noticed after large-scale point mutations, possible in electrophysiology, that some mutants show reduced desensitization [88], but only with a detailed spectroscopic analysis of the ChR2 photocycle it is possible to understand the molecular origin of such observed phenomena. This is one of the aims of this thesis, where I investigated the photoexcitation of the last intermediate of the photocycle of ChR2 that has important implications for the deactivation and desensitization of the membranes.

In the framework of the collaborative research center on "protonation dynamics in protein functions" where I actively participated during my PhD, I focused the research on the continuum bands as marker bands for proton transfer from or to protonatable hydrogen bonded networks.

Although BR has less potential than ChR2 in the field of optogenetics, it is a model protein for the study of proton transfer reactions. Once the molecular origin and the chemical mechanism of the continuum band is understood, the knowledge can be transferred to other microbial rhodopsins or generalized to proton transfers in proteins. I investigated the continuum band in BR with different approaches: at first I analyzed its kinetics with a novel method involving pH-sensitive molecular probes, secondly I used polarization-resolved infrared spectroscopy to gain information on the shape of the continuum band in order to understand better which amino acids and/or water molecules are responsible for it. At last I explored the effect of the protein environment on the continuum band signal in BR, asking the questions: is the continuum band a property of the purple membrane lattice? Is the continuum band a property of the protein trimers? Does the protein solubilization affect this broad infrared band?

I did not limit the investigation on the continuum band to BR but I looked also into other microbial rhodopsins that are known to pump chloride ions through the membrane. In these proteins proton transfer is not expected to play any role in the protein function and finding evidences of protonation changes would shed light to new functional mechanisms.

Chapter 2

Methods

2.1 Infrared spectroscopy

Infrared spectroscopy is one of the techniques that can study molecular vibrations, together with Raman and photoacoustic spectroscopy. While infrared and photoacoustic spectroscopy are techniques that involve the absorption of an infrared photon and provide essentially the same information, Raman spectroscopy involves the scattering of a shorter wavelength photon therefore obeys different selection rules and it is considered to be a complementary technique.

The absorption of an infrared photon is achieved by irradiation of molecules with infrared light that matches the energy difference between two vibrational energy levels, the initial state i and the final state f :

$$h\nu = h\nu_f - h\nu_i \quad (2.1)$$

The most simple model for molecular vibrations is a classical approach to a spring connecting two point masses. Solving the differential equation for the harmonic motion leads to:

$$\omega = \sqrt{\frac{k}{\mu}} \quad (2.2)$$

where k is the spring constant and μ is the reduced mass of the system. A molecule with N atoms, with N degrees of freedom, has $3N - 6$ vibrational degrees of freedom excluding the translational and rotational modes.

A quantum mechanical approach is necessary to study the vibrational stationary states, the energy levels and the photon absorption. Again, the simplest system to study is a diatomic molecule. The potential curve for a molecular bond can be approximated with the quadratic behaviour of an harmonic oscillator but is better described by the spherical Morse potential:

$$V(r) = D_e(1 - e^{-a(r-r_e)})^2 \quad (2.3)$$

where D_e is the dissociation energy, r_e is the bond distance at equilibrium, r is the distance between the two atoms and $a = \sqrt{k_e/2D_e}$ governs the width of the potential well. Solving the Schrödinger equation with this potential gives

the eigenvalues and the eigenstates for this system. The probability of the transition between the two states i and f is given by the Fermi golden rule:

$$\Gamma_{i \rightarrow f} = \frac{2\pi}{\hbar} |\langle f | H' | i \rangle|^2 \rho \quad (2.4)$$

where ρ is the density of final states and H' is the operator that describes the perturbation. Applying this concepts with an uniform electric field as electromagnetic perturbation, allows the derivation of the selection rules for photon absorption coupled to vibrational transitions: a change in the dipole moment of the molecule is necessary for IR absorption.

The main information obtained with infrared spectroscopy are the energy of the vibrational transitions and the strength of their interaction with the probing light. Given its high sensitivity to the chemical structure and architecture of the sample, infrared spectroscopy is one of the classical methods for structure determination of molecules and compounds and over the years proved to be valuable to study also complex system such as biological samples [116].

The infrared spectral range spans from 700 nm that is upper limit of human vision in the red, to 1 mm where microwaves start. This interval is often subdivided into three main regions, near infrared (NIR), mid infrared (MidIR) and far infrared (FIR). This division comes from the different nature of the absorbed IR photon but has also historical and technical reasons.

The MidIR region typically contains bands due to fundamental vibrational transitions, the NIR region is characteristic of overtones and combination bands and the FIR region contains information on the vibration of heavy atoms and/or weak bonds such as H-bonds [117]. From here on, throughout the thesis IR will be synonymous of MidIR, as only this range has been investigated.

The vibrational modes of complex molecules in the IR range comprise vibrations where only a few atoms show a displacement whereas the rest of the molecule reacts moderately. The absorption frequency of such modes is characteristic of the chemical identity of the atoms involved in the displacement and does not vary considerably between different molecules. The observation of absorption bands in certain regions of the spectrum can contain chemical information of the bonds involved in the vibration. Charts and tables that correlate absorption frequencies with functional groups have been developed [118].

Complex molecules involve vibrations with the displacement of several atoms, these articulated motions are therefore specific of the single molecules. Such vibrational signatures are called "fingerprint vibrations" as can be used to recognize and detect specific molecules. Databases exist where the fingerprint vibrations of many different molecules are stored and can be compared or accessed by a software for an automated screening [119, 120].

Vibrational-rotational modes of small molecules in the gas phase such as H_2O and CO_2 appear in the MidIR region. The detailed exposition of this subject goes beyond the scope of this thesis, but for the interested reader can

be found [121, 122].

Vibrational frequencies are expressed in terms of wavenumbers, that is the number of waves per centimeter. The wavenumber has therefore the unit cm^{-1} , it is a frequency and is related to wavelength and frequency (Hertz) in the form of $\tilde{\nu} = 1/\lambda = \nu/c$. The symbol for the wavenumber is $\tilde{\nu}$, but ν is also used; in this thesis the frequencies are expressed in wavenumbers if not specified.

2.1.1 Fourier transform infrared spectroscopy

Among the most advanced and used forms of IR spectroscopy is Fourier Transform Infrared Spectroscopy (FTIR), where the essential piece of optical hardware is an interferometer, see Fig. 2.1. This setup has several advantages over conventional spectrometers, among them: a high wavenumber accuracy (about 0.01 cm^{-1}), higher throughput of radiation and the fact that all frequencies from the IR source impinge simultaneously on the detector. The spectrometer (Fig. 2.1) briefly consists of a source of IR radiation called globar (a silicon carbide rod heated to approximately 1000°C that acts as a black body radiator), a set of optics that guide the IR light to the Michelson interferometer and to detector. A monochromatic light source (typically a HeNe laser) is coupled in the IR beam path and needed to precisely determine the mirror positions where the interferogram is sampled.

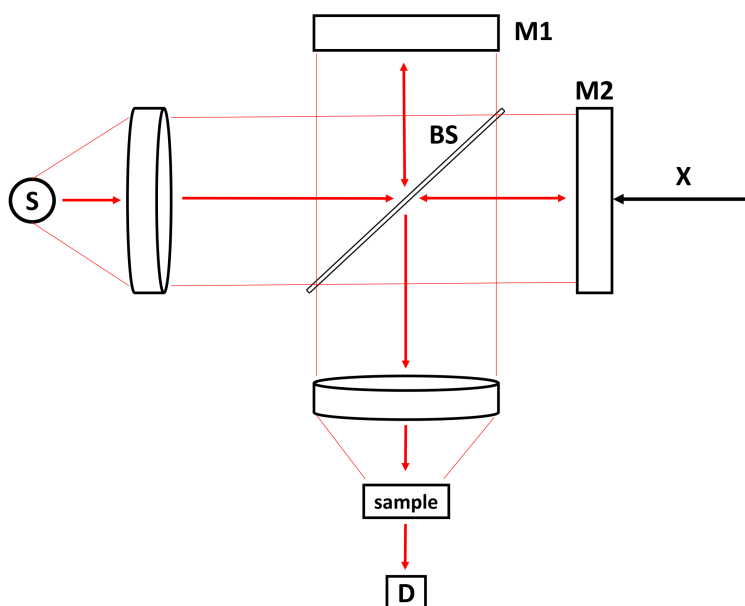


Figure 2.1: Scheme of a Michelson interferometer used in FTIR devices. A light source (S) emits radiation that reaches the beam splitter (BS), gets split to the fixed mirror (M1) and to the movable mirror (M2) and interferes back at the beam splitter. Subsequently reaches the detector (D) after interacting with the sample. The movable mirror can be displaced by a distance X.

The data acquisition yields an interferogram that is, after the sampling during the digitalization, a discrete function. A spectrum is obtained with a

discrete Fourier transformation that is numerically calculated by the computer. The transmittance spectrum can be calculated $T(\nu) = S(\nu)/R(\nu)$ where $R(\nu)$ is the Fourier-transformed reference spectrum without the sample and $S(\nu)$ is the Fourier-Transformed spectrum with the sample. The absorbance is obtained via the Lambert-Beer law:

$$A = -\log_{10} \frac{S(\nu)}{R(\nu)} \quad (2.5)$$

Depending on the path and starting position of the movable mirror, the interferogram can be recorded single-sided, double sided and in a single or double manner. In an ideal interferogram the fringes on the left or right side of the centerburst are perfectly symmetric, it would be therefore enough to record half of the interferogram (single sided) and mirror it before the FT. The spectrometer, though, introduces asymmetries that have to be taken into account. One solution is to measure a double sided spectrometer, with the drawback that doubles the collection time and the number of data points. An alternative solution is to perform a phase correction, that allows to make symmetric the single sided interferograms: a quick double sided scan is performed at the beginning of any measurement and a function of the interferogram asymmetries is stored; all subsequent single sided interferograms are then multiplied by this function and made symmetric.

Before the Fourier transformation, during data processing, it is possible to introduce corrections to the interferogram in order to avoid possible distortions and artifacts. Zero filling adds zeroes at the end of the interferogram, therefore increasing the number of points per wavenumber in the spectrum. Apodisation deals with the problem that a real interferometer cannot measure for an infinite distance of the movable mirror, leading to an interferogram that is abruptly truncated and that might create artifacts. The solution is to choose a cutoff or apodization function that gives less distortion to the final spectrum. The chosen apodization function in this work is Blackman-Harris, that deconvolutes a Gaussian lineshape.

The study of complex biological systems like enzymes and membranes is challenging for infrared spectroscopy. The many different chemical species give bands that overlap over the MidIR range and make it very difficult to discriminate the single vibrations. An absorption spectrum of a membrane protein carries structural information at the level of the secondary structure. At the molecular level only a few chemical species can be detected in a range that does not overlap with other absorption bands, e.g. $S-H$ stretching of the cysteines or the $C=O$ stretching of the carboxylic acids if the sample does not contain ester lipids. More detailed information at the molecular level can be obtained in a difference experiment. Difference absorption spectra can help to select only the vibrations that are affected during a reaction.

For this work the experiments have been performed with commercially available FTIR spectrometers Vertex 80v or IFS66v from Bruker (Bruker Optics, Germany), equipped with MCT (mercury cadmium telluride) and DTGS (deuterated-triglycine sulfate) detectors.

Difference absorption

In a difference absorption experiment the resulting spectrum is the difference in the sample absorption before and after a certain reaction. The difference spectrum shows the absorption bands of the vibrations that change with the reaction. Negative bands report for vibrations that were absorbing before the reaction and changed their absorption frequency, therefore studying the position of the negative bands can give information on the sample in the ground state, or before the reaction. The positive bands rise where there was no absorption before the reaction, so carry information on the chemical species of the products of the reaction.

2.1.2 Time-resolved FTIR spectroscopy

Time-resolved FTIR spectroscopy allows the acquisition of spectra after a particular trigger and is used to study processes that evolve in time, e.g. the reaction steps of the photocycle of a membrane protein after light excitation.

The results presented in this thesis are focused on the use of light as reaction-trigger and in this chapter I am concentrating on experiments and techniques that are started with a laser flash. The applications of time-resolved FTIR are much broader but exceed the aim of this work.

The time-scale of the reaction of interest governs the choice of the time resolution, therefore the choice of the method. Slow-reacting processes that happen in the minutes-to-hours timescales can be tracked by subsequently recording spectra over time. Such an experiment is called Rapid Scan. The time resolution is limited by the scanning speed of the movable mirror and by the spectral resolution of the final spectrum. A modern spectrometer can achieve $\sim ms$ time resolution for a single-sided low-resolution spectrum. As a general principle, the time resolution of the experiment needs to be an order of magnitude faster than the half-life of the dynamic event studied, in order to be able to resolve it. The biggest advantage of Rapid Scan over other time-resolved IR methods is that after a single trigger that starts the reaction, a whole dataset is recorded. This technique is therefore suited for unidirectional reactions.

Another approach is necessary for time resolutions in the order of $\sim 100ns$ or $\sim \mu s$, it is called Step Scan. The interferograms are not recorded at once and the movable mirror does not rapidly scan all its positions. The mirror moves in steps and for each step the time evolution of the interference at that particular position is recorded. Only after the mirror stepped in all the positions and the kinetics of the interferences for each position has been stored, the complete dataset can be reassembled. In this way an interferogram for each time point can be reconstructed and Fourier-transformed.

This measuring approach is not limited by the scanning speed of the movable mirror therefore this is not anymore a limit for the time resolution (typically the time resolution is limited by the sampling rate of the analog-to-digital converter and for this thesis the earliest spectrum was recorded at $6.25 \mu s$). The advantage of a higher time resolution comes with the drawback that the sample

needs to undergo an identical reaction for every step of the mirror, therefore this technique is well suited for samples that undergo a cyclic reaction.

The samples are excited either with a 10 ns pulse of the second harmonic of a Nd:YAG (Minilite II, Continuum) or with a Nd:YAG (Quanta-Ray, Spectra-Physics) emitting at 355 nm and followed by an optical parametric oscillator (OPTA) which allows to adjust the exciting laser pulse to the desired wavelength in the spectral range 410 – 700 nm (and 720 – 2500 nm for the Idler) with a conversion efficiency of $\sim 30\%$ at 520 nm.

2.1.3 Attenuated total reflection spectroscopy

An Attenuated Total Reflection (ATR) accessory can be installed in the FTIR spectrometer instead of the transmission sample holder. ATR allows to measure the absorption of samples adhered to a surface, the IR light probes only the first few μm above the surface and does not need to go through the sample as in a transmission setup. The ATR technique exploits the evanescent wave that is created when the probing light is totally reflected at the interface between the sample and a material with a higher refractive index.

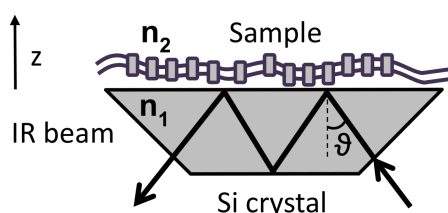


Figure 2.2: Scheme of the ATR cell. The incoming IR beam enters the ATR prism, hits the interface with the sample at an angle θ , gets reflected off the surface and reaches the detector. The internal total reflection is achieved when the index of refraction of the ATR prism ($n_1 \sim 3,42$ for Si) is higher than the one of the sample ($n_2 \sim 1,32$ for water). When is used in combination with a polarizer filter, the parallel polarization is in the plane of the figure, the perpendicular is orthogonal to it.

The evanescent wave decays with an exponential decay that depends on the wavenumber, the indices of refraction of the ATR crystal and the sample, and the angle of incidence.

The IR beam is totally internally reflected only for angles $\theta > \theta_c$ where the critical angle θ_c is defined as $\theta_c = \sin(n_2/n_1)^{-1}$. Given the high absorption yield of water for IR radiation, it is often very difficult to work in a water solution in transmission mode, as the high absorption limits the number of photons reaching the detector. The great advantage of ATR spectroscopy is that if a biological sample is firmly adhered to the ATR crystal, it can be fully hydrated from the top with the solution of choice. It is also possible to dynamically exchange solutions and monitor the changes at the sample.

2.1.4 Polarization-resolved FTIR spectroscopy

Polarization-resolved FTIR spectroscopy involves the use of a polarizer filter (for this thesis an Holographic wire grid, Thorlabs) in the beam path, with the aim to gain additional information from the absorption (or difference) spectra than with traditional FTIR spectroscopy. Typically this technique investigates the orientation of target transition dipole moments in the sample or, more accurately, its relative orientation with respect to another vector.

Several approaches are possible, where setups and data analysis can vary. Here we will focus on ATR and transmission steady-state polarization-resolved spectra of oriented samples, with the aim to calculate the angles of various dipoles in the protein sample with respect to the membrane normal. Another approach that will be here described is photoselection where it is possible to calculate the angle of a target dipole moment change with the dipole of the retinal.

Except for the photoselection experiments, the samples have been excited with a LEDs that are not polarized and placed on top of the sample. Still, the electric field vectors of the light emitted from the LEDs could potentially lie in the plane perpendicular to the propagation direction. If the emitted light were collimated this would lead to a photoselection phenomenon; the incoming radiation is instead emitted hemispherically and focused on the sample with a lens. The polarization distribution of this light source has not been here characterized and an homogeneous distribution of electric field vectors has been assumed (no photoselection).

Polarization-resolved FTIR spectroscopy with the ATR accessory

The combination of a polarized incoming beam and an ATR accessory is well documented in literature [123, 124, 125]. The polarizer filter can be placed before the ATR cell so that the incoming IR beam is either parallel or perpendicular to the plane of incidence, that is depicted in Fig. 2.2. The difference spectra obtained with the incoming beam parallel or perpendicular to the plane of incidence will be indicated respectively as ΔA_{\parallel} and ΔA_{\perp} . The projected absorbance changes on the sample coordinate system, where z direction is the normal to the membrane and the xy plane is the membrane plane, can be calculated as follows [124]:

$$\Delta A_{xy} = \frac{\Delta A_{\perp}}{E_y^2} \quad (2.6)$$

$$\Delta A_z = \left(\Delta A_{\parallel} - \frac{\Delta A_{\perp} E_x^2}{E_y^2} \right) \frac{1}{E_z^2} \quad (2.7)$$

Where E_x , E_y and E_z are the components of the electric field vector of the ATR evanescent wave, normalized to the electric field vector of the incident wave. If the polarizer filter is not perfect, namely it has a small leak f , the above equations can be corrected [125] as:

$$\Delta A_{xy} = \frac{\Delta A_{\perp}(1-f) - \Delta A_{\parallel}f}{E_y^2(1-2f)} \quad (2.8)$$

$$\Delta A_z = \frac{\Delta A_{\parallel}(E_y^2(1-f) + E_x^2f) - \Delta A_{\perp}(E_x^2(1-f) + E_y^2f)}{E_y^2E_z^2(1-2f)} \quad (2.9)$$

The leak factor f for the polarizer filter can be estimated measuring the isotropic ratio ($R^{iso} \sim A_{\parallel}/A_{\perp}$) of the distilled water absorption. The ratio is 2 for a perfect polarizer and decreases for increasing f . This effect is due to the amplitude of the electric field for the parallel polarization being higher than for the perpendicular [123]. Knowing the incident angle θ and the measured isotropic ratio R^{iso} , it is possible to estimate f with the following [126]:

$$f = \frac{n_2^2(R^{iso} - 1) - [R^{iso}(n_2^2 + n_1^2) - 2n_1^2] \sin^2(\theta)}{[R^{iso}(n_1^2 + n_2^2) - 2n_2^2] \sin^2(\theta) + n_2^2} \quad (2.10)$$

The angle θ (see Fig. 2.2) cannot be measured independently and can be estimated only if the value of f is previously known. The IR beam is focused on the ATR crystal with a lens, therefore it has a distribution of incident angles instead of a single value. Due to the impossibility to determine independently both f and θ , at first we used the approximation that the polarization filter is perfect, and estimated θ (see Appendix A.0.1). Later we introduced the correction for a leaky filter and varied θ to check if the results were robust against errors in the estimation of this two values.

The values for E_x , E_y and E_z can be derived from the theory from Harrick and reviewed here [123]. Their exact values cannot be calculated as they depend on parameters that are not controlled in our experiments, like the complex index of refraction of the sample or the film thickness. In the thick film hypothesis however the electric field components can be estimated, assuming that the thickness of the film is much larger than the penetration depth of the evanescent wave and that the sample is a weak absorber. In our experiments both assumptions hold, therefore the electric field amplitude can be expressed as:

$$E_x = \frac{2 \cos \theta (\sin^2 \theta - n_{21}^2)^{1/2}}{(1 - n_{21}^2)^{1/2} [(1 + n_{21}^2) \sin^2 \theta - n_{21}^2]^{1/2}} \quad (2.11)$$

$$E_y = \frac{2 \cos \theta}{(1 - n_{21}^2)^{1/2}} \quad (2.12)$$

$$E_z = \frac{2 \sin \theta \cos \theta}{(1 - n_{21}^2)^{1/2} [(1 + n_{21}^2) \sin^2 \theta - n_{21}^2]^{1/2}} \quad (2.13)$$

Where $n_{21} = n_2/n_1$.

From the dependence of the penetration depths for the parallel and perpendicular polarizations as a function of the incident angle θ (see Fig 15 and 16 in [123]), it can be noted that the closer the incident angle to the critical angle, the higher the difference between the penetration depths at different

polarizations. At angles close to the critical angle the spectra become more distorted with respect to transmission spectra. In Fig. 2.3 the effective penetration depth for Si ATR prism at 40° incident angle.

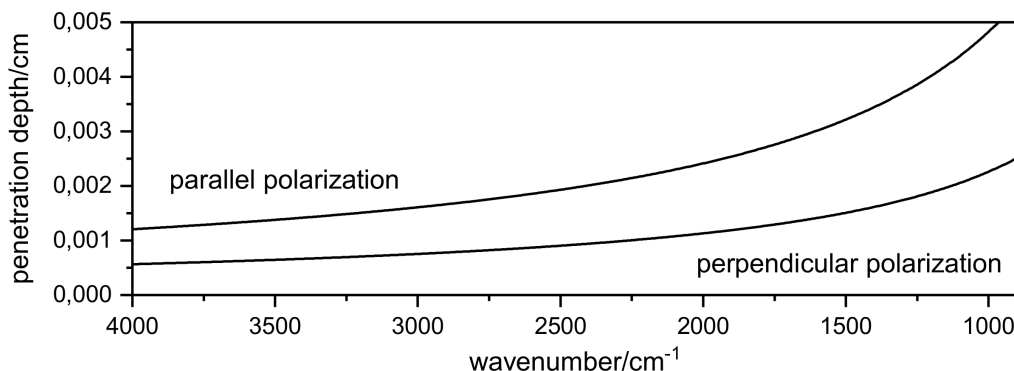


Figure 2.3: Penetration depth in dependence of the wavenumber for a Si ATR prism. For this calculation the incident angle was set to 40° and the sample index of refraction to 1.6.

In order to gain meaningful information from the difference spectra in the xy and z directions, the sample need to have a preferred orientation with respect to the ATR crystal surface.

Polarization-resolved FTIR spectroscopy in transmission

In transmission mode it is also possible to record polarization-resolved spectra and calculate the difference absorption spectra in the membrane plane (ΔA_{xy}) or in the direction of the membrane normal (ΔA_z).

A transmission sample is typically consisting of two infrared-transparent windows that hold the sample between them (see subsection 2.4 for details). The sample holder is than placed in the spectrometer at a variable angle between the incoming beam normal and the surface of the window, as shown in Fig. 2.4. In the setup the probing beam is focused on the sample, but will be considered linear in a first approximation in the following discussion. The diffraction of the sample will be introduced later. The following derivation of the formulas for the absorption differences in the sample coordinate system is the work of Dr. Victor Lorenz Fonfria and is based on [127].

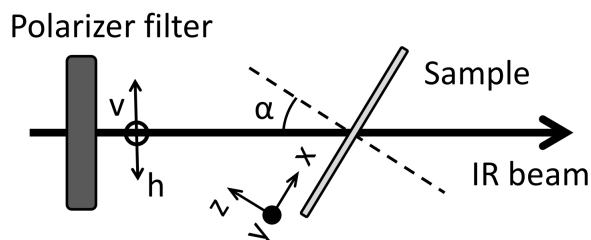


Figure 2.4: Scheme of the infrared tranmission cell.

As the electric field vector of the probing IR beam in either polarization cannot be oriented along the propagation direction, the dipoles moment changes of the sample that are oriented along the z direction can be probed only by tilting the sample holder with an angle $\alpha > 0^\circ$. The absorption differences for vertically polarized light (ΔA_v), for any value of α is:

$$\Delta A_v = \Delta A_y \quad (2.14)$$

The absorption differences for the horizontally polarized light (ΔA_h):

$$\Delta A_h = \Delta A_x \cos^2 \alpha + \Delta A_z \sin^2 \alpha \quad (2.15)$$

According to the characteristics of our samples and the sample preparation (see 2.4.1), the proteins adhered to the IR-transparent windows have an axial symmetry and are distributed so that $\Delta A_x = \Delta A_y$. From Eq. 2.14 and 2.15 we can now extract ΔA_{xy} and ΔA_z :

$$\Delta A_{xy} = \Delta A_v \quad (2.16)$$

$$\Delta A_z = \frac{\Delta A_h - \Delta A_v \cos^2 \alpha}{\sin^2 \alpha} \quad (2.17)$$

With Eq. 2.18 having physical meaning when the tilting angle is not zero.

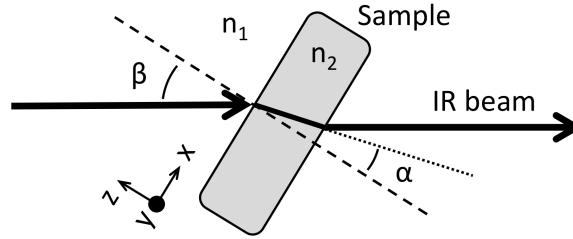


Figure 2.5: Detail of the sample holder in the infrared transmission cell.

At this point we introduce the refraction of the sample, that for simplicity is considered as one single object, with refractive index n_2 as shown in Fig. 2.5. We can now differentiate the angles α between the IR lightbeam through the sample and the sample normal, from the angle β between the incoming IR beam and the sample normal. The two angles are related via the Snell's law: $n_2 \sin \alpha = n_1 \sin \beta$. Considering the index of refraction of air equal to the unity $n_1 = 1$, equation 2.18 becomes then:

$$\Delta A_z = \frac{n_2^2}{\sin^2 \beta} \left[\Delta A_h - \Delta A_v \left(1 - \frac{\sin^2 \beta}{n_2^2} \right) \right] \quad (2.18)$$

Here the value is not defined for small angles. As for the case of the above description of the ATR polarization-resolved spectra, we can take into account the imperfection of the polarizer filter. The formulas for the absorption difference in the coordinate system of the sample are:

$$\Delta A_{xy} = \frac{\Delta A_v(1-f) - \Delta A_h f}{1-2f} \quad (2.19)$$

$$\Delta A_z = \frac{n_2^2}{(1-2f)\sin^2\beta} \left[\Delta A_h \left(1 - \frac{f \sin^2\beta}{n_2^2} \right) - \Delta A_v \left(1 - \frac{(1-f)\sin^2\beta}{n_2^2} \right) \right] \quad (2.20)$$

This formulas and Eq. 2.8 and Eq. 2.9 assume that the sample is perfectly oriented parallel to the surface but isotropic in the plane. Given the geometrical properties of the PM patches it is reasonable to assume that they orient when dried on a surface. Due to the edge overlap of the fragments it is though to expect a misalignment called mosaic spread. It is further discussed in 3.2.1.

The calculated ΔA_{xy} and ΔA_z can be corrected for the mosaic spread, exploiting the axial simmetry. If we call z_2 the average membrane normal and xy_2 the average plane parallel to the membranes (that differ from the surface normal z and parallel plane xy) and assuming that the membranes are tilted with an angle γ , the absorption in the surface coordinate system are:

$$\Delta A_{xy} = \Delta A_{xy2} \frac{\cos^2\gamma + 1}{2} + \Delta A_{z2} \frac{\sin^2\gamma}{2} \quad (2.21)$$

$$\Delta A_z = \Delta A_{z2} \cos^2\gamma + \Delta A_{xy2} \sin^2\gamma \quad (2.22)$$

Since γ does not have a single value but it is a distribution of angles, the expressions $\cos^2\gamma$ and $\sin^2\gamma$ should be substituted by their time and space average values $\langle \cos^2\gamma \rangle$ and $\langle \sin^2\gamma \rangle$. Also, since the distribution has cilindrical symmetry and can be characterized by a serie of Legendre polynomials [128], it is convenient to rewrite the Eq. 2.21 and Eq. 2.22 in dependence of the second order parameter that we will call mosaic spread parameter p_m :

$$p_m(\gamma) = \frac{3 \langle \cos^2\gamma \rangle - 1}{2} \quad (2.23)$$

After substituting and reversing the formulas we can obtain the expressions for ΔA_{xy2} and ΔA_{z2} corrected for the mosaic spread:

$$\Delta A_{xy2} = \Delta A_{xy} \frac{2p_m + 1}{3p_m} - \Delta A_z \frac{1 - p_m}{3p_m} \quad (2.24)$$

$$\Delta A_{z2} = \Delta A_z \frac{p_m + 2}{3p_m} - \Delta A_{xy} \frac{2(1 - p_m)}{3p_m} \quad (2.25)$$

Once obtained the difference spectra ΔA_{xy} and ΔA_z , we can calculate the angle δ of a certain dipole with respect to the membrane normal (z direction).

$$\delta = \cot^{-1} \sqrt{\frac{\Delta A_z}{2\Delta A_{xy}}} \quad (2.26)$$

The angle is not defined when the fraction results in a negative number, that

is when the values for the absorption changes have different signs, as result for example of the overlap of different bands.

In the transmission experiments the thickness of the sample probed by the IR light is increasing with increasing tilting angle, in this case the spectra were scaled accordingly when compared.

Photoselection

A photoselection experiment uses two polarized beams, the exciting and the probing beam, to selectively probe certain dipole moments changes in the sample. For this work a visible exciting beam (a laser flash) and an IR probing beam have been used. The polarized laser flash excites the optical transition moment of the light-absorbing molecules, the probability of absorption depends on the orientation of the dipole moment change of the molecules with respect with the exciting light source. As the absorption probability is proportional to the squared scalar product of the electric field vector of the light beam and the dipole moment change vector of the molecule, the absorption is proportional to the \cos^2 of the angle between these two vectors.

Typical photoselection experiments have to take into account the movement of the excited molecule between the pump and the probe flashes, in this work we circumvent this issue by drying and rehydrating sheets of native membranes with high protein concentration, called purple membranes. In this way the membrane sheets are immobilized on the BaF_2 surface and allow for ms to s delays between pump and probe beam (in our case continuous light) or steady state experiments.

The aim of such an experiment is to calculate the angle Θ between the projection R' on the membrane plane of the dipole moment change R of the molecule absorbing the pump pulse (retinal) with the projection M' on the membrane plane of a certain dipole moment change M absorbing the probing IR light, as shown in Fig. 2.6

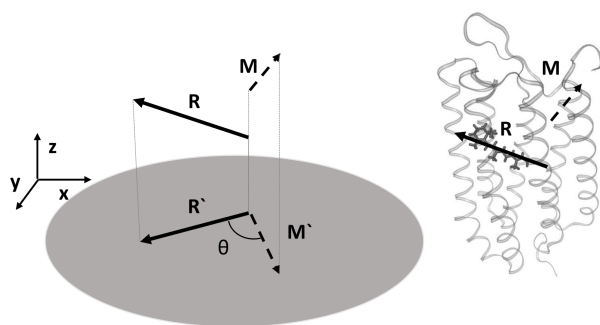


Figure 2.6: Scheme of the protein coordinate system when purple membranes are dried and oriented on the BaF_2 windows: the membrane plane is in the xy plane while the membrane normal points in the z direction. If R is the dipole moment change of the retinal molecule, R' is its projection on the xy plane, the same holds for a target dipole M and its projection M' .

The sample, in a transmission configuration, has been placed perpendicular to the incoming IR beam ($\alpha = 0^\circ$ in Fig. 2.4). The membranes are therefore also perpendicular to the probing beam, but have no preferred orientation on the plane. The laser flash is not perfectly coaxial with the probing IR beam but its angle has been minimized to less than 5° and will be considered as zero as it is comparable with the solid angle created by the focus of the IR probing beam on the sample. Both probing and pumping beams pass through a polarizer filter before hitting the sample.

Two datasets are then recorded with a step scan technique. Time-resolved difference absorption recorded when the IR and visible flash have parallel polarizations (ΔA_{\parallel}) or perpendicular (ΔA_{\perp}) polarizations. If the two datasets are to be compared and analyzed together, both need to be recorded on the same sample, with identical laser energy power and at the same temperature; practically small variations in the hydration level and on the sample quality (in terms of amount of functional proteins) are hard to avoid in an experiment that lasts for several hours, time needed to record enough averages. The measurement protocol that has been followed to minimize the impact of this changes is to alternate short measurements of 10 conditions per 666 points of the interferogram, lasting about 20 minutes each.

The angle Θ can be calculated with the equation [129]:

$$p = \frac{\Delta A_{\parallel} - \Delta A_{\perp}}{\Delta A_{\parallel} + \Delta A_{\perp}} = \frac{\cos 2\Theta}{2} \quad (2.27)$$

The relation between p and Θ applies for ideal conditions with perfect polarizers and no light scattering from the sample. Since the retinal molecule is known to have its infrared dipole moment change parallel to the electronic transition moment [130], we can use the bands assigned to the retinal vibrations to define a parameter c that quantifies the photoselection efficiency. In particular it is known that the band at 1525 cm^{-1} should give an angle $\theta = 0$. The parameter c is then defined as the ratio of the amplitude of the parallel absorption over the perpendicular absorption at 1525 cm^{-1} . The corrected formula for the angle θ is [131]:

$$\tan^2 \theta = \frac{\Delta A_{\parallel} + \Delta A_{\perp} - c(\Delta A_{\parallel} - \Delta A_{\perp})}{\Delta A_{\parallel} + \Delta A_{\perp} + c(\Delta A_{\parallel} - \Delta A_{\perp})} \quad (2.28)$$

2.1.5 Quantum cascade lasers as infrared light source

Quantum cascade lasers (QCL) [132], since their first experimental implementation, have been widely used in a large number of applications. As powerful and tunable IR-emitting light source it has a natural application in IR spectroscopy.

QCL are semiconductor lasers based on thin layers of semiconductors with different band gaps forming a superlattice. The recombination of electrons with holes does not happen in a single transition as in standard laser systems, they recombine instead with many transitions of lower energy, therefore longer wavelength, e.g. in the infrared. Each electron therefore can cause the emission

of multiple photons traversing the QCL structure, giving rise to the so called "cascade" and leading to its very high output power. A diffraction grating can be added to the setup to be able to tune the emission of the laser around its center wavelength.

QCL can be then used as monochromatic tunable probing beam in a IR flash-photolysis setup [133]: the protein sample is excited with a visible laser pulse and the evolution of a specific IR band can be resolved in a time-resolved experiment. An advantage of this setup over a conventional FTIR spectroscopy setup is the fact that a kinetic trace can be recorded after a single exciting flash with a high time resolution, allowing the study of non cyclic reactions. The time resolution that is limited by the length of the exciting pulse and on the reaction time of the detector and pre-amplifier, with the state-of-the-art technology can be reduced to ~ 20 ns [133]. Another advantage is the possibility to study samples in a liquid environment, given the high output power of the QCL.

The setup used for this thesis consists of several external cavities (Day-light solutions) that can be switched according to necessity and that together cover the spectral range from $\sim 1565\text{ cm}^{-1}$ to $\sim 2610\text{ cm}^{-1}$ with some small intervals missing. Each cavity covers a spectral range of $\sim 100\text{ cm}^{-1}$ and consists of a monochromatic continuous light source with the width of less than 0.01 cm^{-1} . The beams were conducted through a variable aperture that can control the light flux to the sample and eventually to the detector (MCT KV104-0.5-A3/11, Kolm ar Tech Inc.). The signal is then preamplified and digitalized by two oscilloscopes (Picoscope 4227, Pico Technology) with maximum sampling rate of 250 MS/s (1 MSample is one million). The samples are excited either with a 10 ns pulse of the second harmonic of a Nd:YAG (Minilite II, Continuum) or with a Nd:YAG (Quanta-Ray, Spectra-Physics) emitting at 355 nm and followed by an optical parametric oscillator (OPTA) with the same specifications already described in 2.1.2.

2.2 Visible and fluorescence spectroscopy

Visible and fluorescence spectroscopy have a wide application in biophysics.

Visible spectroscopy is a powerful tool for the study of retinal proteins as their chromophore is sensitive to visible light.

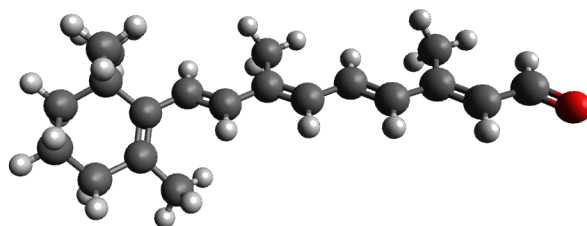


Figure 2.7: Ball-and-stick model of all-*trans* retinal. Grey is for carbon, white for hydrogen and red for oxygen.

The retinal molecule, that is covalently bound to the protein backbone in microbial rhodopsins, has in fact a conjugated system of p-orbitals that has a HOMO-LUMO transition in the visible range. It absorbs at about 440nm in organic solvents but shifts drastically its absorption maximum when inserted into the apoprotein, ranging from 360 to 635 nm. The electrostatic environment of the retinal in the protein interior is fundamental for the color tuning [134].

A UV/Visible absorption spectrum of the sample is therefore useful to check for the quality of the sample: a partially unfolded protein or a retinal molecule that is not covalently bound to the apoprotein will give rise to absorption bands in regions different from the characteristic absorption of that protein.

The experimental absorption spectrum of a light-sensitive protein is a result of the absorption of an ensemble of molecules (typically $\sim 10^{15}$ molecules), the distribution of the environments determined by protein fluctuations and flexibility of the neighbouring amino acids lead to an inhomogeneous broadening of the optical transition. The result is a broad absorption spectrum where for simplicity only the peak maximum is reported.

Aromatic residues of proteins also have conjugate systems of p-orbitals, their optical transitions fall in the UV range. A characteristic absorption band of the aromatic amino acids peaks at ~ 280 nm and is a marker band often used to quantify the amount of apoprotein in the sample.

In this work we used steady state visible spectroscopy to monitor the quality of the sample and to calculate the concentrations via the Lambert-Beer law:

$$A = \log_{10}\left(\frac{I_0}{I_t}\right) = \epsilon_{\lambda}cl \quad (2.29)$$

The quantities measured by the spectrometer are the intensity of the incoming light I_0 and the intensity of the light after the sample I_t , calculating the absorption A . Knowing the extinction coefficient at a specific wavelength ϵ_{λ} and the thickness of the measured sample solution l , it is possible to calculate the concentration c .

Time-resolved visible spectroscopy is here applied to study the changes in the absorption properties of the retinal during the protein photocycle.

Fluorescence spectroscopy has various applications in biophysics. The photosensitive dyes have the peculiarity to have a high fluorescent yield, absorbing and emitting a visible photon. In addition pH-sensitive probes have the peculiarity to change their absorption and fluorescence characteristics depending on their protonation state. In this work the high fluorescent yield of a pH indicator, pyranine (trisodium 8-hydroxypyrene-1,3,6-trisulfonate), has been used to detect transient pH changes in solution. Visible absorption spectra have been measured with a UV-2450-PC spectrometer from Shimadzu, fluorescence was measured with a Cary Eclipse spectrometer from Agilent.

2.2.1 Time-resolved visible spectroscopy

Time-resolved visible spectroscopy is used in biophysics to study the evolution of the absorption properties of a chromophore after it receives a stimulus. The study of retinal proteins requires a light flash to start the reaction, if this is achieved with a short laser pulse it is possible to follow the kinetics with a time resolution that spans from femtoseconds to seconds (to hours if needed). This very broad time range can be covered only with different setups and techniques.

The ultra-fast time range from fs to ns is covered by pump-probe spectroscopy where two ultra-short laser pulses come to the sample with a variable delay, the first as excitation, the second as probe. In this time-range the focus is on the early stages of the retinal excitation: the excited state, the isomerization process and the first photoproducts.

After the retinal isomerization the protein surroundings start to react in the vicinity of the chromophore leading to the first intermediates. Proton transfer reactions and structural changes that involve the rearrangement of many amino acids are fundamental steps for the the accomplishment of the protein function, they happen typically in the μs to ms time range in microbial rhodopsins [2] and they are at the center of the investigation of this work.

The time-range from ns to s can be efficiently investigated with a flash photolysis setup: a ns laser pulse excites the sample while the light of a lamp probes the sample's reaction at various wavelengths, selected with a monochromator. The device used for this work is LKS80 from Applied photophysics, equipped with a Xenon lamp. The exciting laser was a Nd:YAG Quanta-Ray from Spectra-Physics emitting at 355 nm and followed by an optical parametric oscillator from OPTA, able to convert the input laser wave into two output beams with tunable frequencies via a non-linear optical crystal. BR was excited with 532 nm pulses from a Nd:YAG Minilite laser from Continuum.

2.3 Data analysis

The raw measured data can be processed using mathematical models, with the assumptions that the sample is homogeneous (a discrete set of parameters can describe the data) and separable (the spectroscopic properties of a mixture of components is a superposition of the properties of the single components weighted by their concentration). Both IR and visible time-resolved data can be processed with the same approach.

2.3.1 Global fit kinetic analysis

As chemical kinetics are described by first order differential equations, they allow exponential decays as solutions. Single kinetics in the visible or in the infrared range can be fitted with exponential decay functions as shown in Eq. 2.30, to determine the time constants τ_i of the transitions between the different states n of the photoreaction.

Data sets of time-resolved difference absorption experiments are matrices that if analyzed as whole can bring several advantages. First, they can be fitted globally, this means that we use an unified model to describe all the kinetics at each spectral point: they will be all fitted with the same exponential decays. The result is that a kinetic model can be build incorporating information measured in different conditions, for example at different wavenengths. The number of exponential decays needed for the fit is to be estimated before the fit, together with the starting values for the parameters of the fit. In both cases a few iteration of the fit are necessary for the best estimation of the starting values.

$$\Psi(t, \lambda) = \sum_{i=1}^n DAS_i(\lambda) e^{-\frac{t}{\tau_i}} \quad (2.30)$$

In Eq. 2.30 the amplitudes of the exponential decays are named DAS, for decay associated spectra in the case of a global fit analysis.

If not mentioned otherwise, the kinetic model applied for the data analysis is the unbranched unidirectional model, where the photoreaction proceeds via sequential intermediates and backreactions are ignored. This simplification is necessary to reduce the degrees of complexity typical of a photochemical reaction in a membrane protein. If needed, other models can be applied for a more detailed kinetic study.

2.3.2 Singular value decomposition

In addition to the fit of the data, another powerful analysis tool is singular value decomposition (SVD) analysis, reviewed here [135]. In a matrix notation, the matrix Ψ of the measured time-resolved spectra has m rows as the number of time points and n columns as many spectral points. Each row (so each spectrum at time i) can be expressed as a linear combination of the pure spectra of the different intermediates, weighted by their concentration. This can be expressed in matrix formalism as:

$$\Psi = CE^T + N \quad (2.31)$$

Where E is the matrix that has as columns the pure spectra of the intermediates and is of dimentions $n \times p$ where p is the number of intermediates in the reaction. C is the matrix of the time evolution of the relative concentrations of intermediates, with dimensions $m \times p$. As our experimental method measures the data with an intrinsic random noise level (excluding sistematic errors), this information is also contained in the matrix and called N .

The aim of an SVD analysis is to retrieve the matrices C and E from the data Ψ . SVD analysis divides the spectrally-resolved and time-resolved information into two matrices, V and U , a third square and diagonal matrix S contains the so called "singular values"; the three new matrices are factorized in this way:

$$\Psi = USV^T \quad (2.32)$$

The singular values weight the vectors in the U and V matrices, quantifying the relative importance. The factorization can be modified in order to penalize noise over the actual signal.

2.4 Sample preparation

2.4.1 Preparation of hydrated films for FTIR

A detailed description of the sample preparation for FTIR experiments is provided in [136]. Briefly, wild type BR and BR variants were prepared as described in [137] and stored in a solution of 0.02% sodium azide from the collaboration partner Dr. Ramona Schlesinger and her lab. The purple membranes were subsequently washed by centrifugation at least 10 times with a 3 mM NaCl and 3 mM MES (2-N-morpholino ethanesulfonic acid) buffer solution at pH=6.3 for the measurements in 3.1 and in a 3 mM NaCl and 3 mM HEPES (4-(2-hydroxyethyl)-1-piperazineethanesulfonic acid) buffer solution at pH=7.2 if not specified. Around 10 – 20 μ l of this solution is dried on the surface of a Ba_2F window at ambient humidity. A sandwich is formed with a spacer and a second window and the sample is rehydrated laying next to it (not in contact) 3/4 drops of mixed water and glycerol at different ratios allowing for desired levels of relative humidity; if not specified in the text, the sample was rehydrated with a water/glycerol of 8/2 that corresponds to a 99% relative humidity [138].

A truncated construct (amino acids 1-307) of ChR2 from *Chlamydomonas reinhardtii* was expressed in *Pichia pastoris* and purified by Ni-NTA affinity chromatography as described elsewhere [97]. The purified protein was stabilized in 0.2% decylmaltoside. The solubilised samples were delivered from Dr. Schelisnger's lab. The protein film for FTIR experiments in detergent have been prepared as described in the paragraph above, else ChR2 was reconstituted in liposomes. The buffer exchange of detergent-solubilised proteins is performed with Amicon Ultra centrifugal filters from Millipore.

2.4.2 Preparation of samples for flash photolysis

The solubilised and reconstituted proteins are diluted with a desired buffer, specified in the text each time. The solution was added to a quartz cuvette of 1 cm path length and the final protein concentration was adjusted so that the maximum visible absorption of the retinal band is 0.5-0.8. If not specified, the sample cuvette holder was kept at 23° C using a circulating water bath (F25; Julabo) during the measurements.

2.4.3 Proteoliposomes formation

In order to probe the functionality of microbial rhodopsins, ion pumps are typically incorporated in artificial closed systems like proteoliposomes where a net protein orientation assures a charge transfer across the membrane during illumination [139, 107, 140, 4].

Liposomes formation is essential as it is the basis for the protein incorporation. Liposomes can be formed by swelling: lipids can be dried on a bottom-round-flask and resuspended with water or buffer. This leads to multilamellar liposomes, meaning several smaller liposomes trapped into larger ones, of undefined size.

Multilamellar liposomes can be fully solubilized with detergent and mixed with solubilized proteins; after detergent removal with Bio-Beads (SM-2 Bio-Rad) multilamellar liposomes are formed again with proteins incorporated. These liposomes of mixed size and unoriented proteins are not optimal for probing the function of target proteins but can be used to form a pellet and prepare a reconstituted sample for FTIR spectroscopy.

Unilamellar liposomes can be prepared from multilamellar vesicles with freeze-thaw cycles [141] and subsequently made uniform in size with extrusion [142]. Unilamellar vesicles of uniform size can be destabilized with a detergent amount close to the CMC, at this point the suspension can be mixed with the solubilized protein solution and the detergent carefully removed with Bio-Beads. This protocol assures a slow protein incorporation into destabilized unilamellar vesicles, achieving a net final protein orientation that is ideal for probing the function of microbial rhodopsins [143].

Another possible approach to reconstitute solubilized membrane proteins into unilamellar vesicles involves the presence of an His-tag to the proteins and Ni-NTA silicate beads [144]. This approach unfortunately cannot be applied with proteins expressed in native membranes like bacteriorhodopsin.

Bacteriorhodopsin can be extracted from purple membranes after incubation with a strong detergent, in this thesis work I followed the solubilization protocol from [145].

In this thesis the lipids used for protein reconstitution were DMPC (1,2-dimyristoyl-sn-glycero-3-phosphocholine), PC (L- α -phosphatidylcholine) and PS (L- α -phosphatidylserine), purchased from Avanti and stored at -20°C in chloroform. When dried, the lipids were kept under a controlled nitrogen atmosphere to prevent oxidation.

Bacteriorhodopsin-incorporated nanodiscs were kindly prepared by Nils Krause (from the group of Dr. R. Schlesinger), briefly: detergent-solubilized DMPC lipids were mixed with MSP1D1 scaffold proteins and with detergent-solubilized bacteriorhodopsin respectively at a ratio 50:1:0.5, the detergent was removed with Bio-Beads obtaining reconstituted BR in nanodiscs that are purified via size exclusion chromatography to remove residual components or aggregates.

Chapter 3

Results

3.1 The kinetics of the continuum band in BR

Given the lack of details of how a proton is stored in the PRC and the relevant and still unanswered question whether a proton can be stored in a cluster of water molecules in BR, new experimental approaches are needed to gain new informations, give additional constrains to the current models and help future simulations to refine their calculations. The two main approaches in this work are the use of buffer molecules as pH-sensitive vibrational probes and the use of polarization-resolved spectroscopy on oriented samples. The first approach allows us to compare for the first time in a single experiment, the kinetics of proton release and uptake with the intra-protein proton transfer reaction, conformational changes and continuum changes. The second approach is needed to indirectly gain information on the shape of the chemical entity that originates the continuum band.

3.1.1 MES buffer as pH-sensitive vibrational probe: an accurate kinetic study of the proton release and uptake in BR

MES buffer is one of the Good's buffers, as it meets important criteria of value in biological research [146]. The advantages of using a buffer over a pH indicator to detect the kinetics of proton release and uptake are several: Good's buffers are highly soluble even at high concentrations and still compatible with biological samples, they ensure a full control of the pH of the sample during the experiment and they are known to quickly respond to a change in the pH, accelerating the migration of protons from the protein surface to the bulk [77] [147]. The use of buffer molecules as pH sensitive vibrational probes has been already used to detect light-induced release of protons from photosystem II under steady-state conditions [148]. The challenge is to separate the difference bands of the buffer from the ones coming from the protein in a light-induced experiment, as the region between 1500 cm^{-1} and 900 cm^{-1} is crowded and typically several bands overlap as they absorb in the same range [149]. In this pioneering experiment [148] two different ligh-induced FTIR experiments

have been carried out in the exactly the same conditions and pH but using two different buffer molecules. The double difference spectrum cancels out the protein bands and results in the signal coming merely from the two buffers accepting a proton. This methodology was recently improved by performing experiments with natural and perdeuterated buffer molecules [150]. Here we show how this powerful approach can be used to understand better the details of protein-bulk proton transfers in BR and gain informations on the continuum band.

MES buffer is here used as pH-sensitive vibrational probe to detect the transfer of protons between BR and the bulk solution. In addition, as the kinetics of the detection of protons by the buffer molecules were measured with FTIR spectroscopy, such an experiment allows us to probe in the same experiment all the proton transfers happening during the protein photocycle: protons exchanges between protein residues, proton transfers from and to protonated water clusters (or protonated LAN of hydrogen bonds) and proton transfers from and to the bulk solution. As MES buffer has infrared absorption bands that overlap with the ones from proteins and lipids (see Fig. 3.1.1), it is very difficult to separate the buffer difference bands from the protein ones. One approach could be to run two parallel experiments where all experimental conditions (temperature, pH, hydration level, ...) are kept as much as possible similar and the only difference is the choice of the buffer: the two experiments can be carried out with two different buffers having similar pK_a [148] or with the same buffer but in a different isotopically labelled version [150]. A second approach could be to use an isotopically labelled buffer where some absorption bands fall in a range free of protein bands (e.g. above 1800 cm^{-1}). This is a novel approach and its potential is discussed in subsection 3.1.3. The following results describe a set of experiments carried out using the approach of two parallel experiments carried out with MES and perdeuterated MES ($\text{MES}d_{12}$) buffers. The measurements in this section were performed with Dr. V. Lorenz-Fonfria who also did most of the data analysis.

The detection of the continuum band with Step Scan FTIR

The photocycle of BR, described in 1.2.2 can be investigated with Step Scan FTIR (2.1.2), a technique that proved to be very succesful for the investigation of internal proton transfer steps [3]. Fundamental steps for the understanding of the proton pumping mechanism are the proton release and uptake from and to the bulk solution. While the proton uptake has been found concomitant with the reprotonation of Asp96 [26][151], the proton release does not correlate with the deprotonation of the Schiff base proton acceptor Asp85.

The absorption changes measured in a typical Step Scan experiment (see 2.1.2 for details) are reported in 3.1. The internal protonation changes of carboxylic acids during the protein photocycle can be followed by looking at the difference signal in the range between $1770 - 1700\text{ cm}^{-1}$. In Fig. 3.1 this area is enlarged in a contour plot. The most evident band is the positive feature at 1761 cm^{-1} , that shows the transient protonation of Asp85 [152]. What we detect in this wavenumber range is the $C = O$ stretching vibration that occurs

only if the carboxylic acid is protonated. A seven wavenumbers red shift of this frequency occurs in the M-to-N transition [153]. Asp96 absorbs at 1742 cm^{-1} in the ground state and shifts its frequency in the early stages of the photocycle before transiently deprotonating in the millisecond range. Additional changes in this range come from the H-bonding changes of the protonated Asp115. The rest of the spectral range below 1700 cm^{-1} is dominated by the absorption changes of the retinal chromophore and by the protein conformational changes. These bands will not be discussed here as they are not in the focus of this experiment.

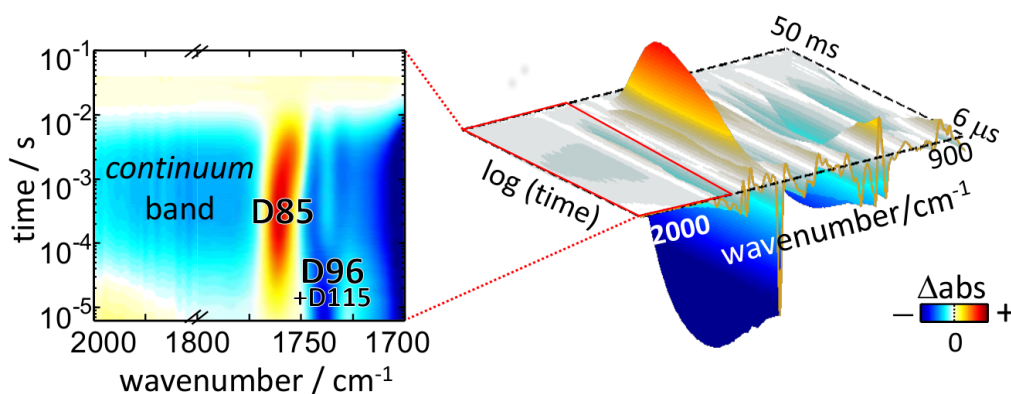


Figure 3.1: On the right side the time-resolved difference absorption spectra measured in a step-scan FTIR experiment. In the inset the expanded absorption changes in the region where the continuum band is visible.

Overlapped with these changes and extending over more than 200 wavenumbers is the continuum band, a transient broad negative absorption that extends from around 2200 cm^{-1} to well below 1700 cm^{-1} . Assigned to the proton release complex (see 1.2.2), its behaviour can be studied in the mid-IR in a time-resolved IR experiment with enough time-resolution to resolve its rise (~ 40 and $150\text{ }\mu\text{s}$ in our experimental conditions, see 2.1.2) and decay (4, 5 ms). Among other methods, Step Scan FTIR is more suitable to study the continuum band given its high temporal resolution and its broad measuring range (respectively $6\text{ }\mu\text{s}$ and between 900 and 2200 cm^{-1} in our experimental settings, see 2.1.2).

The continuum band has a broad difference absorption in BR and it is not trivial to choose a frequency or a frequency interval that is representative for its kinetics. It is known that the exciting laser pulse of $\sim 10\text{ ns}$, typically used to start the reaction, induces a heat jump to the sample [154]. Not all incoming photons that are absorbed by the retinal molecules start the photocycle ([155] [156]) and the exceeding energy is dissipated and heats up the surrounding water molecules [154]. This is reflected by an absorption change of the bulk water molecules in response to the temperature change. These changes are maximal close to the regions where the water absorbs that are, within the measured range, at $\sim 1650\text{ cm}^{-1}$ (the water bending mode) and at $\sim 2140\text{ cm}^{-1}$

(a combination of the H_2O bending and the libration modes). We therefore restricted our analysis to the range $1950 - 1800\text{ cm}^{-1}$.

The infrared fingerprint of MES and perdeuterated MES, $MESd_{12}$

MES and $MESd_{12}$ have a characteristic absorptions in the IR range. The two molecules differ in their absorption in all the bands where C-H (or C-D) bonds are involved, due to the different mass of the atoms involved. Both buffers change their absorption also upon protonation/deprotonation, as the additional charge affects electrostatically the vibrations of the whole molecule.

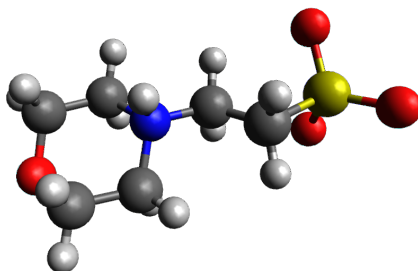


Figure 3.2: A schematic representation of the acidic form of MES buffer. In grey the carbon atoms, nitrogen is depicted in blue, oxygen atoms in red, sulfur in yellow and hydrogen atoms are in light-grey. The excess proton is at the nitrogen atom as shown in [157]

The absolute absorption of MES and $MESd_{12}$ have been measured below and above its $pK_a = 6.1$ and are shown in Fig. 3.3.A. The spectra were measured in solution with the ATR accessory and the water contribution to the absorption spectrum has been subtracted.

An assignment of the bands here is complicated by the high overlap of the many bands present, due to the complexity of the molecule.

By subtracting the acidic from the basic form of the two buffers (MES and $MESd_{12}$) and taking into account their concentration and the penetration depth in the ATR setup, we can obtain the molar absorption IR spectra of the protonation of the buffers, shown in Fig. 3.3.B. This difference pattern will transiently appear in a Step Scan experiment when the buffer takes up the protons pumped from the proteins, in an experiment like the one shown in Fig. 3.1.

In this absorption range the complex signature of the protonation of the MES buffer overlaps with the protein and cofactor signals making it very challenging to separate the bands. Only a double-difference experiment can remove the difference signal from the protein, leaving the double-difference of the protonation of MES and $MESd_{12}$, shown in Fig. 3.3.B.

It is important to note that the protonation of MES leads to a negative band at 1112 cm^{-1} . At a similar frequency, at 1115 cm^{-1} a positive band indicates the protonation of $MESd_{12}$.

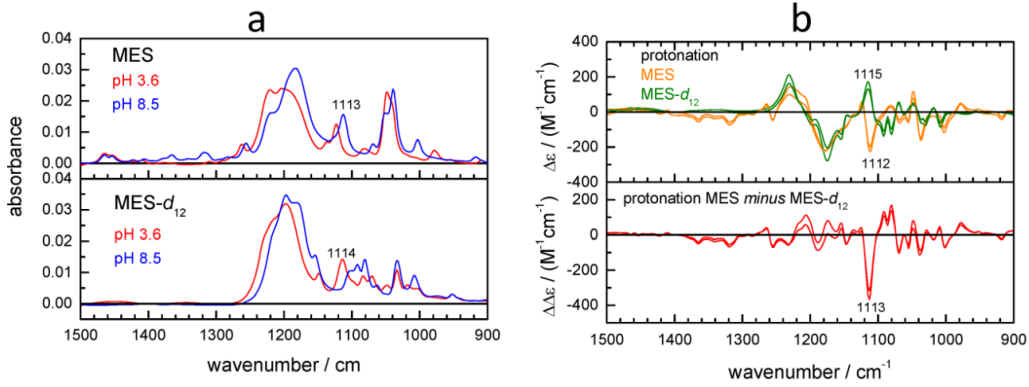


Figure 3.3: A. The infrared absorption spectra of MES and MES d_{12} in the protonated ($pH = 3.6$) and unprotonated ($pH = 8.5$) forms. The concentration was approximately 50mM. B. On top the difference between the absorption spectra showed in A. For both MES and MES d_{12} , this difference spectrum represents the absorption changes upon buffer protonation. Below, in a double difference absorption spectrum, the difference in the protonation between MES and MES d_{12} , mimicking the double difference spectrum with BR.

Molar absorption coefficient in the membrane plane of BR determined by transmission FTIR spectroscopy

Knowing the infrared molar absorption coefficient of BR in the membrane plane (the plane where the FTIR measurements showed in this chapter are performed) can help to estimate the molar ratio between protein, buffer and water in our sample.

Here the molar absorption coefficient is calculated for the whole BR molecule that consist of of a multitude of IR-absorbing units. The values correspond therefore to the superposition of the absorption coefficients of all amino acids and cofactors (retinal, lipids and water molecules) in the protein. A BR film was prepared without buffer, drying PM patches on a BaF_2 window, as explained in 2.4. An iris of ~ 4 mm, small enough to ensure that both visible and IR light probe the same sample area, was placed in front of the sample. We measured visible and infrared spectra of the same light-adapted sample, placed perpendicular to the incoming probing beam. The spectra are shown in Fig. 3.4.

Given the the known isotropic extinction coefficient of BR determined in solution in the visible range, $\epsilon_{iso}(570) = 62700 \text{ M}^{-1}\text{cm}^{-1}$ [158] and the known angle of the retinal electric transition moment $\theta = 69^\circ$ [159], we could use the relations for axially oriented samples [159] (equations 3.1 and 3.2) to estimate the IR molar absorption coefficient of light-adapted BR in the membrane plane from the extinction coefficient of the retinal chromophore.

$$\epsilon_{iso} = \frac{(\epsilon_z + 2\epsilon_{xy})}{3} \quad (3.1)$$

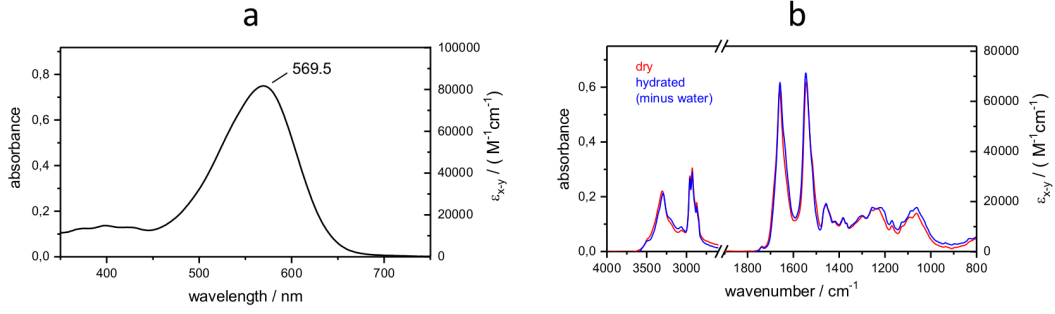


Figure 3.4: UV-Vis (a) and IR (b) spectrum of light-adapted BR in purple membranes for the determination of the molar absorption coefficient in the membrane plane. In the IR, the coefficient has been calculated for both the dry and hydrated sample, after the subtraction of water.

$$\frac{(\epsilon_z - \epsilon_{xy})}{(\epsilon_z + 2\epsilon_{xy})} = 0.5(3 \cos^2 \theta - 1) \quad (3.2)$$

The estimated IR molar absorption coefficient in the plane of the membrane for BR is shown in Fig. 3.4, based on the calculated value of the extinction coefficient in the membrane plane in the visible $\epsilon_{xy}(570) = 82000 \text{ M}^{-1}\text{cm}^{-1}$.

Note that BR is measured here is in the native membranes (Purple Membranes) and the extinction coefficient is not related to only one molecule but contains information on the chromophore, the protein, the lipids and in minor amounts also contaminant molecules that could be carried along through the purification process.

Characterization of the protein film and determination of its pH

We prepared two films consisting of PM, NaCl and buffer, drying the two samples on BaF_2 and rehydrating them as explained in 2.4.1. The two films, with similar absolute concentration but same relative concentration of all the constituents of the suspension, differ for the buffer used: MES and MES d_{12} . In the rehydrated film, we can fit the absolute absorption with the sum of the spectra of all the constituents and more precisely estimate the molar ratio of BR/MES/water molecules in the sample, that is respectively 1/18,1/1570. The results are shown in Fig. 3.5.

The spectral decomposition can also provide informations on the actual pH of the film. The starting solution was at $pH = 6,3$, after the drying and rehydrating processes we found a value of $pH = 6.25$, that is very close to the mother solution. The determination of the real pH of the film is important here as we measure the changes of the populations of acidic and basic buffers: the signals are bigger if the measurement is carried out at a pH close to the pK_a of the molecule.

At this concentration of buffer in the film, $\sim 600 \text{ mM}$ (one MES molecule every ~ 90 water molecules), any proton released from the protein is taken by the buffer within the time resolution of our measurements. It is known

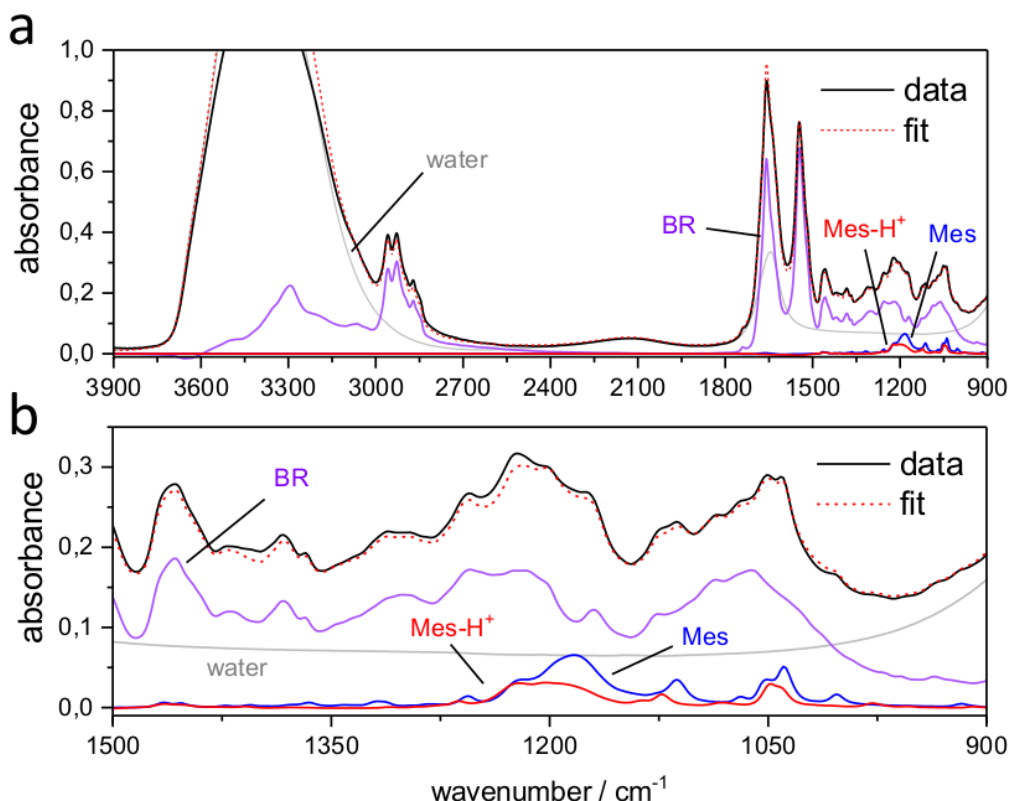


Figure 3.5: A. Absorption spectrum of the rehydrated purple membrane film with MES buffer (black), fitted (red, dotted) with the spectra of dry BR (purple), distilled water (grey), protonated and deprotonated buffer (respectively red and blue). B. Enlarged area between 1500 and 900cm⁻¹.

infact that in absence of buffer the protons that are released by BR can move along the membrane surface before reaching the bulk solution, but increasing the buffer concentration in the solution, the movement of the protons to the bulk is accelerated [20].

The effective response time of the MES buffer in our case is unknown but can be roughly estimated from the literature [72], giving a time constant of ~ 100 ns although measured in different experimental conditions (in solution and at different salt concentration). In our experimental conditions we are able to detect a signal from MES as early as $8 \mu\text{s}$ (see the following chapter) so this is the minimum response time in our case.

Transient protonation changes of MES buffer during BR photocycle

Two parallel Step Scan FTIR experiments have been carried out as described previously in this chapter. The final absolute concentration of excited molecules of the two samples was not exactly the same, the two experiments have been scaled with a proper factor (in this case was 1.04). The result of the operation is reasonable, given the broad spectral range measured.

The difference spectra at $370 \mu\text{s}$ after laser excitation are shown in Fig. 3.6.

At this time point a proton is released to the bulk solution where it is captured by the buffer. A small negative band at 1112 cm^{-1} appears in the spectrum buffered with MES and a positive feature appears at 1115 cm^{-1} in the sample with MESd_{12} .

The subtraction of the two spectra is shown in Fig. 3.7.A where it is compared with the band pattern from the subtraction of the protonation of the pure buffer solutions measured with the ATR, as already shown in Fig. 3.3. All the bands are in perfect agreement, an excellent result given that the two experiments are performed with different setups, at different hydration conditions, one in a time-resolved experiment and the other in a steady state measurement. The striking similarity of the two double difference spectra suggests that the MES molecules in the Step Scan sample are in an environment that is very close to the bulk solution, escluding the possibility that they might penetrate in the protein interior or close to the membrane.

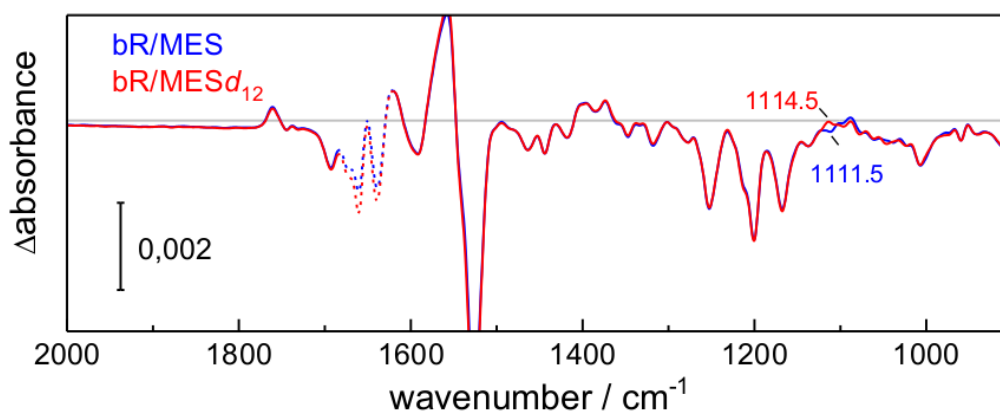


Figure 3.6: FTIR difference spectra at $370\mu\text{s}$ after the laser excitation, measured with MES (blue) or MESd_{12} (red) buffer.

We analyzed the kinetics of the protonation changes of the MES buffer following the area of the two biggest bands in the double difference spectra. Kinetics of the area of the bands measured with an internal baseline have the advantage to be free of baseline oscillations.

The results, reported in Fig. 3.7.B show two similar kinetics with the results from the area at 1113 cm^{-1} providing a better S/N. In Fig. 3.8 the comparison of the measured kinetics integrated in the interval $1123 - 1104\text{ cm}^{-1}$ for the samples without buffer, with MES buffer, with MESd_{12} and the subtracted kinetic. This last trace has been further used in the data analysis as buffer protonation kinetic.

A multiexponential fit of this kinetics (Fig. A.2) gives the time constants for the proton release and uptake from the bulk in BR. The proton release happens with time constants $52 \pm 10\mu\text{s}$ and $150 \pm 40\mu\text{s}$, while the proton uptake with a single exponential at $4.3 \pm 0.4\text{ ms}$. The data have been further analyzed by Victor Lorenz Fonfria reconstructing the lifetime distributions using the maximum entropy method [160]. This analysis has the advantage

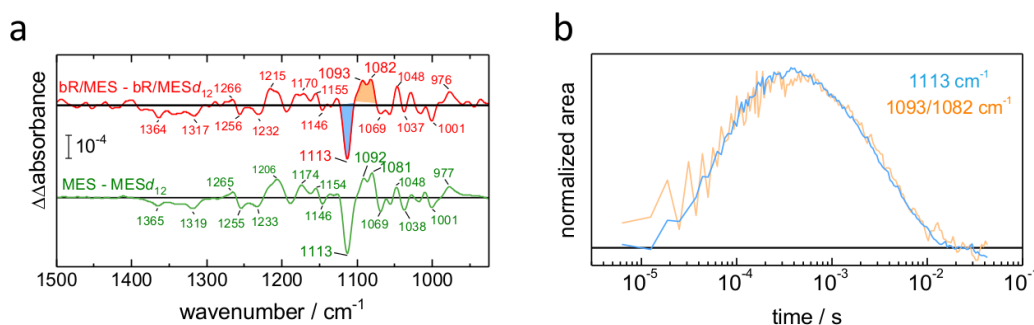


Figure 3.7: A. Double difference spectra of the absorption changes shown in Fig. 3.6 (top), compared with the double difference spectra already shown in Fig. 3.3.B. The kinetics of the main bands highlighted in blue and orange can be followed in B. The spectra in Fig. 3.6 have been scaled with a factor 1.04 before the subtraction.

that does not need to assume a priori the number of exponentials for the fit, important here to determine precisely the number of steps in proton release and uptake.

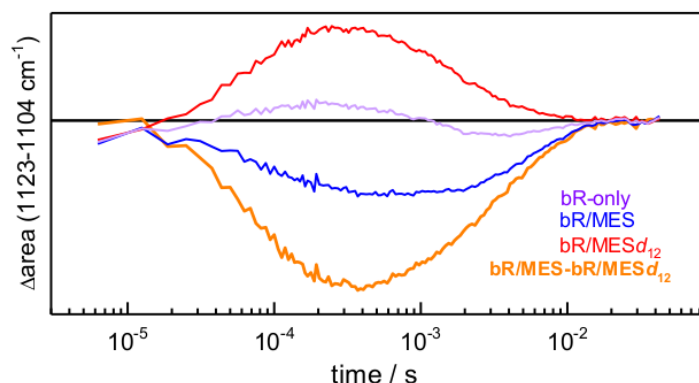


Figure 3.8: Kinetics of the wavenumber interval 1123 to 1104 cm⁻¹ of BR with MES (blue), BR with MESd₁₂ (red), only buffer (BR with MES-minus-BR with MESd₁₂, orange), and only BR (BR plus MES-minus-MESd₁₂, purple).

The proton release kinetics

The proton release from BR has been measured before with soluble pH-indicating dyes such as *p*-nitrophenol [161] or pyranine (also called HPTS) [77] in weakly buffered solutions. It has been soon noted that the response time of these dyes was ~ 1 ms because the protons in absence of mobile buffers were trapped along the membrane surface of purple membrane sheets, delaying the detection from soluble dyes [161][77][16][72]. Another approach is to covalently bind a pH-sensitive dye to the protein surface [20][75] obtaining a fast response to proton release but with the drawback that the dyes might respond to surface polarity

changes and often need protein genetic engineering in order to introduce the dye at a proper position [75].

Our results can be compared with the kinetics measured with covalently bound dyes, with the advantage that no protein engineering is needed and that we measure in the same experiment also the kinetics of all other internal proton transfers. The proton release of BR was reported to be monoexponential with a time constant of $\tau \sim 75 \mu\text{s}$ [76, 74, 35]. The one exponential fit of the curve in Fig. A.2 gave a time constant of $80 \pm 4 \mu\text{s}$ that is compatible with the literature value.

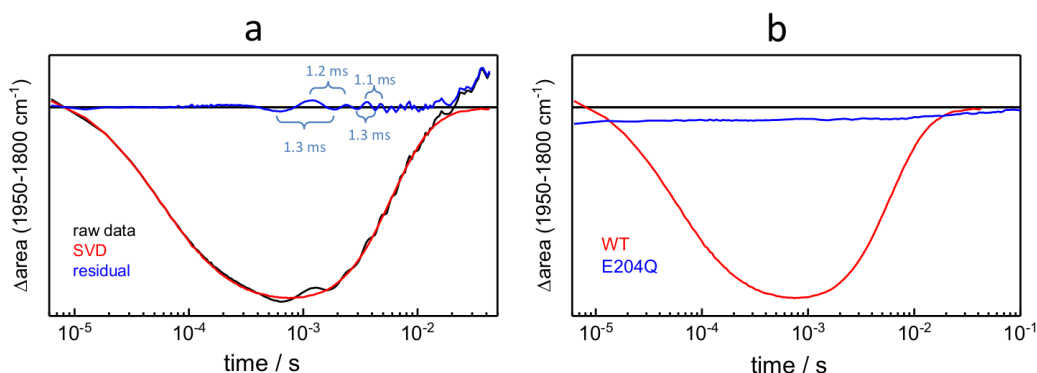


Figure 3.9: Time-resolved evolution of the integrated area between 1950 – 1800 cm⁻¹ for wild type BR (a), compared with the E204Q mutant (b). In (a) the raw data (black) is compared with the kinetics after SVD analysis (red) and the corresponding residuals (blue). A small oscillation in the raw signal is an artifact from the spectrometer and can be removed with a proper SVD, (see section 2.3).

The lifetime distribution approach using the maximum entropy method suggested that the best fit could be obtained with two time constants at $52 \pm 10 \mu\text{s}$ and $150 \pm 40 \mu\text{s}$. Repeating the fit of the data from [20] with the same approach and two components could be clearly resolved with $59 \pm 3 \mu\text{s}$ and $200 \pm 20 \mu\text{s}$, further confirming that the proton release from BR is biexponential (Fig. A.3). The kinetics of the proton uptake follow a single exponential decay with time constant of $\tau = 4.3 \pm 0.4 \text{ ms}$.

A fast time constant of $\tau = 10 \pm 2 \mu\text{s}$ for the proton uptake has been found analyzing the data obtained with fluorescein [20], before the proton release time constant. The time resolution of our experiment with MES buffer was not enough to fully resolve this fast component but the lifetime distribution analysis gave a peak at $\tau = 8 \pm 4 \mu\text{s}$, confirming this result.

The kinetics of the continuum band can be followed extracting kinetic traces from the interval 1950 – 1800 cm⁻¹ but given the small intensity of the signal in this region and the consequent small signal-to-noise, it is common to study the time evolution of the continuum band integrating the kinetics over the whole spectral range 1950 – 1800 cm⁻¹ as can be seen in Fig. 3.9a. Small oscillations in the $\sim \text{ms}$ range can be corrected with a proper SVD analysis (see section 2.3 and Fig. 3.9.a). A control measurement with the mutant E204Q, that is known

to have no continuum band [42], ensures that the region we are integrating is free of any artifact from the heating of bulk water [154], as shown in Fig. 3.9b.

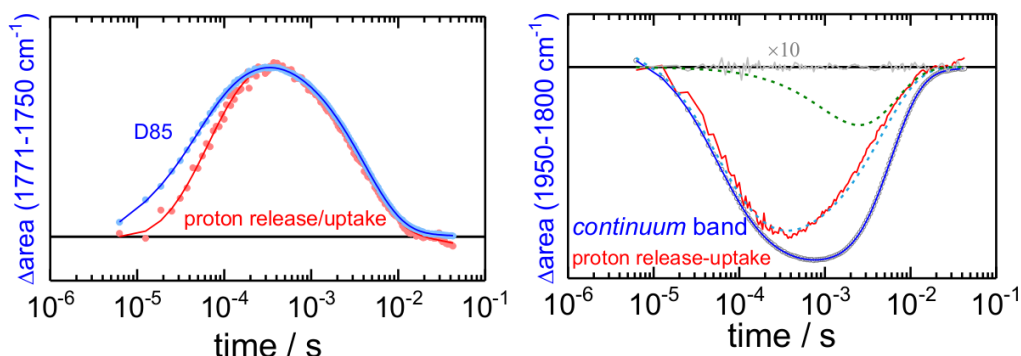


Figure 3.10: Kinetics of the proton release and uptake revealed by analysis of the MES buffer bands (red) compared with the kinetics of the protonation of D85 (A) and the continuum band (B). The dashed lines are the decomposition of the continuum band kinetics into two components, one that correlates with the proton release (blue) and one that follows the later rise of the continuum band (blue); in grey the standard deviation from the fit.

We can now compare the kinetics of proton release and uptake with the kinetics of other events happening during the photocycle. Of major interest are the comparisons between the proton release and the protonation of *D85* or the rise of the continuum band.

It is known that the protonation of *D85* from the SB triggers the reorientation of *R82* and consequently the release of a proton to the bulk (see 1.2.2 for more details). We can here separate in time the two events and show that the protonation of *D85* proceeds the release of a proton. In Fig. 3.10.A are shown the kinetic comparison between this two events. The rise of the *D85* band involves two major exponential decay steps at $\tau = 38 \pm 3 \mu\text{s}$ and $\tau = 115 \pm 10 \mu\text{s}$. This time constants precede the ones for the proton release ($52 \pm 10 \mu\text{s}$ and $150 \pm 40 \mu\text{s}$) although the deviation is modest considering the statistical uncertainties.

The comparison of the proton release and uptake kinetics with the continuum band kinetics revealed at first that the time constants for the rise of the continuum band of $42 \pm 3 \mu\text{s}$ and $150 \pm 6 \mu\text{s}$ are, within the uncertainties, equal to the time constants of the proton release to the bulk measured with MES buffer. This result confirms the hypothesis that the PRC is the terminal release group in BR.

As can be observed in Fig. 3.10B, the kinetics of the continuum band shows an additional rise component with time constant of $\tau = 1.5 \pm 0.1 \text{ ms}$ that is not associated with any proton release or uptake from/to the bulk. The continuum band kinetic can be decomposed into two components, one that reflects the proton release kinetics and one that comes from the additional rise component at 1.5 ms, as shown with dashed lines in Fig. 3.10B. This second component is likely to follow the N intermediate kinetics, as suggested by a kinetic analysis

of the positive retinal C-C stretching band at 1187 cm^{-1} (not shown).

3.1.2 The proton uptake complex, a new protonated cluster in the photocycle of BR

The recorded time-resolved datasets can be further analyzed with global fit and spectral informations related to the time constants can be extracted. In Fig. 3.11 the decay associated spectra (DAS) are shown for the six time constants that describe the photocycle.

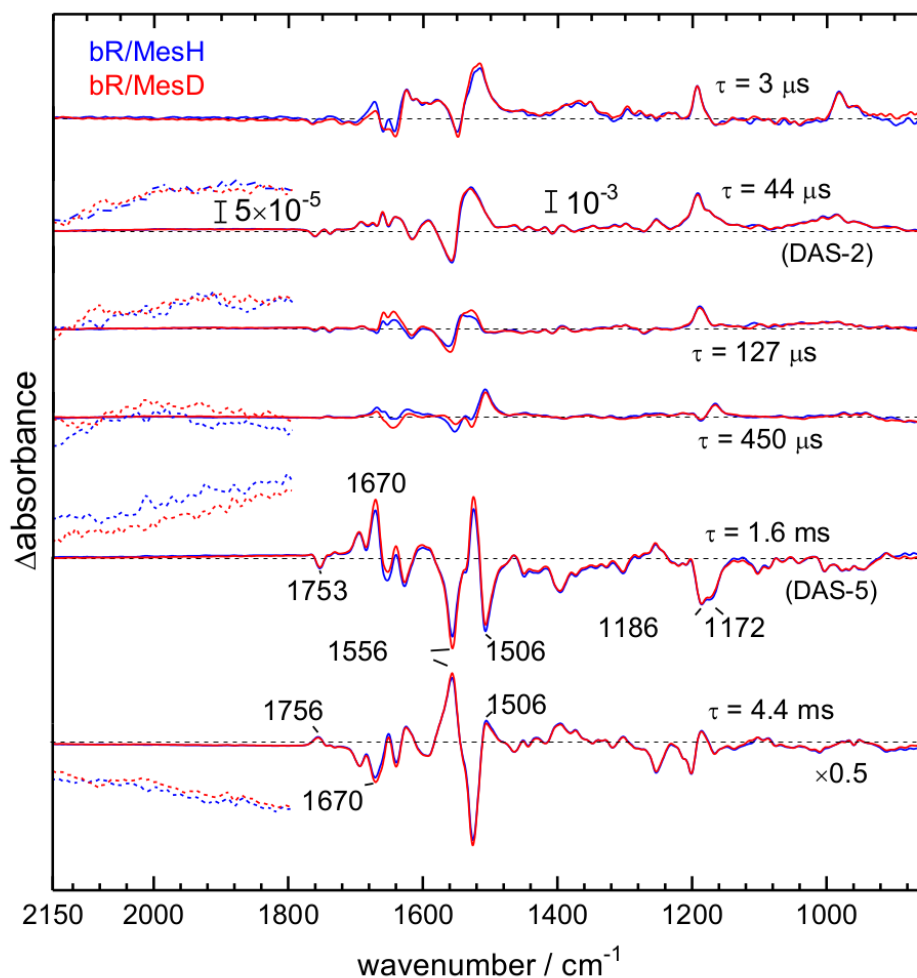


Figure 3.11: Decay Associated Spectra (DAS) obtained from a global exponential fit of Step Scan measurements of BR with MES or MES d_{12} (blue and red, respectively). Dashed lines represent a 20-fold magnification of the region from 2200 cm^{-1} to 1800 cm^{-1} . The DAS-6 at $\tau = 4.4\text{ ms}$ is scaled at half of its size for displaying purposes.

The DAS represent the changes in the spectrum that are associated with a specific time constant. Positive features represent the rise of a signal, negative the decay.

The continuum band can be observed above the noise level in the DAS-2 with $\tau = 44 \mu\text{s}$, in DAS-3 with $\tau = 127 \mu\text{s}$ and DAS-5 with $\tau = 1,6 \text{ ms}$ as a positive signal, meaning that in a difference spectrum there is a rise of a negative band. These three signals present spectral differences as in DAS-2 and DAS-3, the ones kinetically connected to proton release, the absorption changes rise in intensity from 2200 cm^{-1} to 2000 cm^{-1} and remain constant until 1800 cm^{-1} . The absorption changes in DAS-5 instead have a different spectral shape, continuously rising in intensity from 2200 cm^{-1} to 1800 cm^{-1} . This band shapes are reproducible as the same measurement has been repeated in total 5 times with MES or MES d_{12} buffers, see Fig. 3.12.

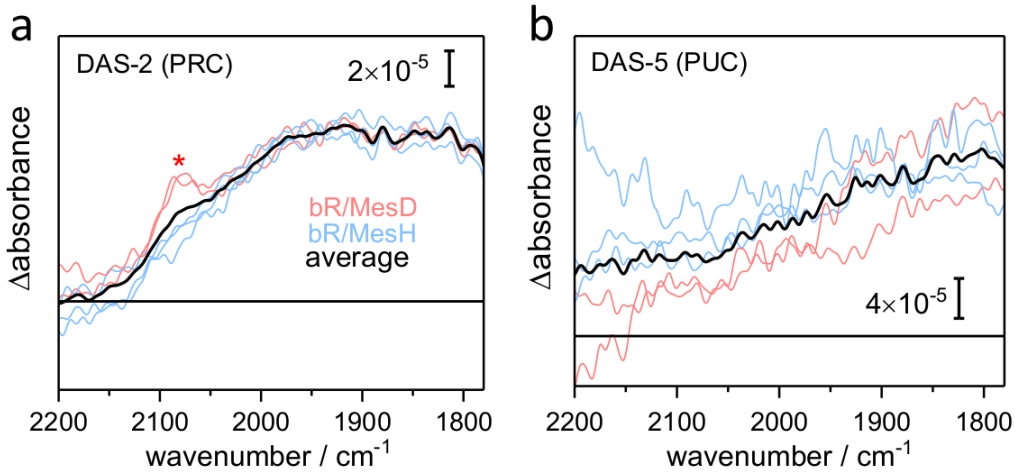


Figure 3.12: DAS-2 (A) and DAS-5 (B) from Fig. 3.11 of the spectral range typical of the continuum band from 2200 cm^{-1} to 1800 cm^{-1} . Blue spectra come from the measurements with MES buffer, red with MES d_{12} and black is the average of all the spectra, irrespective from the buffer used. In (A) a sharp band is marked, it comes from the protonation of MES d_{12} and it will be further analyzed in 3.1.3.

Given this spectral differences, DAS-5 must have a different chemical origin respect to DAS-2 and DAS-3. The rise of a continuum band at $\tau = 1,6 \text{ ms}$ does not correlate with any proton release or uptake events. This continuum band observed in DAS-5 presumably represents a deprotonation of an unknown protonated cluster of water and/or amino acid residues. We will call this cluster proton uptake complex (PUC) because of the following reasons.

DAS-5 shows a negative band at 1186 cm^{-1} that is characteristic for the reprotonation of the SB in a 13-*cis* retinal [162] but lacks a positive band at 1742 cm^{-1} that would indicate the deprotonation of D96 [29]. We need then to distinguish two N states, N_1 and N_2 with the difference that in N_1 D96 is deprotonated (in favour of the SB) and in N_2 D96 is already reprotonated [29]. DAS-5 shows characteristic bands for the formation of N_2 at $\tau = 1,6 \text{ ms}$ but as can be seen from the kinetics in section 3.1.1, the proton uptake from the bulk happens only at $4.3 \pm 0.4 \text{ ms}$. After $\tau = 1,6 \text{ ms}$ the SB has been already reprotonated, D96 has also been reprotonated but no protons have

been uptaken from the bulk solution from the cytoplasmic side.

We therefore propose that the deprotonation event that we assign to a transient negative continuum band comes from an unknown H-bonded network that is located between the protein cytoplasmic side and D96 (a proposed photocycle is shown in Fig. 4.1).

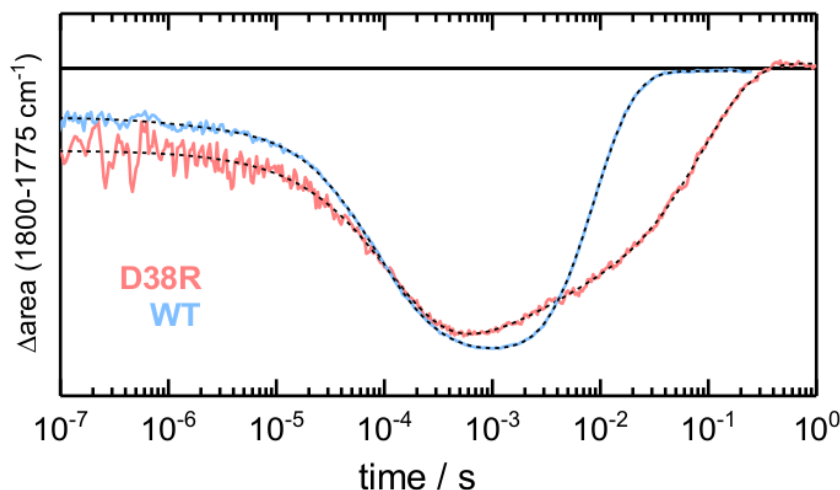


Figure 3.13: Kinetics of the continuum band of wild type BR (blue) and of the mutant D38R (red) in the spectral interval $1800 - 1775 \text{ cm}^{-1}$ measured with the QCL setup. The fit is shown as dotted black lines.

In order to localize and identify the key amino acids or water molecules of the PUC, a systematic work of single point mutations is needed. We started with a mutation of D38 that is known to alter the proton uptake kinetics [163]. D38 is water exposed, therefore deprotonated and negatively charged. The replacement with a positively charged Arg residue (D38R) affects the reaction steps in the last part of the photocycle and the last reaction intermediates N and O are not populated: the protein relaxes back to the ground state directly from the M intermediate [163].

The kinetics of D38R have been measured with the QCL setup covering the spectral range between $1800 - 1700 \text{ cm}^{-1}$, the kinetics of the continuum band are reported in Fig. 3.13 in comparison with the wild type BR. From a global fit analysis it is possible to observe that the continuum band of the mutant D38R lacks the late rising component that we attributed to the PUC, suggesting that indeed the non-conservative mutation could have disrupted the protonated network of the PUC.

3.1.3 Other potential vibrational probes

The deuterated form of the buffer, $\text{MES}d_{12}$, shows absorption bands in the region between 2000 cm^{-1} and 2300 cm^{-1} . As can be observed in Fig. 3.14 the deprotonated form of $\text{MES}d_{12}$ has two bands with absorption maxima at 2220 cm^{-1} and 2085 cm^{-1} while the protonated form has a smaller absorption

band at 2114 cm^{-1} . In a difference experiment, the protonation of the buffer would result in two distinct negative peaks as shown in Fig. 3.14b.

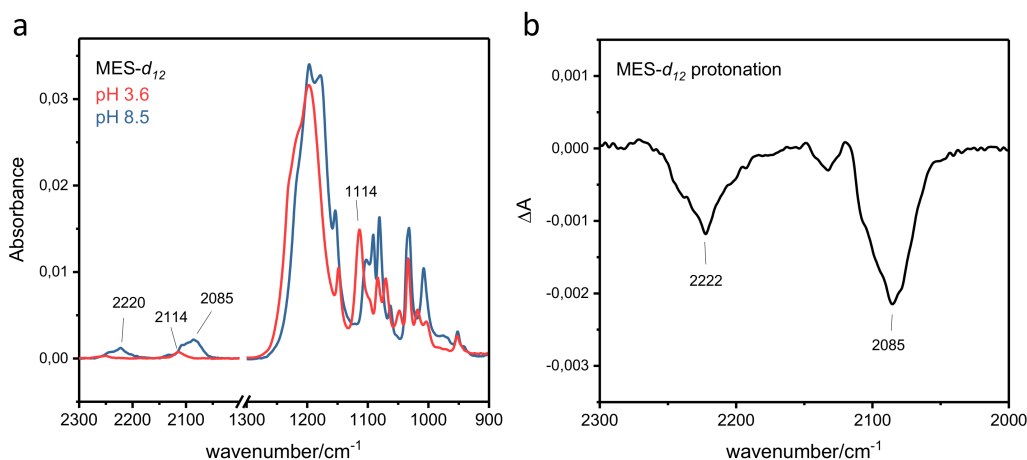


Figure 3.14: (a) Absorption spectra of protonated and deprotonated MESd_{12} as shown before in Fig. 3.3, here a broader range is showed where peaks appear at 2085 cm^{-1} , 2114 cm^{-1} and 2220 cm^{-1} . (b) Deprotonated-protonated MESd_{12} difference spectrum representing the difference signal of the protonation event.

In this region, in a standard non deuterated FTIR sample, there are no absorption bands except for a weak broad band coming from the bending mode of water in combination with libration modes. The absence of overlapping bands is important as the signal of the buffer protonation can be detected in a single experiment without the need of subtracting two datasets, as done in 3.1.1.

The spectral analysis of the time-resolved data of BR with MESd_{12} as buffer, infact, revealed a negative transient band that appears at $\sim 2085\text{ cm}^{-1}$. The detection of the band at 2220 cm^{-1} was prohibited by a filter used to improve the signal-to-noise ratio that cuts the wavenumbers above 2200 cm^{-1} .

Fig. 3.15a shows the negative band from the protonation of MESd_{12} at $370\mu\text{s}$ after the laser flash in a step scan experiment with BR. In Fig. 3.15b the kinetics of the proton release and uptake from BR, measured integrating the area of the peak at 2085 cm^{-1} . The time constants obtained from a multi-exponential fit analysis are identical (within the noise) to the ones obtained in 3.1.1 substrating two datasets and analysing the kinetics at 1114 cm^{-1} .

In our Step Scan data the kinetics obtained from the area of the 1114 cm^{-1} band show a better signal-to-noise ratio, therefore we based our analysis on those data. The absence of overlapping peaks with the 2085 cm^{-1} and 2220 cm^{-1} bands opens although the possibility to work with only one sample; the signal could be furthermore amplified by preparing thicker samples.

Preliminary DFT calculations of MES and MESd_{12} buffers suggest that it is the coupled C-D stretching mode of the morpholine ring to give rise to this high-frequency bands in MESd_{12} (data not shown).

Simulations of other buffers that share with MES the morpholine ring such as HEPES (4-(2-hydroxyethyl)-1-piperazineethanesulfonic acid), MOPS (3-(N-

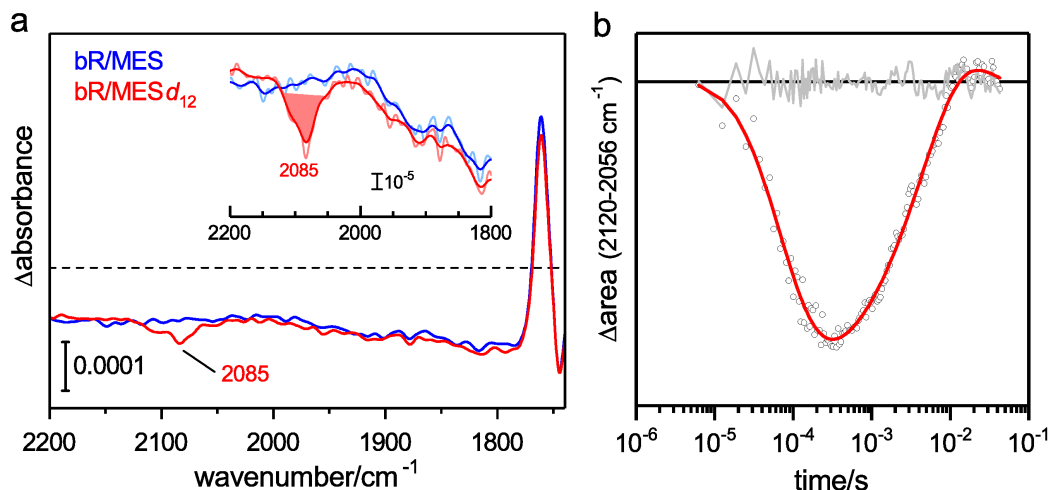


Figure 3.15: (a) FTIR difference absorption at $370\mu\text{s}$ after excitation of BR hydrated films buffered with MES and MESd₁₂, enlarged spectral region from Fig. 3.6. A peak at $\sim 2085\text{ cm}^{-1}$ rises from the absorption difference of the protonation of MESd₁₂; after smoothing at 12 points, the area of the peak shown in the inset is calculated at every time step and its kinetics are shown in (b). Grey empty dots are the data points, in red the fit and in grey the residuals.

morpholino) propanesulfonic acid) and CAPS (N-cyclohexyl-3-aminopropane sulfonic acid) in their deuterated form also show absorption bands in the same region between 2000 cm^{-1} and 2300 cm^{-1} that differ in the protonated and deprotonated form.

The still untested use of different deuterated buffers (with different pK_a) for the detection of proton release and uptake from proteins in the IR, would give the possibility to measure proton transfers to and from the bulk in a single measurement and at different pH values.

3.2 The dichroism of broad IR difference bands during the photocycle of BR

The aim of this section is to better define the properties of broad IR bands with polarization-resolved FTIR and to contribute to define their shape and molecular origin. Two main approaches have been used: the dichroism with respect to the membrane normal axis has been investigated with transmission and ATR steady-state measurements, whereas the dichroism in the membrane plane (see Fig. 2.6) has been studied with a photoselection approach in steady-state and time-resolved experiments.

As already mentioned in 1.2.2, broad bands in the broad spectral region $2200-1800\text{ cm}^{-1}$ are assigned to protonated clusters of water molecules and/or amino acid residues in BR, the negative difference band in this range has been called continuum band. Below $\sim 1770\text{ cm}^{-1}$ it overlaps with infrared bands coming from the protein amino acids and the chromophore and it has been therefore not studied in this range. Above 2200 cm^{-1} a different transient broad band can be observed with maximum intensity at $\sim 2500\text{ cm}^{-1}$; the origin of this band can be attributed to a neutral cluster of water molecules and will be analyzed in 3.2.2.

The kinetics of the continuum band have been examined in 3.1 where two contributions are found to come from two different protonated water clusters, an earlier continuum band comes from the PRC and a later one comes from the PUC. This section will be focused on the first continuum band, that appears during the M intermediate.

Dr. V. Lorenz-Fonfria gave a crucial contribution in the data analysis and in the theory of the polarization-resolved IR spectroscopy.

3.2.1 The dichroism of the continuum band in BR

The continuum band, a transient negative band absorbing below 2200 cm^{-1} is assigned to a cluster of water molecules and amino acid residues in BR that are protonated in the resting state. Since the precise chemical nature of the network of amino acids and water molecules that share a proton is controversial and cannot be seen in the high resolution crystal structures of BR, a useful approach to determine the shape of this network can come from polarization-resolved IR spectroscopy.

The use of polarized light allows for the measurement of the dichroism of the many bands that populate the difference absorption spectra in the IR range. We exploit here the property of purple membrane sheets to spontaneously orient on a surface during a controlled drying process, to calculate the difference absorption spectra in the samples's coordinate system.

At first we investigated the dichroism with respect to the membrane normal (the direction z in Fig. 2.6) with steady state ATR and with transmission spectroscopy. These two approaches measure the same process in the protein but have different advantages and disadvantages. Both results will be presented here and compared. Ab-initio calculations of IR signatures of proto-

nated water clusters, performed by Jan Daldrop as collaborating partner, help the interpretation of the measured spectra.

Secondly we performed a photoselection experiment in transmission, to characterize the dichroism in the plane of the membrane (xy plane in Fig. 2.6). Any additional property that we can learn from these experiments can help to select between the different options and hypothesis on the nature of the continuum band.

The advantage of a controlled semi-dry state of the protein sample

The photocycle of BR, in solution and at neutral pH, lasts ~ 100 ms before the protein relaxes back to the resting state [18]. The M intermediate, the first intermediate where the continuum band related to the PRC appears [43, 44, 35], rises with $\sim 200 \mu\text{s}$ and decays in ~ 2 ms. Under continuous illumination conditions the most populated state is the resting state and the M intermediate is poorly accumulated because of the fast recovery of the initial state. The use of light at high energy density does not solve the problem as it may induce secondary photoexcitation [164].

A common approach is a time-resolved experiment but the low transparence of the polarizer filter lowers the signal-to-noise ratio, making the detection of a small band like the continuum band more challenging. An alternative approach is to slow down the protein reaction reaction, making the accumulation of reaction intermediates possible. The photocycle of BR is known to be slowed down lowering the temperature [18] and decreasing the hydration level [165]. Since the continuum band disappears at low temperatures [43], a semi-dried state has been preferred.

A preferred orientation of the sample is needed for a meaningful data interpretation, as an isotropic sample would give in our measurements the same results for each orientation of the polarizer filter. Purple membrane patches have typical size of ~ 5 nm in thickness and ~ 500 nm [166].

The membranes have been oriented on solid supports via controlled drying [167, 168, 169] or via isopotential spin-dry centrifugation [170, 171]. A parameter p_m called mosaic spread can quantify the degree of orientation of purple membrane sheets on the surface and is defined in Eq. 2.23, an estimation of the mosaic spread is needed for the angle calculations in the following chapters. Values of p_m between 0,95 and 1 have been estimated for both the drying procedures used in literature. We will assume a mosaic spread parameter $p_m = 0,95$ for the angle calculations, as in transmission at zero-tilting the measured ratio of $\frac{amideI}{amideII} = 1,02$ is the same as in literature [171].

In order to achieve a controlled hydration, the sample has been rehydrated in a sealed atmosphere with drops at a 2:8 ratio of water:glycerol next to it, reaching an expected relative humidity of 46% [138] (see Methods 2.4.1).

From the IR absorption spectrum of the sample it is possible to estimate the molar fraction of water molecules and proteins in the film, as shown in Fig. A.4. The spectrum of the sample is fitted with the absorption spectra of water and the one of dried protein; knowing the IR extinction coefficient of

water [172] and BR (see 3.1.1), we can estimate in this case the presence of 750 ± 70 water molecules per protein monomer.

The advantage over a fully-hydrated sample is the higher accumulation of the M intermediate that means that signals in a difference spectrum have higher intensities, as can be seen in Fig. A.7. This increases the signal-to-noise ratio and makes the analysis of smaller bands like the continuum band more meaningful. The results are reproducible also with a more hydrated sample, where the signals and the difference bands only change in their intensity (see A.0.3).

Polarization-resolved ATR difference spectra show the dichroism of the continuum band

The sample was prepared as described in 2.4.1. Here, instead of drying it on a BaF_2 window as done in transmission, it has been dried on the silicon surface of the ATR prism. The drying process ensures the orientation of the purple membrane sheets: from the absorption spectra measured at parallel and perpendicular polarizations (shown in Appendix A.5), it is possible to see the dichroism of amide I (at $\sim 1655 \text{ cm}^{-1}$) and amide II ($\sim 1543 \text{ cm}^{-1}$) and amide A ($\sim 3290 \text{ cm}^{-1}$) bands that reflects the relative orientation of the α -helices and the surface of the Si prism.

The following analysis will show the results obtained with a sample kept at a controlled low hydration (3.2.1) with an estimate of 750 ± 70 water molecules per protein monomer. The results with a more hydrated sample are shown and commented in A.0.3.

The measured difference absorption spectra for perpendicular and parallel polarized light is shown in Fig. 3.16

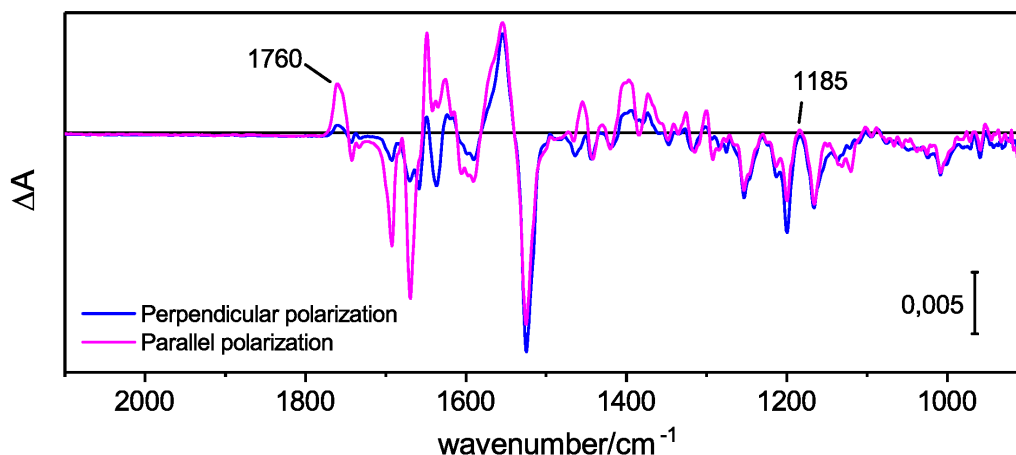


Figure 3.16: Light-dark FTIR-ATR difference spectra of BR measured with parallel and perpendicular polarizations. Marker bands that allow the assignment of the trapped intermediate state are marked.

From the spectra it is evident that the intermediate trapped is a late M state, with minor contribution from the N state. The marker band at

1185 cm^{-1} is infact negative in the M intermediate and becomes positive during N [25]; it is here close to zero. The carboxylic positive band at 1760 cm^{-1} is another marker band for the formation of the M state, its shoulder at 1754 cm^{-1} is also indicative of a contribution of the N intermediate [25]. From a fit with voigt functions, the relative area of the peak at 1761 cm^{-1} and at 1754 cm^{-1} gives an estimate of 70 % M and 30 % N (see A.6).

With the help of Eq. 2.8 and Eq. 2.9 it is possible to calculate the difference absorption spectra in the coordinate system of the sample: ΔA_{xy} and ΔA_z , but some parameters are needed in the equations.

An estimation of the incident angle of the IR beam to the ATR crystal is shown in A.0.1. As result, an incident angle of 39° is used in the following data evaluation. The refractive index of the sample is another parameter that needs to be estimated. Based on literature average values for the refractive indices of proteins $n_{\text{protein}} = 1.7$, $n_{\text{lipids}} = 1.4$ and $n_{\text{water}} = 1.3$ [123], a value of $n_{\text{sample}} = 1.6$ has been chosen. In A.8 it is shown how our results are robust upon small changes in the estimation of the incident angle and the refractive of the sample.

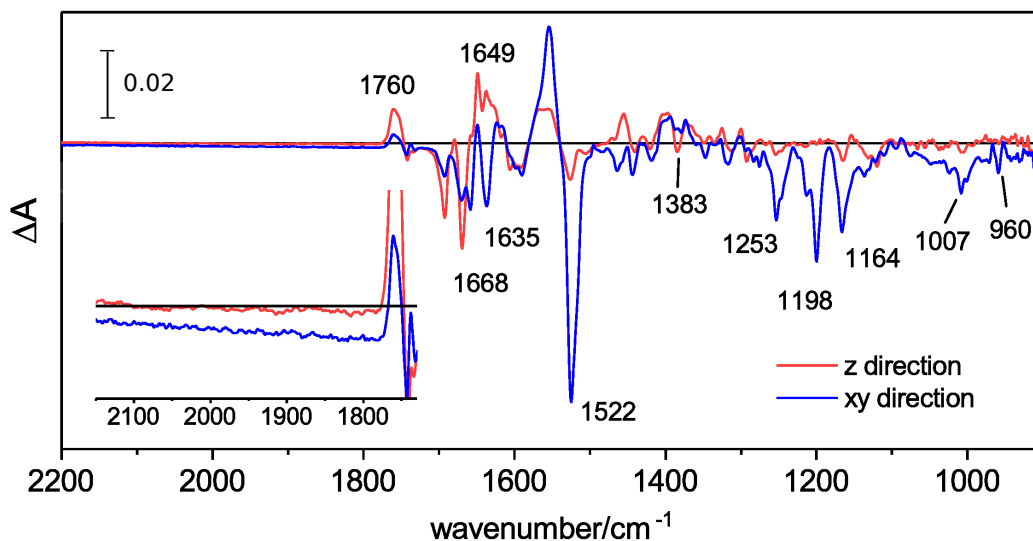


Figure 3.17: FTIR light-induced difference spectra calculated in the xy and z directions, the continuum band in enlarged in the inset and the major dichroic bands of known assignment are marked.

In Fig. 3.17 the light-induced difference spectra in the xy and z direction (calculated as explained in 2.1.4) show clearly bigger signals in the xy direction for most of the bands. This dichroism is due to the orientation of the dipole moment changes relative to the membrane normal.

Many bands that show a strong dichroism are assigned to retinal vibrations: at 960 cm^{-1} the hydrogen-out-of-plane (HOOP) mode, at 1007 cm^{-1} the methyl rock mode, at 1164 cm^{-1} , 1198 cm^{-1} , 1253 cm^{-1} the $C - C$ stretching modes and at 1522 cm^{-1} the $C = C$ stretch [173]. This dichroism is expected since it is well known that the retinal chromophore lies at $\sim 70^\circ$ with respect to the

membrane normal [171](see Fig. 1.2) and most vibrations are aligned to the retinal axis (see Fig. 2.7).

The dichroism of a band at 1383 cm^{-1} mirrors the dichroic behaviour of the well known band of the protonated D85 at 1760 cm^{-1} , suggesting that at least a contribution could come from the negative feature of the aspartate [174, 175]. The bands at 1649 cm^{-1} , 1668 cm^{-1} and 1693 cm^{-1} , are characteristic amide I modes and appear very intense in the N state [176, 25], their dichroism comes from the strong orientation of the transmembrane α -helices. The strongly dichroic band at 1635 cm^{-1} could be the C=N vibration of the protonated Schiff base [177], but it might overlap with other vibrations.

The continuum band, enlarged in the figure, shows also a strong dichroism: it is clearly evident as a broad negative feature in the ΔA_{xy} spectrum and absent or very close to zero in the ΔA_z spectrum. The cluster responsible for the continuum band absorbs almost exclusively in the xy plane.

Since the difference spectrum accumulated in Fig. 3.16 and Fig. 3.17 is a mixture of the intermediates M and N as discussed above, it is possible that two distinct signals from two spectrally overlapped continuum bands are present (in 3.1.2 it is shown how a second protonated water cluster can cause a continuum band in the time-scale of the N intermediate). The existence of two chemically different continuum bands overlapping in the light-dark difference spectrum makes it difficult to draw conclusions on the orientation of the two protonated clusters.

For this purpose a variant D38R has been investigated with the same approach. The D38R variant is known to prolongue the lifetime of the M intermediate and shows no (or very low accumulations) N or O intermediates [163], therefore is a perfect candidate to study the M intermediate with little or no N accumulation.

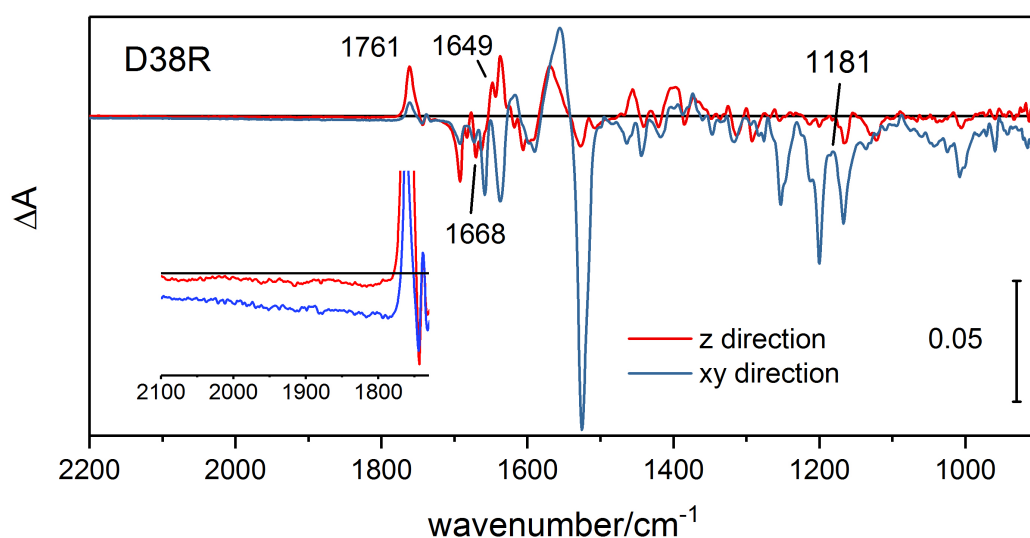


Figure 3.18: FTIR light-induced difference spectra of the variant D38R calculated in the xy and z directions, the continuum band is enlarged in the inset and some bands of interest are marked.

Fig. 3.18 shows the light-induced difference spectra of the D38R variant in the xy and z directions. A sharp 1761 cm^{-1} band without a lower-energy shoulder, together with a negative feature at 1181 cm^{-1} indicates a typical M state accumulation [25]. To be noticed also the reduced intensity of the amide bands at 1668 cm^{-1} and 1649 cm^{-1} in the M state.

As for wild type BR the continuum band shows a dichroic behaviour, with strong absorption in the xy plane.

Polarization-resolved transmission difference spectra confirm the continuum band's dichroism

Transmission FTIR represents an alternative approach to ATR for the calculation of the absorption in the coordinate system of the sample (x, y and z). A transmission measurement has the advantage that the absorption intensity is not affected by the penetration depth (dependent on the sample refractive index) and not dependent on the wavelength of the incident IR light, as for ATR. A drawback is that a high tilting angle is necessary to retrieve informations in the z direction and in our case it was not possible to extend the measurements over a 40° tilt.

As can be seen in Fig. 2.4, vertically polarized light probes the xy plane independently of the tilting angle. At higher angles the amount of probed sample increases because of the tilt, increasing the intensity of the signal. Horizontally polarized light probes a higher component of the z direction the higher the tilt angle.

The difference spectra are shown in A.10; the sample has been measured at angles $0^\circ, 10^\circ, 20^\circ, 30^\circ, 40^\circ$. In Fig. 3.19 the same data have been normalized to have the same difference signal at 1525 cm^{-1} for the vertically polarized light at each tilt angle, the horizontally polarized data have also been rescaled accordingly.

The bands that show higher dichroism are highlighted in the graph and have been already discussed in 3.2.1. Using Eq. 2.19 and 2.20 we could calculate the difference absorption spectra in transmission in the xy and z directions and they are shown in Fig. 3.20. As already shown in 3.2.1, the amide I bands appear intense in the z oriented difference spectrum, the bands assigned to the retinal appear in the membrane plane as well as the continuum band.

Positions and dichroic behaviour of all the bands as measured in ATR mode (Fig. 3.17) are here reproduced and the results are consistent. The intensities of the amide I bands cannot be compared as the refractive index of water and the sample change dramatically in this spectral range and the penetration depth of the ATR beam is affected. Also ATR spectra show a known wavelength-dependent penetration depth (therefore absorption intensities) making the absorption intensities not comparable to transmission experiments.

From Eq. 2.26 it is possible to calculate the angles with respect to the membrane normal of the dipole moment changes that give dichroic bands in the spectra showed above. A similar approach described in [170] has also been used and showed in A.0.4. Since in transmission we probe the whole sample

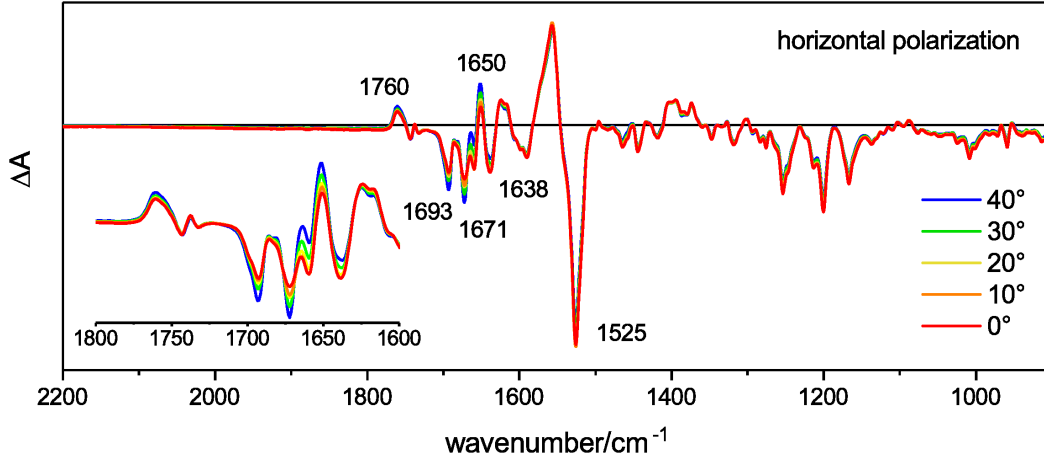


Figure 3.19: Measured BR light-dark difference absorption spectra measured in transmission at different tilting angles with horizontally polarized IR light. Spectra measured with vertically polarized light are indistinguishable with the spectra at 0° tilt. The difference spectra have been rescaled in order to account for the higher signal intensities with increasing tilting angles.

and not only the layers close to the surface, we assumed here a higher mosaic spread of $p_m = 0,9$; a polarizer leak of $f = 0,1$ and a sample refractive index of $n = 1,6$ have been also used.

The calculation of the angles of certain dipoles of the major bands in the IR has been already reported (some relevant works are [169, 171, 168]) and a comparison of these results with our calculations confirms the validity of our measurements and methods.

Vibrations	ATR	Transm.	[169]	[171]	[167, 168]
D85 C=O (1760 cm^{-1})	36°	34°	35°	43°	36°
Retinal C=C (1525 cm^{-1})	73°	68°	66°	69°	72°

Table 3.1: Calculated angles δ between target dipoles and the membrane normal. Comparison between the measured angles in ATR and transmission modes with literature values. The measured angles have an error of respectively 4 and 5 degrees, estimated from the noise level.

The continuum band, differently from the bands reported in 3.1, is broad and it is therefore hard to define the position of its minimum or integrate it in order to calculate the angle of its dipole. In the transmission experiment we selected an interval from 1800 cm^{-1} to 2100 cm^{-1} and corrected the baseline of the z oriented spectrum to zero: the average angle for the continuum band is $\delta = 76^\circ \pm 5^\circ$, the error is given by the standard deviation from the average value.

For the ATR measurements the value in the same interval is $\delta = 75^\circ \pm 4^\circ$. The D39R variant angle calculations resulted in $77^\circ \pm 5^\circ$ for the C=C stretching at 1525 cm^{-1} , $36^\circ \pm 5^\circ$ for the C=O of D85 and an average of $72^\circ \pm 5^\circ$ for the continuum band.

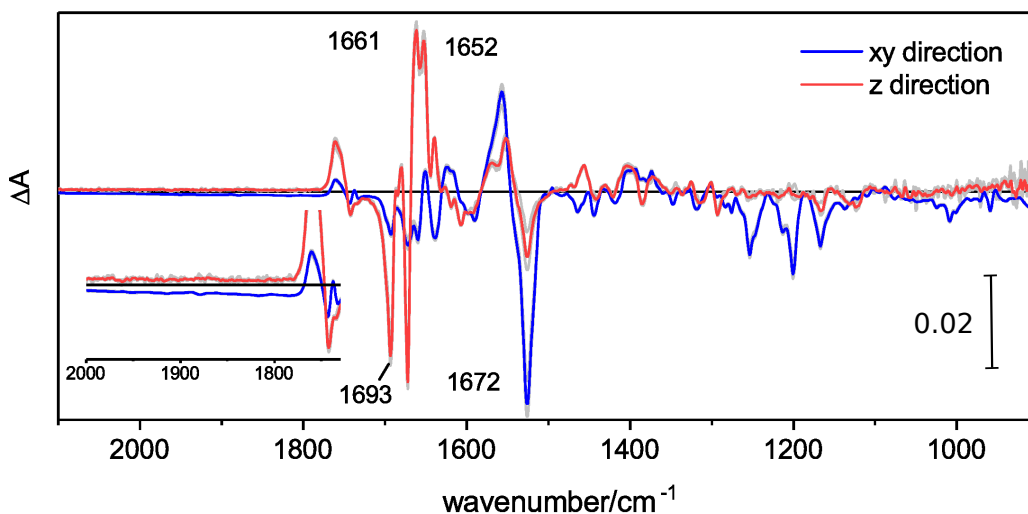


Figure 3.20: Calculated difference absorption spectra in the coordinate system of the protein, along the membrane direction xy and the membrane normal z . Difference spectra were calculated from the results in Fig. 3.19 at each tilt angle (grey) and averaged (blue and red).

The angle calculations for the C=O vibration of D85 were not corrected for the offset of the continuum band. If that is taken into consideration, the resulting angles for both the transmission and ATR experiments increase by $\sim 3^\circ$.

Time-resolved photoselection in the membrane plane

We performed a photoselection experiment (see 2.1.4 and Fig. 2.6) with the step scan technique, obtaining a time-resolved data set that contains not only the kinetic information of the photocycle intermediates, but also the angle θ of the dipole moment changes on the xy plane with respect to the retinal (see Fig. 2.6). The sample transmission window has been kept perpendicular to the incoming IR beam. Measurement blocks of 10 coconditions each have been measured alternating parallel and perpendicular polarizations (of the linearly polarized probing and exciting beams) to ensure similar conditions of hydration and bleaching (less than 10%) for both datasets.

The measurement was restricted to the spectral interval $2200 - 900 \text{ cm}^{-1}$ due to the use of a filter in the spectrometer that enhances the signal-to-noise ratio.

The pure spectra of the main reaction intermediates are obtained after merging the datasets for the two polarizations, performing a SVD analysis and applying a linear kinetic model, where they appear at $12 \mu\text{s}$, $340 \mu\text{s}$ and 7 ms . The spectra have been assigned to the L, M and N intermediates after a comparison of the positions of the characteristic bands with literature values [25] and are shown in Fig. A.12. A second step scan experiment performed as control is showed in A.12.

The focus of the photoselection results is the analysis of the continuum

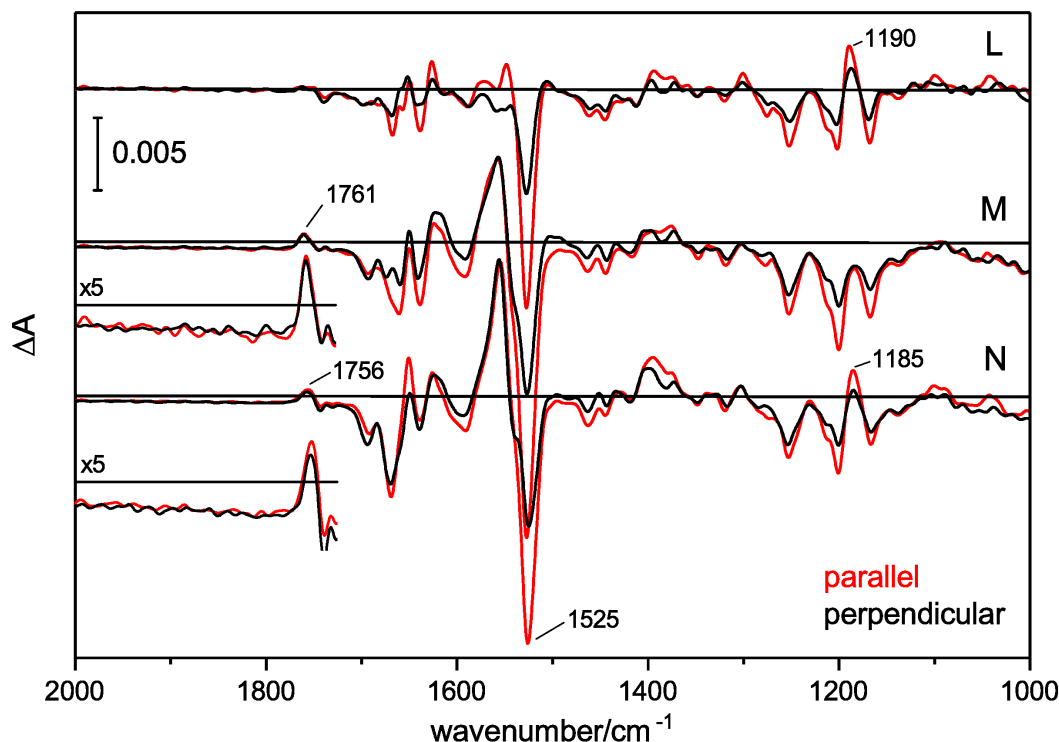


Figure 3.21: Pure spectra of the main intermediates of BR measured in a step scan experiment in transmission at two different polarizations of the probing beam: parallel and perpendicular to the laser flash polarization. The measurement was performed at $pH = 7.5$, the spectral resolution was 8 cm^{-1} .

band, but first our results will be compared with other photoselection experiments on BR from literature. Retinal bands, specially the one at 1525 cm^{-1} , are known to show the strongest dichroism, as the IR dipole moment change is parallel to the optical transition [130]. As explained in 2.1.4, we assume that the retinal vibrations at 1525 cm^{-1} should give an angle $\theta = 0$. We can then calculate the photoselection efficiency c from the relative intensity of this band in the two polarization orientations. The higher the dichroic ratio the higher is the photoselection efficiency. At the same noise level, a better photoselection efficiency allows to resolve dichroisms of bands that are close to 45° with respect to the excitation radiation.

Other prominent bands in the amide I region are the result of the overlap of different contribution, therefore less indicated for angle calculations.

We compare the angles calculated from the main bands in the caboxylic region of the pure spectra intermediate spectra shown in Fig. A.12, the ones calculated from the dataset in Fig. A.12 and obtained from a steady state experiment that will be described later.

The averaged experiment values are compared with literature values [131, 129, 178] in 3.3.

The values reported in 3.2 are in good agreement with the literature values, considering an error of $\sim 4^\circ$ due to the noise level. In the specific, the value that is in strongest disagreement with literature is the angle of the negative band

Vibrations	Step scan 1	Step scan 2	Steady state
D85 C=O (M int.1760 cm ⁻¹)	40°	36°	36°
D85 C=O (N int.1755 cm ⁻¹)	37°	42°	-
D96 C=O (L int.1740 cm ⁻¹)	59°	58°	-

Table 3.2: Calculated angles θ in the xy plane between a certain dipole and the axis of the retinal. Comparison between the measured angles in a transmission step scan experiments and steadystate. The angles are calculated using the area of a voigt peak fit. Errors due to the noise level are $\sim 4^\circ$.

Vibrations	Exp. Av.	[131]	[129]	[178]
D85 C=O (M int.1760 cm ⁻¹)	$37^\circ \pm 4^\circ$	-	45°	25 – 30°
D85 C=O (N int.1755 cm ⁻¹)	$40^\circ \pm 4^\circ$	-	-	47 – 55°
D96 C=O (L int.1740 cm ⁻¹)	$59^\circ \pm 4^\circ$	$70^\circ \pm 4^\circ$	-	-

Table 3.3: Averaged values θ from 3.2 in the first column (Experimental Averaged) are compared with literature values.

at 1740 cm⁻¹ in L. This is the first time-resolved photoselection experiment at room temperature of BR to my knowledge and the values could reflect differences between the cryo-trapped and room temperature L states. The discrepancy can be also explained by a contamination of this pure spectrum with the M intermediate, since a small positive band at 1760 cm⁻¹ can be observed in this region. For a more precise determination of angles of carboxylic acids (not the aim of this work), a spectral resolution of at least 4 cm⁻¹ is required.

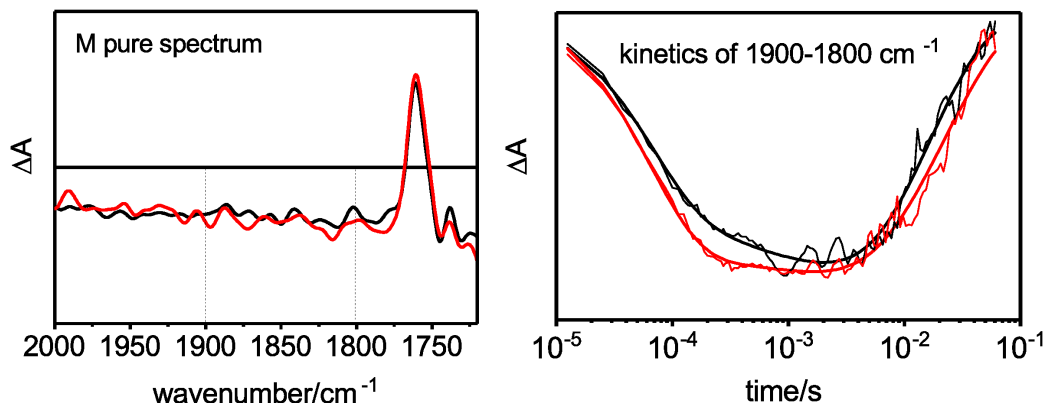


Figure 3.22: Left the enlarged spectrum of the continuum band and D85 positive band from the pure M intermediate showed in Fig. 3.21, the spectral region between 1900 cm⁻¹ and 1800 cm⁻¹ is highlighted, the kinetics of of this region in parallel and perpendicular polarization are shown on the right with the fit from a global analysis. The measurements were performed at $pH = 7.5$.

The continuum band in the M intermediate of Fig. 3.21 is enlarged in Fig. 3.22, its kinetics are also shown. A dichroism can be observed at the limit of the noise level. A similar result was obtained in the second time-resolved dataset in Fig. A.12.

In case of an oriented dipole, a small dichroism would indicate a $\sim 45^\circ$ orientation, as in the case of the D85 band. As the accepted interpretation of the continuum band is a delocalized network of H-bonds, its dipole moment change could depend on the shape of the cluster, opening the possibility for a delocalized proton without a preferred orientation in the xy plane.

The average angle calculated for the pure spectrum assigned to the M intermediate in the interval 1900 to 1800 cm^{-1} is $\theta = 41^\circ \pm 4^\circ$, indicating a dichroism but also compatible with a non dichroic band.

I confirmed the dichroism of the continuum band with a time-resolved QCL measurement where the signal-to-noise ratio was improved respect to the step scan measurements, but limited to a restricted spectral range. The results are shown in A.13.

Steady state photoselection in the membrane plane

Additionally, a steady state broad difference photoselection spectrum (see 2.1.4) was obtained by continuously flashing at 20 Hz with the exciting laser at 2 mJ per pulse, while measuring with a polarized IR beam. The sample was kept in a semi-dry state, hydrated with a glycerol:water ratio of 5:5 (see 2.4.1), allowing for the retardation of the M-to-N transition and the steady state accumulation of M [165]. Advantages of this approach are the broad measured range at 4 cm^{-1} spectral resolution and the low energy density of the flash laser, optimizing the efficiency of the photoselection. In order to avoid baseline drifts, short measurement of 100 coaditions each were alternated with background scans to a total of 2000 coaditions.

In Fig. 3.23 the steady state difference spectra at parallel and perpendicular polarization respect to the exciting laser flash. The accumulated spectra show characteristic features of the M intermediate, with traces of N. A marker band for the transition from M to N is the position of the D85 protonation band that shifts from 1761 cm^{-1} to 1754 cm^{-1} ; a peak fit with two voigt functions at this two wavenumbers gave an estimate of the relative accumulation of the two intermediates in the steady state spectra, resulting in $\sim 80\%$ M and $\sim 20\%$ N.

The enlarged spectral range 2000 – 1730 cm^{-1} reveals a clear dichroism of the continuum band in the region from 1900 cm^{-1} to below 1800 cm^{-1} . I repeated the experiment with the D38R BR variant, whose photocycle lacks the N intermediate. The accumulated difference spectrum is a pure M and the continuum band presents the same dichroic behaviour of the wild type difference spectra.

This result, consistent with the step scan and QCL measurements (see above and A.13), confirms the dichroism of the continuum band in the xy plane during the M intermediate. I focused the investigation on the continuum band in the M intermediate as the noise level in the $\sim ms$ range in the step scan measurements does not allow an analysis of the dichroism during the N intermediate. Also the N intermediate has a low accumulation in the steady state difference spectra.

The average angle calculated from the dichroism of the continuum band in Fig. 3.23 in the spectral interval 1900 – 1800 cm^{-1} is $\theta = 36^\circ \pm 3^\circ$, in agreement

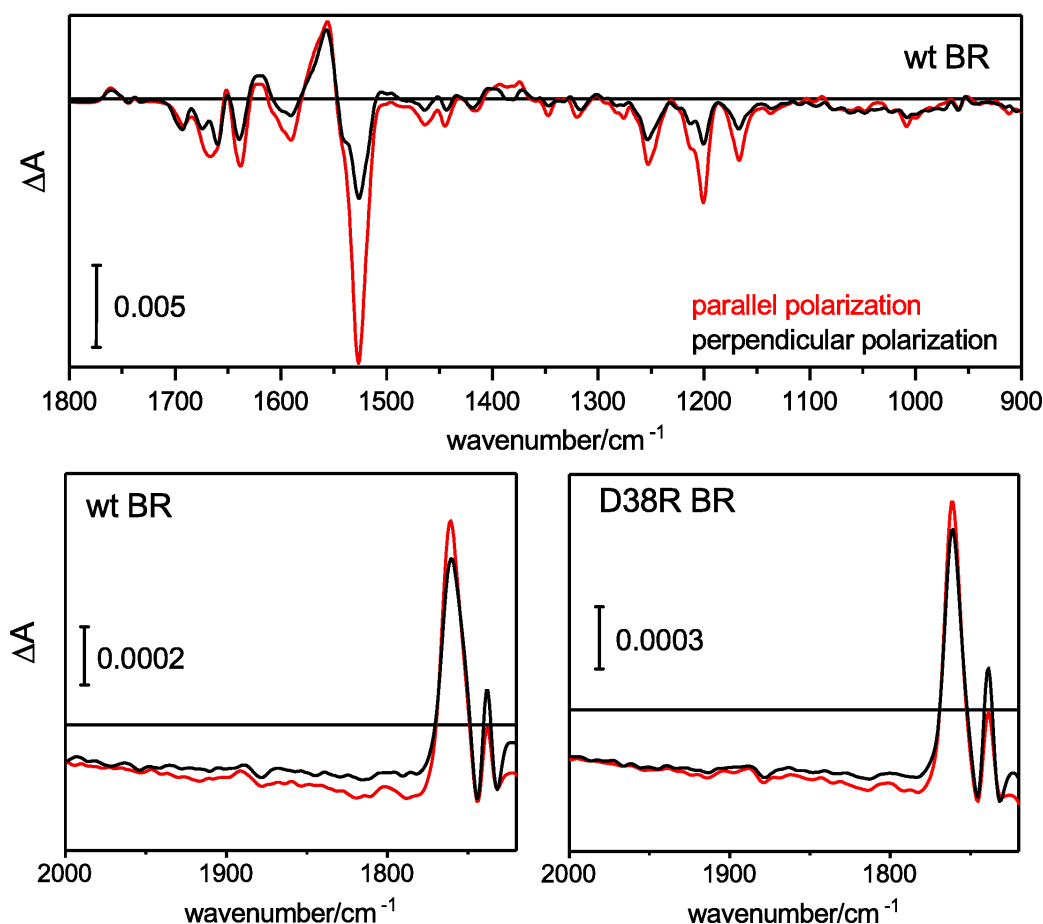


Figure 3.23: FTIR steady state difference absorption spectra of BR wild type (a and b) and D38R (c) during laser flash excitation at 20 Hz and 2 mJ, measured with probing light polarized parallel (red) and perpendicular (black) to the exciting laser polarization. The wild type sample was kept in a controlled semi-dry state (surrounded by drops of 5:5 glycerol:water, see 2.4.1 and 3.2.1), the D38R sample has a slower photocycle and the signal intensity guaranteed a sufficient signal-to-noise ratio at a good hydration level (2:8 glycerol:water).

with the result obtained in the step scan experiment. The continuum band is however a broad band and its maximum intensity might be around or below 1800 cm^{-1} . For the D38R mutant the angle calculated in the same spectral range is $\theta = 41^\circ \pm 2^\circ$.

A plot of the calculated angle over the broad spectral range $2000\text{--}1780\text{ cm}^{-1}$ shows (see A.14) indeed a trend where θ has values close to 45° around 2000 cm^{-1} , going down to $\sim 30^\circ$ at 1780 cm^{-1} . The optimal strategy to measure the value of θ would be to compare the areas at two polarizations, fitted with voigt functions, this approach is here not possible as part of the broad band is overlapped with sharper signals below 1780 cm^{-1} .

If we interpret this result with the model of the protonated network of H-bonded residues and water molecules at the extracellular side of BR, we can conclude that the averaged dipole moment change of the protonated cluster

lies at an angle $\theta = 36^\circ \pm 3^\circ$ respect to the retinal axis in the xy plane. Another scenario compatible with the angle at $\theta = 36^\circ \pm 3^\circ$ is a single vibration oriented with this angle with respect to the retinal.

In Fig. 3.24 the orientation of some key amino acids with respect to the retinal is showed from the crystal structure in the xy plane.

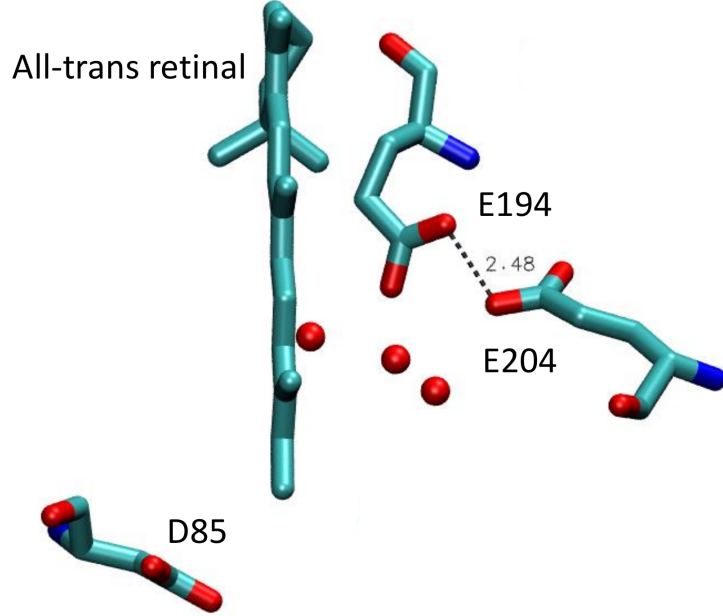


Figure 3.24: Crystal structure of BR (PDB:5B6V) in the resting state from the top view (z direction). Only the retinal, D84, E204 and E194 are displayed to show the relative orientation of the C=O groups of these carboxylates and the retinal in the xy plane. Red dots are the oxygens of the water molecules in proximity of the PRC, a black dotted line connects the two oxygens from E204 and E194 that are at a distance of 2.48 Å.

The vector connecting the closest oxygens of E204 and E194 is oriented at $\sim 35^\circ$ with respect to the retinal axis. The two glutamates E204 and E194 could indeed represent the proton release complex and be responsible for the continuum band. It has been infact shown in simulations [38, 39] that experimental results on the continuum band can be reproduced from simulations where the proton is shared between the oxygen atoms of the two glutamates, that are only 2,48Å apart in the resting state crystal structure [9].

The proposed model of a partially delocalized proton between the two glutamates E204 and E194 [38], compatible with the experimental results, would explain the close vicinity of two repulsive groups like the deprotonated glutamates and is so far never been tested. Our photoselection results are compatible with this model if we assume that a proton delocalized between two oxygens would produce a continuum signal oriented along the line connecting the two oxygens [179].

From our results we cannot distinguish between the two models of a proton shared by the two glutammates E204 and E194 or a proton delocalized

in a network of H-bonds whose averaged dipole moment change has an angle of $\sim 35^\circ$ respect to the retinal (the same angle of the vector connecting E204 and E194). We can exclude all configurations of the H-bonded network that don't satisfy the above mentioned requirement. We notice the remarkable concurrence of the measured angle θ coming from the dichroism of the continuum band and the same value for the orientation of the vector connecting the oxygens of E204 and E194.

3.2.2 The dichroism of a broad IR band above 2200 cm^{-1}

The same experimental approaches used in 3.2.1 have been applied also to investigate the dichroism of the broad IR difference band absorbing in the interval $2700 - 2400\text{ cm}^{-1}$. This spectral region is characterized by sharp bands coming from the $X - H$ stretching mode, notably O-H, N-H or C-H [149], and by broad bands assigned to strongly hydrogen bonded O-H or N-H stretching modes [48, 47, 180]. In this region the absorption of neutral and protonated water clusters is also to be considered (see 1.2.2).

Not many bands in this region have been assigned in the M or N states [43]. Weakly H-bonded water molecules (called also dangling water molecules) absorb above 3500 cm^{-1} , the negative band at 3644 cm^{-1} for example is assigned to a specific water molecule, water401 [47](see Fig. 1.4). Amide A bands absorb in the region 3100 cm^{-1} to 3400 cm^{-1} , some bands in this region have been assigned in the K intermediate [176], but the positions are not conserved in the M intermediate. Since the backbone C=O (amide I) and the backbone N-H (amide A) form a hydrogen bond in α -helices, it is expected that bands in amide A and amide I range show the same spectral changes.

Strongly H-bonded O-H groups can give rise to broad bands, in particular the broad band centered at $\sim 2650\text{ cm}^{-1}$ is compatible with a neutral cluster of strongly H-bonded water molecules in BR [48]. The strongly H-bonded Schiff base N-H stretch could also give rise to broad bands but in the more limited range $2900 - 2750\text{ cm}^{-1}$ [47, 180]. Sharp bands in the interval 2550 cm^{-1} to 3000 cm^{-1} are not assigned and show no shift in $H_2^{18}\text{O}$ when studied in the xy plane [43].

The kinetics of the broad negative band between 3000 cm^{-1} and 2400 cm^{-1} show it is negative already at 100 ns and stays negative until the L-toM transition at $\sim 200\text{ }\mu\text{s}$ when it is positive before going to zero in the M decay [44, 54]. Mutations at the residues D85 and D212 strongly affect the broad negative signal in the early photocycle intermediates [44]. Mutations at residues E204 and E194, as well as residues in the reprotonation pathway of the Schiff base, affect the positive broad band in the M intermediate [44, 54].

These results have been assigned to the perturbation of a strongly H-bonded water molecule (most probably W402 that is H-bonded to the positively charged Schiff base and the negatively charged aspartated D85 and D212, see Fig. 1.4) that leads to a negative band that recovers only at the end of the photocycle; this negative broad band overlaps with the rise of a positive band in the same spectral region that comes from strongly H-bonded water

molecules in the reprotonation pathway of the Schiff base from D96.

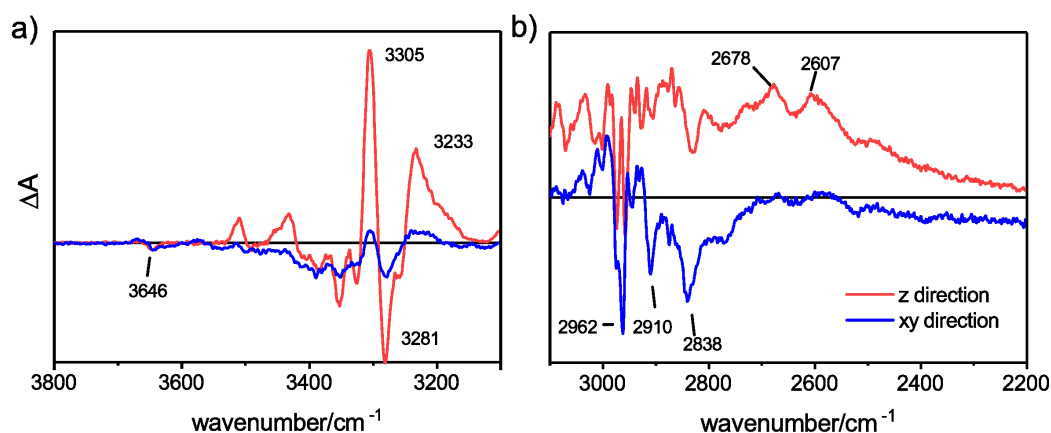


Figure 3.25: Calculated difference absorption spectra in the coordinate system of the protein, along the membrane direction xy and the membrane normal z . Difference spectra were calculated from the results ATR mode from Fig. 3.16 in the same way as for Fig. 3.17.

Fig. 3.25 shows the light-dark absorption changes in the ATR mode, almost indistinguishable results are obtained with transmission in the same spectral range and showed in A.11.

The xy difference spectrum is comparable to the literature results of the M state in the same range [43, 44], a negative band is observed in this range between 2900 cm^{-1} and 2750 cm^{-1} , overlapped with sharper bands. The spectral features in this spectral range have been assigned to the N-H stretching of the SB and to the pentagonal water cluster present in the GS in the vicinity of D85 (see Fig. 1.4) [47, 180].

This bands in the region 2900 – 2750 cm^{-1} , together with sharper C-H peaks, overlap with a broader transient band in the interval $\sim 3200\text{--}2400\text{ cm}^{-1}$ assigned to strongly H-bonded water molecules. Literature spectra of the M intermediate in this region report a small positive feature at $\sim 2600\text{ cm}^{-1}$, that is also observed in Fig. A.11. This positive feature is resolved in the difference spectrum along the z direction, where it appears as a very broad band spanning from $\sim 3100\text{ cm}^{-1}$ to $\sim 2400\text{ cm}^{-1}$. Its maximum lies at $\sim 2600\text{ cm}^{-1}$.

Our polarization resolved data reveal that the broad band is around zero in the xy plane, but shows a strong dichroism and has a pronounced positive contribution in the z direction. This dichroism is a property of the M state as confirmed by the difference spectrum in this region of the variant D38R shown in A.9, where a pure M state is accumulated.

The positive broad absorption observed here in the M state is compatible with the hypothesis of a neutral cluster of water molecules forming in the z direction during the M state [54]. These water molecules would then be responsible for the reprotonation of the SB via the Grotthus mechanism. The absorption of this band is although much broader than the interval proposed by simulations in literature [48].

On the contrary of what done in 3.2.1, it is not possible to estimate an average angle δ with respect to the membrane normal for this broad band. Opposite to the continuum band region, the overlap of this broad band with other sharper or broader bands makes the calculation of the angle not accurate [47, 180, 43].

We analyzed this spectral range also in a photoselection experiment, the results are shown in Fig. 3.26.

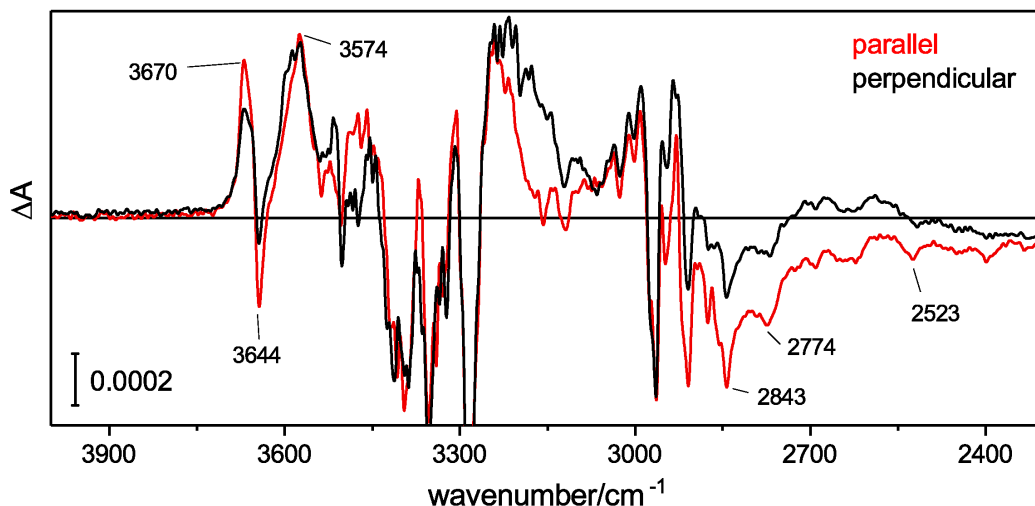


Figure 3.26: Steady state difference spectrum of BR in a photoselection experiment performed as described in 2.1.4. The polarization directions are defined with respect to the retinal axis and the measurements are performed with the sample perpendicular to the IR beam. The proteins are excited with short laser pulses at a repetition rate of 20 Hz.

As already shown in other steady state photoselection experiments (see 3.2.1), for the measurement in Fig. 3.26 the sample was excited with a sequence of 10 ns laser pulses with 20 Hz repetition rate and ~ 2 mJ per pulse. It is well known that *ns* laser pulses induce an energy dissipation from the retinal molecules that heats up the sample. This transient temperature jumps are reflected by typical difference bands in the IR spectrum that can be identified with a test measurement in the presence of a dye [154].

In the region between ~ 3000 cm^{-1} and ~ 2400 cm^{-1} , free of heating artifacts, the dichroism of a broad band can be observed. This difference spectra both refer to the xy plane as they were measured in transmission at $\beta = 0^\circ$ tilt angle (see 2.5). The results shown here are part of the same measurement shown in Fig. 3.23 and the trapped intermediates are, as explained above, 80 % M and 20 % N. The dichroism indicates a preferred orientation of this broad band parallel to the retinal in the ground state.

If we assume that the origin of this broad band is a neutral cluster of water molecules (or a single one, like proposed for W402 [44]), this cluster needs to be present in the ground state, with the strongly hydrogen bonded O-H group oriented along the retinal axis, and perturbed in the M intermediate.

Since a positive feature in this range appeared in the M intermediate in the z direction, this two signals overlap resulting is the weak positive band reported in literature [44, 43].

The observation of overlapping negative and positive signals in this range revealed by the polarization-resolved measurements complicates the assignment and interpretation of this band and confirms the intuition that in the M intermediate two difference broad absorbing signals overlap in the range $\sim 3000 - 2400 \text{ cm}^{-1}$ [54]. The assignment of the the negative contribution to the GS absorption of the W402, strongly H-bonded with the positively charged Schiff base and the aspartates D85 and D212 [44] (see Fig. 1.4), is not compatible with the results showed in this section if we assume that the dipole moment change of a strongly H-bonded O-H is oriented along the O-H axis. W402 in fact has none of the two O-H groups oriented along the retinal (see Fig. 1.4).

3.3 The influence of the protein environment on the continuum band

Purple membrane is the native membrane of *Halobacterium salinarum* where BR trimers form a crystalline lattice (see 1.2.2).

BR can be extracted from the native membrane and solubilized to monomers with detergents like n-octyl- β -D-glucoside (OG) and Triton X-100 [181, 182] (see 2.4.3). After solubilization it can be reconstituted in artificial membranes like liposomes [143]. The aggregation state of BR can be deduced via the absorption maximum of the retinal in the visible range that is typically 550 nm for the monomers and 555 – 558 nm for trimers in the dark adapted form [183].

The BR solubilization and reconstitution are known to affect the protein photocycle, that however maintains key features like a similar absorption maximum and the transient deprotonation of the Schiff base after illumination (M intermediate) [183, 184]. Both monomers and trimers are capable to pump protons after light excitation, the monomer is the functional unit [185].

BR can also be reconstituted in nanodiscs (ND), a phospholipid bilayer wrapped into a scaffold protein [186] (see methods 2.4.3). The size of the scaffold proteins define the diameter of the nanodiscs and the aggregation state of the reconstituted BR is also affected: only scaffold circumferences above ~ 350 Å can accomodate trimers like in the native membrane, according to CD spectra [186].

The stability of the water clusters in solubilized and reconstituted BR can be assessed by X-ray crystallography: a vast number of BR structures is available, obtained with different methods and in different environments [187]. Crystallization in detergent led to a trimer arrangement different from the native purple membrane [188], whereas crystallization in a lipidic cubic phase led to the native crystal lattice pattern [187], both this arrangements kept the position of the intra-protein water molecules almost unaltered. The structure of monomeric BR has been successfully resolved in bicelle crystals [189], there the position and number of water molecules is different but differs also within the two proteins of the lattice unit (PDB: 1kme).

What is not possible to retrieve from the crystal structures is the stability of a protonated network of water molecules and amino acids such as the one that is believed to give rise to the continuum band. Here I investigated the behaviour of the continuum band signal in solubilized and reconstituted BR.

All samples have been measured in solution and with a transmission cell, in a sandwich of two BaF_2 windows separated by a $100\text{ }\mu\text{m}$ spacer, measured in a QCL setup. The solution consisted in 200 mM $NaCl$, 50 mM Hepes buffer at $pH = 7.2$ and detergent when needed. Two detergents were selected for the experiments, OG and n-Dodecyl- β -D-Maltoside (DDM), the first is a well known and established detergent for BR solubilization, with the advantage over Triton X-100 to have a higher critical micelle concentration and is therefore easier to remove [181]. DDM is a mild detergent that has been shown to successfully solubilize integral membrane proteins preserving their functionality [190]. It was not possible to solubilize PM with DDM so I solubilized BR in

3.3. THE INFLUENCE OF THE PROTEIN ENVIRONMENT ON THE CONTINUUM BAND

OG and exchanged the detergent afterward. The samples in detergent have been measured at the QCL setup together with B. Shultz.

The measurements are performed in solution, as the process of drying the solubilized samples led to the denaturation of the protein (loss of color, in the case of OG) or a red shift of the retinal absorption maximum, indicating the possible formation of a trimeric structure (in DDM) [183]. Working in solution allows also a precise control of the buffer and salt concentration, as well as the pH. A drawback is the limited spectral interval accessible with the QCL, from 1800 cm^{-1} to $\sim 1740\text{ cm}^{-1}$.

The spectra measured with the samples solubilized in the two detergent, in nanodiscs and in purple membranes are showed in Fig. 3.27 compared with the spectrum of a dried and rehydrated PM film. All spectra have been scaled to the D85 positive peak at 1760 cm^{-1} . All spectra were extracted at the timepoint when the D85 band shows its maximum (M intermediate).

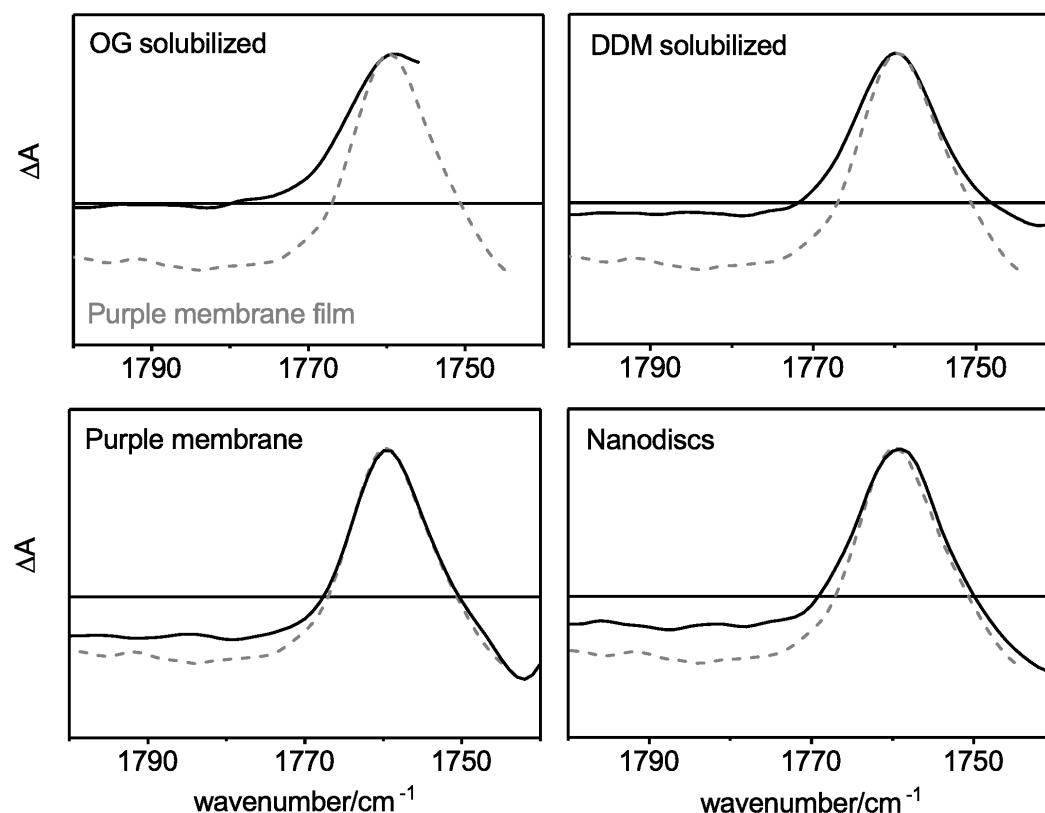


Figure 3.27: Difference absorption spectra of BR solubilized in OG, solubilized in DDM, in the native purple membranes, in nanodiscs and in a hydrated film of native membranes (grey dashed, shown as comparison) measured with a QCL setup. All spectra in black are measured in solution with a $100\text{ }\mu\text{m}$ thick sample in transmission and are extracted from the time-resolved datasets at the time of the maximum accumulation of the D85 positive band at 1760 cm^{-1} , see Fig. 3.28. Due to the high absorption of the sample solubilized in OG, it was not possible to measure kinetics below 1755 cm^{-1} .

In the light of what previously shown in this section, it becomes clear why

the continuum band signal in PM is more intense in the case of the rehydrated film (grey traces in Fig. 3.27) than in all other samples in solution. The PM film has membranes oriented perpendicular to the probing beam, which measures the absorption changes in the xy plane, where the continuum band has maximum intensity. In the case of PM in solution, the orientation of the membranes is randomly defined, therefore the intensity of the broad band is lower (close to $2/3$ of the oriented sample, as expected).

The striking result is the absence of continuum band in the sample solubilized in OG and a very reduced intensity in the DDM-solubilized BR. The continuum band is also less intense in the sample in nanodiscs, if compared to purple membrane in solution. Kinetics of the positive band at 1760 cm^{-1} and of the integrated broad continuum band $1800 - 1780\text{ cm}^{-1}$ are shown in Fig. 3.28.

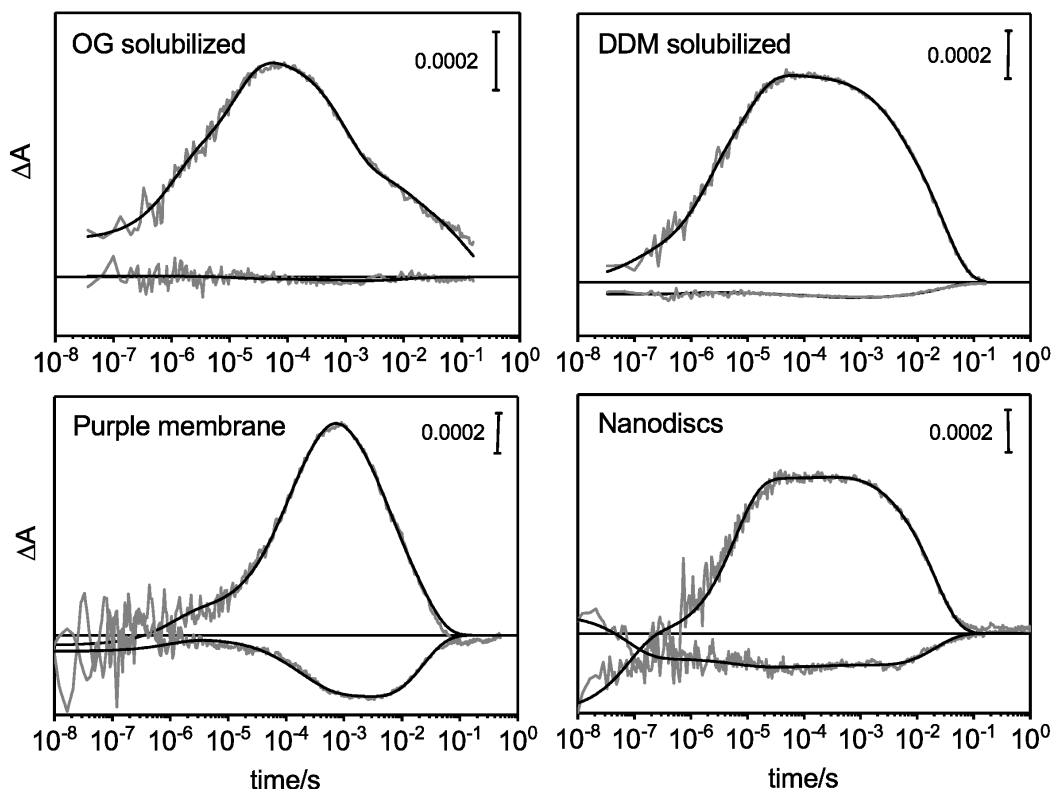


Figure 3.28: Time-resolved absorption changes of two characteristic bands in the IR carboxylic region of BR in different environments: solubilised in OG, in DDM, in the native purple membranes and in nanodiscs. In grey the measured kinetics, in black the fit from a global analysis. The transient traces refer to the same experiments shown in the Fig. 3.27, the positive kinetics describe the signal at 1760 cm^{-1} , the negative or zero lines describe the absorption changes integrated in the spectral range $1800 - 1780\text{ cm}^{-1}$. The zero level is an horizontal black line.

The visible absorption spectra (see A.15) show a visible absorption maximum at $\sim 550\text{ nm}$, typical of monomeric BR [183]; the CD spectra of OG-solubilized and nanodisc-reconstituted (MSP1D1, see subsec:Proteoliposomes

formation) in literature also show characteristic features of monomeric proteins [186, 183]. Assuming that these three samples have BR molecules in the monomeric state, our results indicate that the continuum band is not a specific property of the trimer but is present also in monomers. The absence of the broad negative absorption in the solubilized samples could indicate that the arrangement of the protonated H-bonded network at the extracellular side of the protein is disrupted or destabilized.

Since in solubilized BR the continuum band is not present, I investigated the functionality of BR in detergent as a proton pump.

As introduced in 1.2.5, it is possible to use pH-sensitive dyes to detect, in a time-resolved experiment, the release and uptake of protons in BR. The pumping activity of BR in DDM is reported in Fig. 3.29, it is detected with the water soluble pH-sensitive dye, pyranine. Measured in the same way, the proton pumping activity of proteins in OG and in nanodiscs are shown in A.16.

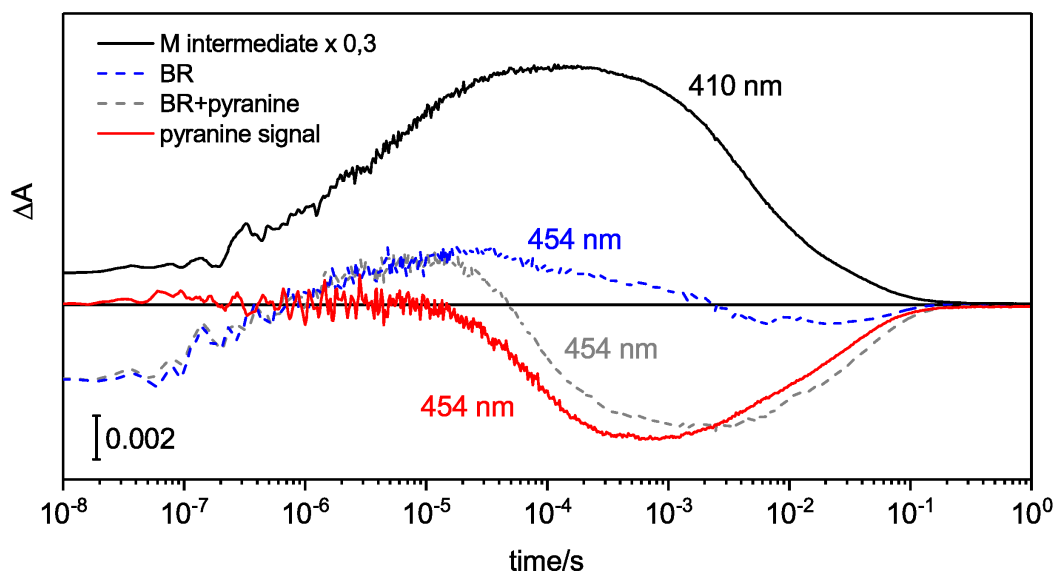


Figure 3.29: Time-resolved visible spectral changes measured in a flashphotolysis experiment of BR in DDM detergent. In red the signal of the pH-sensitive dye pyranine as result of the subtraction of the kinetics at 454 nm with and without the dye. A negative decay represents a proton released to the bulk, a positive decay a proton uptake from the bulk. In black the kinetics at 410 nm representing the deprotonation and subsequent reprotonation of the Schiff base, are shown for comparison.

Fig. 3.29 shows the kinetics at 410 nm which report on the deprotonation of the Schiff base in favour of D85 and the subsequent reprotonation from D96. In red the kinetics of the proton release and uptake from the protein to the bulk solution. The release shows a time constant of $97 \pm 2 \mu\text{s}$.

It is well known that protons once released from the protein can remain temporarily trapped on the membrane surface and are detected in the bulk solution with a typical time-delay of $\sim 0.5 - 1 \text{ ms}$ [77, 20]. A time release as fast as $97 \mu\text{s}$ can be explained by the fact that in this sample the proteins

are solubilized as monomers and there is no membrane for the protons to be transiently trapped. We cannot exclude though that protons could be linger on the detergent micelle surface or protein surface, for this reason we cannot assume that this time constant is accurate for the proton release from the protein.

The same measurements performed on the OG solubilized and ND reconstituted BR samples confirmed also for this two samples the ability of BR to release and uptake a proton from the bulk. These three results together show that independently from the presence or not of a continuum band in the time-resolved IR experiment, BR is still capable of transiently release and uptake protons, just like in the native membrane.

3.4 Continuum bands measured in Cl-pumping rhodopsins

Proton transfer has been recently associated with the chloride transport mechanism in halorhodopsin [109, 111] but lacking of the evidences for a protonation or a deprotonation of an amino acid group.

As transient continuum bands are associated with proton transfer, it is possible that a proton dislocation does not involve carboxylic acids but water molecules as it happens in bacteriorhodopsin. Here I show that a continuum band can be detected in halorhodopsin and another Cl-pumping microbial rhodopsin called MastR displays distinct bands both in the IR regions characteristic of the carboxylic amino acids and strongly H-bonded water molecules.

3.4.1 A continuum band in halorhodopsin

I have measured with the QCL setup a time-resolved map of the carboxylic spectral range of Halorhodopsin in a special sample holder for liquid samples. The sample was infact squeezed between two BaF_2 windows with a $50\mu\text{m}$ spacer, the salt concentration was 3M NaCl and the solution was buffered with 50 mM HEPES at pH 7.2. The exact same measurement was repeated with a BR sample at the same salt and buffer concentrations to ensure that no significant laser artifact contributes in the measured spectral range (data not shown).

The IR interval measured spans from 1725 cm^{-1} to 1800 cm^{-1} and is shown at three different time points in Fig. 3.30a that according to the photocycle at high salt concentrations refer respectively to the K, L_1 and L_2/N intermediates [112]. The kinetics of the positive and negative features at 1736 cm^{-1} and at 1742 cm^{-1} and the kinetics of the negative broad that is visible over the whole measured range (but analyzed only above 1760 cm^{-1}) are shown in Fig. 3.30b.

The difference bands at 1736 cm^{-1} and at 1742 cm^{-1} are assigned to the downshift of the frequency of a protonated aspartic acid D141, in analogy with the protonated D115 in BR [191, 192]. This frequency change could be explained by a change in hydrogen-bonding partner between the ground state and the intermediates and is not related to any protonation change. This difference bands are known to be present in the K intermediate [193], vanish in the L_1 intermediate and appear in the L_2 intermediate at the same positions [192].

What is here evident for the first time is the presence of a broad negative difference band, reminiscent of the continuum band in BR. This negative feature is rising in the transition between K and L_1 and decays to the ground state at the end of the photocycle. The intensity of this difference band band was only ~ 0.1 but it is above the noise level and reproducible.

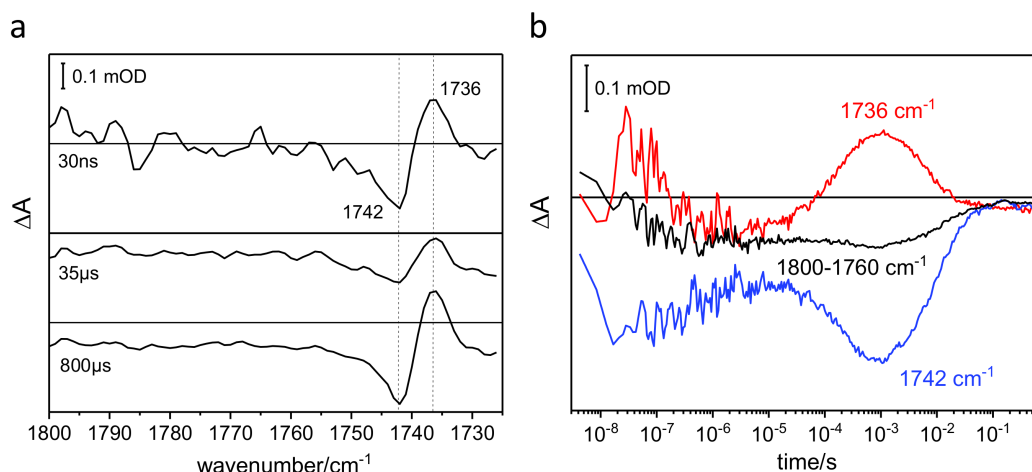


Figure 3.30: a) Time-resolved difference spectra of the photocycle of halorhodopsin in the carboxylic range measured in a 50 μm thick liquid sample. The spectra shown are extracted at three different time points, at 30 ns, 35 μs and 800 μs. b) Time-resolved difference absorption kinetics of the positive band at 1736 cm⁻¹, the negative band at 1742 cm⁻¹ and the integrated area of the spectral region 1760 cm⁻¹ to 1800 cm⁻¹.

3.4.2 A broad transient band in MastR

MastR is a chloride pump found in cyanobacteria that shares many similarities with BR, although it has a different function and comes from a different organism[12].

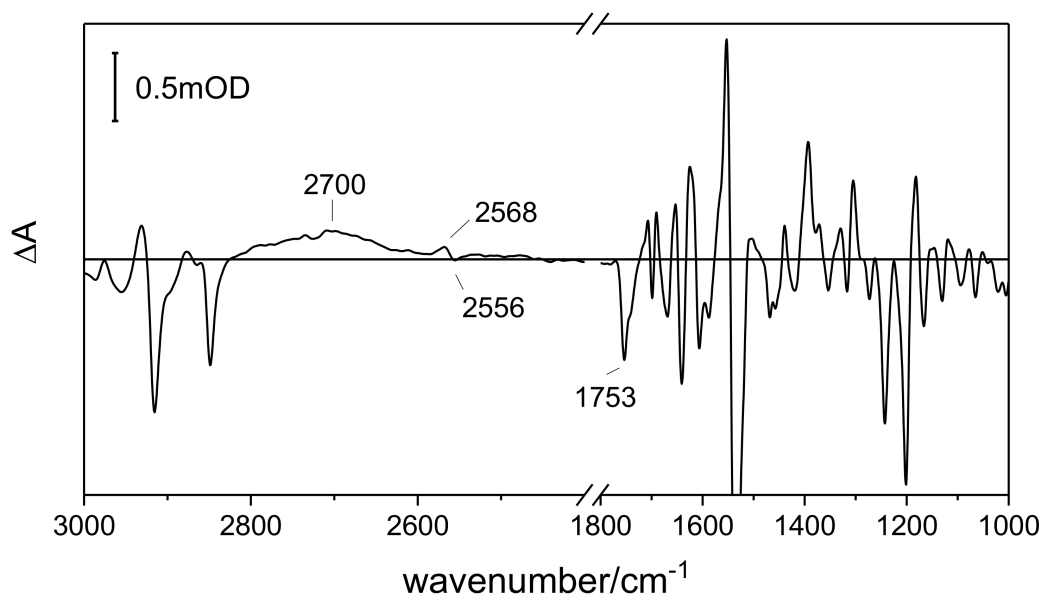


Figure 3.31: Time-resolved difference spectrum of MastR integrated in the interval between 10 μs and 6 ms, measured in a step scan experiment.

We characterized the protein photocycle with visible and infrared spec-

troscopy and found evidences for a deprotonation event, assigned to the aspartic acid D85, and perturbation of a lipid headgroup. These results are discussed in detail in A.0.9.

A broad range transient difference absorption spectrum in the time interval between $10\ \mu\text{s}$ and $6\ \text{ms}$ revealed a transient positive band in the spectral range between $2600\ \text{cm}^{-1}$ and $2800\ \text{cm}^{-1}$ with maximum at $2700\ \text{cm}^{-1}$. A broad positive band has been observed in BR in the same spectral region and discussed in 3.2.2. In BR broad transient bands in this region have been assigned to strongly H-bonded water molecules inside the protein [48]. The origin of this band in MastR in analogy with BR is tentatively assigned to a strongly H-bonded water molecule (or group of water molecules) that rearrange its position and H-bonds during the photocycle. The measurements have been performed together with Prof. L. Brown who also provided the sample.

3.5 The functionality of lipid-reconstituted ChR2

This section aims to a explorative investigation of the influence of protein reconstitution on the ChR2 photocycle and the development of a method to study the function in-vitro of ChR2 (expressed in *Pichia pastoris*) as cation channel.

At first I investigated the effect of the protein reconstitution in artificial membranes on the photocycle intermediates in the visible and in the infrared, secondly I developed an essay to test the functionality of ChR2 as a light-activated cation channel in liposomes.

3.5.1 The influence of the reconstitution of ChR2 on the protein photocycle

The details of protein reconstitution is described in 2.4. The lipid composition of the eye spot of the green algae *Chlamydomonas reinhardtii* is not known [194] but among the lipids constituting the algal membrane, a specific lipid with a serine group is present. Choline and serine headgroups are also found in the lipid composition of rat brain membranes [195], therefore are relevant lipid species for the reconstitution of ChR2.

I investigated the effect of four different lipid compositions of the proteoliposomes: a phosphatidylcholine/phosphatidylserine (PC/PS) mixture with ratio 8/2, a pure PS membrane, a lipid mixture from the purple membrane extract from *Halobacterium salinarum* [196, 197] and 1,2-Dimyristoyl-sn-glycero-3-phosphocholine (DMPC) nanodiscs. The first lipid composition has been chosen because PC has already been used for spectroscopical studies on ChR2 [101, 198] and the negatively charged PS help preventing liposomes fusion and sedimentation. The influence of the negative charges of PS have been investigated with PS only liposomes reconstitution. The polar lipid extract has been chosen because of the lack of ether lipid species containing a C=O group in the headgroup, allowing for measurements in the carboxylic IR range. Nanodiscs offer a membrane mimetic system with defined size, no membrane curvature and where each protein dimer is confined.

The analysis of the data measured in PS lipids, in nanodiscs and in polar lipids are shown and discussed in the appendix.

Fig. 3.32 shows the visible kinetics of ChR2 reconstituted in PC/PS liposomes in a protein/lipid ratio (weight/weight) of 1/5, in comparison with the kinetics of the detergent solubilized proteins. Visible kinetics of samples in nanodiscs and in polar lipids are shown in Fig. A.17 and A.22.

The samples in liposomes showed a smaller signal at 380 nm with respect to the ground state absorption depletion. As if the P_2 intermediate would have less accumulation in these samples. The time constants for the rise and decay of P_2 , respectively $0.5 \mu\text{s}$ and $10 \mu\text{s}$ for the rise and 8 ms make the P_2 intermediate spanning 5 orders of magnitude of time. The first component of the rise is 20 times faster and the decay is ~ 4 times slower than in detergent. Similar time constants are obtained also with ChR2 in polar lipids (see Fig. A.22). The

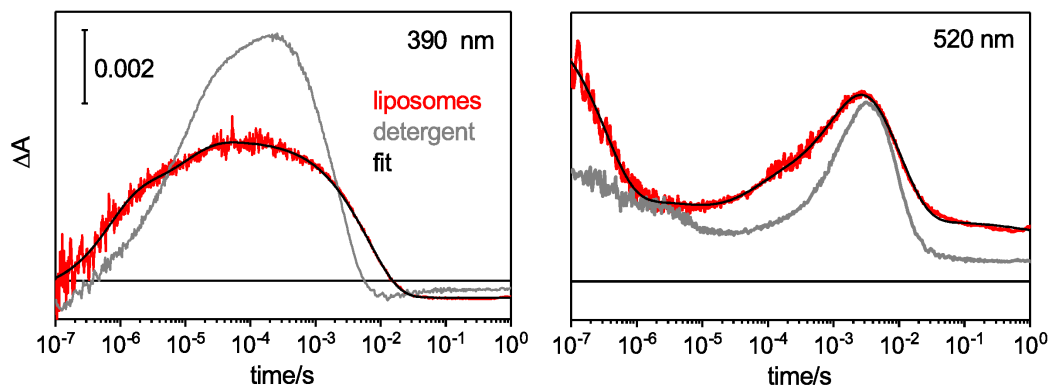


Figure 3.32: Transient visible absorption changes after a short laser pulse of ChR2 reconstituted in PC/PS liposomes (red) and compared with solubilised in DM (grey). Both measurements have been performed at room temperature in a solution containing 100 mM NaCl and 20 mM Hepes buffer at $pH = 7.4$. Kinetics were measured at the characteristic wavelengths of the ground state absorption maximum (480 nm), the P_2 maximum absorption (380 nm) and the P_3 maximum absorption (520 nm). The absorption changes were scaled to have the same intensity in the ground state signal. Each trace is the result of 30 averages and the repetition rate of the exciting laser flashes is 20 s.

P_3 intermediate is also affected by reconstitution in liposomes, with an earlier rise (1.2 ms respect to 2 ms) and a longer lifetime (decay at 10 ms similar to the decay in detergent) this red shifted intermediate is broadened in time and strongly overlapped with P_2 .

The time constants of the kinetics measured with nanodiscs revealed only minor deviations respect to the detergent solubilised sample. In order to understand the reason of the different kinetics between the liposomes-reconstituted and the nanodisc-reconstituted ChR2, I investigated the effect of the negatively charged headgroups of PS (see A.18) and of the relative density of lipids/proteins in the liposomes (see A.19). Both these factors have an influence on the protein photocycle intermediates: PS accelerates both the rise and the decay of the P_2 intermediate, the time constants of the P_2 and P_3 accumulation are closer to the values in nanodiscs when ChR2 is reconstituted in liposomes with high lipids/protein ratios.

It is possible that the reasons of the similar visible kinetics between the detergent-solubilised and nanodisc-reconstituted ChR2 are the absence of negatively charged lipid headgroups and the absence of dimer-dimer contacts.

In light of the results in Section 3.6.1, the low accumulation of the P_2 intermediate and the broadening of the P_3 intermediate could be the result of a higher accumulation of the P_4 intermediate and its consequent photoexcitation. It is possible that the lipidic environment stabilizes the P_4 intermediate or enhances the ratio of proteins decaying to the P_4 state from the P_3 intermediate (see the photocycle in Fig. 1.6).

Ideal for the visible and IR photocycle characterizations are well defined (in time) protein photocycle intermediates so that the extraction of spectra

at selected times can be assigned to specific intermediates unequivocally. In this respect ChR2 in detergent or in nanodiscs represent better samples for an IR spectroscopic investigation. In the native membranes, though, or in the neuronal membranes where ChR2 is expressed for optogenetic purposes the protein environment could be different than in nanodiscs, therefore it is relevant to investigate the protein photocycle also in artificial membranes.

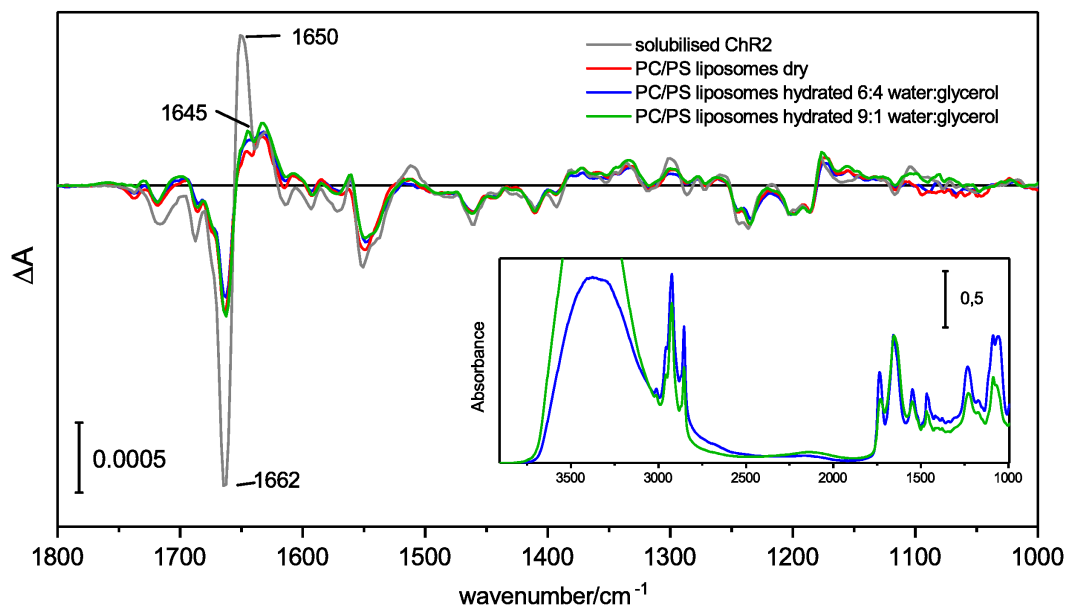


Figure 3.33: light-dark IR spectra of ChR2 in PC/PS liposomes at different hydration conditions, compared with the light-dark spectra in detergent. Proteins were excited with an LED emitting at 455 nm. In the inset the absolute absorption spectra of the rehydrated reconstituted ChR2 are shown. Samples hydrated with 6/4 and 9/1 water/glycerol mixtures were reported to have respectively $\sim 95\%$ and $> 99\%$ relative humidity [138]. All difference spectra have been scaled to the retinal C-C stretching band at 1200 cm^{-1} .

In Fig. 3.33 the light-induced IR difference spectrum of ChR2 in PC/PS (lipid/protein in a 5/1 ratio) is shown in comparison with the difference spectrum of a detergent-solubilised sample. The spectra are in overall good agreement, except for the intensity and position of the positive band at 1650 cm^{-1} , downshifted to 1645 cm^{-1} in lipids, and the intensity of negative band at 1662 cm^{-1} . The effect of the sample hydration level has been here studied and the absorption changes during illumination have been measured at three different hydration levels: the same sample has been measured dried, rehydrated with a water/glycerol mixture of 6/4 and fully rehydrated with a water/glycerol mixture of 9/1 (see 2.4), the last two corresponding respectively to $\sim 95\%$ and $> 99\%$ relative humidity [138].

An effect of the hydration level on the intensity of these two amide I bands can be clearly observed, favouring bigger conformational changes at higher hydrations. The intensity of the changes of the sample in detergent are still more than two times bigger than the most hydrated sample.

The intense negative band at 1662 cm^{-1} has been assigned to conformational changes, like helix tilting, that are present already in the early stages of the photocycle [96, 198] and last until the proteins return to the resting state [97, 96, 198]. A negative band appears at 1665 cm^{-1} on a subpicosecond time scale [199] and could be the result of a very early disruption of the coupling of the amide I vibration in one or more helices. At 1658 cm^{-1} absorbs the C=N stretching vibration of the protonated Schiff base [93] that is expected to give a negative contribution during the P_2 intermediate. At 1664 cm^{-1} the transient hydration of the α -helices during the channel opening also contributes to the negative signal [13].

Pulsed electron-electron double resonance (pELDOR) spectroscopy experiments showed the outward movement of the intracellular end of helix B; the entity of the movement was observed to be similar ($\sim 2.5\text{ \AA}$) in the P_3 intermediate when the channel is open and in the P_4 intermediate after the pore closure [103, 100].

The positive band at 1650 cm^{-1} is almost absent in the ultra-fast spectra [199], appears in the spectra of P_1 measured at 80 K but disappears in D_2O [199, 96]. At the same position a positive band rises in detergent solubilised samples in the transition between P_1 and P_2 , has a maximum during P_3 and decays to P_4 without disappearing and remaining the most intense among the positive signals [97]. The rise and decay of this band correlate with the channel opening and is assigned to the helix hydration [13] although the band is still present in P_4 that is not conductive, indicating perhaps a still hydrated channel pore in P_4 . In contrast to the results at 80 K, this positive band at 1650 cm^{-1} in the P_4 intermediate is not sensitive to D_2O exchange; in lipids the band that appears in the P_4 intermediate at 1645 cm^{-1} upshifts to 1650 cm^{-1} in D_2O as shown in Fig. A.20.

This band loses its intensity in lipid reconstituted samples during the whole photocycle (see SI in [198], Fig. A.21 and Fig. 3.33) if compared to detergent. A possible reason of this behaviour is the environment of the detergent being more flexible than the ordered lipid bilayer, allowing for more pronounced conformational changes. On the other hand smaller conformational changes or ineffective hydration of the helices in the reconstituted sample might result in a loss of function.

The amide region of reconstituted ChR2 in PC/PS lipids has been further investigated with QCL at different tilting angles respect to the probing light, as it has been done in 3.2.1. Like the PM spontaneously orients on the Ba_2F window's surface, so do the ChR2 proteoliposomes. As the α -helices orient perpendicular to the surface, the changes in their conformation appear more intense in the axis spanned by the helices. The dichroism of the 1645 cm^{-1} band is shown in Fig. 3.34a and shows clearly that the intensity of the changes increases with the tilt angle.

The kinetics of this positive band are shown in Fig. 3.34b, compared with the kinetics of the 1650 cm^{-1} band from the detergent-solubilised sample. Both bands have their maximum at $\sim 1\text{ ms}$ that is concomitant with the maximum of the current after a laser pulse measured in HEK cells expressing ChR2 (data

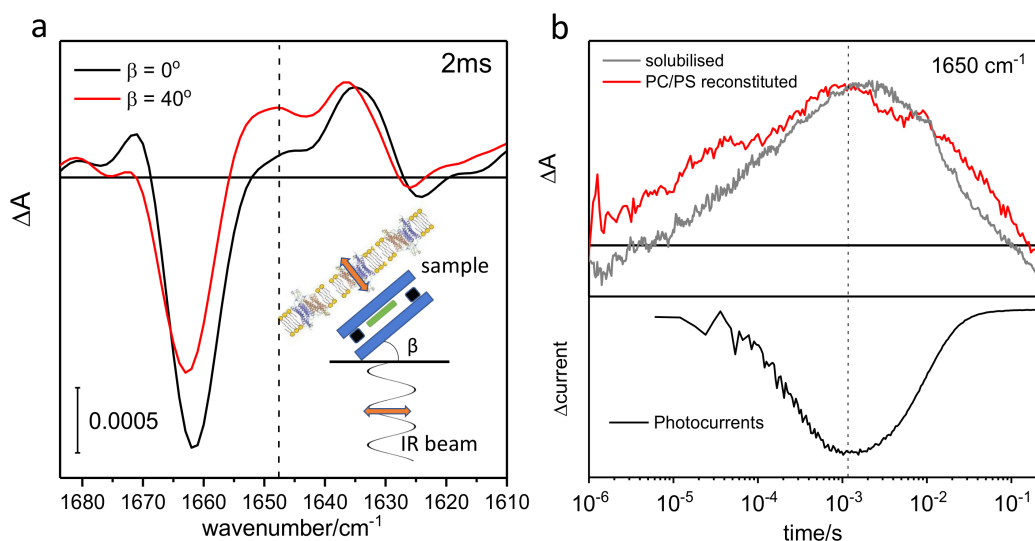


Figure 3.34: (a) Difference absorption spectra of ChR2 reconstituted in PC/PS lipids at 2 ms after the laser flash measured in a QCL setup at two different tilting angles respect to the probing IR beam, as described in the inset sketch. The kinetics at 1650 cm^{-1} are shown in (b) compared to the kinetics of the same band measured in detergent. All traces have been scaled to the same maximum. These kinetics are compared to the photocurrents at -40 mV measured in HEK cells after a short laser pulse, data recorded by Dr. Christian Bamann [13].

from [13]); the current measures the flow of cations through the ChR2 pore, the conductance is highest at the highest hydration of the transmembrane α -helices.

The photocycle of ChR2 reconstituted in polar lipids has been investigated in the carboxylic region in a QCL experiment and shown in the appendix (A.0.7). Protonation dynamics of key amino acids during the photocycle could be affected by the reconstitution, but the overlap of the P_2 and P_3 intermediates in time complicates the data interpretation. A suggestive hypothesis is that, as mentioned above, in the reconstituted ChR2 the P_4 intermediate is stabilized and the observed differences in the carboxylic range are due to a contamination with the P_4 photocycle (see subsec: The photocycle of the P_4 intermediate of ChR2).

3.5.2 Co-reconstitution of BR and ChR2 in proteoliposomes to probe the functionality of yeast-expressed ChR2

Since IR spectroscopy revealed that the conformational changes and helix hydration of ChR2 is less pronounced when ChR2 is reconstituted in lipids in comparison with detergent (see 3.5.1), I investigated the functionality of ChR2 in lipid vesicles.

At first I characterized BR proteoliposomes where the protein insertion

favoured a preferred orientation. The procedure is described in 2.4.3 and it has been described earlier [200]. In A.0.8 I show how BR can be inserted in preformed liposomes that contain pyranine, a pH-indicator. The proteoliposomes are passed through a size exclusion chromatography column to remove the dye molecule from the solution outside the vesicles. The net orientation of BR molecules in the liposomes was tested by exploiting the proteins' function as proton pumps: during LED illumination BR molecules pump protons prevalently from the bulk to the inner volume of the liposomes. The depletion of H^+ from the bulk was measured with a pH electrode in the solution, the accumulation of charges in the liposomes was in the mean time detected by the pH indicator inside the liposomes in a spectrofluorimetry setup.

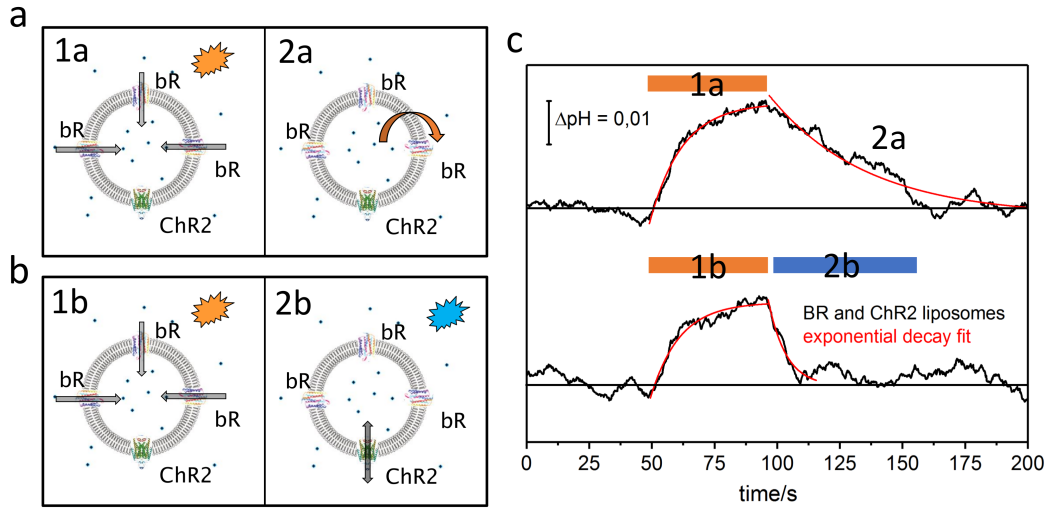


Figure 3.35: (a) and (b) are the sketches of the sample LED illumination protocol used for the measurements in (c) where the pH of an unbuffered suspension of mixed BR and ChR2 proteoliposomes was measured by a pH electrode before, during and after LED illumination as indicated by the colored bars.

In order to test the functionality of ChR2, I coreconstituted it together with BR in a ratio 1/10 of ChR2/BR. BR proteins were excited with a 605 nm LED to prevent photon absorption from ChR2 (whose maximum absorption lies at 470 nm). The bulk pH was measured with a pH electrode as reported in A.0.8. As shown in Fig. 3.35a and c, orange light excites BR creating a alcalinization of the bulk water that rises with a time constant of 11 ± 1 s and dissipates with $\tau = 39 \pm 1$ s through the membrane.

In Fig. 3.35b a different illumination pattern excites ChR2 after the proton gradient is established, in Fig. 3.35c the effect of the blue light (LED at 450 nm) illumination on the bulk pH. the excitation of ChR2 led to the dissipation of the pH gradient with $\tau = 7 \pm 1$ s, 5,5 times faster than without blue illumination. As a control the same illumination pattern has been applied to BR-only proteoliposomes, shown in Fig. 3.36.

Blue light is able to excite the proton pumping in BR proteoliposomes and does not favour the dissipation of the established proton gradient. The lower

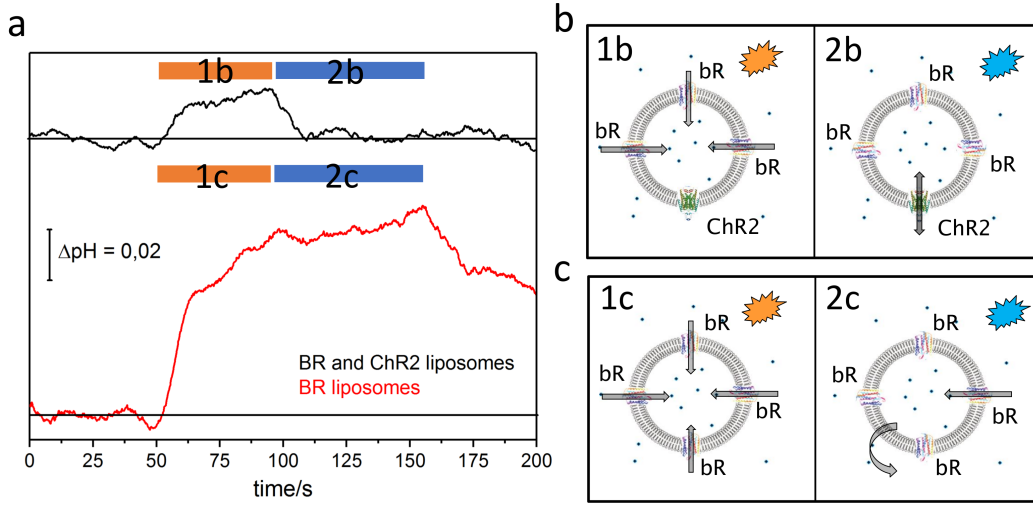


Figure 3.36: (a) Electrode-mediated pH measurements of two suspensions of proteoliposomes, BR and ChR2 coreconstituted (top) and BR reconstituted liposomes (bottom) prepared in parallel under the same conditions are measured under the same illumination conditions.

intensity of the pH gradient in BR/ChR2 liposomes under orange illumination might be explained by the activation of ChR2 channels by the LED.

These results together report on the functional activity of ChR2 reconstituted in PC/PS liposomes as proton channel. This essay could be used to test in vitro the functionality of heterogeneously expressed and purified ChRs in parallel to their spectroscopic investigation.

3.6 The photocycle of the P_4 intermediate of ChR2

The photocycle of *CrChR2* has been extensively studied with visible and infrared time-resolved spectroscopy under single turnover conditions [97, 95, 13] and continuous illumination [6, 104, 99]. The results lead to the understanding that a single unidirectional photocycle could not accurately describe the protein behaviour, leading to photocycle branching [97, 89] or to separate photocycles [6, 105, 104, 106]. Being the last intermediate of the photocycle, P_4^{480} , stable for several seconds (decay time constant of 10 – 20 s) it is of high relevance to investigate whether this long-lived intermediate is photo-active and if it could lead to a separate photocycle.

Phenomena like desensitisation and inactivation arise under continuous illumination and might be connected with the excitation of the P_4^{480} intermediate [89]. Although desensitization is common in membrane channels [201, 202, 203], it is one of the major drawbacks for the optogenetic applications of ChR2 [204].

A better understanding of the source of these phenomena would provide the knowledge to better design efficient optogenetic tools.

The measurements showed in this section were performed with F. Pranga-Sellnau and the data analysis together with Dr. V. Lorenz Fonfria.

3.6.1 The P_4^{480} intermediate is photoactive

Time-resolved UV/vis experiments has been performed on both dark-adapted and pre-illuminated ChR2 samples to study the behaviour of the P_4^{480} intermediate of the protein photocycle. A solution of *CrChR2* (solubilized with 0.2% decyl maltoside, 100 mM NaCl and 20 mM Hepes, see 2.4.2 for details) has been excited every 60 s with a 10 ns laser flash at 470 nm and kinetic traces have been recorded every 10 nm in the range from 360 to 560 nm (Fig. 3.37A). The results, shown in Fig. 3.37A, mostly represent the photocycle of the dark-state ChR2, as the repetition rate is low enough to allow the full recovery of the ground state after every laser flash.

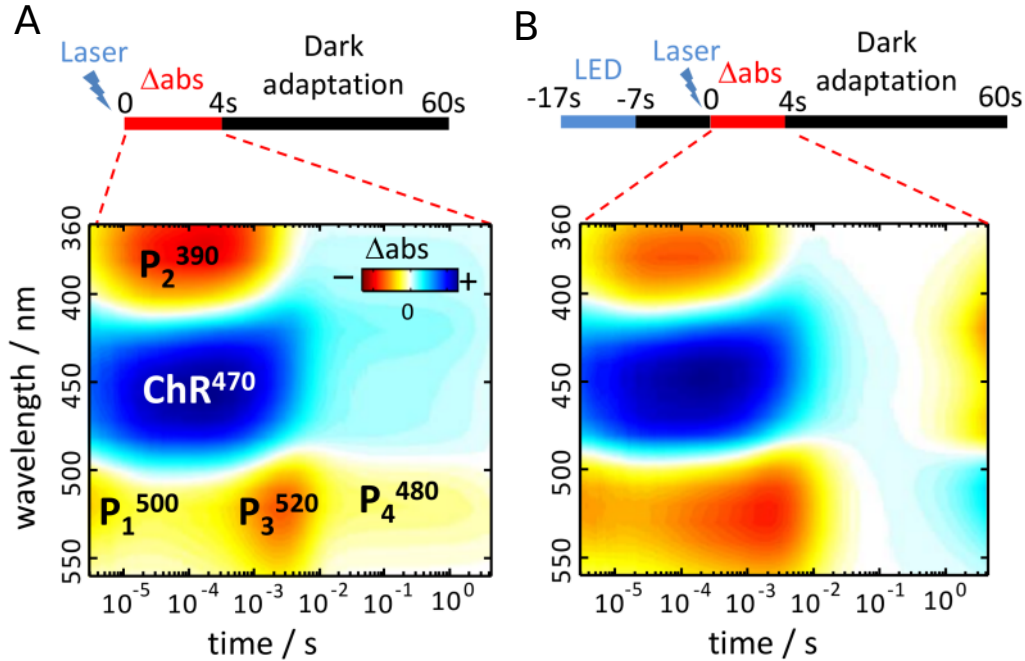


Figure 3.37: Difference absorption maps obtained with a flasphotolysis experiment on the same ChR2 solution under different illumination conditions: A single turnover with a laser flash every 60s .B LED illumination for 10s followed by a recovery delay in the dark of 7s before the laser flash. Each map consists of 17 kinetic traces.

The experiment has been repeated with the same sample and exactly the same conditions (temperature, laser flash energy density, spectral range) but introducing an additional illumination step in the measurement (Fig. 3.37B).

As the aim of the experiment is to study the kinetics of the photocycle obtained exciting the P_4^{480} intermediate, we pre-illuminated the sample for 10 s with blue LED light to deplete the population of proteins in the ground

state. A waiting time of 7 s was inserted between the LED illumination and the laser flash to allow all intermediates to decay except for the P_4^{480} that is over three orders of magnitude slower than all other intermediates. When the laser flash hits the sample, the only populated intermediates are the ground state $ChR2^{470}$ and the P_4^{480} . The data is recorded only after the laser flash, as in the previous experiment. The illumination patterns are depicted as sketches in Fig. 3.37.

If we assume that the P_4^{480} intermediate is not photoactive, we would expect the two experiments in Fig. 3.37 to give the same result: the pure photocycle of $ChR2^{470}$. It is evident from the results in Fig. 3.37 that the two kinetic maps have differences that must originate from the excitation of P_4^{480} , namely the P_2 intermediate has smaller amplitude and the P_3 intermediate rises earlier.

The other difference between the two photocycle maps can be seen after 1 s but cannot be attributed to the excitation of P_4^{480} . It comes from the fact that the laser flash excites only a fraction of the population of P_4^{480} accumulated with the LED illumination, the rest thermally relaxes back to the ground state with a single time constant of 9 s. This contribution of the relaxation of the non-excited P_4^{480} to the ground state can be modelled and removed from the data. For simplicity we will show in the following analysis the corrected versions of the kinetic traces.

As P_4^{480} can be photoexcited, it is of crucial importance to study its photocycle in details and most importantly define if it gives rise to a P_3 -like intermediate, where we expect the channel to be open and the cations to flow through the protein. Secondly it is interesting to investigate whether the excitation of P_4^{480} gives rise to the deprotonation of the Schiff base and a blue-shifted intermediate, in analogy with the $ChR2^{470}$ excitation.

3.6.2 The excitation of P_4^{480} leads to a low accumulated P_2 -like and a P_3 -like intermediates

We investigated the absorption changes at 380 nm and 520 nm, where respectively the P_2 and P_3 intermediates absorb, pre-illuminating the sample with a blue LED at different delay times between the LED illumination and the laser flash. We can affect the relative population of the P_4^{480} intermediate and the ground state changing the delay time between the LED illumination and the laser flash: the shorter the delay, a higher percentage of P_4^{480} over the ground state is excited. For longer delays almost only the ground state is excited as the P_4^{480} decay is exponential.

The results are shown in Fig. 3.38 where the kinetics for all the time delays are plotted together. We performed a SVD analysis of all the results showed in Fig. 3.38, joined together in a single matrix. This rank analysis confirmed that all the kinetics could be described as a linear combination of only two kinetics (for each wavelength) coming from two photocycles. We could therefore exclude the possibility that the measured kinetics come from different photocycles, maybe exciting another intermediate present at shorter timescales.

We globally fitted the data at 380 nm for different delays together with the

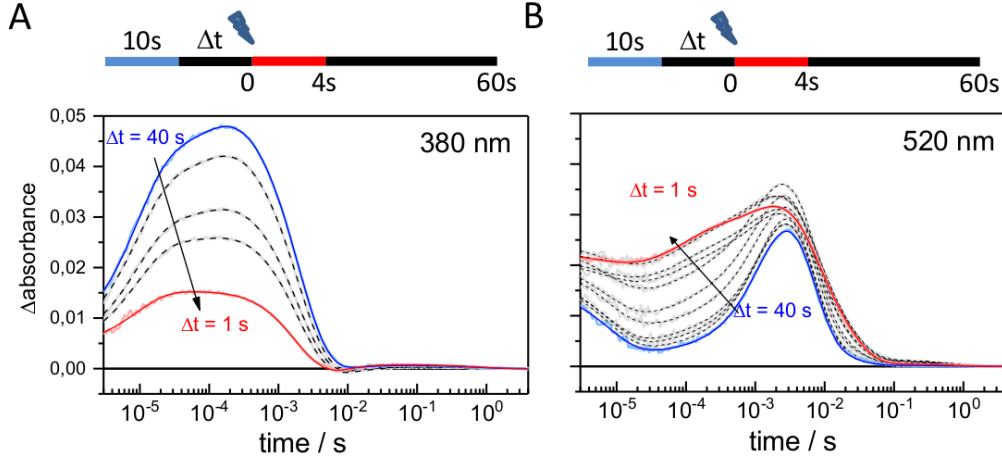


Figure 3.38: Difference absorption kinetics obtained with a flasphotolysis experiment, at different delays after 10 s LED illumination ranging from 40 s to 1 s. The kinetics were measured at 380 nm A and at 520 nm B.

data at 520 nm (see methods), obtaining the following time constants: $9 \pm 1 \mu\text{s}$, $90 \pm 10 \mu\text{s}$, $1.7 \pm 0.1 \text{ ms}$, $4.4 \pm 0.2 \text{ ms}$, $18 \pm 1 \text{ ms}$.

The exponential decay amplitudes for the same global time constants are shown in Fig. 3.39.A. As shown before, the amplitude of the rise and decay of the P_2 and P_3 intermediates are strongly influenced by the LED illumination. The obtained curves in Fig. 3.39A have been fitted with an exponential decay with time constant of $9.5 \pm 1.5 \text{ s}$ that agrees, as expected, with the decay of the P_4^{480} intermediate to the ground state obtained with the fit of the spectral map in Fig. 3.37.B.

At 520 nm the two main time constants that describe the P_3^{520} intermediate at 40 s delay are $\tau = 1.7 \text{ ms}$ for the rise (from P_2^{380}) and $\tau = 4.4 \text{ ms}$ for the decay (Fig. 3.39.A). The amplitude for this two time constants decreases with the time delay, as expected for changes that come from the ground state excitation. Following the same behaviour $\tau = 9 \mu\text{s}$ describes the decay of the P_1^{500} intermediate. Two additional time constants $\tau = 90 \mu\text{s}$ and $\tau = 18 \text{ ms}$ are present with the opposite trend: they increase in amplitude with decreasing time delay.

These time constants rise from the excitation of the P_4^{480} intermediate with a laser flash, the more we accumulate the P_4^{480} intermediate with the LED, the higher is the amplitude of the time constants of its photocycle. We assign this components to the rise ($\tau = 90 \mu\text{s}$) and decay ($\tau = 18 \text{ ms}$) of a P_3 – like intermediate that we will call I_3 .

In order to estimate the fraction of the populated intermediate after the 10 s delay we had to make two assumptions: at long Δt there is no contribution from the P_4^{480} photocycle (justified by the P_4^{480} decay time constant of 10–20 s) and the two main components at $\tau = 1.7 \text{ ms}$ and $\tau = 4.4 \text{ ms}$ come exclusively from the $Chr2^{470}$ photocycle. Given this two assumptions, the fraction of

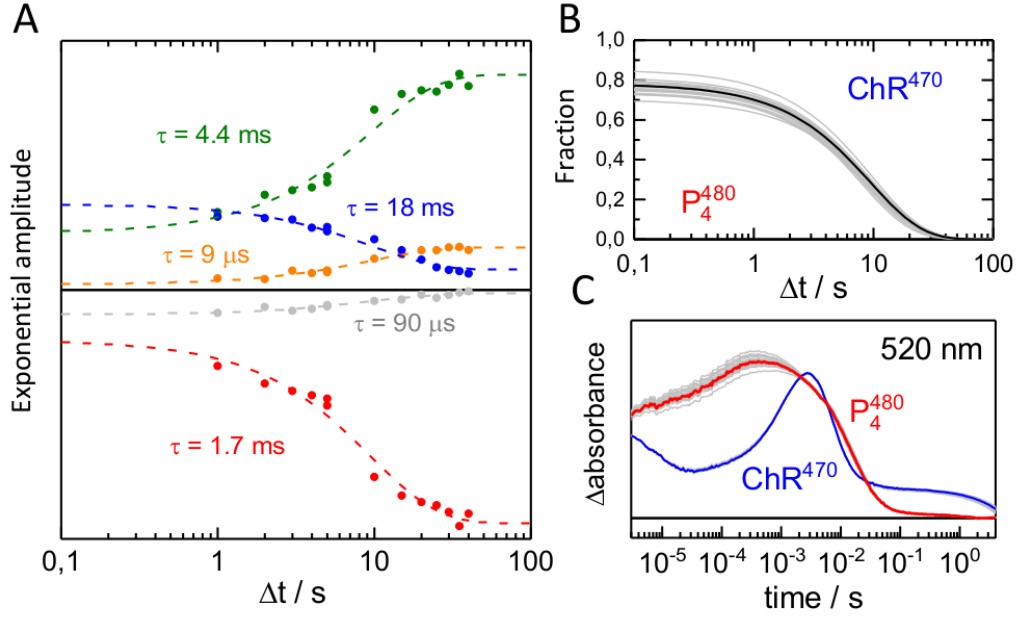


Figure 3.39: A) Amplitudes of the exponential decays needed to fit the data in Fig. 3.38.B with a global fit analysis. In red and grey the negative amplitudes, representing the rise of an intermediate. In green, blue and orange the positive amplitudes representing the intermediate decay. B) The estimated fraction of the population of the intermediates at the moment of the laser flash, in dependence of the time delay after the LED illumination. In grey their uncertainties. C) The absorption changes at 520 nm for the pure intermediates of the $ChR2^{470}$ or the P_4^{480} photocycles.

$ChR2^{470}$ can be calculated from Fig. 3.39.A, following the relative amplitude of the components at $\tau = 1,7$ ms and $\tau = 4,4$ ms. The fraction of P_4^{480} is complementary as only this two intermediates are populated at the time of the laser flash.

The exponential amplitudes of the time constants $\tau = 1,7$ ms and $\tau = 4,4$ ms extrapolated to $\Delta t = 0$ give an estimate of the relative population of the $ChR2^{470}$ or P_4^{480} intermediates during illumination of respectively $24 \pm 8\%$ and $76 \pm 8\%$. Knowing the starting population of this two states and the time constant of the decay of P_4^{480} ($\tau = 9.3 \pm 1.5$ s), it is possible to calculate the estimated fractions of $ChR2^{470}$ or P_4^{480} in function of Δt . Knowing the fraction of the P_4^{480} intermediate in dependence of Δt allows the determination of the pure intermediate kinetics. The pure absorption changes at 520 nm coming from the excitation of either $ChR2^{470}$ or P_4^{480} are shown in Fig. 3.39.C, estimated by linear least squares, with the relative uncertainties.

Intermediates that have a strongly blue-shifted absorption, like what we measure at 380 nm, typically represent a state where the Schiff base of the retinal is deprotonated. In the case of the $ChR2^{470}$ photocycle the Schiff base donates a proton to D253 [97].

As can be seen in Fig. 3.38A the intensity of this blue-shifted intermediate

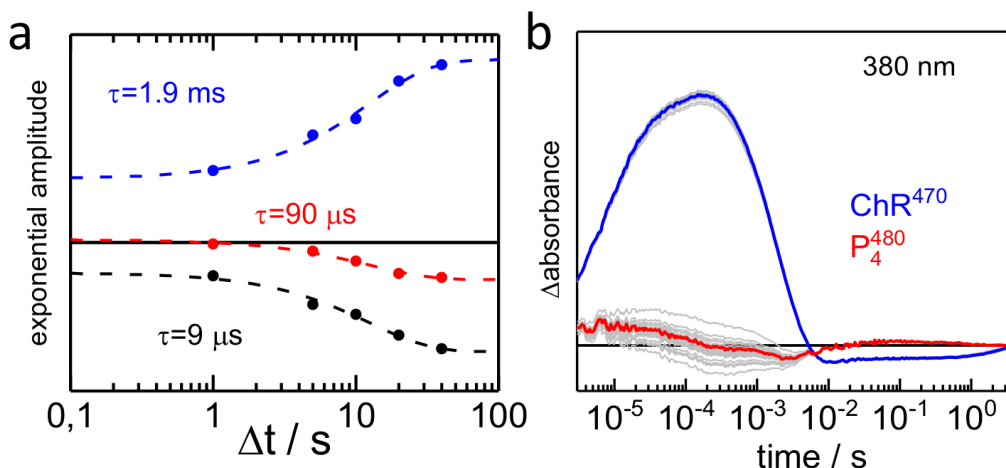


Figure 3.40: A) Amplitudes of the exponential decays needed to fit the data in Fig. 3.38.A with a global fit analysis. In red and grey the negative amplitudes, representing the rise of an intermediate. In blue the positive amplitude representing the intermediate decay. B) The absorption changes at 380 nm for the pure intermediates of the ChR^{470} or the P_4^{480} photocycles.

scales with the time delay between the LED illumination and the laser flash, slightly changing the shape.

In Fig. 3.40A are reported the time constant amplitudes for the rise of P_2 (two exponentials) and its decay in dependence of the time delay between the LED and the laser flash (time constants that are close to zero or not affected by the LED illumination are not shown).

The amplitudes in Fig. 3.40A are inversely proportional to the accumulation of P_4^{480} at the moment of the laser flash. At 380 nm there are no time constants that increase in amplitude with decreasing time delay, suggesting that a P_2 -like intermediate has a very low accumulation or is not present in the P_4^{480} photocycle.

A more accurate analysis with SVD reveals that at least two photocycles are needed to describe the absorption changes at this wavelength. As shown before in Fig. 3.39C, from the estimated fractions in Fig. 3.39B we know at each time delay Δt which is the contribution of the P_4^{480} photocycle and the pure kinetics at 380 nm can be calculated (Fig. 3.40B) with the relative uncertainties (grey). This results suggest that the P_4^{480} photocycle has a blue-shifted P_2 -like intermediate absorbing at 380 nm that rises and decays much earlier than the P_2 intermediate and has a very low accumulation, therefore gives rise to a small signal.

The fact that there are no exponential decays that increase in amplitude at small Δt in Fig. 3.40.A can be explained with an overlap of more than one exponentials with the same time constant. A candidate is the decay with time constant 90 ± 10 μ s, that unlike the other exponentials goes to zero at small time delays suggesting a possible overlap with a positive contribution. The kinetics in Fig. 3.40B of the P_2 - like intermediate indicate a submicrosecond

rise of this blue-shifted intermediate and support the decay with $90 \pm 10 \mu\text{s}$ time constant.

3.6.3 The P_4^{480} photocycle

With the informations learned from the experiments at 380 nm and 520 nm, we performed a global exponential analysis of the absorption difference maps in Fig. 3.37 in order to obtain additional spectral informations on the P_4^{480} photocycle. The global fit resulted in time constants that are compatible with the ones obtained from the data in Fig. 3.38, the results of the fit and the DAS are shown in the appendix A.29 for both the dark adapted and the pre-illuminated samples.

In Fig. 3.41A the most relevant DAS are reported, at 4.2 ms and at 20 ms. the DAS for the P_4^{480} photocycle have been calculated by subtraction of the DAS of the dark adapted sample from the DAS of the pre-illuminated sample, after a proper scaling factor. The resulting factor is 0.45, obtained from the calculated fraction of intermediates $ChR2^{470} / P_4^{480}$ after 7 s in Fig. 3.39B.

The resulting calculated DAS at 20 ms shows that the P_4^{480} photocycle generates a P_3 -like intermediate (I_3^{530}) that has an absorption maximum at 530 nm and decays with a 20 ms time constant, 4 – 5 times slower than the P_3^{520} that is present in the DAS at 4.2 ms. With less accumulation, we were able to resolve also a P_2 -like intermediate with an absorption maximum at 390 nm (I_2^{390}) that rises and decays much earlier than the homologue intermediate of the $ChR2^{470}$ photocycle.

We do not exclude the presence of an earlier photocycle intermediate I_1 , whose rise and decay need to be faster than our first data point at $1 \mu\text{s}$. I_2^{390} also rises faster than $1 \mu\text{s}$ and decays with $\tau \approx 100 \mu\text{s}$ to I_3^{530} . The P_3 -like intermediate present also an earlier rise at $\tau < 1 \mu\text{s}$. The kinetics of the I_2^{390} and I_3^{530} intermediates, extracted from the dataset in 3.41B are shown in 3.41C compared to their parent states from the $ChR2^{470}$ photocycle.

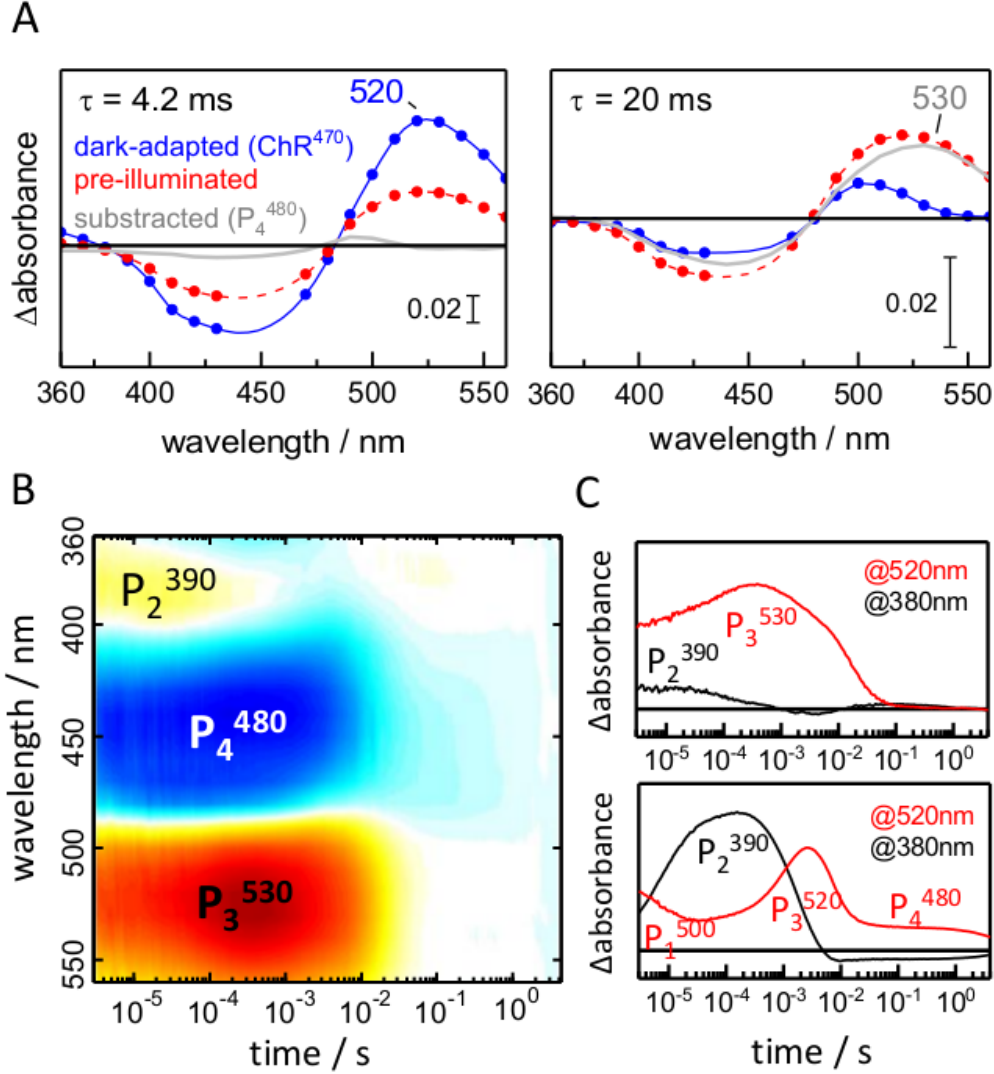


Figure 3.41: Kinetic analysis of the photocycle of P_4^{480} . A) The DAS of the decay of P_3^{520} at 4.2 ms compared to the DAS of the decay of I_3^{530} at 20 ms. In blue the results from the dark-adapted photocycle, in red the pre-illuminated photocycle and in grey the subtraction of the two resulting in the DAS of the isolated P_4^{480} photocycle. B) Time-resolved spectral map of the calculated P_4^{480} photocycle from the maps in 3.37. C) Kinetics of the main intermediates of the P_4^{480} photocycle I_2^{390} and I_3^{530} (top) as compared to the kinetics of the intermediates of the P_4^{480} photocycle P_2^{380} and P_3^{520} .

Chapter 4

General discussion

4.1 A novel method for the investigation of solvent-protein proton transfers with IR spectroscopy

Buffer molecules such as MES can trace protonation changes in the water environment surrounding membrane proteins during their functional mechanism. The main advantages over the conventional method of pH-sensitive dyes is the ability, with the use of infrared spectroscopy, to trace at the same time internal and external protonation changes in proteins. Additionally, the fast response time of buffer molecules at high concentrations [72] allows an accurate kinetic comparison between the protonation states of amino acids and bulk water.

We have demonstrated the potential of this approach studying the kinetics of proton release and uptake of bacteriorhodopsin, revealing new insights on the proton uptake mechanism and allowing to formulate new hypothesis on a mechanism accepted for the last 25 years.

As proton transfer reactions are often fundamental in the functional mechanism of many proteins, we are confident that similar experiments might help to investigate other systems.

4.2 New insight on bacteriorhodopsin's photoreaction

The use of MES buffer to track the proton exchange between protein and bulk confirmed in the first place that the proton release complex is the terminal group releasing the proton to the extracellular medium. The negative broad continuum rises in fact with two time constants that match the time constants of the buffer protonation in the bulk.

The appearance of a proton in the bulk lags the protonation of D85 from the Schiff base; this result favours photocycle models where the proton release happens during the transition between the M_1 and M_2 intermediates.

An additional component of the continuum band rise was noted before

[35]; our results reveal that this component is not related to the proton release, therefore we conclude it cannot be originated from the proton release complex. We have here infact resolved a second continuum band, spectrally overlapped with the one assigned to the proton release complex. Its kinetics do not correlate with the proton release and we tentatively assigned it to a protonated network of amino acids and/or water molecules called proton uptake complex and located at the cytoplasmic side of BR.

Based on its kinetics properties and on preliminary mutation work, we propose the H-bonded network in the vicinity of D38 at the origin of this second continuum band.

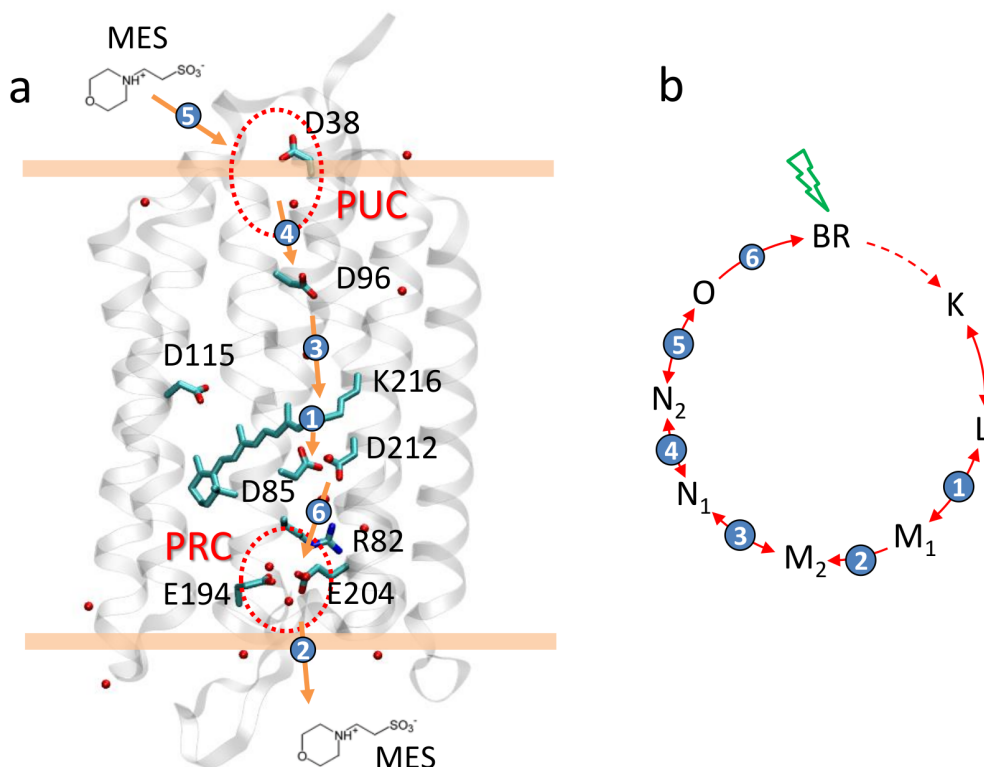


Figure 4.1: Proposed refined photocycle model for bacteriorhodopsin: a) the new pumping mechanism with all proton transfer steps highlighted with an arrow, referring to the photocycle intermediates in b).

The current model for the description of the photocycle of bacteriorhodopsin needs to be updated with new proton transfer steps and needs to explicitly differentiate the intermediates M_1 from M_2 and N_1 from N_2 .

We suggest infact that D96 gets reprotonated in the N_1 to N_2 transition from the newly discovered proton uptake complex, refining the last steps of the photocycle. As our results show that the release of a proton to the bulk is kinetically separated from the protonation of D85, we suggest to assign it to the M_1 to M_2 transition instead of the M_1 rise.

As bacteriorhodopsin serves as model system for the study of other membrane proteins involving proton transfer reaction, our results can be applied

to the investigation of other proteins.

4.3 Polarization-resolved FTIR is a powerful method for the shape determination of water clusters in proteins

The identity of the elusive proton release complex in bacteriorhodopsin has been investigated in various theoretical works that aimed in reproducing the spectral shape of the continuum band measured in experiments [50, 38, 39].

From spectroscopy, the only information we have on the chemical nature of the proton release complex come from mutational studies [42] or from a small red shift of the continuum band measured in $H_2^{18}O$ [43]. The first, localize the proton release complex at the extracellular side of the protein, in vicinity of E194 and E204 but cannot distinguish between different amino acids or water molecules as the mutations affect the protein geometry and photocycle. The second suggests that water molecules might be involved in the complex.

With the help of polarization-resolved infrared spectroscopy we were able to resolve the dichroism of the continuum band both respect to the membrane normal and in the membrane plane. The characteristics of the continuum band being a broad band overlapping with other bands prevents a precise angle calculation, but the analysis of the portion of the continuum band free of contamination from other bands reveals a strong absorption in the membrane plane and close to no absorption in the membrane normal direction. In the plane of the membrane we could resolve a little dichroism in favour of the direction of the retinal molecule.

The small dichroism could come both from a strongly oriented dipole in a direction close to 45° from the retinal or the absorption of a dipole distributed along the plane with a shape that slightly favours the retinal molecule. The geometry of the sample and the nature of the experiment makes this two scenarios indistinguishable.

Based on the dichroism of the continuum band we could indicate a tentative shape of the proton release complex. The absorption of the continuum band in the membrane plane suggests an orientation of the proton release complex along the membrane with almost no contribution from residues or water molecules located away from the two glutamates E204 and E194 that are known to be part of the network and lie in the membrane plane (Fig. 4.2a).

From a top view of the extracellular side of bacteriorhodopsin, (Fig. 4.2b) the proton release complex could be a broad network of H-bonds with a shape that to a small degree favours the retinal direction. Alternatively, a proton shared between two oxygens whose axis is at $\sim 35^\circ$ tilt from the retinal axis. As can be observed in Fig. 4.2b, a proton shared between E194 and E204 would fit the experimental results.

The above discussion is based on the verified assumption that the anisotropy of the continuum band is reflected by the orientation of the protonated cluster at its origin [179].

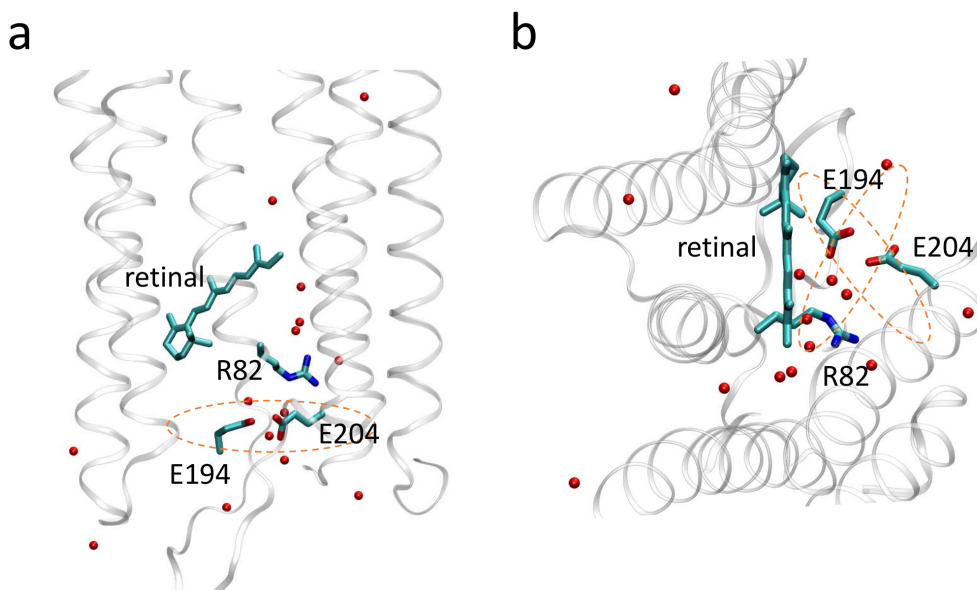


Figure 4.2: Structural model of BR (PDB:5B6V) from side view (a) and top view (b). Highlighted in red is the proposed shape of the proton release complex that generates the continuum band, according to our polarization resolved IR experiments.

Further simulations are needed in order to identify the chemical nature of the proton release complex, but our data impose important restriction on the shape of the protonated complex and on the orientation of its dipole moment change.

4.4 The continuum band is not a prerequisite for proton pumping in bacteriorhodopsin

One of the greatest advantages in the investigation of bacteriorhodopsin over other retinal proteins is the possibility to study the protein in its native membrane, its natural environment of lipids and protein aggregation state. In order to study the effect of the protein environment on the continuum band signal, I disrupted, via detergent solubilisation, the peculiar arrangement of the two dimensional crystal lattice of protein trimers and studied the behaviour of the continuum band when the protein was solubilised in different detergents or reconstituted in nanodiscs.

The protein solubilisation dramatically affected the continuum band, that is no longer present in the difference spectra. The reconstitution in nanodiscs partially recovers the negative absorption difference signal of the continuum band, demonstrating that the continuum band is not a property of the crystal lattice arrangement of the purple membranes. When solubilised in detergent, bacteriorhodopsin (originally organized in trimers) is isolated in monomers [181, 182] so it is possible that the monomeric proteins lack of the stability

at the extracellular side to stabilize the protonated complex. A confirmation of this comes from the crystal structure of monomeric BR obtained in bicelles where the number and arrangement of water molecules at the extracellular side is different than in the trimeric structures [189] (PDB 5B6V vs 1KME).

The proton pumping activity of the protein in detergent and in nanodiscs has been investigated: all samples showed proton release and uptake in a similar fashion as the native membranes. Even though we cannot measure directly the proton translocation from one side to the other of the solubilized proteins, the knowledge that protein monomers are functional [185] and comparable photocycle intermediates (for example involving the deprotonation of the Schiff base in favour of D85) makes us assume that solubilised BR monomers are functional proton pumps that don't exhibit the continuum band in the region between 1770 cm^{-1} and 1800 cm^{-1} .

Among the possible scenarios, there is the possibility that the continuum band shifts to higher or lower wavenumbers or that the proton release complex does not generate a broad transient band. Experiments in a broader infrared spectral range are necessary to investigate in details the poorly understood photocycle of monomeric bacteriorhodopsin.

4.5 Continuum bands are not exclusive to proton pumping proteins

I have presented in this work two experimental evidences of the presence of continuum bands in chloride-pumping rhodopsins. The continuum bands have been observed both in the spectral region around 1800 cm^{-1} and around 2700 cm^{-1} that is where similar broad bands have been studied in bacteriorhodopsin [154].

The broad negative band observed in bacteriorhodopsin between 1770 cm^{-1} and 2200 cm^{-1} , in particular, is assigned to the deprotonation of a H-bonded network of water molecules and/or amino acids (see 1.2.2). A similar broad negative band has been observed in this work during the photocycle of halorhodopsin from *Halobacterium salinarium* and, in analogy with bacteriorhodopsin, we can tentatively assign it to the deprotonation of H-bonded cluster that is still yet to be identified.

This negative continuum band appears in the transition between the K and L_1 intermediates that corresponds to a small displacement (0.3 \AA) of the chloride ion at the vicinity of the Schiff base [115] and does not involve protonation changes of carboxylic groups [192].

According to the photocycle model based on the crystal structure of the intermediates of *NpHR* [109], the following transition from L_1 to L_2 involves the translocation of the chloride ion across the Schiff base region, towards the cytoplasmic side. This model proposes also a mechanism for the chloride ion to escape the positively charged Schiff base region that involves a proton either donated from an amino acid or uptaken from the cytoplasmic side [110, 109]: the formed HCl is then able to diffuse to the cytoplasmic medium.

In the light of our results, the proton binding the chloride ion and require-

ment for the chloride translocation could come from a protonated complex of water molecules and/or amino acid residues. This reaction would take place early in the photocycle, before the first chloride translocation step.

4.6 Yeast-expressed and reconstituted CrChR2 is functional as a channel

ChR2's function as cation channel has been successfully studied with electrophysiology [205], a method that allows to test for selectivity [6, 206], conductance [98] response to different potentials [6], time-resolved conductance after a light flash [102] and even detect proton pumping at zero potential [98]. The method is robust and allows for fast screening of many protein variants in order to design proteins that have better applications in the optogenetic field [207]. The organisms that are typically used for electrophysiology measurements with ChR2 are oocytes and HEK cells; their membranes express not only the target ion channels, on contrary they are biomembranes whose environment could influence the ChR2 functional behaviour.

The expression system could also play a role in the protein folding mechanism and post-translational modifications could affect the protein function or mechanism.

ChR2 has been spectroscopically investigated in reconstituted lipid artificial membranes [93, 101, 198], solubilized in detergent [96, 208, 97] or in non native HEK cells [105], but the effect of the reconstitution was never investigated. Also, probing the function of a cation channel like ChR2 needs a compartmentized system and the application of a membrane potential; both are very challenging in a sample optimized for spectroscopy. Heterogeneously expressed, purified and reconstituted (or solubilized) ChR2 samples for spectroscopy are not tested for their functionality.

ChR2 expressed in *Pichia pastoris* has been here reconstituted in liposomes and its behaviour in lipids has been characterized with visible and infrared spectroscopy. I also developed an assay to coreconstitute the protein together with BR in order to test the functionality as cation channel.

Visible kinetics of reconstituted ChR2 show in general a lower accumulation of the P_2 intermediate and a faster rise and longer lifetime of the P_3 intermediate, although many factors including lipid headgroup, protein density and membrane curvature have a strong effect on the photocycle kinetics. Interestingly the protein reconstitution in DMPC nanodiscs did not alter significantly the photocycle. Due to the time overlap of the intermediate lifetimes in the reconstituted samples, it is concluded that detergent-solubilised or nanodisc-reconstituted samples are favoured for spectroscopic investigations.

Infrared spectroscopy revealed smaller conformational changes during the photocycle of reconstituted ChR2 if compared with detergent-solubilised proteins. This could be due to a more restricted movement of the α -helices during the channel opening. In light of the results from 3.6 another hypothesis is that in a lipidic environment a higher fraction of proteins populates the P_4 interme-

diate (for example due to a longer lifetime) respect to the detergent solubilised sample. The kinetic data would result in the mixture of the *ChR2* and P_4 excitation, leading to lower accumulation of P_2 , a broader P_3 and the accumulation of a desensitized state in the infrared experiments, showing smaller helix displacement.

I also investigated the functionality of the reconstituted proteins as cation channel reconstituting *ChR2* in proteoliposomes containing Bacteriorhodopsin acting as an inward proton pump. The results showed indeed the ability of *ChR2* to passively transport protons and depolarize the proteoliposomes with light.

4.7 The photocycle of the P_4^{480} intermediate of *ChR2* and its relevance for optogenetic applications

Compared to other microbial rhodopsins the photocycle of *ChR2* is extremely slow, characterized by a time constant for the complete dark state recovery of 10 – 20 s that is at least 10 times longer than the typical dark state recovery in proteins of the retinal family [18, 112, 209, 210].

The last intermediate, P_4 , responsible for this long lifetime, is populated only by a small fraction of the proteins undergoing the photocycle, with the majority of the proteins recovering the initial dark state in less than 1 s [97], in line with the other proteins of the rhodopsin family.

Our results indicate that P_4 can be excited and its photoexcitation leads to a secondary photocycle characterized by a low-accumulated blue-shifted intermediate called I_2 followed by a red-shifted I_3 . We therefore propose a branched photocycle as showed in Fig. 4.3 where the excitation of P_4 leads to a secondary photoreaction.

This modified scheme can be compared with the proposed photocycle scheme that explain the protein photocurrents under continuous illumination, in electrophysiology experiments [105, 106]. This latter predicts two different closed states, C_1 and C_2 , that can be excited and lead to two distinct open states, one giving rise to a peak current O_1 , the other to a stationary current O_2 .

The two photocycles present several common features. P_4 thermally decays to the ground state with the same slow time-constant of the C_2 to C_1 transition. Another similarity is that the I_3 to P_4 transition is 4 – 5 times slower than the P_3 to ground state transition, exactly like the O_2 to C_2 transition is 4 – 5 times slower than the O_1 to C_1 transition. According to the photocycle in 4.3, continuous light illumination would lead in the millisecond time scale to the accumulation of P_3 and later to the accumulation of P_4 that is itself excited populating I_3 , just like a peak current in the milliseconds leaves room for a stationary current in electrophysiology experiments during continuous illumination.

The novel photocycle explains therefore the light adaptation and desensitisation phenomena (see 1.3.1), studied with electrophysiology, with the

4.7. THE PHOTOCYCLE OF THE P_4^{480} INTERMEDIATE OF CHR2 AND ITS RELEVANCE FOR OPTOGENETIC APPLICATIONS

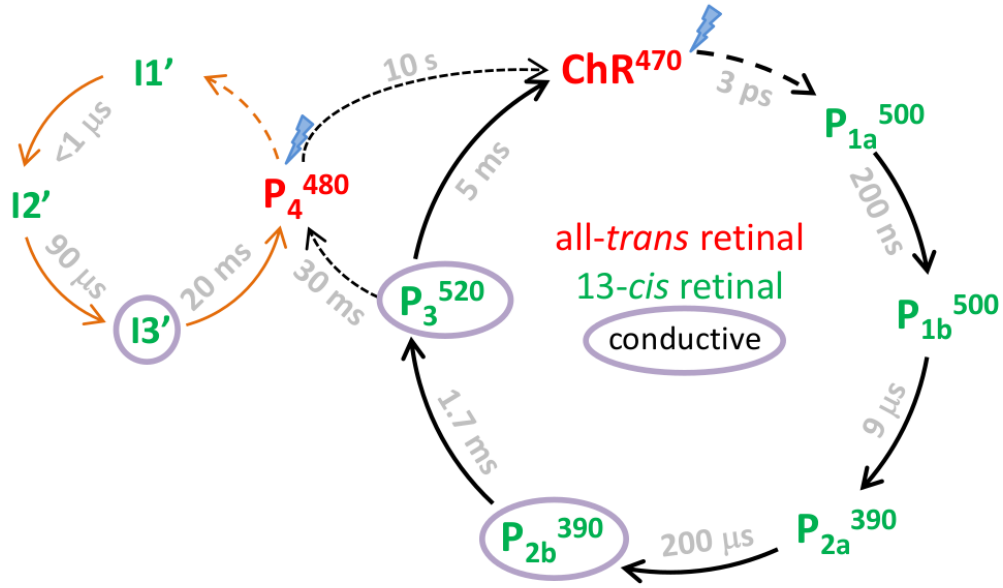


Figure 4.3: Proposed photocycle of ChR2 under single turnover conditions. A branched reaction partially populates the long-lived P_4 that, once excited with a second photon, leads to a secondary photocycle.

different population of the ground state or P_4 intermediates during illumination. The conductivity of I_3 is expected to be 10 – 20 times slower than P_3 , based on the O_1/O_2 conductivity ratio [105, 204].

Bibliography

- [1] R. B. Gennis, *Biomembranes: molecular structure and function*. Springer Science & Business Media, 2013.
- [2] O. P. Ernst, D. T. Lodowski, M. Elstner, P. Hegemann, L. S. Brown, and H. Kandori, “Microbial and animal rhodopsins: structures, functions, and molecular mechanisms,” *Chem. Rev.*, vol. 114, no. 1, pp. 126–163, 2013.
- [3] J. K. Lanyi, “Bacteriorhodopsin,” *Annu. Rev. Physiol.*, vol. 66, pp. 665–688, 2004.
- [4] K. Inoue, H. Ono, R. Abe-Yoshizumi, S. Yoshizawa, H. Ito, K. Kogure, and H. Kandori, “A light-driven sodium ion pump in marine bacteria,” *Nat. Commun.*, vol. 4, p. 1678, 2013.
- [5] J. K. Lanyi, “Halorhodopsin, a light-driven electrogenic chloride-transport system,” *Physiol. Rev.*, vol. 70, no. 2, pp. 319–330, 1990.
- [6] G. Nagel, T. Szellas, W. Huhn, S. Kateriya, N. Adeishvili, P. Berthold, D. Ollig, P. Hegemann, and E. Bamberg, “Channelrhodopsin-2, a directly light-gated cation-selective membrane channel,” *Proc. Natl. Acad. Sci.*, vol. 100, no. 24, pp. 13940–13945, 2003.
- [7] R. Moukhametzianov, J. P. Klare, R. Efremov, C. Baeken, A. Göppner, J. Labahn, M. Engelhard, G. Büldt, and V. I. Gordeliy, “Development of the signal in sensory rhodopsin and its transfer to the cognate transducer,” *Nature*, vol. 440, no. 7080, pp. 115–119, 2006.
- [8] K. Gerwert, E. Freier, and S. Wolf, “The role of protein-bound water molecules in microbial rhodopsins,” *Biochim. Biophys. Acta, Bioenerg.*, vol. 1837, no. 5, pp. 606–613, 2014.
- [9] E. Nango, A. Royant, M. Kubo, T. Nakane, C. Wickstrand, T. Kimura, T. Tanaka, K. Tono, C. Song, R. Tanaka, *et al.*, “A three-dimensional movie of structural changes in bacteriorhodopsin,” *Science*, vol. 354, no. 6319, pp. 1552–1557, 2016.
- [10] G. Váró and J. Lanyi, “Distortions in the photocycle of bacteriorhodopsin at moderate dehydration,” *Biophys. J.*, vol. 59, no. 2, pp. 313–322, 1991.

- [11] M. Kolbe, H. Besir, L.-O. Essen, and D. Oesterhelt, "Structure of the light-driven chloride pump halorhodopsin at 1.8 Å resolution," *Science*, vol. 288, no. 5470, pp. 1390–1396, 2000.
- [12] A. Harris, M. Saita, T. Resler, A. Hughes-Visentin, R. Maia, F. Pranga-Sellnau, A.-N. Bondar, J. Heberle, and L. S. Brown, "Molecular details of the unique mechanism of chloride transport by a cyanobacterial rhodopsin," *Phys. Chem. Chem. Phys.*, 2018.
- [13] V. A. Lórenz-Fonfría, C. Bamann, T. Resler, R. Schlesinger, E. Bamberg, and J. Heberle, "Temporal evolution of helix hydration in a light-gated ion channel correlates with ion conductance," *Proc. Natl. Acad. Sci.*, vol. 112, no. 43, pp. E5796–E5804, 2015.
- [14] R. Henderson and P. N. T. Unwin, "Three-dimensional model of purple membrane obtained by electron microscopy," *Nature*, vol. 257, no. 5521, pp. 28–32, 1975.
- [15] R. Neutze, E. Pebay-Peyroula, K. Edman, A. Royant, J. Navarro, and E. M. Landau, "Bacteriorhodopsin: a high-resolution structural view of vectorial proton transport," *Biochim. Biophys. Acta, Biomembr.*, vol. 1565, no. 2, pp. 144–167, 2002.
- [16] J. Heberle, "Proton transfer reactions across bacteriorhodopsin and along the membrane," *Biochim. Biophys. Acta, Bioenerg.*, vol. 1458, no. 1, pp. 135–147, 2000.
- [17] J. K. Lanyi and A. Pohorille, "Proton pumps: mechanism of action and applications," *Trends Biotechnol.*, vol. 19, no. 4, pp. 140–144, 2001.
- [18] K. Ludmann, C. Gergely, and G. Váró, "Kinetic and thermodynamic study of the bacteriorhodopsin photocycle over a wide pH range," *Biophys. J.*, vol. 75, no. 6, pp. 3110–3119, 1998.
- [19] J. K. Lanyi, "Proton transfers in the bacteriorhodopsin photocycle," *Biochim. Biophys. Acta, Bioenerg.*, vol. 1757, no. 8, pp. 1012–1018, 2006.
- [20] J. Heberle and N. A. Dencher, "Surface-bound optical probes monitor protein translocation and surface potential changes during the bacteriorhodopsin photocycle," *Proc. Natl. Acad. Sci.*, vol. 89, no. 13, pp. 5996–6000, 1992.
- [21] L. Zimanyi, G. Varo, M. Chang, B. Ni, R. Needleman, and J. K. Lanyi, "Pathways of proton release in the bacteriorhodopsin photocycle," *Biochemistry*, vol. 31, no. 36, pp. 8535–8543, 1992.
- [22] G. Varo and J. K. Lanyi, "Kinetic and spectroscopic evidence for an irreversible step between deprotonation and reprotonation of the schiff base in the bacteriorhodopsin photocycle," *Biochemistry*, vol. 30, no. 20, pp. 5008–5015, 1991.

- [23] V. A. Lorenz-Fonfria and H. Kandori, "Spectroscopic and kinetic evidence on how bacteriorhodopsin accomplishes vectorial proton transport under functional conditions," *J. Am. Chem. Soc.*, vol. 131, no. 16, pp. 5891–5901, 2009.
- [24] G. Souvignier and K. Gerwert, "Proton uptake mechanism of bacteriorhodopsin as determined by time-resolved stroboscopic-ftir-spectroscopy," *Biophys. J.*, vol. 63, no. 5, pp. 1393–1405, 1992.
- [25] C. Zscherp and J. Heberle, "Infrared difference spectra of the intermediates l, m, n, and o of the bacteriorhodopsin photoreaction obtained by time-resolved attenuated total reflection spectroscopy," *J. Phys. Chem. B*, vol. 101, no. 49, pp. 10542–10547, 1997.
- [26] H. Otto, T. Marti, M. Holz, T. Mogi, M. Lindau, H. G. Khorana, and M. P. Heyn, "Aspartic acid-96 is the internal proton donor in the reprotonation of the schiff base of bacteriorhodopsin," *Proc. Natl. Acad. Sci.*, vol. 86, no. 23, pp. 9228–9232, 1989.
- [27] L. S. Brown and J. K. Lanyi, "Determination of the transiently lowered pka of the retinal schiff base during the photocycle of bacteriorhodopsin," *Proc. Natl. Acad. Sci.*, vol. 93, no. 4, pp. 1731–1734, 1996.
- [28] J. B. Ames and R. A. Mathies, "The role of back-reactions and proton uptake during the n. fwdarw. o transition in bacteriorhodopsin's photocycle: a kinetic resonance raman study," *Biochemistry*, vol. 29, no. 31, pp. 7181–7190, 1990.
- [29] A. K. Dioumaev, L. S. Brown, R. Needleman, and J. K. Lanyi, "Coupling of the reisomerization of the retinal, proton uptake, and reprotonation of asp-96 in the n photointermediate of bacteriorhodopsin," *Biochemistry*, vol. 40, no. 38, pp. 11308–11317, 2001.
- [30] S. P. Balashov, "Protonation reactions and their coupling in bacteriorhodopsin," *Biochim. Biophys. Acta, Bioenerg.*, vol. 1460, no. 1, pp. 75–94, 2000.
- [31] S. P. Balashov, M. Lu, E. S. Imasheva, R. Govindjee, T. G. Ebrey, B. Othersen, Y. Chen, R. K. Crouch, and D. R. Menick, "The proton release group of bacteriorhodopsin controls the rate of the final step of its photocycle at low ph," *Biochemistry*, vol. 38, no. 7, pp. 2026–2039, 1999.
- [32] A. K. Dioumaev, L. S. Brown, R. Needleman, and J. K. Lanyi, "Fourier transform infrared spectra of a late intermediate of the bacteriorhodopsin photocycle suggest transient protonation of asp-212," *Biochemistry*, vol. 38, no. 31, pp. 10070–10078, 1999.

- [33] C. Zscherp, R. Schlesinger, and J. Heberle, "Time-resolved ft-ir spectroscopic investigation of the ph-dependent proton transfer reactions in the e194q mutant of bacteriorhodopsin," *Biochem. Bioph. Res. Co*, vol. 283, no. 1, pp. 57–63, 2001.
- [34] J. Sasaki, J. K. Lanyi, R. Needleman, T. Yoshizawa, and A. Maeda, "Complete identification of c: O stretching vibrational bands of protonated aspartic acid residues in the difference infrared spectra of m and n intermediates versus bacteriorhodopsin," *Biochemistry*, vol. 33, no. 11, pp. 3178–3184, 1994.
- [35] R. Rammelsberg, G. Huhn, M. Lübben, and K. Gerwert, "Bacteriorhodopsin's intramolecular proton-release pathway consists of a hydrogen-bonded network," *Biochemistry*, vol. 37, no. 14, pp. 5001–5009, 1998.
- [36] L. S. Brown, J. Sasaki, H. Kandori, A. Maeda, R. Needleman, and J. K. Lanyi, "Glutamic acid 204 is the terminal proton release group at the extracellular surface of bacteriorhodopsin," *J. Biol. Chem.*, vol. 270, no. 45, pp. 27122–27126, 1995.
- [37] Y. Xiao, M. S. Hutson, M. Belenky, J. Herzfeld, and M. S. Braiman, "Role of arginine-82 in fast proton release during the bacteriorhodopsin photocycle: a time-resolved ft-ir study of purple membranes containing ^{15}n -labeled arginine," *Biochemistry*, vol. 43, no. 40, pp. 12809–12818, 2004.
- [38] P. Phatak, N. Ghosh, H. Yu, Q. Cui, and M. Elstner, "Amino acids with an intermolecular proton bond as proton storage site in bacteriorhodopsin," *Proc. Natl. Acad. Sci.*, vol. 105, no. 50, pp. 19672–19677, 2008.
- [39] S. Wolf, E. Freier, and K. Gerwert, "A delocalized proton-binding site within a membrane protein," *Biophys. J.*, vol. 107, no. 1, pp. 174–184, 2014.
- [40] S. Wolf, E. Freier, M. Potschies, E. Hofmann, and K. Gerwert, "Directional proton transfer in membrane proteins achieved through protonated protein-bound water molecules: A proton diode," *Angew. Chem. Int. Edit.*, vol. 49, no. 38, pp. 6889–6893, 2010.
- [41] G. Zundel, "Hydrogen Bonds with Large Proton Polarizability and Proton Transfer Processes in Electrochemistry and Biology," in *Advances in Chemical Physics* (I. Prigogine and S. A. Rice, eds.), pp. 1–217, John Wiley & Sons, Inc., 1999.
- [42] F. Garczarek, L. S. Brown, J. K. Lanyi, and K. Gerwert, "Proton binding within a membrane protein by a protonated water cluster," *Proc. Natl. Acad. Sci. of the United States of America*, vol. 102, no. 10, pp. 3633–3638, 2005.

-
- [43] V. A. Lórenz-Fonfría, Y. Furutani, and H. Kandori, “Active internal waters in the bacteriorhodopsin photocycle. a comparative study of the l and m intermediates at room and cryogenic temperatures by infrared spectroscopy,” *Biochemistry*, vol. 47, no. 13, pp. 4071–4081, 2008.
- [44] F. Garczarek and K. Gerwert, “Functional waters in intraprotein proton transfer monitored by ftir difference spectroscopy,” *Nature*, vol. 439, no. 7072, p. 109, 2006.
- [45] M. Shibata, T. Tanimoto, and H. Kandori, “Water molecules in the schiff base region of bacteriorhodopsin,” *J. Am. Chem. Soc.*, vol. 125, no. 44, pp. 13312–13313, 2003.
- [46] A. Maeda, “Internal water molecules as mobile polar groups for light-induced proton translocation in bacteriorhodopsin and rhodopsin as studied by difference ftir spectroscopy,” *Biochemistry (Moscow)*, vol. 66, no. 11, pp. 1256–1268, 2001.
- [47] M. Shibata and H. Kandori, “Ftir studies of internal water molecules in the schiff base region of bacteriorhodopsin,” *Biochemistry*, vol. 44, no. 20, pp. 7406–7413, 2005.
- [48] S. Wolf, E. Freier, Q. Cui, and K. Gerwert, “Infrared spectral marker bands characterizing a transient water wire inside a hydrophobic membrane protein,” *J. Chem. Phys.*, vol. 141, no. 22, p. 12B625_1, 2014.
- [49] M. Baer, G. Mathias, I.-F. W. Kuo, D. J. Tobias, C. J. Mundy, and D. Marx, “Spectral signatures of the pentagonal water cluster in bacteriorhodopsin,” *ChemPhysChem*, vol. 9, no. 18, pp. 2703–2707, 2008.
- [50] G. Mathias and D. Marx, “Structures and spectral signatures of protonated water networks in bacteriorhodopsin,” *Proc. Natl. Acad. Sci.*, vol. 104, no. 17, pp. 6980–6985, 2007.
- [51] J. Olejnik, B. Brzezinski, and G. Zundel, “A proton pathway with large proton polarizability and the proton pumping mechanism in bacteriorhodopsin fourier transform difference spectra of photoproducts of bacteriorhodopsin and of its pentademethyl analogue,” *J. Mol. Struct.*, vol. 271, no. 3, pp. 157–173, 1992.
- [52] E. C. Saint Clair, J. I. Ogren, S. Mamaev, J. M. Kralj, and K. J. Rothschild, “Conformational changes in the archaerhodopsin-3 proton pump: detection of conserved strongly hydrogen bonded water networks,” *J. Biol. Phys.*, vol. 38, no. 1, pp. 153–168, 2012.
- [53] B. C. Polander and B. A. Barry, “Detection of an intermediary, protonated water cluster in photosynthetic oxygen evolution,” *Proc. Natl. Acad. Sci.*, vol. 110, no. 26, pp. 10634–10639, 2013.

- [54] E. Freier, S. Wolf, and K. Gerwert, "Proton transfer via a transient linear water-molecule chain in a membrane protein," *Proc. Natl. Acad. Sci.*, vol. 108, no. 28, pp. 11435–11439, 2011.
- [55] J. Breton and E. Nabedryk, "Proton uptake upon quinone reduction in bacterial reaction centers: Ir signature and possible participation of a highly polarizable hydrogen bond network," *Photosynth. Res.*, vol. 55, no. 2-3, pp. 301–307, 1998.
- [56] S. Hermes, J. M. Stachnik, D. Onidas, A. Remy, E. Hofmann, and K. Gerwert, "Proton uptake in the reaction center mutant l210dn from rhodobacter sphaeroides via protonated water molecules," *Biochemistry*, vol. 45, no. 46, pp. 13741–13749, 2006.
- [57] J. Xu, M. A. Sharpe, L. Qin, S. Ferguson-Miller, and G. A. Voth, "Storage of an excess proton in the hydrogen-bonded network of the d-pathway of cytochrome c oxidase: identification of a protonated water cluster," *J. Am. Chem. Soc.*, vol. 129, no. 10, pp. 2910–2913, 2007.
- [58] H. Kandori, "Role of internal water molecules in bacteriorhodopsin," *Biochim. Biophys. Acta, Bioenerg.*, vol. 1460, no. 1, pp. 177–191, 2000.
- [59] T. Ackermann, "Das Absorptionsspektrum wäßriger Säure- und Alkali-hydroxydlösungen im Wellenlängenbereich von 2,5 bis 9 μ^* ," *Zeitschrift für Physikalische Chemie Neue Folge*, vol. 27, no. 3-4, pp. 253–276, 1961.
- [60] F. H. Stillinger, "Water revisited," *Science*, vol. 209, no. 4455, pp. 451–457, 1980.
- [61] M. Eigen, "Protonenübertragung, säure-base-katalyse und enzymatische hydrolyse. teil i: Elementarvorgänge," *Angew. Chem.*, vol. 75, no. 12, pp. 489–508, 1963.
- [62] D. Marx, "Proton transfer 200 years after von grotthuss: Insights from ab initio simulations," *ChemPhysChem*, vol. 7, no. 9, pp. 1848–1870, 2006.
- [63] J. Han and K. Burgess, "Fluorescent indicators for intracellular ph," *Chem. Rev.*, vol. 110, no. 5, pp. 2709–2728, 2009.
- [64] D. Wencel, T. Abel, and C. McDonagh, "Optical chemical ph sensors," *Anal. Chem.*, vol. 86, no. 1, pp. 15–29, 2013.
- [65] Y. Yue, F. Huo, S. Lee, C. Yin, and J. Yoon, "A review: the trend of progress about ph probes in cell application in recent years," *Analyst*, vol. 142, no. 1, pp. 30–41, 2017.
- [66] M. Seigneuret and J.-L. Rigaud, "Use of the fluorescent ph probe pyranine to detect heterogeneous directions of proton movement in bacteriorhodopsin reconstituted large liposomes," *FEBS Lett.*, vol. 188, no. 1, pp. 101–106, 1985.

- [67] M. G. Palmgren, "An h^+ -atpase assay: proton pumping and atpase activity determined simultaneously in the same sample," *Plant physiology*, vol. 94, no. 3, pp. 882–886, 1990.
- [68] A. Galkin, S. Dröse, and U. Brandt, "The proton pumping stoichiometry of purified mitochondrial complex i reconstituted into proteoliposomes," *Biochim. Biophys. Acta, Bioenerg.*, vol. 1757, no. 12, pp. 1575–1581, 2006.
- [69] N. Dencher and M. Wilms, "Flash photometric experiments on the photochemical cycle of bacteriorhodopsin," *Biophys. Struct. Mech.*, vol. 1, no. 3, pp. 259–271, 1975.
- [70] R. H. Lozier, R. A. Bogomolni, and W. Stoeckenius, "Bacteriorhodopsin: a light-driven proton pump in halobacterium halobium.," *Biophys. J.*, vol. 15, no. 9, p. 955, 1975.
- [71] M. Nack, I. Radu, B.-J. Schultz, T. Resler, R. Schlesinger, A.-N. Bondar, C. del Val, S. Abbruzzetti, C. Viappiani, C. Bamann, *et al.*, "Kinetics of proton release and uptake by channelrhodopsin-2," *FEBS Lett.*, vol. 586, no. 9, pp. 1344–1348, 2012.
- [72] D. Porschke, "Reaction coupling, acceptor pk, and diffusion control in light induced proton release of bacteriorhodopsin," *J. Phys. Chem. B*, vol. 106, no. 39, pp. 10233–10241, 2002.
- [73] P. Scherrer, U. Alexiev, T. Marti, H. G. Khorana, and M. P. Heyn, "Covalently bound ph-indicator dyes at selected extracellular or cytoplasmic sites in bacteriorhodopsin. 1. proton migration along the surface of bacteriorhodopsin micelles and its delayed transfer from surface to bulk," *Biochemistry*, vol. 33, no. 46, pp. 13684–13692, 1994.
- [74] U. Alexiev, R. Mollaaghababa, P. Scherrer, H. Khorana, and M. Heyn, "Rapid long-range proton diffusion along the surface of the purple membrane and delayed proton transfer into the bulk.," *Proc. Natl. Acad. Sci.*, vol. 92, no. 2, pp. 372–376, 1995.
- [75] U. Alexiev, T. Marti, M. P. Heyn, H. G. Khorana, and P. Scherrer, "Covalently bound ph-indicator dyes at selected extracellular or cytoplasmic sites in bacteriorhodopsin. 2. rotational orientation of helices d and e and kinetic correlation between m formation and proton release in bacteriorhodopsin micelles," *Biochemistry*, vol. 33, no. 46, pp. 13693–13699, 1994.
- [76] J. Heberle, J. Riesle, G. Thiedemann, D. Oesterhelt, and N. A. Dencher, "Proton migration along the membrane surface and retarded surface to bulk transfer," *Nature*, vol. 370, no. 6488, pp. 379–382, 1994.

- [77] S. Grzesiek and N. A. Dencher, “Time-course and stoichiometry of light-induced proton release and uptake during the photocycle of bacteriorhodopsin,” *FEBS Lett.*, vol. 208, no. 2, pp. 337–342, 1986.
- [78] S. Grzesiek and N. A. Dencher, “Monomeric and aggregated bacteriorhodopsin: Single-turnover proton transport stoichiometry and photochemistry,” *Proc. Natl. Acad. Sci.*, vol. 85, no. 24, pp. 9509–9513, 1988.
- [79] S. A. Waschuk, A. G. Bezerra, L. Shi, and L. S. Brown, “Leptosphaeria rhodopsin: bacteriorhodopsin-like proton pump from a eukaryote,” *Proc. Natl. Acad. Sci. of the United States of America*, vol. 102, no. 19, pp. 6879–6883, 2005.
- [80] Q. Li, Q. Sun, W. Zhao, H. Wang, and D. Xu, “Newly isolated archaeerhodopsin from a strain of chinese halobacteria and its proton pumping behavior,” *Biochim. Biophys. Acta, Biomembr.*, vol. 1466, no. 1-2, pp. 260–266, 2000.
- [81] M. Ziegler and H. Penefsky, “The adenine nucleotide translocase modulates oligomycin-induced quenching of pyranine fluorescence in submitochondrial particles,” *J. Biol. Chem.*, vol. 268, no. 34, pp. 25320–25328, 1993.
- [82] A. Adamantidis, S. Arber, J. S. Bains, E. Bamberg, A. Bonci, G. Buzski, J. A. Cardin, R. M. Costa, Y. Dan, Y. Goda, *et al.*, “Optogenetics: 10 years after chr2 in neurons views from the community,” 2015.
- [83] E. S. Boyden, F. Zhang, E. Bamberg, G. Nagel, and K. Deisseroth, “Millisecond-timescale, genetically targeted optical control of neural activity,” *Nat. Neurosci.*, vol. 8, no. 9, p. 1263, 2005.
- [84] H. P. Scholl, R. W. Strauss, M. S. Singh, D. Dalkara, B. Roska, S. Picaud, and J.-A. Sahel, “Emerging therapies for inherited retinal degeneration,” *Science translational medicine*, vol. 8, no. 368, pp. 368rv6–368rv6, 2016.
- [85] T. Moser, “Optogenetic stimulation of the auditory pathway for research and future prosthetics,” *Curr. Opin. Neurobiol.*, vol. 34, pp. 29–36, 2015.
- [86] F. Zhang, A. M. Aravanis, A. Adamantidis, L. de Lecea, and K. Deisseroth, “Circuit-breakers: optical technologies for probing neural signals and systems,” *Nat. Rev. Neurosci.*, vol. 8, no. 8, p. 577, 2007.
- [87] E. G. Govorunova, O. A. Sineshchekov, R. Janz, X. Liu, and J. L. Spudich, “Natural light-gated anion channels: A family of microbial rhodopsins for advanced optogenetics,” *Science*, p. aaa7484, 2015.
- [88] L. Fenno, O. Yizhar, and K. Deisseroth, “The development and application of optogenetics,” *Annu. Rev. Neurosci.*, vol. 34, 2011.

- [89] V. A. Lórenz-Fonfría and J. Heberle, “Channelrhodopsin unchained: structure and mechanism of a light-gated cation channel,” *Biochim. Biophys. Acta, Bioenerg.*, vol. 1837, no. 5, pp. 626–642, 2014.
- [90] O. Volkov, K. Kovalev, V. Polovinkin, V. Borshchevskiy, C. Bamann, R. Astashkin, E. Marin, A. Popov, T. Balandin, D. Willbold, *et al.*, “Structural insights into ion conduction by channelrhodopsin 2,” *Science*, vol. 358, no. 6366, p. eaan8862, 2017.
- [91] M. Müller, C. Bamann, E. Bamberg, and W. Kühlbrandt, “Projection structure of channelrhodopsin-2 at 6 Å resolution by electron crystallography,” *J. Mol. Biol.*, vol. 414, no. 1, pp. 86–95, 2011.
- [92] M. Nack, I. Radu, M. Gossing, C. Bamann, E. Bamberg, G. F. von Mollard, and J. Heberle, “The dc gate in channelrhodopsin-2: crucial hydrogen bonding interaction between c128 and d156,” *Photochemical & Photobiological Sciences*, vol. 9, no. 2, pp. 194–198, 2010.
- [93] M. Nack, I. Radu, C. Bamann, E. Bamberg, and J. Heberle, “The retinal structure of channelrhodopsin-2 assessed by resonance raman spectroscopy,” *FEBS Lett.*, vol. 583, no. 22, pp. 3676–3680, 2009.
- [94] S. Bruun, D. Stoeppler, A. Keidel, U. Kuhlmann, M. Luck, A. Diehl, M.-A. Geiger, D. Woodmansee, D. Trauner, P. Hegemann, *et al.*, “Light-dark adaptation of channelrhodopsin involves photoconversion between the all-trans and 13-cis retinal isomers,” *Biochemistry*, vol. 54, no. 35, pp. 5389–5400, 2015.
- [95] V. A. Lorenz-Fonfría, B.-J. Schultz, T. Resler, R. Schlesinger, C. Bamann, E. Bamberg, and J. Heberle, “Pre-gating conformational changes in the cheta variant of channelrhodopsin-2 monitored by nanosecond ir spectroscopy,” *J. Am. Chem. Soc.*, vol. 137, no. 5, pp. 1850–1861, 2015.
- [96] I. Radu, C. Bamann, M. Nack, G. Nagel, E. Bamberg, and J. Heberle, “Conformational changes of channelrhodopsin-2,” *J. Am. Chem. Soc.*, vol. 131, no. 21, pp. 7313–7319, 2009.
- [97] V. A. Lorenz-Fonfría, T. Resler, N. Krause, M. Nack, M. Gossing, G. F. von Mollard, C. Bamann, E. Bamberg, R. Schlesinger, and J. Heberle, “Transient protonation changes in channelrhodopsin-2 and their relevance to channel gating,” *Proc. Natl. Acad. Sci.*, vol. 110, no. 14, pp. E1273–E1281, 2013.
- [98] K. Feldbauer, D. Zimmermann, V. Pintschovius, J. Spitz, C. Bamann, and E. Bamberg, “Channelrhodopsin-2 is a leaky proton pump,” *Proc. Natl. Acad. Sci.*, vol. 106, no. 30, pp. 12317–12322, 2009.
- [99] E. Ritter, K. Stehfest, A. Berndt, P. Hegemann, and F. J. Bartl, “Monitoring light-induced structural changes of channelrhodopsin-2 by uv-visible and fourier transform infrared spectroscopy,” *J. Biol. Chem.*, vol. 283, no. 50, pp. 35033–35041, 2008.

- [100] T. Sattig, C. Rickert, E. Bamberg, H.-J. Steinhoff, and C. Bamann, "Light-induced movement of the transmembrane helix b in channelrhodopsin-2," *Angew. Chem. Int. Ed.*, vol. 52, no. 37, pp. 9705–9708, 2013.
- [101] K. Eisenhauer, J. Kuhne, E. Ritter, A. Berndt, S. Wolf, E. Freier, F. Bartl, P. Hegemann, and K. Gerwert, "In channelrhodopsin-2 glu-90 is crucial for ion selectivity and is deprotonated during the photocycle," *J. Biol. Chem.*, vol. 287, no. 9, pp. 6904–6911, 2012.
- [102] C. Bamann, T. Kirsch, G. Nagel, and E. Bamberg, "Spectral characteristics of the photocycle of channelrhodopsin-2 and its implication for channel function," *J. Mol. Biol.*, vol. 375, no. 3, pp. 686–694, 2008.
- [103] N. Krause, C. Engelhard, J. Heberle, R. Schlesinger, and R. Bittl, "Structural differences between the closed and open states of channelrhodopsin-2 as observed by epr spectroscopy," *FEBS Lett.*, vol. 587, no. 20, pp. 3309–3313, 2013.
- [104] A. Berndt, M. Prigge, D. Gradmann, and P. Hegemann, "Two open states with progressive proton selectivities in the branched channelrhodopsin-2 photocycle," *Biophys. J.*, vol. 98, no. 5, pp. 753–761, 2010.
- [105] K. Nikolic, N. Grossman, M. S. Grubb, J. Burrone, C. Toumazou, and P. Degenaar, "Photocycles of channelrhodopsin-2," *Photochem. Photobiol.*, vol. 85, no. 1, pp. 400–411, 2009.
- [106] P. Hegemann, S. Ehlenbeck, and D. Gradmann, "Multiple photocycles of channelrhodopsin," *Biophys. J.*, vol. 89, no. 6, pp. 3911–3918, 2005.
- [107] B. Schobert and J. K. Lanyi, "Halorhodopsin is a light-driven chloride pump," *J. Biol. Chem.*, vol. 257, no. 17, pp. 10306–10313, 1982.
- [108] L.-O. Essen, "Halorhodopsin: light-driven ion pumping made simple?," *Curr. Opin. Struct. Biol.*, vol. 12, no. 4, pp. 516–522, 2002.
- [109] T. Kouyama, H. Kawaguchi, T. Nakanishi, H. Kubo, and M. Murakami, "Crystal structures of the l1, l2, n, and o states of pharaonis halorhodopsin," *Biophys. J.*, vol. 108, no. 11, pp. 2680–2690, 2015.
- [110] T. Kouyama, S. Kanada, Y. Takeguchi, A. Narusawa, M. Murakami, and K. Ihara, "Crystal structure of the light-driven chloride pump halorhodopsin from natronomonas pharaonis," *J. Mol. Biol.*, vol. 396, no. 3, pp. 564–579, 2010.
- [111] X.-R. Chen, Y.-C. Huang, H.-P. Yi, and C.-S. Yang, "A unique light-driven proton transportation signal in halorhodopsin from natronomonas pharaonis," *Biophys. J.*, vol. 111, no. 12, pp. 2600–2607, 2016.

- [112] G. Váró, L. Zimányi, X. Fan, L. Sun, R. Needleman, and J. K. Lanyi, "Photocycle of halorhodopsin from halobacterium salinarium," *Biophys. J.*, vol. 68, no. 5, pp. 2062–2072, 1995.
- [113] G. Váró, L. S. Brown, R. Needleman, and J. K. Lanyi, "Proton transport by halorhodopsin," *Biochemistry*, vol. 35, no. 21, pp. 6604–6611, 1996.
- [114] E. Bamberg, J. Tittor, and D. Oesterhelt, "Light-driven proton or chloride pumping by halorhodopsin," *Proc. Natl. Acad. Sci.*, vol. 90, no. 2, pp. 639–643, 1993.
- [115] W. Gmelin, K. Zeth, R. Efremov, J. Heberle, J. Tittor, and D. Oesterhelt, "The crystal structure of the 11 intermediate of halorhodopsin at 1.9 Å resolution," *Photochem. Photobiol.*, vol. 83, no. 2, pp. 369–377, 2007.
- [116] A. Barth, "Infrared spectroscopy of proteins," *Biochim. Biophys. Acta, Bioenerg.*, vol. 1767, no. 9, pp. 1073–1101, 2007.
- [117] W. Hug, J. Chalmers, and P. Griffith, "Handbook of vibrational spectroscopy," *(John Wiley and Son Ltd., Chichester 2002)*, 2002.
- [118] D. Lin-Vien, N. B. Colthup, W. G. Fateley, and J. G. Grasselli, *The handbook of infrared and Raman characteristic frequencies of organic molecules*. Elsevier, 1991.
- [119] G. Bellisola and C. Sorio, "Infrared spectroscopy and microscopy in cancer research and diagnosis," *Am. J. Cancer Res.*, vol. 2, no. 1, p. 1, 2012.
- [120] J. Gasteiger *et al.*, *Handbook of chemoinformatics*, vol. 1. Wiley Online Library, 2003.
- [121] H. C. Allen Jr and W. Olson, "Vibrational-rotational spectroscopy," *Annu. Rev. Phys. Chem.*, vol. 13, no. 1, pp. 221–240, 1962.
- [122] P. R. Griffiths, "Introduction to vibrational spectroscopy," *Handbook of vibrational spectroscopy*, 2006.
- [123] E. Goormaghtigh, V. Raussens, and J.-M. Ruysschaert, "Attenuated total reflection infrared spectroscopy of proteins and lipids in biological membranes," *Biochim. Biophys. Acta, Rev. Biomem.*, vol. 1422, no. 2, pp. 105–185, 1999.
- [124] D. Marsh, "Quantitation of secondary structure in atr infrared spectroscopy," *Biophys. J.*, vol. 77, no. 5, pp. 2630–2637, 1999.
- [125] V. A. Lorenz-Fonfria, M. Granell, X. Leon, G. Leblanc, and E. Padrós, "In-plane and out-of-plane infrared difference spectroscopy unravels tilting of helices and structural changes in a membrane protein upon substrate binding," *J. Am. Chem. Soc.*, vol. 131, no. 42, pp. 15094–15095, 2009.

- [126] N. Dave, V. A. Lórenz-Fonfría, G. Leblanc, and E. Padrós, “Ftir spectroscopy of secondary-structure reorientation of melibiose permease modulated by substrate binding,” *Biophys. J.*, vol. 94, no. 9, pp. 3659–3670, 2008.
- [127] R. Fraser, “The interpretation of infrared dichroism in fibrous protein structures,” *The Journal of Chemical Physics*, vol. 21, no. 9, pp. 1511–1515, 1953.
- [128] C.-P. Lafrance, A. Nabet, R. E. Prud’homme, and M. Pérolet, “On the relationship between the order parameter and the shape of orientation distributions,” *Can. J. Chem.*, vol. 73, no. 9, pp. 1497–1505, 1995.
- [129] J. Breton and E. Navedryk, “Light-induced polarized fourier transform infrared spectroscopy of bacteriorhodopsin a study of the m412 intermediate by photoselection,” *Biochim. Biophys. Acta, Bioenerg.*, vol. 973, no. 1, pp. 13–18, 1989.
- [130] K. Fahmy, F. Siebert, M. Grossjean, and P. Tavan, “Photoisomerization in bacteriorhodopsin studied by ftir, linear dichroism and photoselection experiments combined with quantum chemical theoretical analysis,” *J. Mol. Struct.*, vol. 214, pp. 257–288, 1989.
- [131] K. Fahmy, F. Siebert, and P. Tavan, “Structural investigation of bacteriorhodopsin and some of its photoproducts by polarized fourier transform infrared spectroscopic methods-difference spectroscopy and photoselection,” *Biophys. J.*, vol. 60, no. 5, pp. 989–1001, 1991.
- [132] J. Faist, F. Capasso, D. L. Sivco, C. Sirtori, A. L. Hutchinson, A. Y. Cho, *et al.*, “Quantum cascade laser,” *Science-AAAS-Weekly Paper Edition-including Guide to Scientific Information*, vol. 264, no. 5158, pp. 553–555, 1994.
- [133] B.-J. Schultz, H. Mohrmann, V. A. Lorenz-Fonfría, and J. Heberle, “Protein dynamics observed by tunable mid-ir quantum cascade lasers across the time range from 10 ns to 1 s,” *Spectrochim. Acta, Part A: Molecular and Biomolecular Spectroscopy*, vol. 188, pp. 666–674, 2018.
- [134] K. Fujimoto, S. Hayashi, J.-y. Hasegawa, and H. Nakatsuji, “Theoretical studies on the color-tuning mechanism in retinal proteins,” *Journal of chemical theory and computation*, vol. 3, no. 2, pp. 605–618, 2007.
- [135] R. W. Hendler and R. I. Shrager, “Deconvolutions based on singular value decomposition and the pseudoinverse: a guide for beginners,” *J. Biochem. Biophys. Meth.*, vol. 28, no. 1, pp. 1–33, 1994.
- [136] V. A. Lórenz-Fonfría and J. Heberle, “Proton transfer and protein conformation dynamics in photosensitive proteins by time-resolved step-scan fourier-transform infrared spectroscopy,” *J Vis Exp*, no. 88, 2014.

- [137] D. Oesterhelt and W. Stoeckenius, “[69] isolation of the cell membrane of halobacterium halobium and its fractionation into red and purple membrane,” in *Methods Enzymol.*, vol. 31, pp. 667–678, Elsevier, 1974.
- [138] T. Noguchi and M. Sugiura, “Flash-induced ftir difference spectra of the water oxidizing complex in moderately hydrated photosystem ii core films: effect of hydration extent on s-state transitions,” *Biochemistry*, vol. 41, no. 7, pp. 2322–2330, 2002.
- [139] E. Racker and W. Stoeckenius, “Reconstitution of purple membrane vesicles catalyzing light-driven proton uptake and adenosine triphosphate formation,” *J. Biol. Chem.*, vol. 249, no. 2, pp. 662–663, 1974.
- [140] T. Friedrich, S. Geibel, R. Kalmbach, I. Chizhov, K. Ataka, J. Heberle, M. Engelhard, and E. Bamberg, “Proteorhodopsin is a light-driven proton pump with variable vectoriality,” *J. Mol. Biol.*, vol. 321, no. 5, pp. 821–838, 2002.
- [141] M. Traïkia, D. E. Warschawski, M. Recouvreur, J. Cartaud, and P. F. Devaux, “Formation of unilamellar vesicles by repetitive freeze-thaw cycles: characterization by electron microscopy and 31 p-nuclear magnetic resonance,” *Eur. Biophys. J.*, vol. 29, no. 3, pp. 184–195, 2000.
- [142] L. Mayer, M. Hope, and P. Cullis, “Vesicles of variable sizes produced by a rapid extrusion procedure,” *Biochim. Biophys. Acta, Biomembr.*, vol. 858, no. 1, pp. 161–168, 1986.
- [143] J.-L. Rigaud, B. Pitard, and D. Levy, “Reconstitution of membrane proteins into liposomes: application to energy-transducing membrane proteins,” *Biochim. Biophys. Acta, Bioenerg.*, vol. 1231, no. 3, pp. 223–246, 1995.
- [144] N. Pflieger, A. C. Wörner, J. Yang, S. Shastri, U. A. Hellmich, L. Aslimovska, M. S. Maier, and C. Glaubitz, “Solid-state nmr and functional studies on proteorhodopsin,” *Biochim. Biophys. Acta, Bioenerg.*, vol. 1787, no. 6, pp. 697–705, 2009.
- [145] V. I. Gordeliy, R. Schlesinger, R. Efremov, G. Büldt, and J. Heberle, “Crystallization in lipidic cubic phases,” in *Membrane Protein Protocols*, pp. 305–316, Springer, 2003.
- [146] N. E. Good, G. D. Winget, W. Winter, T. N. Connolly, S. Izawa, and R. M. Singh, “Hydrogen ion buffers for biological research,” *Biochemistry*, vol. 5, no. 2, pp. 467–477, 1966.
- [147] W. Junge and S. McLaughlin, “The role of fixed and mobile buffers in the kinetics of proton movement,” *Biochim. Biophys. Acta, Bioenerg.*, vol. 890, no. 1, pp. 1–5, 1987.

- [148] C. Berthomieu and R. Hienerwadel, "Iron coordination in photosystem ii: interaction between bicarbonate and the qb pocket studied by fourier transform infrared spectroscopy," *Biochemistry*, vol. 40, no. 13, pp. 4044–4052, 2001.
- [149] A. Barth, "The infrared absorption of amino acid side chains," *Progress in biophysics and molecular biology*, vol. 74, no. 3, pp. 141–173, 2000.
- [150] H. Suzuki, M. Sugiura, and T. Noguchi, "Monitoring proton release during photosynthetic water oxidation in photosystem ii by means of isotope-edited infrared spectroscopy," *J. Am. Chem. Soc.*, vol. 131, no. 22, pp. 7849–7857, 2009.
- [151] B. Heßling, G. Souvignier, and K. Gerwert, "A model-independent approach to assigning bacteriorhodopsin's intramolecular reactions to photocycle intermediates," *Biophys. J.*, vol. 65, no. 5, pp. 1929–1941, 1993.
- [152] M. S. Braiman, T. Mogi, T. Marti, L. J. Stern, H. G. Khorana, and K. J. Rothschild, "Vibrational spectroscopy of bacteriorhodopsin mutants: light-driven proton transport involves protonation changes of aspartic acid residues 85, 96, and 212," *Biochemistry*, vol. 27, no. 23, pp. 8516–8520, 1988.
- [153] M. S. Braiman, O. Bousche, and K. J. Rothschild, "Protein dynamics in the bacteriorhodopsin photocycle: submillisecond fourier transform infrared spectra of the l, m, and n photointermediates," *Proc. Natl. Acad. Sci.*, vol. 88, no. 6, pp. 2388–2392, 1991.
- [154] F. Garczarek, J. Wang, M. A. El-Sayed, and K. Gerwert, "The assignment of the different infrared continuum absorbance changes observed in the 3000–1800-cm⁻¹ region during the bacteriorhodopsin photocycle," *Biophys. J.*, vol. 87, no. 4, pp. 2676–2682, 2004.
- [155] J. Tittor and D. Oesterhelt, "The quantum yield of bacteriorhodopsin," *FEBS Lett.*, vol. 263, no. 2, pp. 269–273, 1990.
- [156] R. Govindjee, S. Balashov, and T. Ebrey, "Quantum efficiency of the photochemical cycle of bacteriorhodopsin," *Biophys. J.*, vol. 58, no. 3, pp. 597–608, 1990.
- [157] M. Kubicki, D. A. Adamiak, W. R. Rypniewski, and A. Olejniczak, "A synchrotron redetermination of 2-(morpholinium-4-yl) ethanesulfonate monohydrate, including a disordered water molecule," *Acta Crystallographica Section E: Structure Reports Online*, vol. 63, no. 5, pp. o2604–o2606, 2007.
- [158] M. Rehorek and M. P. Heyn, "Binding of all-trans-retinal to the purple membrane. evidence for cooperativity and determination of the extinction coefficient," *Biochemistry*, vol. 18, no. 22, pp. 4977–4983, 1979.

-
- [159] M. P. Heyn, B. Borucki, and H. Otto, "Chromophore reorientation during the photocycle of bacteriorhodopsin: experimental methods and functional significance," *Biochim. Biophys. Acta, Bioenerg.*, vol. 1460, no. 1, pp. 60–74, 2000.
- [160] J.-C. Brochon, "[13] maximum entropy method of data analysis in time-resolved spectroscopy," *Methods Enzymol.*, vol. 240, pp. 262–311, 1994.
- [161] L. Drachev, A. Kaulen, and V. Skulachev, "Correlation of photochemical cycle, h⁺ release and uptake, and electric events in bacteriorhodopsin," *FEBS Lett.*, vol. 178, no. 2, pp. 331–335, 1984.
- [162] A. Maeda, "Application of ftir spectroscopy to the structural study on the function of bacteriorhodopsin," *Israel journal of chemistry*, vol. 35, no. 3-4, pp. 387–400, 1995.
- [163] J. Riesle, D. Oesterhelt, N. A. Dencher, and J. Heberle, "D38 is an essential part of the proton translocation pathway in bacteriorhodopsin," *Biochemistry*, vol. 35, no. 21, pp. 6635–6643, 1996.
- [164] L. S. Brown, L. Zimanyi, R. Needleman, M. Ottolenghi, and J. K. Lanyi, "Photoreaction of the n intermediate of bacteriorhodopsin, and its relationship to the decay kinetics of the m intermediate," *Biochemistry*, vol. 32, no. 30, pp. 7679–7685, 1993.
- [165] R. Korenstein and B. Hess, "Hydration effects on the photocycle of bacteriorhodopsin in thin layers of purple membrane," *Nature*, vol. 270, no. 5633, p. 184, 1977.
- [166] A. E. Blaurock and W. Stoeckenius, "Structure of the purple membrane," *Nature New Biol.*, vol. 233, no. 39, p. 152, 1971.
- [167] H. Kandori, N. Kinoshita, Y. Shichida, and A. Maeda, "Protein structural changes in bacteriorhodopsin upon photoisomerization as revealed by polarized ftir spectroscopy," *J. Phys. Chem. B*, vol. 102, no. 40, pp. 7899–7905, 1998.
- [168] M. Hatanaka, H. Kandori, and A. Maeda, "Localization and orientation of functional water molecules in bacteriorhodopsin as revealed by polarized fourier transform infrared spectroscopy," *Biophys. J.*, vol. 73, no. 2, pp. 1001–1006, 1997.
- [169] E. Navedryk and J. Breton, "Polarized fourier transform infrared (ftir) difference spectroscopy of the m412 intermediate in the bacteriorhodopsin photocycle," *FEBS Lett.*, vol. 202, no. 2, pp. 356–360, 1986.
- [170] K. Rothschild and N. Clark, "Polarized infrared spectroscopy of oriented purple membrane," *Biophys. J.*, vol. 25, no. 3, pp. 473–487, 1979.

- [171] T. N. Earnest, P. Roepe, M. S. Braiman, J. Gillespie, and K. J. Rothschild, "Orientation of the bacteriorhodopsin chromophore probed by polarized fourier transform infrared difference spectroscopy," *Biochemistry*, vol. 25, no. 24, pp. 7793–7798, 1986.
- [172] J. E. Bertie, M. K. Ahmed, and H. H. Eysel, "Infrared intensities of liquids. 5. optical and dielectric constants, integrated intensities, and dipole moment derivatives of water and water-d2 at 22. degree. c," *J. Phys. Chem.*, vol. 93, no. 6, pp. 2210–2218, 1989.
- [173] S. O. Smith, M. S. Braiman, A. B. Myers, J. A. Pardoen, J. M. Courtin, C. Winkel, J. Lugtenburg, and R. A. Mathies, "Vibrational analysis of the all-trans-retinal chromophore in light-adapted bacteriorhodopsin," *J. Am. Chem. Soc.*, vol. 109, no. 10, pp. 3108–3125, 1987.
- [174] K. Fahmy, O. Weidlich, M. Engelhard, H. Sigrist, and F. Siebert, "Aspartic acid-212 of bacteriorhodopsin is ionized in the m and n photocycle intermediates: an ftir study on specifically carbon-13-labeled reconstituted purple membranes," *Biochemistry*, vol. 32, no. 22, pp. 5862–5869, 1993.
- [175] C. Zscherp, R. Schlesinger, J. Tittor, D. Oesterheld, and J. Heberle, "In situ determination of transient pka changes of internal amino acids of bacteriorhodopsin by using time-resolved attenuated total reflection fourier-transform infrared spectroscopy," *Proc. Natl. Acad. Sci.*, vol. 96, no. 10, pp. 5498–5503, 1999.
- [176] H. Kandori, "Polarized ftir spectroscopy distinguishes peptide backbone changes in the m and n photointermediates of bacteriorhodopsin," *J. Am. Chem. Soc.*, vol. 120, no. 18, pp. 4546–4547, 1998.
- [177] K. J. Rothschild and H. Marrero, "Infrared evidence that the schiff base of bacteriorhodopsin is protonated: br570 and k intermediates," *Proc. Natl. Acad. Sci.*, vol. 79, no. 13, pp. 4045–4049, 1982.
- [178] L. Kelemen and P. Ormos, "Structural changes in bacteriorhodopsin during the photocycle measured by time-resolved polarized fourier transform infrared spectroscopy," *Biophys. J.*, vol. 81, no. 6, pp. 3577–3589, 2001.
- [179] J. O. Daldrop, M. Saita, M. Heyden, V. A. Lorenz-Fonfria, J. Heberle, and R. R. Netz, "Orientation of non-spherical protonated water clusters revealed by infrared absorption dichroism," *Nat. Commun.*, vol. 9, no. 1, p. 311, 2018.
- [180] H. Kandori, M. Belenky, and J. Herzfeld, "Vibrational frequency and dipolar orientation of the protonated schiff base in bacteriorhodopsin before and after photoisomerization," *Biochemistry*, vol. 41, no. 19, pp. 6026–6031, 2002.

- [181] N. Dencher and M. Heyn, "Formation and properties of bacteriorhodopsin monomers in the non-ionic detergents octyl- β -d-glucoside and triton x-100," *FEBS Lett.*, vol. 96, no. 2, pp. 322–326, 1978.
- [182] N. A. Dencher and M. P. Heyn, "[2] preparation and properties of monomeric bacteriorhodopsin," in *Methods Enzymol.*, vol. 88, pp. 5–10, Elsevier, 1982.
- [183] N. A. Dencher, K. D. Kohl, and M. P. Heyn, "Photochemical cycle and light-dark adaptation of monomeric and aggregated bacteriorhodopsin in various lipid environments," *Biochemistry*, vol. 22, no. 6, pp. 1323–1334, 1983.
- [184] M. Sonoyama, T. Kikukawa, Y. Yokoyama, M. Demura, N. Kamo, and S. Mitaku, "Effect of molecular assembly on photocycle of reconstituted bacteriorhodopsin: Significant blue shift of the late m photointermediate in the liquid crystalline phase," *Chem. Lett.*, vol. 38, no. 12, pp. 1134–1135, 2009.
- [185] N. A. Dencher and M. P. Heyn, "Bacteriorhodopsin monomers pump protons," *FEBS Lett.*, vol. 108, no. 2, pp. 307–310, 1979.
- [186] T. H. Bayburt, Y. V. Grinkova, and S. G. Sligar, "Assembly of single bacteriorhodopsin trimers in bilayer nanodiscs," *Arch. Biochem. Biophys.*, vol. 450, no. 2, pp. 215–222, 2006.
- [187] E. Pebay-Peyroula, R. Neutze, and E. M. Landau, "Lipidic cubic phase crystallization of bacteriorhodopsin and cryotrapping of intermediates: towards resolving a revolving photocycle," *Biochim. Biophys. Acta, Bioenerg.*, vol. 1460, no. 1, pp. 119–132, 2000.
- [188] L.-O. Essen, R. Siegert, W. D. Lehmann, and D. Oesterhelt, "Lipid patches in membrane protein oligomers: crystal structure of the bacteriorhodopsin-lipid complex," *Proc. Natl. Acad. Sci.*, vol. 95, no. 20, pp. 11673–11678, 1998.
- [189] S. Faham and J. U. Bowie, "Bicelle crystallization: a new method for crystallizing membrane proteins yields a monomeric bacteriorhodopsin structure1," *J. Mol. Biol.*, vol. 316, no. 1, pp. 1–6, 2002.
- [190] A. M. Seddon, P. Curnow, and P. J. Booth, "Membrane proteins, lipids and detergents: not just a soap opera," *Biochim. Biophys. Acta, Biomembr.*, vol. 1666, no. 1, pp. 105–117, 2004.
- [191] K. J. Rothschild, O. Bousche, M. S. Braiman, C. Hasselbacher, and J. L. Spudich, "Fourier transform infrared study of the halorhodopsin chloride pump," *Biochemistry*, vol. 27, no. 7, pp. 2420–2424, 1988.
- [192] Y.-S. Chon, H. Kandori, J. Sasaki, J. K. Lanyi, R. Needleman, and A. Maeda, "Existence of two l photointermediates of halorhodopsin from

- halobacterium salinarum, differing in their protein and water ftir bands,” *Biochemistry*, vol. 38, no. 29, pp. 9449–9455, 1999.
- [193] A. K. Dioumaev and M. S. Braiman, “Nano-and microsecond time-resolved ftir spectroscopy of the halorhodopsin photocycle,” *Photochem. Photobiol.*, vol. 66, no. 6, pp. 755–763, 1997.
- [194] A. Vieler, C. Wilhelm, R. Goss, R. Süß, and J. Schiller, “The lipid composition of the unicellular green alga *chlamydomonas reinhardtii* and the diatom *cyclotella meneghiniana* investigated by maldi-tof ms and tlc,” *Chem. Phys. Lipids*, vol. 150, no. 2, pp. 143–155, 2007.
- [195] W. Breckenridge, G. Gombos, and I. Morgan, “The lipid composition of adult rat brain synaptosomal plasma membranes,” *Biochim. Biophys. Acta, Biomembr.*, vol. 266, no. 3, pp. 695–707, 1972.
- [196] H. Belrhali, P. Nollert, A. Royant, C. Menzel, J. P. Rosenbusch, E. M. Landau, and E. Pebay-Peyroula, “Protein, lipid and water organization in bacteriorhodopsin crystals: a molecular view of the purple membrane at 1.9 Å resolution,” *Structure*, vol. 7, no. 8, pp. 909–917, 1999.
- [197] A. Corcelli, V. M. Lattanzio, G. Mascolo, P. Papadia, and F. Fanizzi, “Lipid-protein stoichiometries in a crystalline biological membrane: Nmr quantitative analysis of the lipid extract of the purple membrane,” *J. Lipid. Res.*, vol. 43, no. 1, pp. 132–140, 2002.
- [198] J. Kuhne, K. Eisenhauer, E. Ritter, P. Hegemann, K. Gerwert, and F. Bartl, “Early formation of the ion-conducting pore in channelrhodopsin-2,” *Angew. Chem. Int. Ed.*, vol. 54, no. 16, pp. 4953–4957, 2015.
- [199] M.-K. Neumann-Verhoeven, K. Neumann, C. Bamann, I. Radu, J. Heberle, E. Bamberg, and J. Wachtveitl, “Ultrafast infrared spectroscopy on channelrhodopsin-2 reveals efficient energy transfer from the retinal chromophore to the protein,” *J. Am. Chem. Soc.*, vol. 135, no. 18, pp. 6968–6976, 2013.
- [200] J. L. Rigaud, M. T. Paternostre, and A. Bluzat, “Mechanisms of membrane protein insertion into liposomes during reconstitution procedures involving the use of detergents. 2. incorporation of the light-driven proton pump bacteriorhodopsin,” *Biochemistry*, vol. 27, no. 8, pp. 2677–2688, 1988.
- [201] J. H. Naismith and I. R. Booth, “Bacterial mechanosensitive channels mscs: evolution’s solution to creating sensitivity in function,” *Annu. Rev. Biophys.*, vol. 41, pp. 157–177, 2012.
- [202] F. Bezanilla, “How membrane proteins sense voltage,” *Nat. Rev. Mol. Cell Biol.*, vol. 9, no. 4, p. 323, 2008.

- [203] A. Keramidas and J. W. Lynch, “An outline of desensitization in pentameric ligand-gated ion channel receptors,” *Cell. Mol. Life. Sci.*, vol. 70, no. 7, pp. 1241–1253, 2013.
- [204] J. Wietek and M. Prigge, “Enhancing channelrhodopsins: an overview,” *Optogenetics: Methods and Protocols*, pp. 141–165, 2016.
- [205] F. Schneider, C. Grimm, and P. Hegemann, “Biophysics of channelrhodopsin,” *Annu. Rev. Biophys.*, vol. 44, pp. 167–186, 2015.
- [206] F. Schneider, D. Gradmann, and P. Hegemann, “Ion selectivity and competition in channelrhodopsins,” *Biophys. J.*, vol. 105, no. 1, pp. 91–100, 2013.
- [207] J. Y. Lin, “A user’s guide to channelrhodopsin variants: features, limitations and future developments,” *Exp. Physiol.*, vol. 96, no. 1, pp. 19–25, 2011.
- [208] C. Bamann, R. Gueta, S. Kleinlogel, G. Nagel, and E. Bamberg, “Structural guidance of the photocycle of channelrhodopsin-2 by an interhelical hydrogen bond,” *Biochemistry*, vol. 49, no. 2, pp. 267–278, 2009.
- [209] G. Váró, L. S. Brown, M. Lakatos, and J. K. Lanyi, “Characterization of the photochemical reaction cycle of proteorhodopsin,” *Biophys. J.*, vol. 84, no. 2, pp. 1202–1207, 2003.
- [210] I. Chizhov, G. Schmies, R. Seidel, J. R. Sydor, B. Luttenberg, and M. Engelhard, “The photophobic receptor from natronobacterium pharaonis: temperature and ph dependencies of the photocycle of sensory rhodopsin ii,” *Biophys. J.*, vol. 75, no. 2, pp. 999–1009, 1998.

Abbreviations

ATR	attenuated total reflection
BR	bacteriorhodopsin
ChR2	channelrhodopsin-2
ChRs	channelrhodopsins
CMC	critical micelle concentration
CD	circular dichroism
DAS	decay-associated spectra
DDM	n-Dodecyl- β -D-Maltoside
DFT	density functional theory
DMPC	1,2-dimyristoyl-sn-glycero-3-phosphocholine
FTIR	Fourier-transform infrared spectroscopy
GS	ground state
HEK	human embryonic kidney
HR	halorhodopsin
IR	infrared
LAN	local area network
LED	light-emitting diode
MES	2-(N-morpholino)ethanesulfonic acid
ND	nanodisc
OG	n-octyl- β -D-glucoside
PDB	protein data bank
PM	purple membrane

PRC	proton release complex
PUC	proton uptake complex
PC	L- α -phosphatidylcholine
PS	L- α -phosphatidylserine
QCL	quantum cascade laser
SB	Schiff base
SVD	singular value decomposition
UV	ultraviolet
WT	wild type

Appendix A

Appendix

A.0.1 Determination of ATR incident angle from water dichroism

Under the thick film hypothesis (for a good review [123]) and assuming no leak from the polarizer, it is possible to determine the average incident angle of the IR beam focused on the ATR using measuring the dichroism of a liquid (in our case water, shown in Fig. A.1) and using the formula:

$$R_{ATRiso} = \frac{2 \sin^2(\theta) - n_{21}^2}{(1 + n_{21}^2) \sin^2(\theta) - n_{21}^2} \quad (A.1)$$

Where $n_{21} = n_2/n_1 = 1,32/3,42$. As can be seen in Fig. A.1, $R = 2,1$, therefore we obtain an average value for the incident angle $\theta = 39^\circ$.

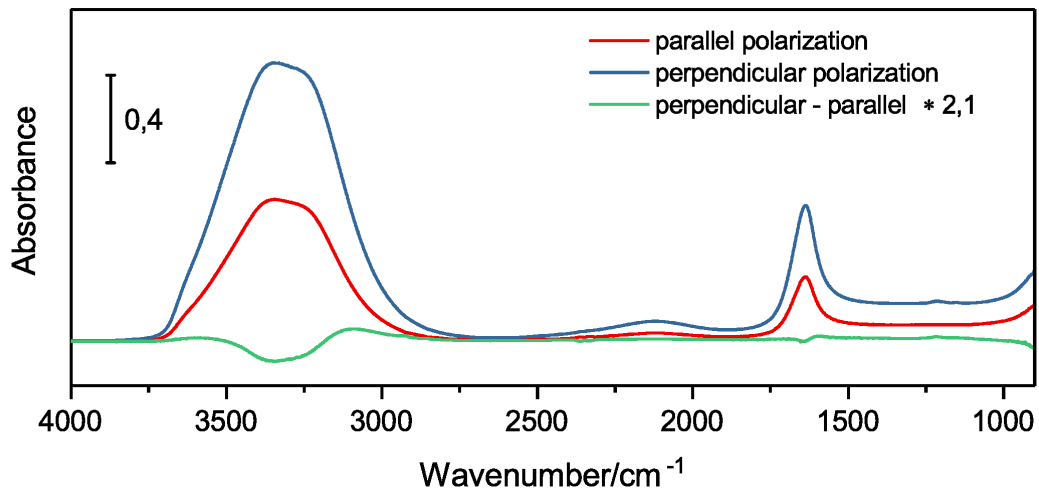


Figure A.1: IR ATR absorption spectra of water with parallel and perpendicular polarized incoming radiation.

The intensity difference of the absorption of liquid water in Fig. A.1 is due to the different effective penetration depth at different polarizations of the incoming IR beam. As the penetration depth is the same for the parallel and perpendicular polarizations, the effective penetration depth changes due

to the different interaction of the evanescent wave field with the sample. The absorbance is proportional to the effective penetration depth defined as:

$$d_e = \frac{n_{21}}{\cos(\theta)} \int_0^\infty E^2 dz = \frac{n_{21} E_0^2 d_p}{2 \cos(\theta)} \quad (\text{A.2})$$

where E_0^2 in the geometry of the ATR showed in Fig. 2.2 can be expressed as $E_{\perp,0} = E_{y,0}$ and $E_{\parallel,0} = \sqrt{E_{x,0}^2 + E_{z,0}^2}$. The expression for $E_{x,0}$, $E_{y,0}$ and $E_{z,0}$ are reported in 2.1.4 [123].

A.0.2 IR and visible Kinetics of pH-sensitive probes during the photocycle of BR

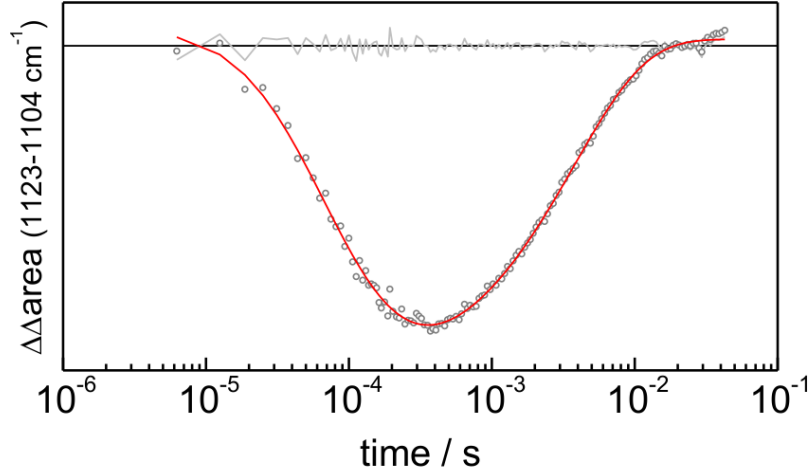


Figure A.2: Kinetics of the area of the peak at 1113 cm^{-1} obtained from the subtraction of two time-resolved FTIR experiments, BR was measured with MES and MES d_{12} . This peak reveals the protonation of the buffer molecules, therefore the kinetics of the proton release and uptake to ad from the bulk. In open grey circles the data points, in red the fit from a lifetime distribution analysis performed by Dr. V. Lorenz Fonfria. Around zero, in grey, the residuals of the fit.

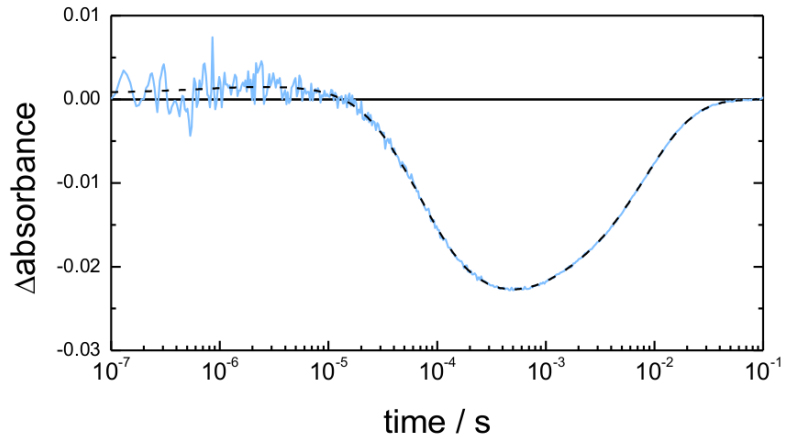


Figure A.3: Kinetics of the proton detection during the photocycle of BR from the pH-indicator fluorescein (blue) covalently bound to Lys129, measured in a flashphotolysis setup at 489 nm and described in [20]. The data has been analyzed with a maximum entropy lifetime distribution by Dr. V. Lorenz Fonfria, the dashed black lines show the corresponding fit.

A.0.3 Polarization-resolved ATR difference spectroscopy with samples at different hydrations

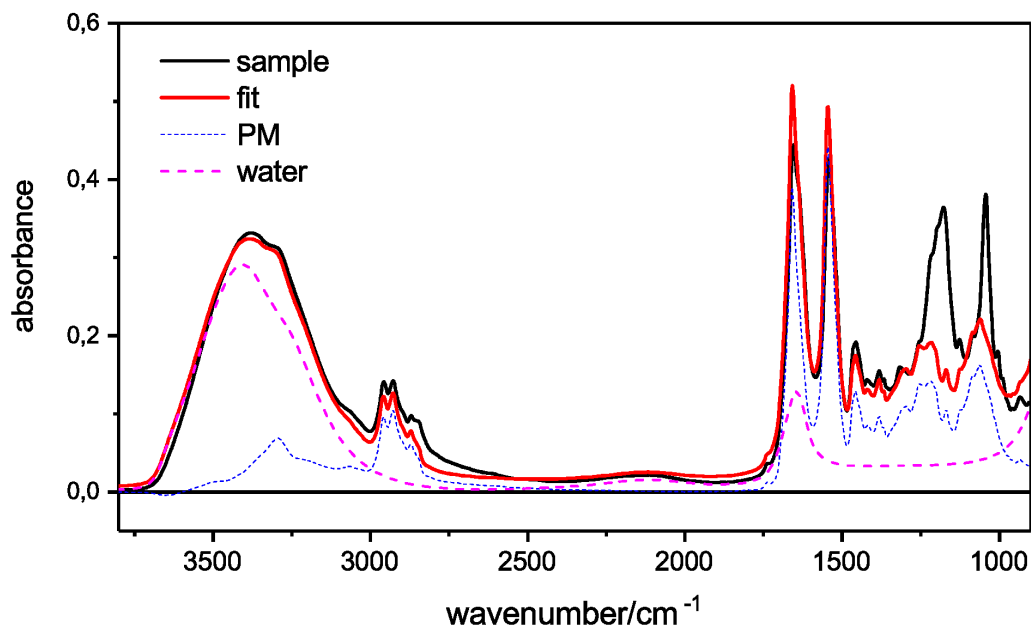


Figure A.4: Absolute absorption spectra of a purple membrane film in a ATR FTIR setup at perpendicular polarization, hydrated with drops of water/glycerol mixture of 2/8. The spectrum (black) is compared with a fit (red) with the extinction coefficient of liquid water (dotted, red) and the extinction coefficient of dry purple membrane in the xy direction (dotted, blue) in order to estimate the effective hydration of the sample. Intense absorption bands below 1200 come from the absorption of HEPES buffer molecules that are present in the solution but not included in the fit. The molar fraction of water molecules per BR monomer was estimated to be 750 ± 70 .

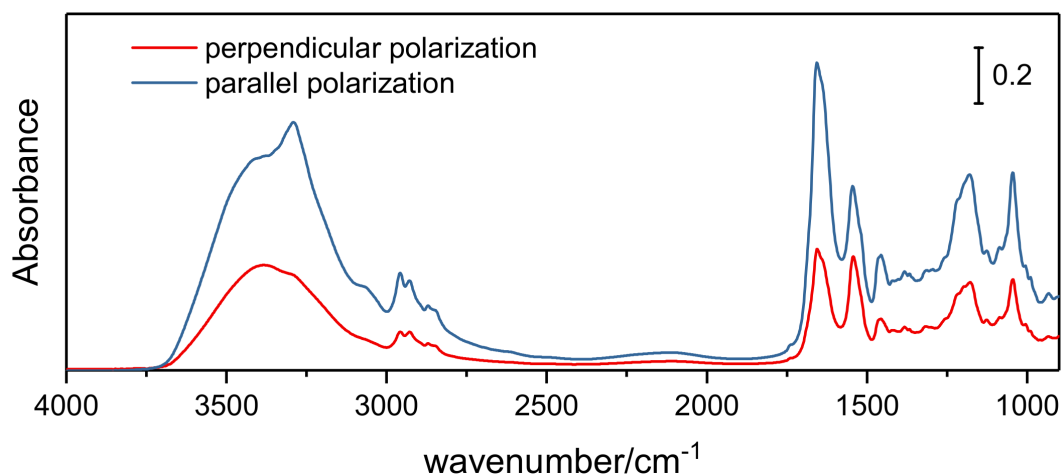


Figure A.5: Absolute absorption of the purple membrane film hydrated with 4/6 glycerol/water drops measured at parallel (blue) and perpendicular (red) polarizations. The molar fraction of water per BR molecules from a fit performed as in Fig. A.4 was estimated to be 1000 ± 100 . The difference in intensity for the two absorption spectra is due to the different effective penetration depth, see A.0.1.

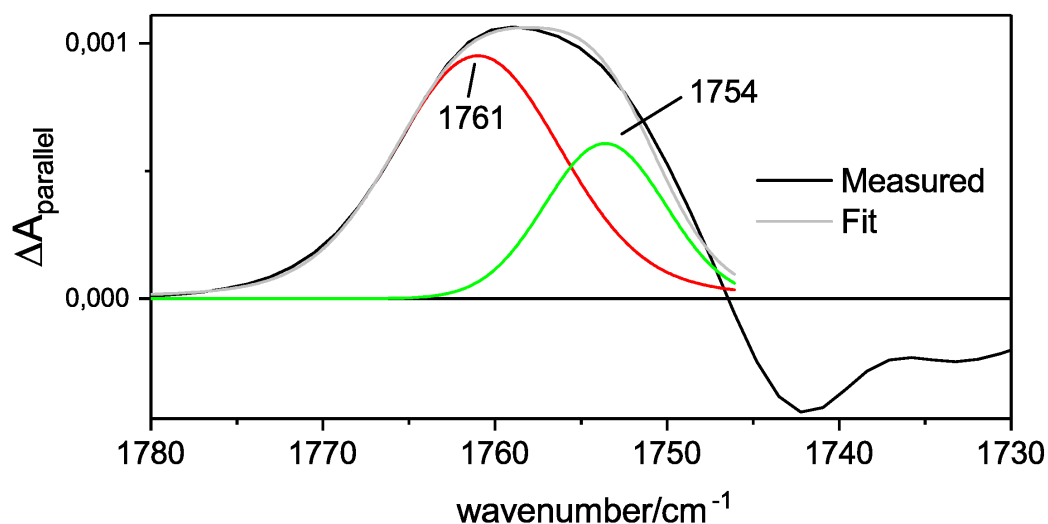


Figure A.6: Difference absorption light-dark spectrum of BR in the carboxylic region. A fit with two voigt functions centered at 1761 cm^{-1} and 1754 cm^{-1} resulted in a difference in the peak area of respectively 70% and 30%.

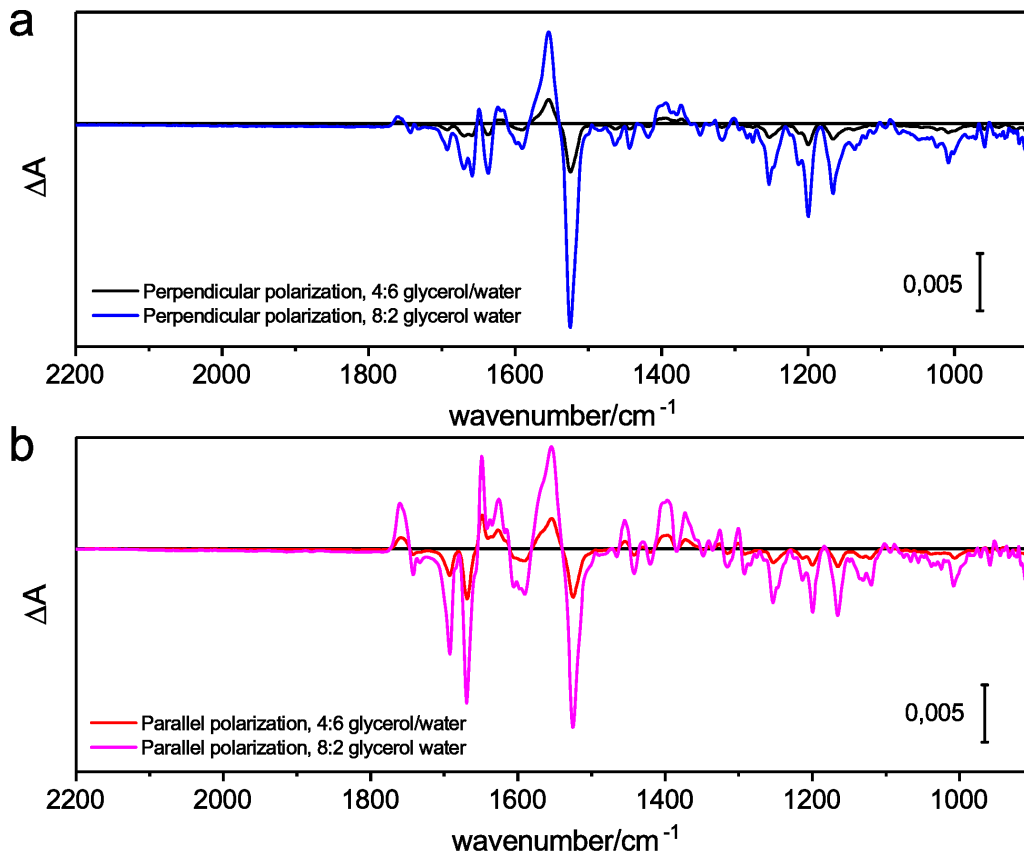


Figure A.7: Light-dark FTIR-ATR difference absorption spectra of the two BR samples at different hydrations, measured with (a) perpendicular and (b) parallel polarized light. The sample hydrated with drops of a 8/2 glycerol/water mixture showed higher intensity of the absorption differences due to a slower photocycle kinetics respect to the sample hydrated with a 4/6 glycerol/water mixture.

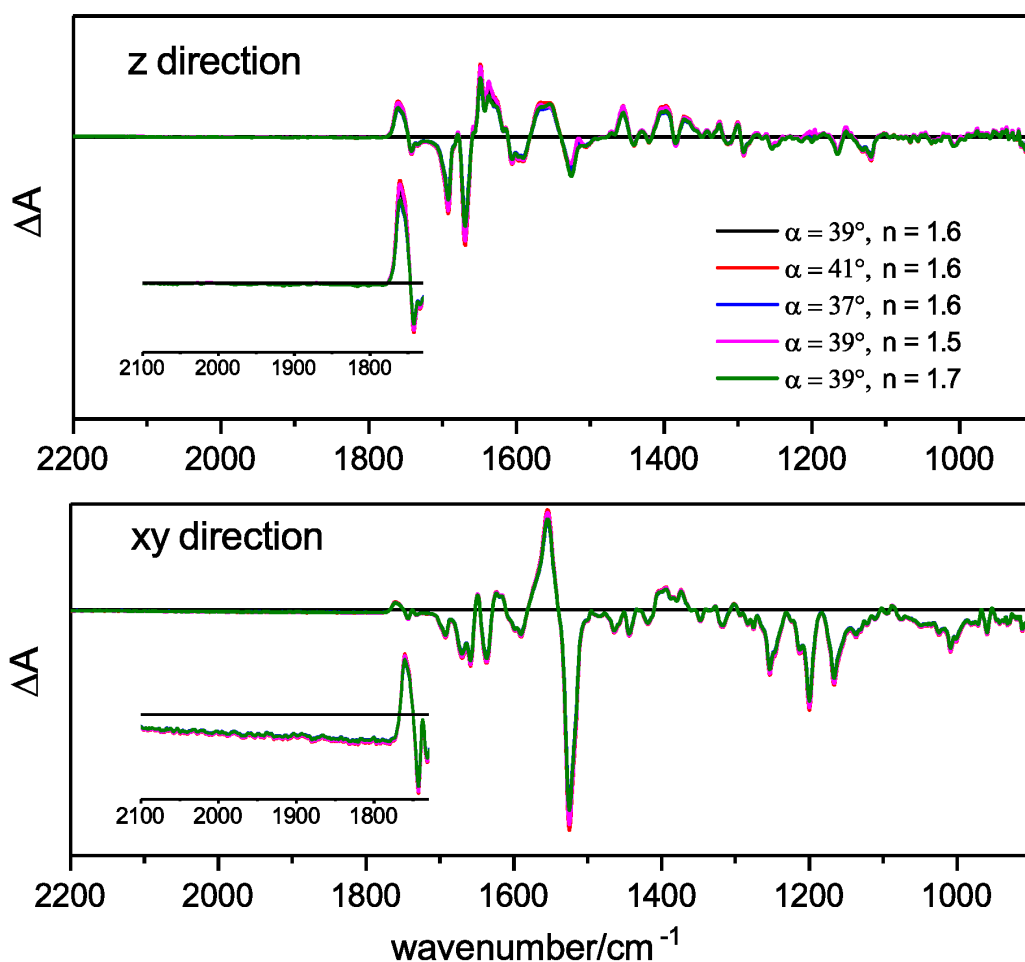


Figure A.8: Light-induced difference absorption spectra measured in a ATR FTIR experiment, calculated for the z (top) and xy (bottom) directions. In the calculation, parameters like the incident angle α of the infrared beam to the ATR crystal and the extinction coefficient of the sample have been varied to demonstrate the robustness of our results to uncertainties in the determination of these parameters. The absorption area of the continuum band has been enlarged in the insets.

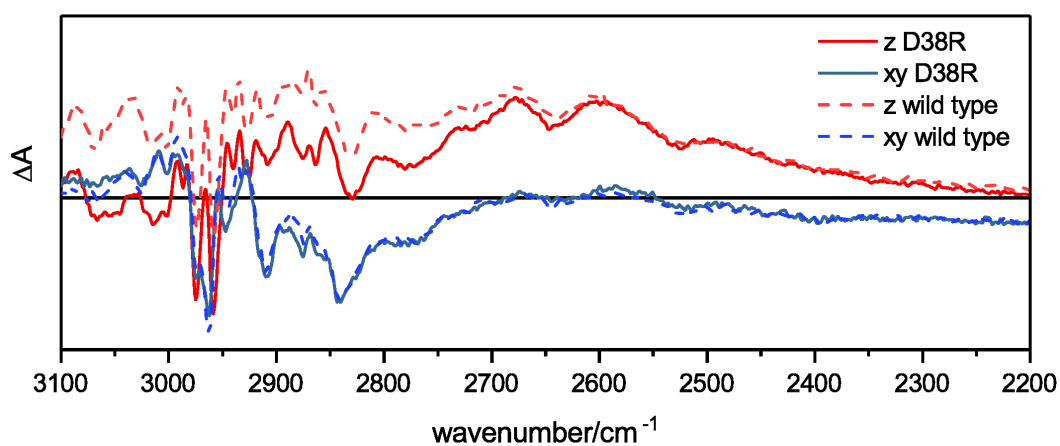


Figure A.9: Light-induced difference absorption spectra measured in a ATR FTIR experiment, calculated for the z (red) and xy (blue) directions in the spectral region between 3100 cm^{-1} and 2200 cm^{-1} for wild type BR (continuous lines) and the D38R mutant (dashed). Under continuous illumination the D38R variant accumulates the M intermediate without consistent amounts of other intermediates.

A.0.4 Polarization-resolved transmission difference spectroscopy with a series of tilting angles

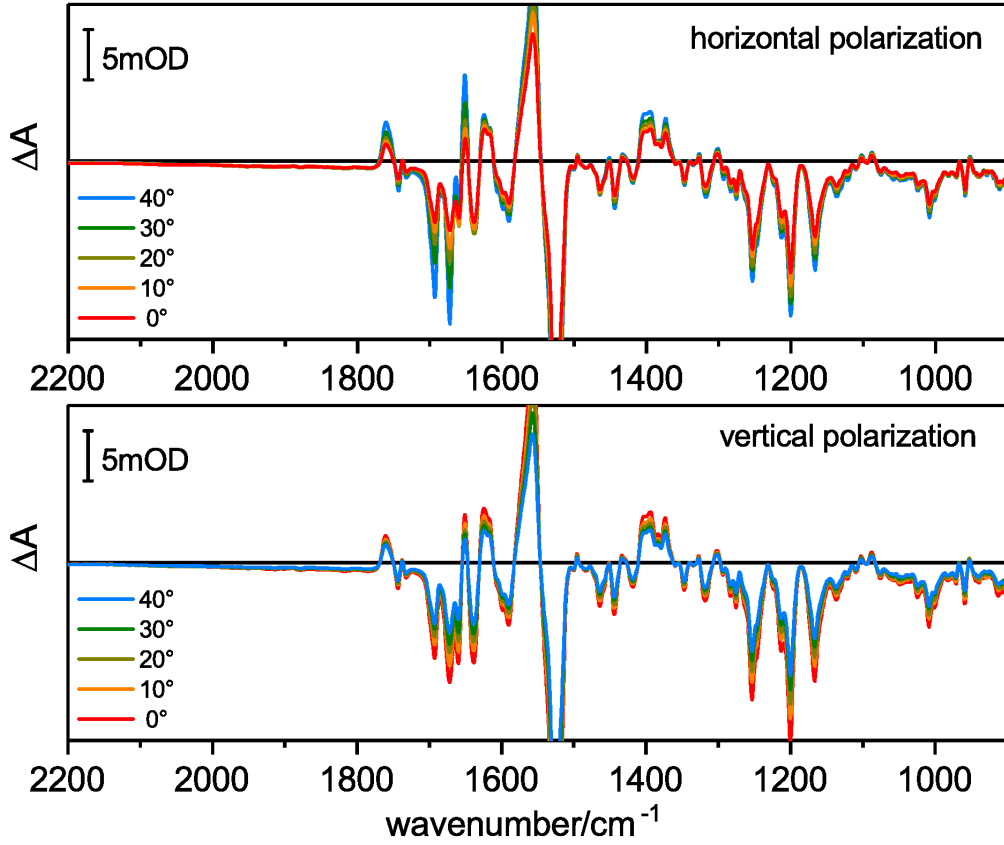


Figure A.10: Light-induced difference absorption spectra measured in a transmission FTIR experiment at different sample tilting angles respect to the incoming infrared beam. The measurements have been carried out for both horizontally polarized (top) and vertically polarized (bottom) infrared beams. The absorption difference spectra measured with vertically polarized light show and increase in intensity proportional to the ammount of sample probed at different tilting angles, the difference spectra with horizontally polarized light include also the informations of the absorption changes in the z direction of the sample.

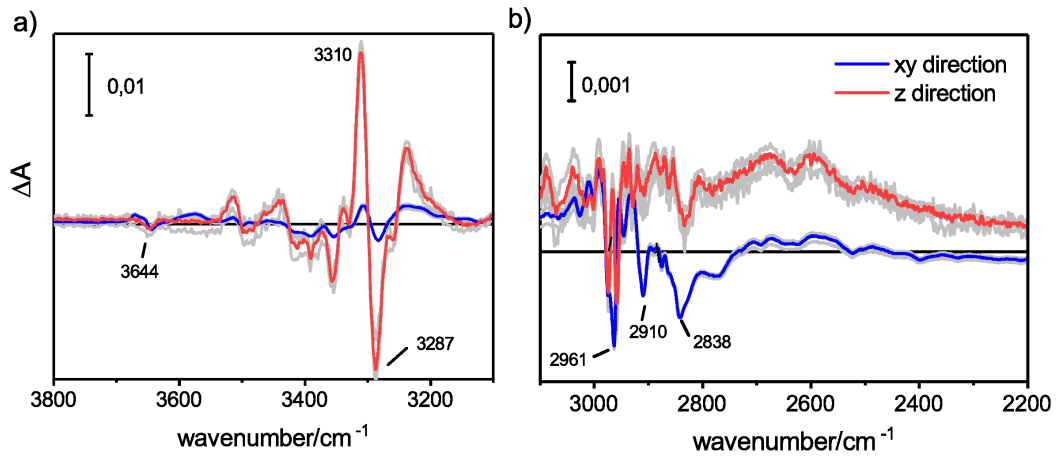


Figure A.11: Light-induced difference absorption spectra measured in a transmission FTIR experiment and calculated in the z (red) and xy (blue) directions in the spectral region between 3800 cm^{-1} and 3100 cm^{-1} (a) and 3100 cm^{-1} and 2200 cm^{-1} . The grey traces represent the calculated absorption differences for each tilting angle, averaged into the red and blue traces.

A.0.5 Photoselection experiment in the xy plane of BR

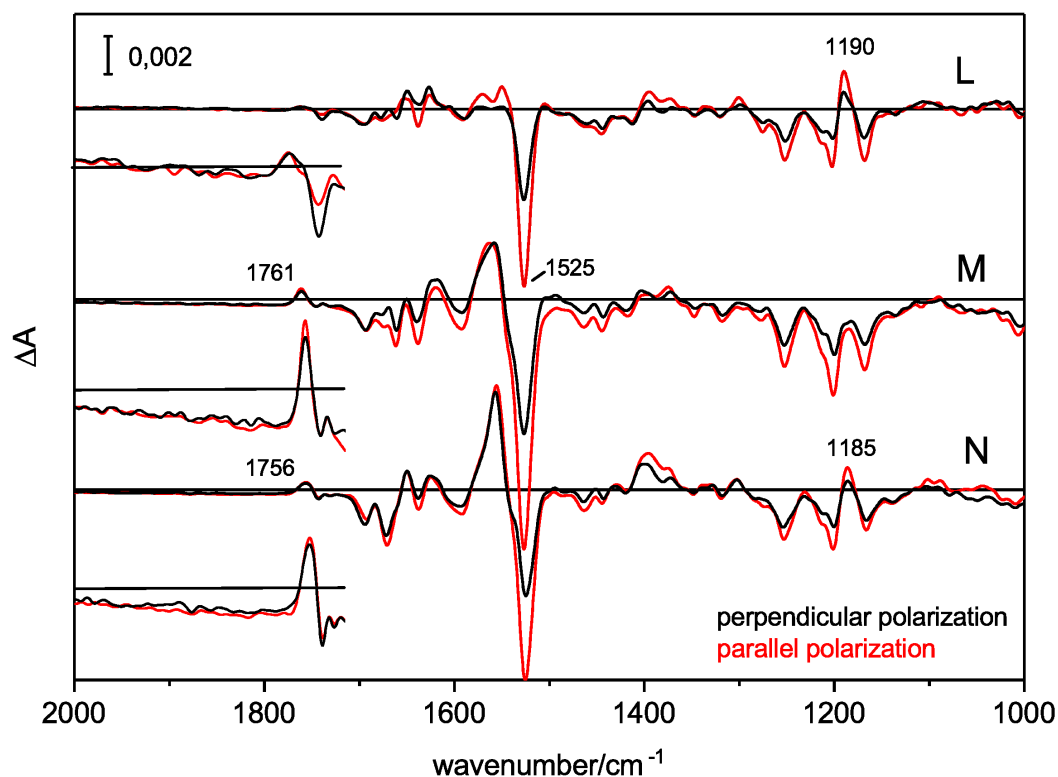


Figure A.12: Difference absorption spectra of BR after a laser pulse measured in a step scan experiment in transmission. A kinetic analysis identified the photocycle intermediates, here reported are the pure spectra of the L, M and N intermediates from the kinetic analysis. In red the results measured with parallel polarization, in black the perpendicular polarization with respect to the exciting polarized visible laser. The experiments have been performed with the sample window perpendicular to the incoming IR beam, that probes the *xy* plane of the sample selectively. The continuum band region is enlarged in the insets and the bands characteristic of the respective intermediates have been marked.

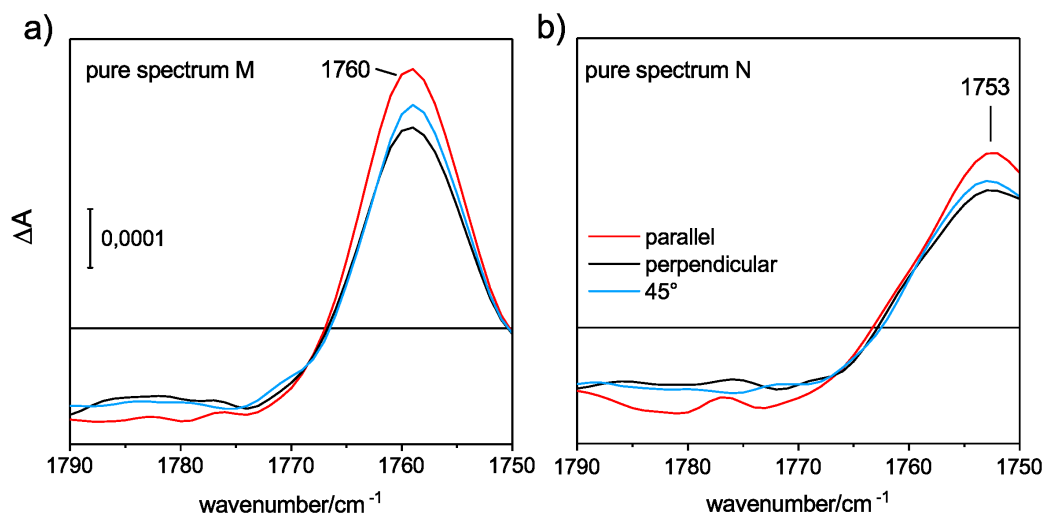


Figure A.13: Pure spectra assigned to the M (a) and N (b) intermediate measured in a time-resolved QCL experiment. Data have been measured at three different polarizations with respect to the exciting laser, parallel (red), perpendicular (black) and at 45° (blue). The three datasets have been merged and SVD analyzed and fitted together using a linear kinetic model, the pure spectra assigned to the M and N intermediates have maximum at $490 \mu\text{s}$ and 8 ms respectively.

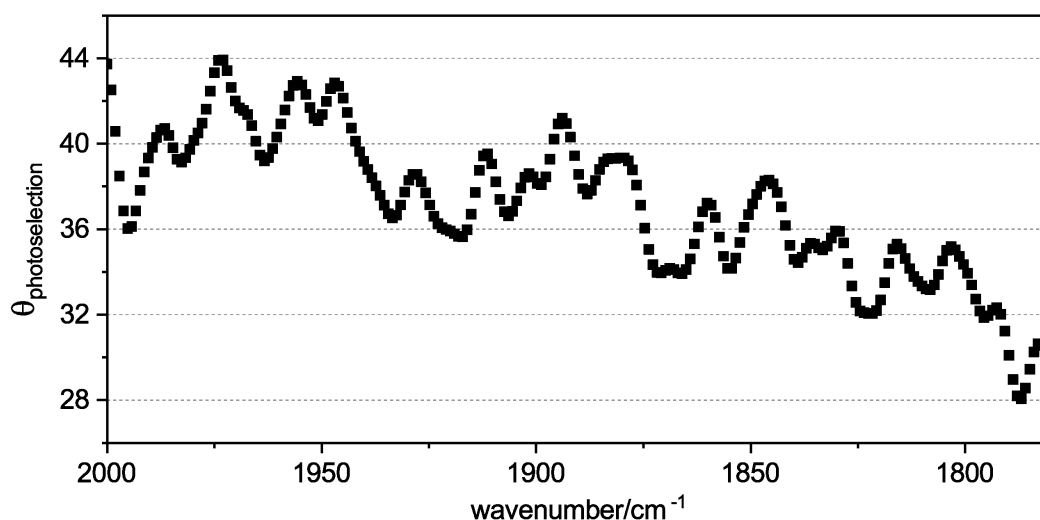


Figure A.14: Angle θ between the dipole moment change of the continuum band and the retinal, projected in the xy plane. The value of the angle has been calculated from the data shown in Fig. 3.23.

A.0.6 Effect of the protein environment on the continuum band: absorption spectra and pumping essays

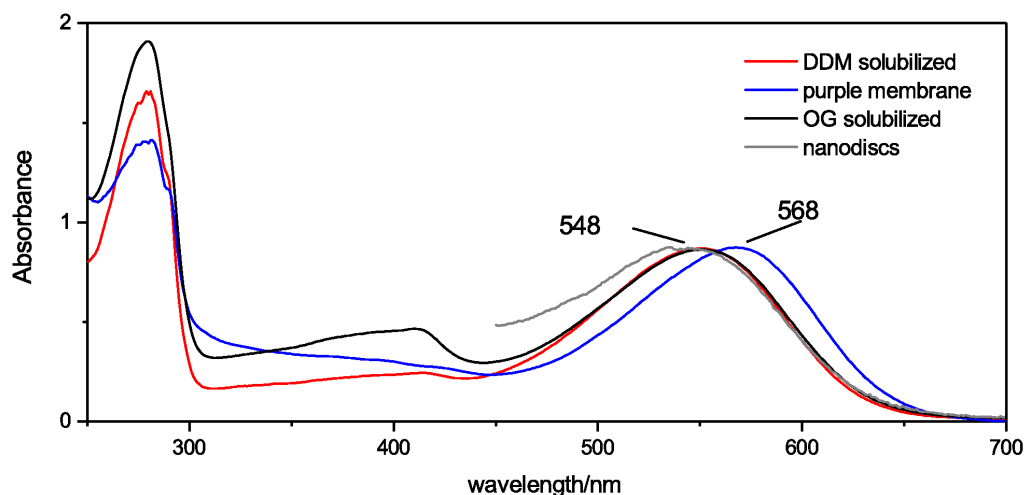


Figure A.15: Visible absorption spectra of BR in the native purple membranes (blue), solubilized in DDM (red), in OG (black) and reconstituted in nanodiscs (grey). The spectrum of BR in nanodiscs was measured in a smaller range due to instability of the spectrometer. The peak at $\sim 280\text{nm}$ comes from the absorption of aromatic amino acids and quantifies the amount of apoproteins, the small peak at $\sim 410\text{nm}$ in the detergent solubilized samples could be the absorption of the retinal molecule in solution (released from denaturated proteins), the peak at $\sim 560\text{nm}$ is the absorption of the covalently bound retinal in BR apoproteins. Spectra were scaled to the absorption maximum at $\sim 560\text{nm}$ for comparison.

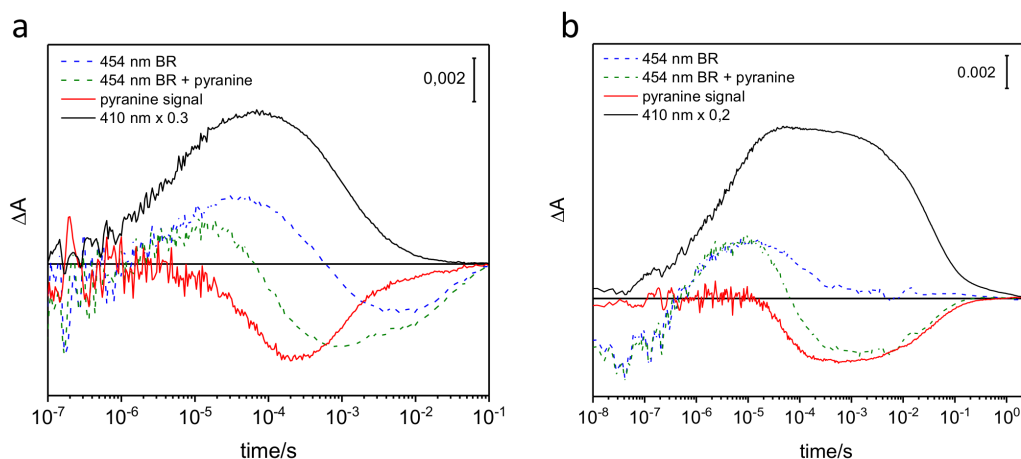


Figure A.16: Measurement of the proton release and uptake activity of BR solubilised in OG (a) and reconstituted in nanodiscs (b) measured in a flash-photolysis experiment with the pH indicator pyranine. Kinetic traces at 454nm have been measured with and without pyranine (dashed lines) in unbuffered solutions at $pH \approx 7.2$ and subtracted to isolate the pyranine response (red). For comparison, the kinetics of the blue shifted intermediate M are scaled and showed in black. Both samples show a negative signal from pyranine indicating first proton release followed by proton uptake from BR.

A.0.7 ChR2 reconstituted in liposomes

ChR2 has been reconstituted in various lipid environments: in a phosphatidylcholine/phosphatidylserine (PC/PS) mixture with ratio 8/2, a pure PS membrane, a lipid mixture from the purple membrane extract from *Halobacterium salinarum* [196, 197] and 1,2-Dimyristoyl-sn-glycero-3-phosphocholine (DMPC) nanodiscs.

While the reconstitution in nanodiscs (A.17) left the visible kinetics almost unaltered as compared to the detergent-solubilized sample, reconstitution in the negatively charged PS lipids (Fig. A.18) showed to strongly influence the protein photocycle in both the P_2 and P_3 intermediates.

The reconstitution in PC or DMPC liposomes led to highly scattering suspensions prone to sedimentation (data not shown), therefore a mixture of PC/PS lipids with ratio 8/2 was preferred because the negative charges of PS lipids help preventing aggregation.

The visible kinetics of ChR2 in this PC/PS lipid mixture has been analysed at different lipid/protein ratio ranging from a w/w ratio of 2 that corresponds to ~ 60 lipid molecules per protein, to a w/w ratio of 20 corresponding to ~ 600 lipids per protein (Fig. A.19). Higher lipids/protein ratios led to highly scattering suspensions and the data are not shown.

The kinetics of the P_2 and P_3 intermediates are affected by the lipid/protein ratio, more specifically both intermediates rise faster at higher protein concentrations. Also the decays of both intermediates are affected by the different lipid/protein ratios, with more relevant changes at a ratio of 2, reminding the

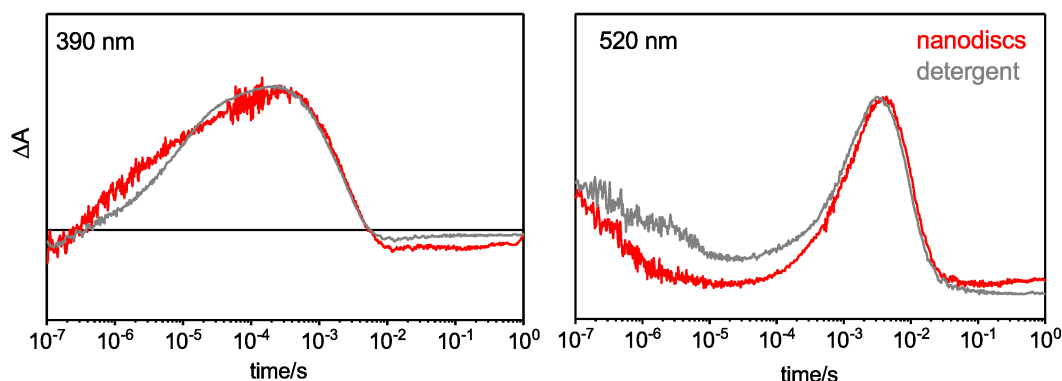


Figure A.17: Visible flashphotolysis kinetics of ChR2 reconstituted in MSP1D1 nanodiscs with DMPC, compared to the same kinetics in detergent solubilised ChR2. The kinetics were scaled to the maximum signal.

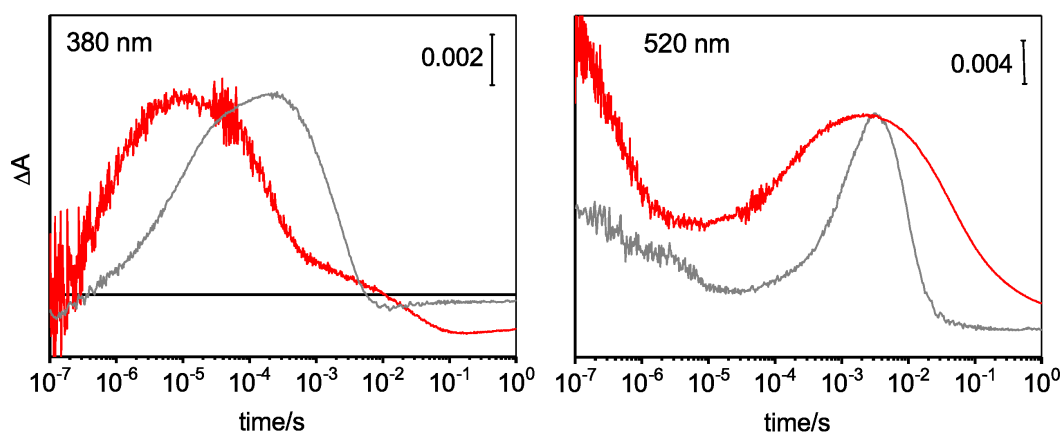


Figure A.18: Visible flashphotolysis kinetics of ChR2 reconstituted in PS liposomes at a lipids/protein weight/weight ratio of 5/1, compared to the same kinetics in detergent solubilised ChR2. The kinetics were scaled to the maximum signal.

kinetics of the PS-reconstituted ChR2. A possible reason for this behaviour is an oligomeric arrangement of the ChR2 dimers when densely reconstituted. Protein-Protein interactions could affect the protein stability and therefore the kinetics. After this analysis a lipid/protein ratio of 5 has been chosen for the IR investigations, where a higher lipid concentration disturbs the measurement due to their high absorption in the Mid-IR range.

ChR2 was also reconstituted in polar lipids from purple membranes, chosen because of the lack of ether lipid species containing a C=O group in the headgroup, allowing for measurements in the carboxylic IR range at improved signal/noise ratios. Unfortunately the reconstitution in polar lipids led to a strong inhibition of the P_2 signal and a broadening in time of the P_3 intermediate: the two intermediates seem to be in equilibrium and are strongly overlapped in time, making interpretation of IR data challenging.

As a remark, solubilised ChR2 presents a photocycle with intermediates

that are well defined in time, facilitating the interpretation of IR spectra. Lipid-reconstituted samples on the other hand show a stronger equilibrium between the P_2 and P_3 intermediates, making time-resolved IR data interpretation not ideal.

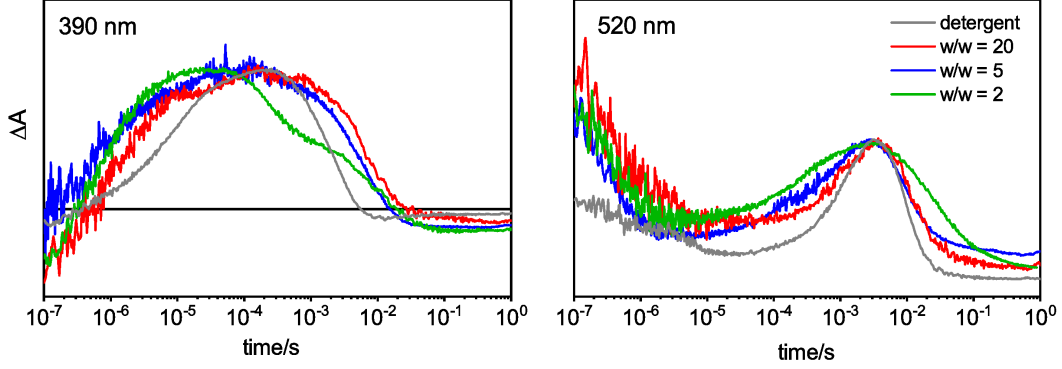


Figure A.19: Visible flashphotolysis kinetics of ChR2 reconstituted in PC/PS liposomes at different lipids/protein weight/weight ratios, compared to the same kinetics in detergent solubilised ChR2. The kinetics were scaled to the maximum signal.

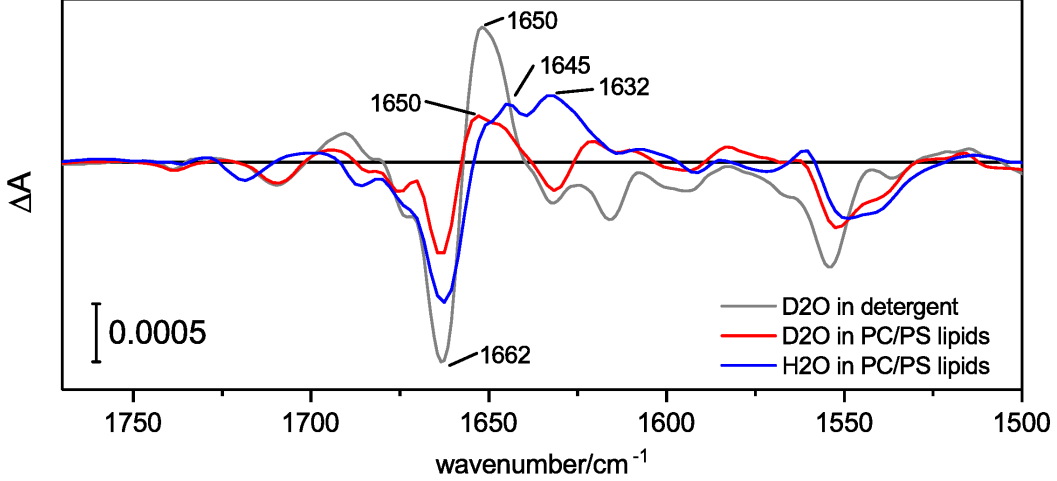


Figure A.20: Light-dark difference infrared spectra of ChR2 in PC/PS lipids in water and in deuterated water, as compared to a solubilised sample in deuterated water. The amide I apparent upshift is probably due to the band overlap with the schiff base.

As polar lipids from *Halobacterium salinarum* don't absorb in the carboxylic range, it was possible to measure reconstituted ChR2 in this range in a QCL experiment. The experiment has been repeated 3 times at different tilting angles to check for possible dichroism caused by a preferred orientation of the sample, the measurements were comparable and no dichroism was observed. Fig. A.23 and Fig. A.24 show the comparisons of this result with the

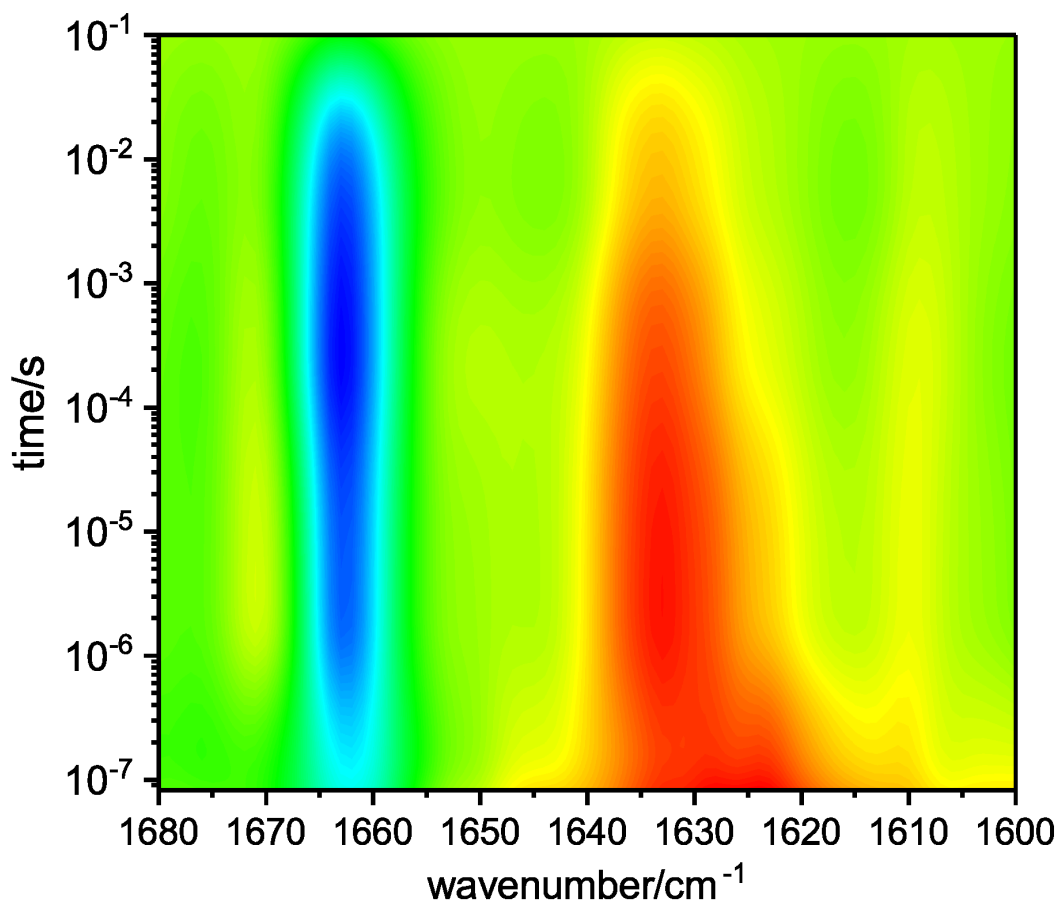


Figure A.21: Time-resolved difference spectra of ChR2 reconstituted in PC/PS lipids measured in a QCL setup and reported here in a contour plot. The color scale goes from the positive values in red to the negative in blue.

kinetics in detergent. The data in detergent were measured by Bernd Schultz and Tom Resler.

In Fig. A.23 the extracted spectra at the time of the maximum absorption of the intermediates P_2 and P_3 as estimated from time-resolved visible spectroscopy in Fig. A.22, in Fig. A.24 the kinetics at 1760 cm^{-1} and at 1737 cm^{-1} after the laser flash.

The photocycle of ChR2 has been well characterized with visible and infrared spectroscopy in detergent [97]. The bands at 1760 cm^{-1} (positive) and at 1737 cm^{-1} (negative) have been assigned to D156, this amino acid is the internal proton donor to the retinal SB. D156 is protonated in the GS and in the first part of the photocycle the frequency of its C=O group upshifts due to H-bonding changes. With the rise of P_3 the positive band at 1760 cm^{-1} vanishes, the negative contribution at 1737 cm^{-1} instead increases its intensity meaning the deprotonation of this amino acid (see Fig. A.24, Fig. A.23 and Fig. 1.6).

As can be observed in Fig. A.24 and Fig. A.23, the spectral and kinetic comparison of the carboxylic difference bands shows some differences between

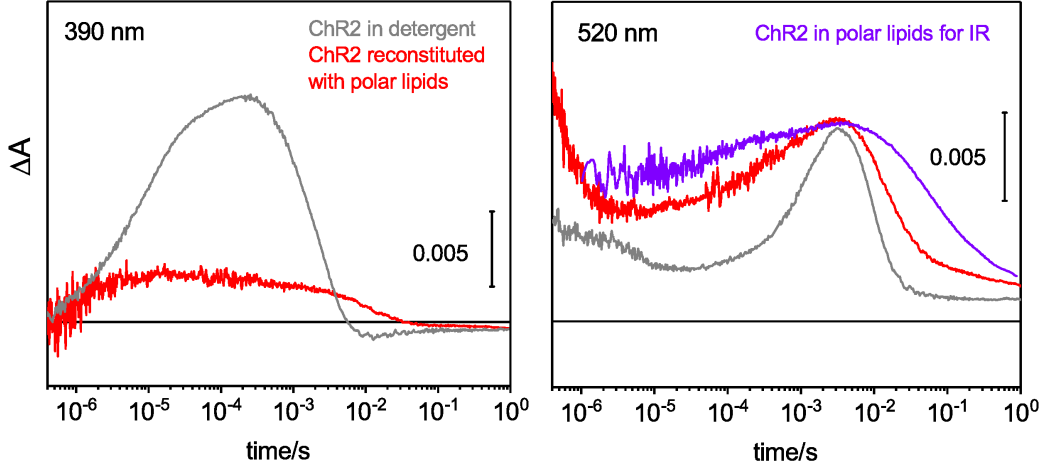


Figure A.22: Visible flashphotolysis kinetics of ChR2 reconstituted in polar lipids from BR (skillfully extracted by Dorothea Heinrich), compared to the same kinetics in detergent solubilised ChR2, the kinetics were scaled on the intensity of the ground state (not shown). In the right panel the kinetics at 520nm are compared with the kinetics of a dried and rehydrated infrared sample.

the detergent-solubilised and lipid-reconstituted samples. The positive band at 1760 cm^{-1} of the reconstituted sample stays positive throughout the whole photocycle and the negative band at 1737 cm^{-1} does not show the kinetics of a deprotonation as can be observed in the detergent-reconstituted sample. Unfortunately the majority of the time-resolved infrared studies on the ChR2 mutants has been performed in detergent-solubilised samples and their results might be not directly applicable to the photocycle of reconstituted samples. The overlap of the P_2 and P_3 in the time domain for the reconstituted ChR2 also complicates the interpretation of the carboxylic bands. It is however to be considered the hypothesis that internal protonation transfers of ChR2 can be affected by reconstitution.

A recent publication that reported on the photocycle of PC-reconstituted ChR2 with time-resolved infrared spectroscopy confirmed the results described above [198] and proposed a different band assignment respect to the detergent-solubilised results.

As mentioned in the main text, the different kinetics of the carboxylic bands in lipid-reconstituted samples could arise from the photoexcitation of the P_4 intermediate (see 3.6), that might have a higher accumulation in the reconstituted samples.

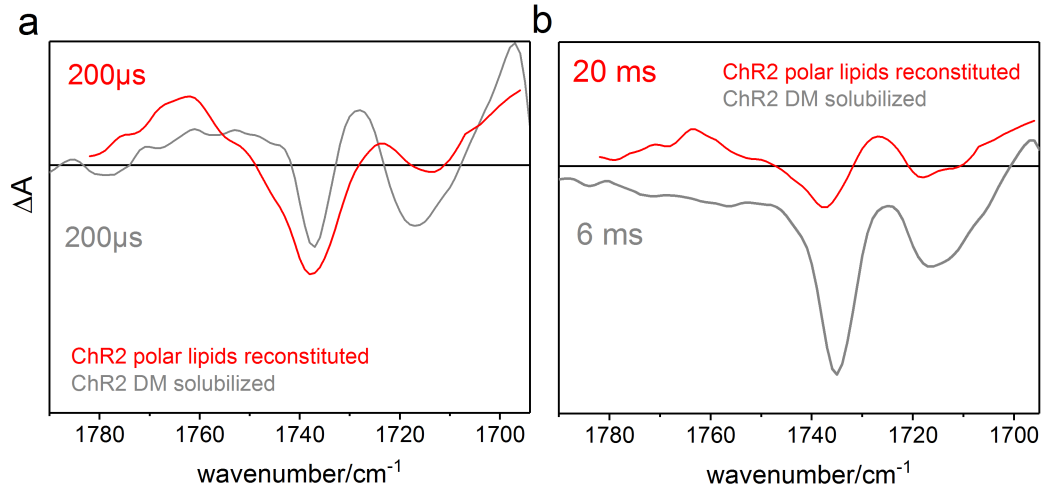


Figure A.23: Time-resolved difference spectra of ChR2 reconstituted in a polar lipid extract from *Halobacterium salinarum*, measured in a QCL setup. The spectra have been extracted at 200 μs, at the maximum accumulation of P_2 , and respectively at 6 ms and 20 ms in detergent and in polar lipids, at the maximum accumulation of P_3

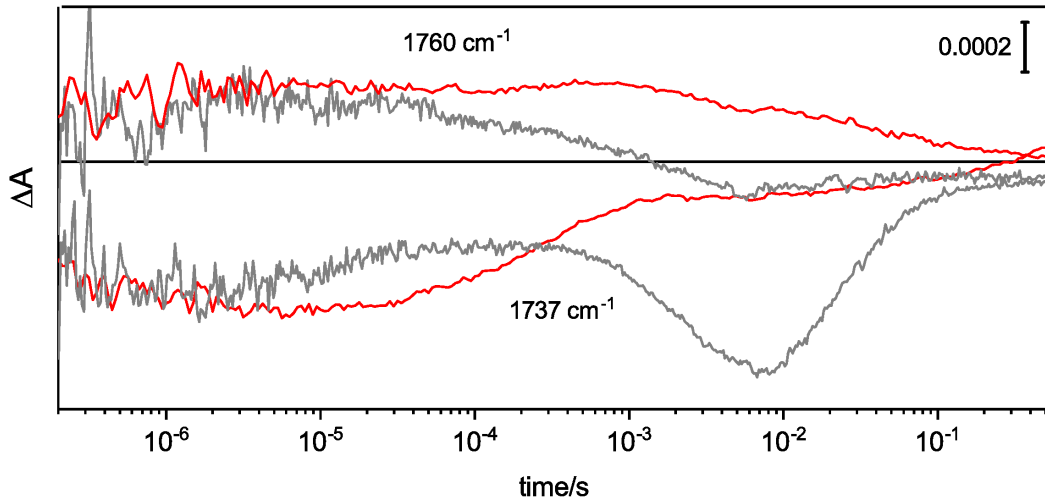


Figure A.24: Kinetics at 1760 cm⁻¹ and at 1737 cm⁻¹ of the photocycle of ChR2 reconstituted in polar lipids from *Halobacterium salinarum* and in detergent.

A.0.8 BR proteoliposomes inwardly pump protons with light

Bacteriorhodopsin is here reconstituted in PC/PS small unilamellar vesicles obtained via freeze-thaw cycles and extrusion through a 100nm polycarbonate filter. The liposomes are formed in an unbuffered solution with pH= ~ 7.2 containing the pH indicator pyranine. The dyes in the volume outside the liposomes have been washed away with size exclusion chromatography (see A.25a). The reconstitution was performed as indicated in [200] to ensure a preferred orientation so that the majority of proteins pump protons inside the liposomes.

With the lipid concentration of 7mg/ml and assuming an average liposome diameter of 100nm I calculated the volume of solution inside the liposomes being 100 times smaller than the outer volume. The starting concentration of pyranine was 50 μ M, in order to end with a final concentration of $\sim 0.5\mu$ M pyranine inside the liposomes.

The removal of the detergent, relevant for the formation of proton-tight membranes, has been followed with infrared spectroscopy, as can be seen in A.25c.

The pH in the external solution has been monitored with a pH-meter, the change in fluorescence of pyranine that follows a change in the pH inside the liposomes has been monitored with a fluorimeter, the proteins have been excited with the continuous light of an LED emitting at 530nm.

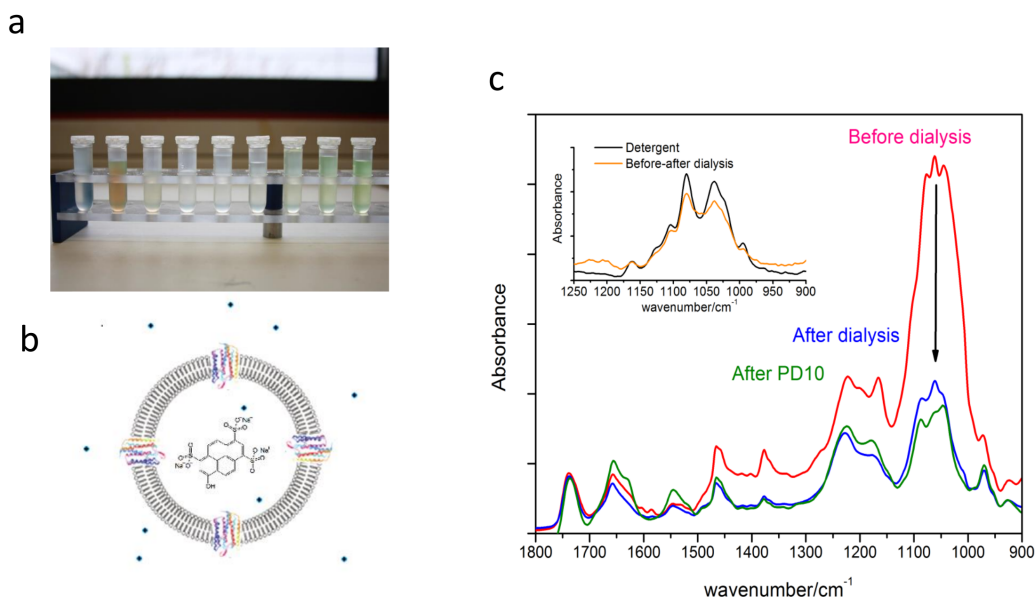


Figure A.25: a) Photo of the result of a size exclusion column (PD10) with aliquots collected from left to right. The second aliquot contains the BR proteoliposomes with pyranine embodied inside, represented in a scheme in b). c) The detergent removal steps are followed via infrared spectroscopy monitoring the absorption bands of detergent vanishing with the subsequent detergent removal steps.

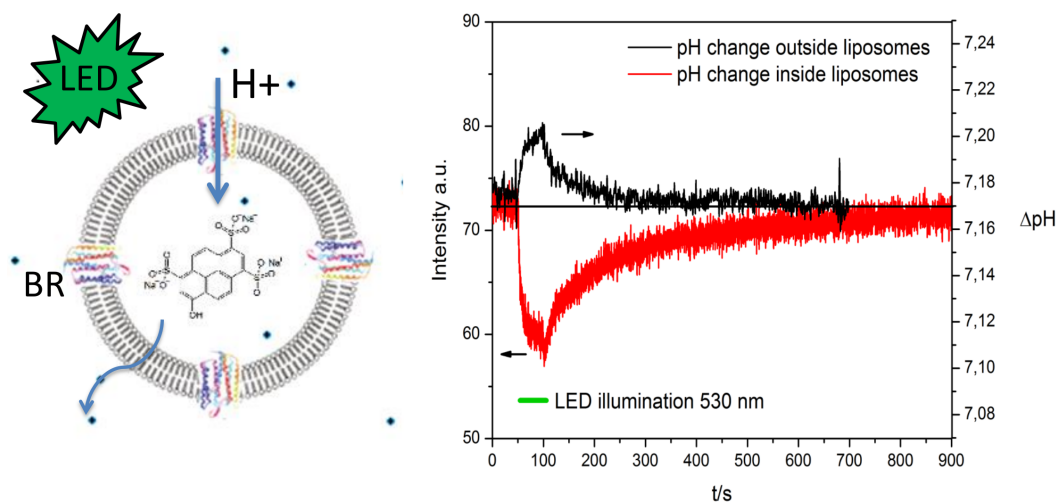


Figure A.26: During green LED illumination (green bar) Bacteriorhodopsin pumps protons inwardly. The acidification of the inner vesicle volume is detected by pyranine (red) while the result of the alcalinization of the outer liposomes volume is detected with a pH-meter (black).

A.0.9 Proton transfers in MastR

At least one unusual deprotonation event has been detected during the photocycle of MastR: in the carboxylic region two negative bands appear after the laser flash at two distinct position and with different kinetics, no positive bands have been observed in this region.

The negative band at 1742 cm^{-1} appears faster than the reaction time of the QCL setup ($\sim 20\text{ ns}$) and decays with the formation of the N/O states. The negative band at 1754 cm^{-1} rises with the formation of the L2 state and decays at the end of the photocycle, as can be seen in Fig. A.27.

The analysis of the photocycle of the D85I variant with FTIR spectroscopy revealed that the intense negative band at 1754 cm^{-1} comes from the deprotonation of the aspartic acid D85 during the photocycle.

The assignment of the negative band at 1742 cm^{-1} is complicated by its ultrafast response, the insensitivity to H/D exchange (data not shown) and the absence of a second carboxylic acid in the membrane region of the protein structure. Two candidates could be the extracellular pair E182/E192, homologous of the E194/E204 in BR. Alternatively the C=O vibration of the ester lipids used for reconstituting the protein could give rise to bands in the carboxylic region although a negative band without positive contributions is highly unlikely.

The reprotonation of D85 during the MastR photocycle is necessary for the completion of the photocycle [12], the proton transfer plays a key role in the chloride translocation. The acceptor(s) of the proton(s) is still unknown and under investigation.

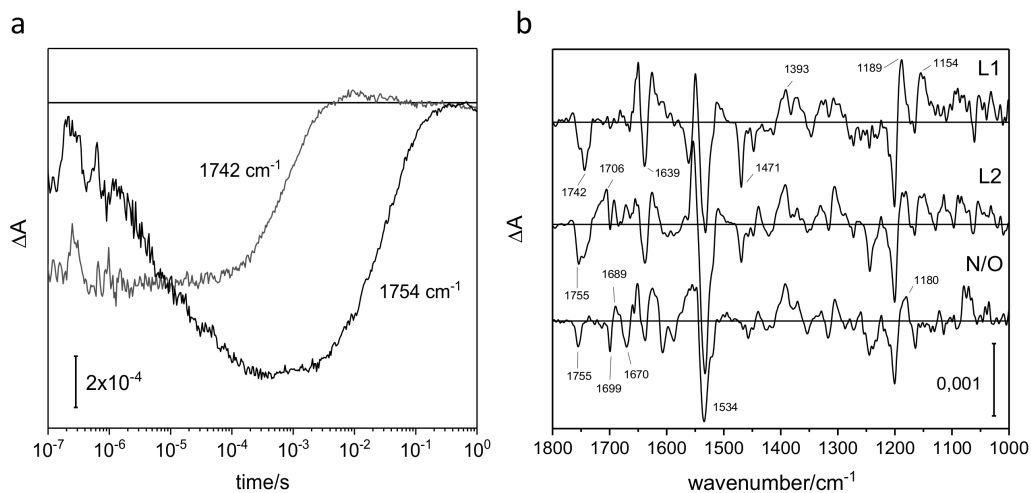


Figure A.27: a) transient absorption changes of two negative carboxylic bands in the photocycle of MastR measured with the QCL setup. b) Time-resolved difference spectra of MastR recorded in a step scan experiment. After a kinetic analysis of time-resolved IR and visible data, the pure spectra of the intermediates L1, L2 and N/O are presented here.

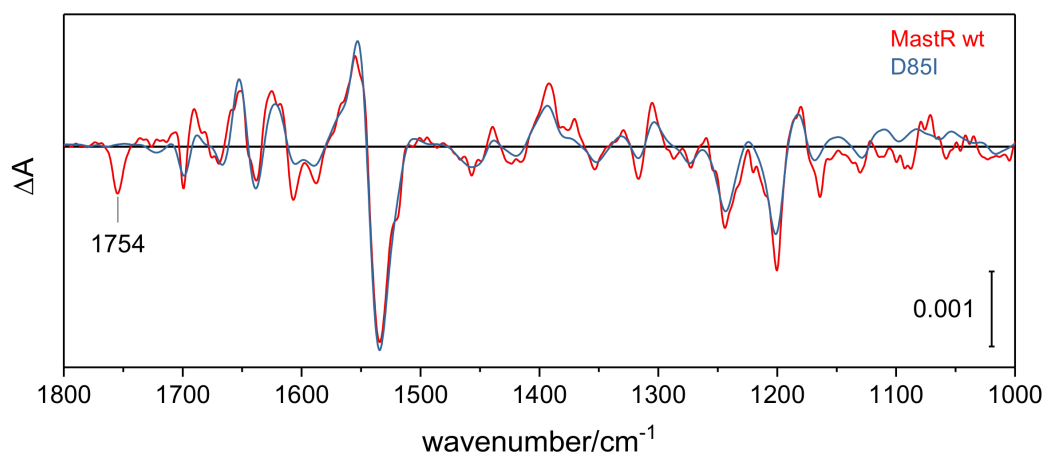


Figure A.28: Difference absorption spectra of wild type and the D85I variant of MastR obtained in step scan experiments. The two difference spectra were measured at two different spectral resolutions, at 4 cm^{-1} for the wt and 8 cm^{-1} for the D85I mutant and extracted at $\sim 1\text{ ms}$.

A.0.10 The photocycle of the P_4 intermediate of ChR2

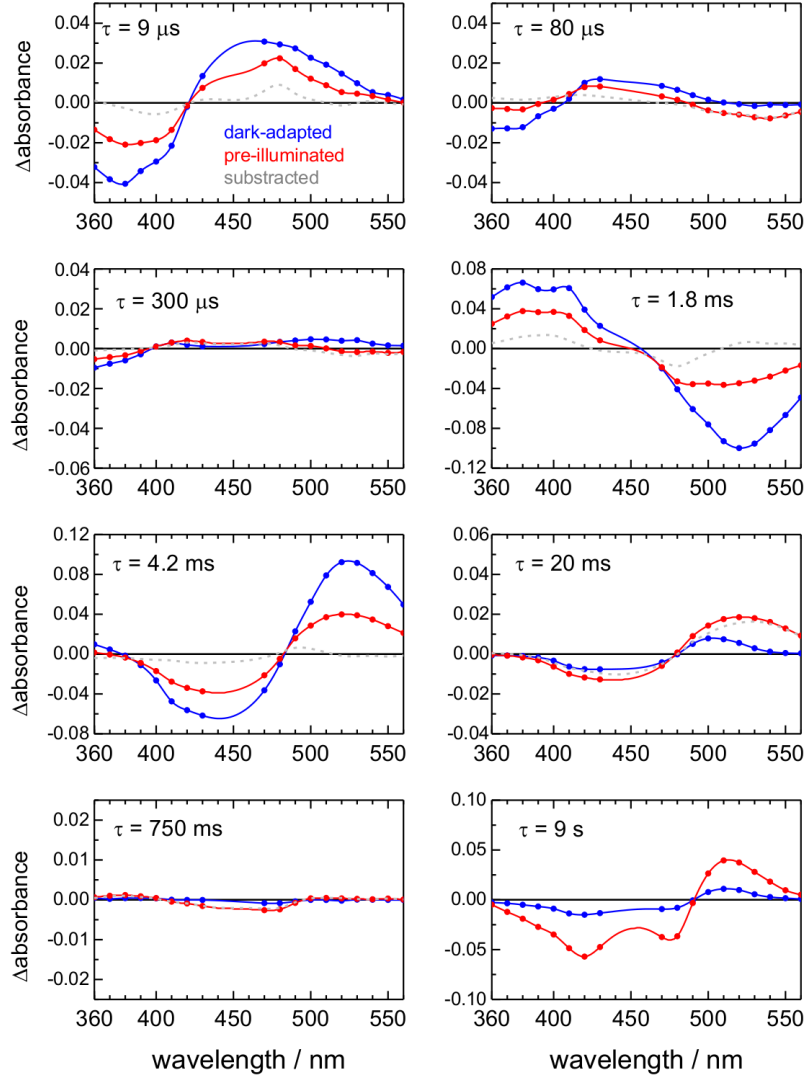


Figure A.29: Decay associated spectra of the time-resolved flashphotolysis difference absorption maps of ChR2 with and without pre-illumination. Each spectrum is associated to the relative time constant indicated in the panel. The subtraction of the spectra with and without pre-illumination gives the DAS of the P_4^{480} photocycle.

Acknowledgements

At first I sincerely thank Prof. J. Heberle for the opportunity to join his group for this thesis work, I am grateful for his support and I value the insights and guidance he provided during this years. He is always wise and appropriate. Many many thanks to Dr. V. Lorenz Fonfria, a lighthouse for any lab-related storm, an open book always helpful with fruitful discussions. Thank you for sharing your expertise.

I thank AG Schlesinger, J. Daldrop, Prof. L. Brown, Prof. I. Shapiro and Prof. S. Ruhman for the successful and pleasant collaborations.

I very much appreciated the great working atmosphere in the AG Heberle and Schlesinger and I have to thank all my colleagues for their joyful support and for the uncountable great moments we spent together.

My gratitude goes also to my parents, my girlfriend and my friends for their continuous and endless support.

I thank the SFB1078 for funding.

Curriculum vitae

Education

Sept 2010-Sept 2012 Master of Science, Physics - Freie Universität, Berlin
Sept 2006-Sept 2010 Bachelor degree, Physics - Università Milano Bicocca

Work experience

March 2013-present PhD student - Freie Universität, Berlin
June-August 2012 Student coworker - Freie Universität
2004-2009 Coordinator of an educational project - ACLI Milano

Interests

Volleyball/Beachvolley
Music, trombone

Selbstständigkeitserklärung

Hiermit bestätige ich, dass die vorliegende Doktorarbeit allein von mir und nur mit Hilfe der angegebenen Hilfsmittel angefertigt wurde. Und ich bestätige hiermit, dass diese Arbeit nicht schon einmal in einem früheren Promotionsverfahren angenommen oder als ungenügend beurteilt wurde.

October 18, 2019

Mattia Saita